Study of Various Graphene and Metal Oxide Containing Nanocomposites as Anode Materials in Li Ion Batteries

A thesis

Submitted by

Shaikshavali Petnikota

in partial fulfilment of the requirement for the award of the degree of

Doctor of Philosophy

in

Nano Science and Technology

Under the supervision of

Dr.-Ing. V. V. S. S. Srikanth

School of Engineering Sciences and Technology

December 2015

DECLARATION

I, **Shaikshavali Petnikota**, declare that this thesis work entitled "**Study of Various Graphene and Metal Oxide Containing Nanocomposites as Anode Materials in Li Ion Batteries**", submitted in partial fulfilment of the requirements for the award of **Doctor of Philosophy** (in Nano Science and Technology) in the School of Engineering Sciences and Technology (SEST), University of Hyderabad is completely my own work except for those referenced. This work was done under the supervision of **Dr.-Ing. V. V. S. S. Srikanth**. This report is a record of the bonafide research work carried out by me and the results incorporated in it have not been reproduced/copied from any source. This work has not been submitted to any other University or Institute for the award of any other degree or equivalent.

Shaikshavali Petnikota
Reg. No.: 10ENPT07
School of Engineering Sciences and Technology
University of Hyderabad

CERTIFICATE

This is to certify that the thesis work entitled "**Study of Various Graphene and Metal Oxide Containing Nanocomposites as Anode Materials in Li Ion Batteries**" submitted by **Shaikshavali Petnikota** (bearing Reg. No. **10ENPT07**) in partial fulfilment of the requirements for the award of the degree of **Doctor of Philosophy** in **Nano Science and Technology** is a bonafide research work carried out by him under my guidance. The thesis work has not been submitted previously in part or in full to this or any other University or Institute for the award of any degree or equivalent.

Thesis supervisor

Dr.-Ing. Vadali V. S. S. Srikanth
Assistant Professor
School of Engineering Sciences and Technology
University of Hyderabad

Prof. R. Singh
Dean
School of Engineering Sciences and Technology
University of Hyderabad

ACKNOWLEDGEMENTS

It is with extreme pleasure I express my sincere, high debt and deep sense of gratitude to my beloved teacher and research supervisor, **Dr.-Ing. V. V. S. S. Srikanth**, with whose benevolent guidance, constant encouragement, constructive criticism, and timely and cheerful cooperation, the present work has taken this form. It is really a great privilege for me to work under his able and pleasant guidance.

I express my heartfelt thanks to **Prof. B. V. R. Chowdari**, Head of Advanced Battery Lab and Executive Director of National University of Singapore-India Research Initiatives (NUS-IRI) for giving me an opportunity to work in Advanced Battery Lab, Department of Physics, NUS, Singapore.

My sincere thanks to **NUS** for financial support through NUS-IRI scheme and giving opportunity for exchange study.

It is my pleasure to acknowledge with heartfelt thanks to **Dr. M. V. Reddy**, Senior Research Fellow, Advanced Battery Lab and Department of Materials Science and Engineering, NUS for his supervision during my exchange studies at NUS, Singapore.

My special thanks to **Assoc**. **Prof. Stefan Adams**, Department of Materials Science and Engineering, NUS for his kind support to my research work.

I acknowledge with gratitude all faculty members of SEST, UoH for training me to adopt good research culture. I also acknowledge with thankfulness **Mr. Naresh Kumar Rotte and Mr. Sandeep Kumar Marka**, PhD scholars, SEST, UoH for their co-operation in experiments and help in writing results and discussion in this thesis.

I will remain ever grateful to Government of India for providing me financial support through Moulana Azad National Fellowship to pursue studies at UoH.

Last but not least, I express my sincere thanks to Mr. Arkaprabha Banerjee, Mr. Keefe Wayne Teo, Mr. Luo Chen, Mr. Amos Sim and my friends and lab mates who have supported my views and ideas. I owe my heartfelt thankfulness for their goodwill, cheerful assistance, incessant help, inspiring discussions, conscientious labour, friendly cooperation, best wishes and advice.

Shaikshavali Petnikota

List of Publications

[1] R. Naresh Kumar, **P. Shaikshavali**, V. V. S. S. Srikanth, K. B. S. Rao, "Reducing agent free synthesis of graphene from graphene oxide", ***AIP Conference Proceedings*** 1538, 262 (**2013**).

[2] **P. Shaikshavali**, N. K. Rotte, V. V. S. S. Srikanth, B. S. R. Kota, M. V. Reddy, K. P. Loh, B. V. R. Chowdari, "Electrochemical studies of few-layered graphene as an anode material for Li ion batteries", ***Journal of Solid State Electrochemistry*** 18(4), 941 (**2014**).

[3] **P. Shaikshavali**, N. K. Rotte, M. V. Reddy, V. V. S. S. Srikanth, B. V. R. Chowdari, "MgO decorated few-layered graphene as an anode for Li ion batteries", ***ACS Applied Materials and Interfaces*** 7, 2301 (**2015**).

[4] **P. Shaikshavali**, S. K. Marka, A. Banerjee, M. V. Reddy, V. V. S. S. Srikanth, B. V. R. Chowdari, "Graphenothermal reduction synthesis of 'exfoliated graphene oxide/iron (II) oxide' composite for anode application in lithium ion batteries", ***Journal of Power Sourc*****es** 293, 253 (**2015**).

[5] **P. Shaikshavali**, S. K. Marka, V. V. S. S. Srikanth, M. V. Reddy, B. V. R. Chowdari, "Elucidation of few layered graphene-complex metal oxide ($A_2Mo_3O_8$, A= Co, Mn and Zn) composites as robust anode materials in Li ion batteries", ***Electrochimica Acta*** 178, 699 (**2015**).

[6] **P. Shaikshavali**, V. V. S. S. Srikanth, Nithyadharseni, M. V. Reddy, S. Adams, B. V. R. Chowdari, "Sustainable graphenothermal reduction chemistry to obtain MnO nanonetworks supported exfoliated graphene oxide composite and its electrochemical characteristics", ***ACS Sustainable Chemistry and Engineering*** 3(12), 3205–3213.

[7] **P. Shaikshavali**, K. W. Teo, L. Chen, A. Sim, S. K. Marka, M. V. Reddy, V. V. S. S. Srikanth, S. Adams, B. V. R. Chowdari, "Insight into intercalation of Li and conversion mechanism of MoO_2 during the cycling of Li ion batteries fabricated with exfoliated graphene oxide/MoO_2 composites as anode materials", to be submitted (2015).

[8] **P. Shaikshavali**, V. V. S. S. Srikanth, M. V. Reddy, S. Adams, B. V. R. Chowdari, "Graphenothermal reduction: Understanding and controlling the reduction of Fe_2O_3 by graphene oxide to synthesize EG/Fe_3O_4, EG/FeO and EG/Fe composites", to be submitted (2015).

Contents

Abstract

Nanocomposites of exfoliated graphene oxide (EG) and few-layered graphene (FLG) with metal oxides are prepared in scalable amounts by easy synthesis approaches. The composites EG/FeO, EG/Fe_3O_4, EG/MnO, EG/MoO_2, FLG/$A_2Mo_3O_8$ (A=Co, Mn and Zn) are synthesized by a novel graphenothermal reduction method. The conversion of solid carbon dioxide was followed to obtain MgO decorated FLG. Afore mentioned as-synthesized composites are characterized systematically for their physical and chemical properties using multitude of characterization techniques. Further, these as-prepared composites are used as active materials to make electrodes which are used as anodes in coin cell Li-ion batteries. The electrochemical properties of the anode materials are studied by Galvanostatic Cycling, Cyclic Voltammetry, Electrochemical Impedance Spectroscopy and Galvanostatic Intermittent Titration techniques. All above mentioned composites are found to be suitable for anodic application in Li-ion batteries. The composites exhibited excellent specific capacities when tested for performance as anode materials in Li-ion batteries.

Chapter 1 Introduction

1.1 Li Ion Batteries

Ever since the Li-ion batteries (LIBs) were commercially introduced, they have become an integral part of everyone's day-to-day life [1,2]. LIBs exhibit enhanced specific capacities enabling them to power electronic gadgets such as smartphones and laptops. Moreover, LIBs are cheaper to manufacture than conventional alkaline batteries such as Pb-acid, Ni-Cd, Ni-MH *etc.*, batteries which lost their market to LIBs due to the presence of toxic elements like Pb and Cd in them, their higher internal resistance and the operational problem like memory effect [1]. Figure 1.1 illustrates the importance of LIBs in comparison to other batteries [1]. Characteristics like high energy density, light weight, compactness, long lifespan, high power capability, high efficiency and eco-friendliness are making LIBs the most promising prospectives for developing electromotive automobiles. However safety and cost are the main issues that are needed to be addressed. Nonetheless, the technology of LIBs is the most efficient and eco-friendly energy storage technology.

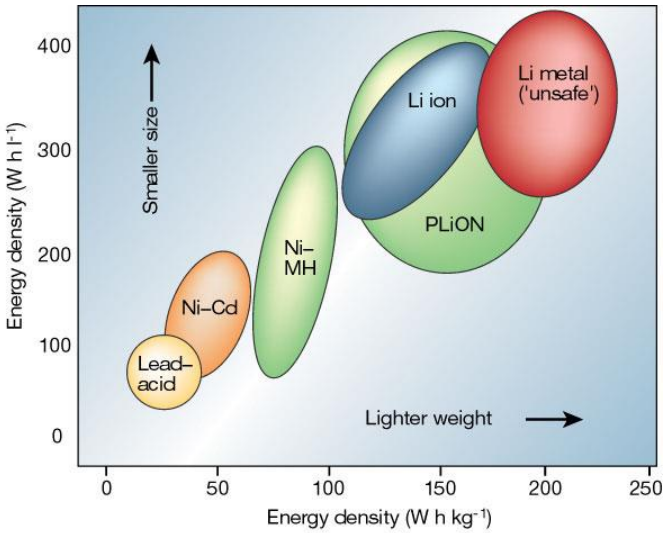

Figure 1.1. Comparison of gravimetric and volumetric energy densities of various secondary batteries. (Adapted with permission from [1])

Introduction

The ever-increasing stringent demands of battery applications implies that the current technology of conventional LIBs need to be re-looked and developed. Current LIBs utilize $LiCoO_2$ as the cathode and graphite as the anode. The principle of operation of LIBs lies in the shuttling of Li-ions between anode and cathode. During the discharge cycle, de-intercalation occurs of the lithiated graphite (LiC_6) which initiates the transfer of Li^+ ions from anode to cathode. The electrons flowing through the external circuit perform the work. The reactions involved during the discharge cycle are shown in Equs. 1.1–1.3. Since these reactions occurring at the cathode and anode are reversible, LIBs can be used for a large number of cycles.

$$\text{Cathode: } Li_{1-x}CoO_2 + x\,Li^+ + x\,e^- \rightarrow LiCoO_2 \quad (1.1)$$

$$\text{Anode: } Li_xC_6 \rightarrow x\,Li^+ + x\,e^- + C_6 \quad (1.2)$$

$$\text{Overall: } Li_{1-x}CoO_2 + Li_xC_6 \leftrightarrow LiCoO_2 + C_6 \quad (1.3)$$

An electrochemical reaction in a cell takes place as long as change in the free energy given by Equ. 1.4 is negative. That is spontaneity of a chemical reaction is the origin of battery's functioning.

$$\Delta G^0 = -nFE^0 \quad (1.4)$$

where F is the Faraday constant (96,496 coulombs per mole), n is number of electrons involved in the reaction, and E^0 is the standard potential of the cell. The overall potential of the cell E^0_{cell} is determined by the electrode potentials of the individual electrodes, the cathode (E^0_{pos}) and the anode (E^0_{neg}) as shown in Equ. 1.5.

$$E^0_{cell} = E^0_{pos} - E^0_{neg} \quad (1.5)$$

The measurable potential of the cell is given by the actual potential difference between the cathode and the anode and is related to the standard potential by Nernst equation (Equ. 1.6).

$$\Delta E = \Delta E^0 - \frac{RT}{nF} \ln \frac{a_i(A)}{a_i(C)} \quad (1.6)$$

where R is the gas constant, T is the absolute temperature and $a_i(\mathrm{C})$ and $a_i(\mathrm{A})$ are the activities of the cathode and anode materials, respectively. The specific capacity $\mathrm{C_{th}}$ of an electrode material can be theoretically calculated by using Equ. 1.7. $\mathrm{C_{th}}$ provides the key information to develop and/or choose new electrode materials.

$$\mathrm{C_{th}} = \frac{\mathrm{N \times F \times 1000}}{\mathrm{3600 \times M}} \qquad (1.7)$$

In Equ. 1.7 $\mathrm{C_{th}}$ is the theoretical capacity in mAh g^{-1}, F is the Faraday constant (obtained by multiplying electron charge (1.6 x 10^{-19} C) and Avogadro's number), N is the number of moles of Li^+ ions/electrons involved in the electrochemical reaction per mole of the electrode material and M is the molar mass of the compound in g mol^{-1}. For example, the theoretical capacity of MnO is (96500 x 2 x 1000)/(3600 x 71) = 755 mAh g^{-1} as 2 moles of Li^+ ions are involved in the Li storage per mole of MnO. The good reversibility in Li cycling of an electrode material is often described by the high capacity retention over a large number of cycles and is usually represented as a plot of specific capacity versus cycle number. The current rate to test the batteries is often selected depending on the theoretical capacity. For example, a current rate of 0.1 C for MnO implies a theoretical capacity of 75.5 mA g^{-1} which means that the current density applied is equivalent to 10 h of discharge or charging time.

$LiCoO_2$–graphite electrode set delivers low capacity and tends to result in the formation of potentially detrimental dendrites while cycling at high current rates. Nonetheless, commercially graphite is still the commercial anode material because it offers maximum discharging and charging capacities in the voltage range 0.15–0.25 V with a negligible hysteresis. However, its shortcomings include low capacities in the range 330–360 mAh/g at low current rates (its theoretical capacity is 372 mAh/g) and high capacity fading at high current rates. Due to rising demands for high battery capacities, especially for electrical cars, it is imperative that research be carried out to develop other anode materials that could make up for the disadvantages of graphite while remaining practical and economical.

1.2 Ideal Characteristics of an Anode Material in LIBs

An ideal anode material for LIBs (i) must be low in weight, capable of yielding large, stable, and reversible gravimetric and volumetric capacities, (ii) must show charge–discharge potential as close as 0 V (versus Li metal), (iii) must be neither soluble in electrolyte nor chemically reactive with electrolyte species like salt or organic solvents of the electrolyte, (iv) must possess good electrical as well as Li-ion conductivity and (v) must be cheaper and eco-friendly [2].

1.3 Graphene as an Anode Material in LIBs

Graphene is an excellent prospective material for various applications owing to its unique one atom thick layered structure in which sp^2 carbons are bonded into hexagons as-like in basal plane of graphite. In fact graphene is nothing but a single basal plane of graphite which is built with AB stacking of several thousand individual graphene layers. Graphene can be classified as a very unique and superior material than many known materials to mankind by its extraordinary properties such as excellent mechanical strength (Young's modulus ~1 TPa and intrinsic strength ~130 GPa) that is 200 times more than steel which ranking it as the strongest thin material ever tested by human beings [3,4]. The exceptional electrical (~2.5 × 10^5 cm^2 V^{-1} s^{-1}; 10 times >Cu) [3,5-7] and thermal (>3000 W m K^{-1}; twice that of graphite or diamond) [8,9] conductivities of graphene makes it very attractive template for various electronic and thermal management applications. In addition graphene possess outstanding properties like huge theoretical specific surface area (up to 2620 m^2 g^{-1}) [3,8], semiconducting nature with zero-band gap which can be tuned easily upon applying voltage [10], very high transparency to white light (97.7%) [11], chemically inert to many species and perfectly impermeable to all species (even gases like H^+ can't pass through its hexagon) [12], it behaves like superconductor at room temperature when coupled with Li atoms [13], it can behave as spintronic material as well as magnetic material simultaneously [14-16], and

capable to show several relativistic quantum mechanical effects like integer and fractional quantum hall effects [16-19]. Graphene alone exhibits all the aforesaid properties and therefore it is one of the distinguished prospective for electrode applications in electrochemical energy storage devices such as Li/Na-ion batteries, supercapacitors *etc.*, [20-24], besides its potential usage in fuel cells [24-27], electromagnetic shielding [28,29], solar cells[24,30,31], transparent, flexible and conducting electrodes for touch screens *etc.,* [32], H_2 and CO_2 storage [33], sensors [34,35], gene sequencing [36], medical diagnostics, drug delivery and bio-sensors [37-40], water desalination [41], ultrahigh frequency transistors (Giga/Tera FET) [42-44], optical modulators [43-47], electrochromoic switching devises [48], anti-bacterial templates [49] and so on.

Graphene is especially very useful as an anode material in LIBs owing to its characteristics listed in the following:

i. Superior electrical conductivity
ii. Exceptional mechanical strength
iii. Chemical inertness towards Li-ions
iv. High theoretical capacity ranging from 744 to 1116 mAh g^{-1}
v. Long-term structural stability over continuous Li-insertion and extraction
vi. In-situ electrochemical exfoliation over long-term cycling

However, there are disadvantages of graphene as an anode material in LIBs. They are:

i. Highly reducing nature towards electrolyte molecules
ii. High Irreversible Capacity Loss (ICL)
iii. High voltage hysteresis
iv. Poor cyclic performance
v. At high current cycling Li-dendrite may form or electroplating takes place
vi. Low volumetric capacity

1.4 Metal Oxides as Anodes in LIBs

Metal oxides (MOs) are another class of materials which have been extensively used as anode materials in LIBs. MOs have very high theoretical capacities and exhibit similar experimental capacities. Even then most of the MOs suffer from poor electronic conductivity and volume changes which limit their practical use. For example, layered MoO_3 possess the highest theoretical capacity of 1117 mAh g^{-1} (when MoO_3 completely reduces and six Li atoms can participate in the conversion reaction) among all the MOs and is capable of showing experimental (reversible) capacity up to 1100 mAh g^{-1} but soon this capacity faded to 750 mAh g^{-1} at the 30^{th} cycle [2]. The advantages of various MOs as anode materials in LIBs are listed in the following:

i. High theoretical and experimental capacities
ii. No Li-dendritic growth or electroplating issue
iii. No current rates restriction
iv. No reduction of electrolyte molecules
v. Very low ICL

However, there are disadvantages of MO's as anode materials in LIBs. They are:

i. Poor electrical conductivity
ii. High volume changes leads to early stage failures
iii. Rapid capacity decay
iv. Poor cyclic performance
v. High voltage hysteresis and high charging – discharging potentials

The MOs as anode materials in LIBs are classified into four categories [2] depending on their interaction mechanism with Li during the reversible Li-insertion and extraction processes. These categories are discussed in the following sections.

1.4.1 Intercalation–Deintercalation Mechanism Based MOs

In these types of MOs, Li-ions intercalate into tetrahedral and octahedral voids of polyhedrons of MO without any chemical interaction and deintercalation too physically takes place. During intercalation volume of polyhedron or unit cell expands but as soon as Li-ion deintercalates unit cell should ideally contract back to attain the original volume. However the lattice of many oxides collapsed and the material became amorphous upon first extraction of Li-ion. The examples of MOs which follow the intercalation−deintercalation mechanism are TiO_2, VO_2, MoO_2, MoO_3, Nb_2O_5, $Li_4Ti_5O_{12}$ (LTO), $MgTi_2O_5$, $LiTiNbO_5$, $TiNb_2O_7$, $LiNbO_3$, $CuNbO_3$, $MgNb_2O_6$, $CaNb_2O_6$, $LiNb_3O_8$, *etc.* [2]. Among these oxides, MoO_2 and MoO_3 will change Li-hosting by intercalation to conversion mechanism upon cycling which further will either increase or decrease the capacity.

1.4.2 Alloying–Dealloying Reactions Based MOs

These types of MOs first undergo reduction by Li to form respective metals under electrochemical conditions. Subsequently, the metals alloy with Li to form intermetallic type compounds. In this case, the best examples are tin based oxides (SnO, SnO_2, *etc.*,). Various reports on SnO and SnO_2 illustrated that they will undergo series of electrochemical reactions as per the Equs. 1.8–1.11.

$$SnO + 2Li^+ + 2\,e^- \rightarrow Sn + Li_2O \quad (1.8)$$

$$SnO_2 + 4Li^+ + 4\,e^- \rightarrow Sn + 2Li_2O \quad (1.9)$$

$$Sn + 4.4Li \leftrightarrow Li_{4.4}Sn \quad (1.10)$$

$$Sn + xLi_2O \leftrightarrow SnO_x + 2xLi^+ + 2xe^- \ (x \leq 2) \quad (1.11)$$

Equations 1.8 and 1.9 are irreversible but as shown in Equ. 1.11, SnO_x can be formed out of Sn in the presence of Li_2O in such a manner that Equ. 1.8 is partially reversible. Other examples of oxides which involve in alloying and dealloying reactions are M_2SnO_4 (M= Mg, Mn, Co, Zn), $ASnO_3$ (A = Ca, Sr, Ba, Co, Mg), Li_2SnO_3, $A_2Sn_2O_7$ (A = Y or Nd),

$K_2(M,Sn)_8O_{16}$ (M = Li, Mg, Fe, Mn, Co, In), SnP_2O_7, $LiSn_2P_3O_{12}$, $Sn_2P_2O_7$, and $Sn_3P_2O_8$, Sb_2O_3, MSb_2O_6 (M = Co, Ni, Cu), $VSbO_4$, $(M_{1/2}Sb_{1/2}Sn)O_4$ (M = V, Fe, In), $BiSbO_4$, $SbPO_4$, and MSb_2O_4 (M = Ni or Co), SiO, SiO_2, GeO, GeO_2, ZnO, CdO, In_2O_3 *etc.* [2].

1.4.3 Conversion (Redox) Reactions Based MOs

Conversion mechanism involves reversible reduction and oxidation reactions (redox couple) of MO according to Equ. 1.12. During the Li-insertion (reduction) metal ion in oxide compounds get reduces and oxygen involves itself in Li_2O formation. Here, freshly formed metal atoms aggregate to nanoparticles which are further surrounded by Li_2O phase. Even though Li_2O is electrochemically inactive, it gets decomposed in the presence of metal nanoparticles to form once again MO during Li-extraction (oxidation).

$$MO + 2Li + 2\ e^- \leftrightarrow M + Li_2O\ (M = Mn, Fe, Co, Ni, Cu) \quad (1.12)$$

There are several examples of conversion type MOs such as MnO, FeO, CoO, NiO, CuO, Cu_2O, Mn_3O_4, Fe_3O_4, Co_3O_4, Mn_2O_3, Fe_2O_3, Cr_2O_3, MnO_2, RuO_2, MoO_2, $MnFe_2O_4$, $ZnFe_2O_4$, $CoFe_2O_4$, $NiFe_2O_4$, $CuFe_2O_4$, $CaFe_2O_4$, $Ca_2Fe_2O_5$, $Ca_2Co_2O_5$, $LiNiVO_4$, $LiCoVO_4$, $LiCuVO_4$, $LiVMoO_6$, $InVO_4$, $Co_2V_2O_7$, $Ni_2V_2O_7$, MnV_2O_6, $Mn(V,Mo)_2O_6$, CoV_2O_6, $MnMoO_4$, $CaWO_4$, $CaMoO_4$, $Co_2Mo_3O_8$, $Mn_2Mo_3O_8$, $Zn_2Mo_3O_8$, $SrTiO_3$, $LaFeO_3$, $LaCoO_3$, $LnFeO_3$, $FeBO_3$, Li_3BO_3, Fe_3BO_6, Cr_3BO_6, FeOOH, $TiOF_2$, NbO_2F *etc.* [2].

1.4.4 Alloy-Dealloying and Conversion Reactions Based MOs

These types of MOs contains both alloy−dealloying element and conversion (transition metal) oxides as a single compound such as $Zn_2Mo_3O_8$ in which Zn is the alloying element whilst Mo phase is conversion oxide as illustrated by Equs. 1.13–1.16. Both conversion and alloying−dealloying mechanisms will either take place simultaneously or alloy-dealloying gets activated slowly after first conversion upon cycling. This synergistic effect may enable Li cycling to yield larger and stable reversible capacities. The main MOs which come under

this category are $ZnCo_2O_4$, $ZnFe_2O_4$, $ZnMn_2O_4$, $CdFe_2O_4$, ZnV_2O_4, Co_2SnO_4, Mn_2SnO_4, Mg_2SnO_4, Zn_2SnO_4, $Sn(II)C_2O_4$ *etc.* [2].

$$Zn_2Mo_3O_8 + Li^+ + e^- \rightarrow Li(Zn_2Mo_3O_8) \quad 1.13$$

$$Li(Zn_2Mo_3O_8) + 15\ Li^+ + 15\ e^- \rightarrow 2\ Zn + 3\ Mo^\circ + 8\ Li_2O \quad 1.14$$

$$2\ Zn + 2\ Li^+ + 2\ e^- \leftrightarrow 2\ ZnLi \quad 1.15$$

$$2\ Zn + 2\ Li_2O \leftrightarrow 2\ ZnO + 4\ Li^+ + 4\ e^- \quad 1.16$$

1.5 Graphene/Metal Oxide Composites as Anodes in LIBs

In the recent past many researchers reported that graphene/metal oxide (G/MO) composites [50-52] as anode materials in LIBs can provide an effective way to simultaneously use all the advantages of graphene and MO while mitigating almost all the drawbacks associated with the individual constituents. In G/MO composites, graphene is expected to offer its excellent electrical conductivity to provide superior reaction environment for MO's electrochemical functionality up to the theoretical limits. It is expected that graphene in G/MO composite acts as mechanical buffer that will enable the suppression of volume change of MO due to lithiation. It also facilitates continuous electrode functioning by avoiding metal or MO agglomeration. Thus graphene can resolve the poor electrical conductivity and mechanical failure due to volume changes of MOs. In a similar way MOs too contribute to overall improvement of composite's anode functioning by sidestepping Li-electroplating or dendritic growth which is the main drawback of graphene when it is cycled at higher current densities. Graphene and MO in the composite are expected to form highly conducting network. G/MO composites are expected to exhibit high capacity and rate capability and improved cycling stability. The details of several studies on G/MO composites relevant to this thesis are discussed in Chapter 2 (Literature Review). Some specific details of MOs as anode materials in LIBs are given in Annexures.

1.6 Problem Definition

In the recent past, researchers worldwide have been working on developing G/MO composites and reported several new synthesis methods (please see Chapter 2). However, there are no path breaking accomplishments with regards to efficient and scalable synthesis methods. For commercialization of graphene and its related materials there is a great need for developing high yield material production methods. This thesis work is an outcome of the effort to obtain various G/MO composites using a simple and effective novel method named graphenothermal reduction (GTR) method. In GTR method, the materials used i.e., Graphene Oxide (GO) prepared by Hummers method [53] and various MO precursors are cheap, easily available and less toxic while there is no requirement for separate reducing agent because GO acts a solid state reducing agent as well as source for exfoliated GO (EG). The simultaneous reduction of both reagents as well as exfoliation of GO lead to the formation of EG/MO composites in the GTR method which does not require any post-synthesis product purification. Due to the innate nature of the synthesis method, GTR method is scalable. In this work, MgO decorated Few-layered Graphene (FLG) was also tested as an anode material in LIBs. Finally systematic physiochemical and electrochemical studies carried on selected materials will be discussed.

1.7 Thesis Objectives

Based on the literature review (to be presented in Chapter 2), the following main thesis objectives were identified:

- Preparation of GOs by Hummers method.
- Understanding and controlling the reduction of Fe_2O_3 by GO to produce EG/Fe_3O_4 and EG/FeO composites.

- GTR synthesis, characterization and electrochemical studies of EG/FeO, EG/MnO, EG/MoO_2, FLG/$A_2Mo_3O_8$ (A= Co, Mn and Zn) composites and testing of these composites as anode materials in LIBs.
- Understanding Li intercalation and conversion mechanisms by MoO_2 in EG/MoO_2 composites
- Electrochemical analysis and testing of MgO decorated FLG as an anode material in LIBs.

Achieving the above objectives will enable an in-depth understanding on various aspects involved in the development of G/MOs composites as anode materials in LIBs.

1.8 Thesis Overview

The thesis work has been organized into 10 chapters. 1st chapter describes the importance and principle of LIBs and the properties of graphene and metal oxides including their importance for Li storage. The aims of the present thesis work and thesis outline are given at the end of this chapter. In the 2nd chapter literature survey highlighting the recent research in the use of graphene/MO composites as anode materials in LIBs has been presented. In the 3rd chapter, materials, synthesis methods and all the experimental procedures (which include general characterization of materials and electrochemical testing of the material) details have been given. 4-8th chapters present the elaborate discussion about various characteristics of different G/MO composites synthesized in this work. 4th chapter describes the reduction of Fe_2O_3 by GO in order to evaluate the controlling parameters of the GTR method. 5th, 6th, 7th, 8th and 9th chapters describe various characteristics including the anodic application in LIBs of EG/FeO, EG/MnO, EG/MoO_2, FLG/$A_2Mo_3O_8$ and MgO decorated FLG composites, respectively. Conclusions and future scope w.r.t this thesis work are given in the final (10th) chapter. The cited references are included under the heading "References" at the end of each chapter and also at appropriate places. Some relevant information has been included under "Annexures".

References

[1] Tarascon JM, Armand M. Issues and challenges facing rechargeable lithium batteries. Nature. 2001;414(6861):359-67.

[2] Reddy MV, Subba Rao GV, Chowdari BVR. Metal oxides and oxysalts as anode materials for Li ion batteries. Chemical Reviews. 2013;113(7):5364-457.

[3] Dreyer DR, Ruoff RS, Bielawski CW. From conception to realization: An historial account of graphene and some perspectives for its future. Angewandte Chemie International Edition. 2010;49(49):9336-44.

[4] Tsoukleri G, Parthenios J, Papagelis K, Jalil R, Ferrari AC, Geim AK, et al. Subjecting a graphene monolayer to tension and compression. Small. 2009;5(21):2397-402.

[5] Geim AK, Novoselov KS. The rise of graphene. Nature Materials. 2007;6(3):183-91.

[6] Geim AK. Graphene: Status and prospects. Science. 2009;324(5934):1530-4.

[7] Chen J-H, Jang C, Xiao S, Ishigami M, Fuhrer MS. Intrinsic and extrinsic performance limits of graphene devices on SiO_2. Nature Nanotechnology. 2008;3(4):206-9.

[8] Liu J, Xue Y, Zhang M, Dai L. Graphene-based materials for energy applications. MRS Bulletin. 2012;37(12):1265-72.

[9] Pop E, Varshney V, Roy AK. Thermal properties of graphene: Fundamentals and applications. MRS Bulletin. 2012;37(12):1273-81.

[10] Cooper DR, D'Anjou B, Ghattamaneni N, Harack B, Hilke M, Horth A, et al. Experimental review of graphene. ISRN Condensed Matter Physics. 2012;2012:56.

[11] S. P. Apell, G. W. Hanson, Hägglund C. High optical absorption in graphene. ArXiv e-prints. 2012;2012.

[12] Berry V. Impermeability of graphene and its applications. Carbon. 2013;62:1-10.

[13] Ludbrook B, Levy G, Nigge P, Zonno M, Schneider M, Dvorak D, et al. Evidence for superconductivity in Li-decorated monolayer graphene. ArXiv e-prints. 2015;2012.

[14] Tombros N, Jozsa C, Popinciuc M, Jonkman HT, van Wees BJ. Electronic spin transport and spin precession in single graphene layers at room temperature. Nature. 2007;448(7153):571-4.

[15] Hashimoto T, Kamikawa S, Yagi Y, Haruyama J, Yang H, Chshiev M. Graphene edge spins: spintronics and magnetism in graphene nanomeshes. Nanosystems: physics, chemistry, mathematics. 2014;5(1):25–38.

[16] Haruyama J. Magnetism and Spintronics in Graphenes: Spin Hall Effect and Edge-Derived Spin Phenomena. Graphene Optoelectronics: Wiley-VCH Verlag GmbH & Co. KGaA 2014, p. 189-208.

[17] Zhang Y, Jiang Z, Small JP, Purewal MS, Tan YW, Fazlollahi M, et al. Landau-level splitting in graphene in high magnetic fields. Physical Review Letters. 2006;96(13):136806.

[18] Du X, Skachko I, Duerr F, Luican A, Andrei EY. Fractional quantum Hall effect and insulating phase of Dirac electrons in graphene. Nature. 2009;462(7270):192-5.

[19] Bolotin KI, Ghahari F, Shulman MD, Stormer HL, Kim P. Observation of the fractional quantum Hall effect in graphene. Nature. 2009;462(7270):196-9.

[20] El-Kady MF, Kaner RB. Scalable fabrication of high-power graphene micro-supercapacitors for flexible and on-chip energy storage. Nature Communications. 2013;4:1475.

[21] Raccichini R, Varzi A, Passerini S, Scrosati B. The role of graphene for electrochemical energy storage. Nature Materials. 2015;14(3):271-9.

[22] Datta D, Li J, Shenoy VB. Defective graphene as a high-capacity anode material for Na- and Ca-ion batteries. ACS Applied Materials & Interfaces. 2014;6(3):1788-95.

[23] Stoller MD, Park S, Zhu Y, An J, Ruoff RS. Graphene-based ultracapacitors. Nano Letters. 2008;8(10):3498-502.

[24] Choi H-J, Jung S-M, Seo J-M, Chang DW, Dai L, Baek J-B. Graphene for energy conversion and storage in fuel cells and supercapacitors. Nano Energy. 2012;1(4):534-51.

[25] Tateishi H, Hatakeyama K, Ogata C, Gezuhara K, Kuroda J, Funatsu A, et al. Graphene oxide fuel cell. Journal of the Electrochemical Society. 2013;160(11):F1175-F8.

[26] Qu L, Liu Y, Baek J-B, Dai L. Nitrogen-doped graphene as efficient metal-free electrocatalyst for oxygen reduction in fuel cells. ACS Nano. 2010;4(3):1321-6.

[27] Zhang Y, Chen B, Zhang L, Huang J, Chen F, Yang Z, et al. Controlled assembly of Fe_3O_4 magnetic nanoparticles on graphene oxide. Nanoscale. 2011;3(4):1446-50.

[28] Yonglai Y, Mool CG, Kenneth LD. Towards cost-efficient EMI shielding materials using carbon nanostructure-based nanocomposites. Nanotechnology. 2007;18(34):345701.

[29] Seul Ki H, Ki Yeong K, Taek Yong K, Jong Hoon K, Seong Wook P, Joung Ho K, et al. Electromagnetic interference shielding effectiveness of monolayer graphene. Nanotechnology. 2012;23(45):455704.

[30] Tielrooij KJ, Piatkowski L, Massicotte M, Woessner A, Ma Q, LeeY, et al. Generation of photovoltage in graphene on a femtosecond timescale through efficient carrier heating. Nature Nanotechnology. 2015;10(5):437-43.

[31] Chang J-H, Lin W-H, Wang P-C, Taur J-I, Ku T-A, Chen W-T, et al. Solution-processed transparent blue organic light-emitting diodes with graphene as the top cathode. Scientific Reports. 2015;5:9693.

[32] Bae S, Kim H, Lee Y, Xu X, Park J-S, Zheng Y, et al. Roll-to-roll production of 30-inch graphene films for transparent electrodes. Nature Nanotechnology. 2010;5(8):574-8.

[33] Ghosh A, Subrahmanyam KS, Krishna KS, Datta S, Govindaraj A, Pati SK, et al. Uptake of H_2 and CO_2 by graphene. The Journal of Physical Chemistry C. 2008;112(40):15704-7.

[34] Rodrigo D, Limaj O, Janner D, Etezadi D, García de Abajo FJ, Pruneri V, et al. Mid-infrared plasmonic biosensing with graphene. Science. 2015;349(6244):165-8.

[35] Vashist SK, Venkatesh AG. Advances in graphene-based sensors and devices. Journal of Nanomedicine & Nanotechnology. 2013;4(1):1000e127.

[36] Merchant CA, Healy K, Wanunu M, Ray V, Peterman N, Bartel J, et al. DNA translocation through graphene nanopores. Nano Letters. 2010;10(8):2915-21.

[37] Feng L, Liu Z. Graphene in biomedicine: opportunities and challenges. Nanomedicine. 2011;6(2):317-24.

[38] Liu J, Cui L, Losic D. Graphene and graphene oxide as new nanocarriers for drug delivery applications. Acta Biomaterialia. 2013;9(12):9243-57.

[39] Weaver CL, LaRosa JM, Luo X, Cui XT. Electrically controlled drug delivery from graphene oxide nanocomposite films. ACS Nano. 2014;8(2):1834-43.

[40] Tehrani Z, Burwell G, Azmi MAM, Castaing A, Rickman R, Almarashi J, et al. Generic epitaxial graphene biosensors for ultrasensitive detection of cancer risk biomarker. 2D Materials. 2014;1(2):025004.

[41] Surwade SP, Smirnov SN, Vlassiouk IV, Unocic RR, Veith GM, Dai S, et al. Water desalination using nanoporous single-layer graphene. Nature Nanotechnology. 2015;10(5):459-64.

[42] Schwierz F. Graphene transistors. Nature Nanotechnology. 2010;5(7):487-96.

[43] Zhang Y, Tang T-T, Girit C, Hao Z, Martin MC, Zettl A, et al. Direct observation of a widely tunable bandgap in bilayer graphene. Nature. 2009;459(7248):820-3.

[44] Liu J, Wright AR, Zhang C, Ma Z. Strong terahertz conductance of graphene nanoribbons under a magnetic field. Applied Physics Letters. 2008;93(4):041106.

[45] Liu M, Yin X, Ulin-Avila E, Geng B, Zentgraf T, Ju L, et al. A graphene-based broadband optical modulator. Nature. 2011;474(7349):64-7.

[46] Li W, Chen B, Meng C, Fang W, Xiao Y, Li X, et al. Ultrafast all-optical graphene modulator. Nano Letters. 2014;14(2):955-9.

[47] Liu M, Yin X, Zhang X. Double-layer graphene optical modulator. Nano Letters. 2012;12(3):1482-5.

[48] Kürüm U, Ekiz OÖ, Yaglioglu HG, Elmali A, Ürel M, Güner H, et al. Electrochemically tunable ultrafast optical response of graphene oxide. Applied Physics Letters. 2011;98(14):141103.

[49] Krishnamoorthy K, Veerapandian M, Zhang L-H, Yun K, Kim SJ. Antibacterial efficiency of graphene nanosheets against pathogenic bacteria via lipid peroxidation. The Journal of Physical Chemistry C. 2012;116(32):17280-7.

[50] Lake JR, Cheng A, Selverston S, Tanaka Z, Koehne J, Meyyappan M, et al. Graphene metal oxide composite supercapacitor electrodes. Journal of Vacuum Science & Technology B. 2012;30(3):03D118.

[51] Xu Y, Yi R, Yuan B, Wu X, Dunwell M, Lin Q, et al. High capacity MoO_2/graphite oxide composite anode for lithium-ion batteries. The Journal of Physical Chemistry Letters. 2012;3:309-14.

[52] Brownson DAC, Kampouris DK, Banks CE. An overview of graphene in energy production and storage applications. Journal of Power Sources. 2011;196(11):4873-85.

[53] Hummers WS, Offeman RE. Preparation of graphitic oxide. Journal of the American Chemical Society. 1958;80(6):1339-1339.

Chapter 2 Literature Review

2.1 Reduction of Metal Oxides by Carbon

It is a common practice to reduce metal oxides or relevant metal precursors with carbon (at temperatures > 600 °C) using a process named carbothermal reduction (CTR) method which is also a well adopted method to synthesize electrode (both anode and cathode) materials for LIBs. For example γ-LiV_2O_5 and $Li_3V_2(PO_4)_3$, and $Mn_2Mo_3O_8$ [1] have been synthesize by CTR method at temperatures in the range 600–750 °C. CTR method has also been usd to synthesize composites such as carbon coated MOs such as Fe_3O_4/C [2], FeO/C [3], MnO/C [4], MoO_2/C [5] etc. In this context it will be intriguing to use GO to reduce metal oxides as GO at elevated temperatures is a rich source of both C atoms (at edges and defects) and gaseous species like CO which can readily reduce MOs or relevant metal precursors. However, it is difficult to imagine GO in place of C as their chemical composition is entirely different. Moreoever, predicting the reduction path will be too difficult unless specific controlled experiments are carried out with the existing relevant literature as the base. In this context, the only instance of GO's use for reduction was during the solution synthesis of few G/MOs composites. In one study both GO and ethanol were collectively used to reduce ammonium heptamolybdate to MoO_2/GO composite [6]. However, the reaction resulted in the formation of MoO_3 when GO was not present in the precursor solution. In another work, hydrothermal synthesis method was used to obtain VO_2-graphene composite by reducing V_2O_5 to VO2 with the use of GO [7]. Similarly, MnO_2 nanorods/GO nanocomposite was first prepared and then it was clacinated at 600 °C to finally obtain MnO nanorods/graphene hybrid material [8]. In another work, GO solution and $KMnO_4$ were reacted to obtain MnO/rGO composite. In this work Mn(VI) was transformed to Mn(II) by managing the GO to $KMnO_4$ weight ratio. In [8,9], the reducing nature of GO was mainly responsible to obtain the final product and therefore GO can be considered as a solid state reducing agent.

2.2 Relevent Graphene-MO Composites

2.2.1 Graphene/FeO Composites

Information on usefulness of iron oxides as anode materials in LIBs is given in *Annexure 1*. Synthesis and chemical stability of FeO is very challenging issue as it readily converts to either Fe and Fe_3O_4 or Fe_2O_3 even at room temperature [10]. FeO can be stabilized by anchoring organic capping agents/surfactants like oleic acid (OA) and oleylamine (OAm) *etc*. Preparing carbon coated FeO (FeO/C) [11] composite is another way to stabilize FeO. FeO/C composite was prepared by reducing Fe_2O_3 by carbon (acetylene black, AB). Fe_2O_3 nanoparticles and AB were taken in different weight ratios and were then mixed by ball milling. The reaction mixture was then heated at 800 °C for 6 h in nitrogen environment to obtain carbon coated FeO composite. Different composites were prepared by changing the AB ratio from 30 to 70 wt.% in the reaction mixture. 50 wt.% composite performed well as an anode material in LIBs. It exhibited a reversible capacity of 510 mA h/g (at 50^{th} cycle and 100 mA/g) that correspond to 96 % retention [11]. Here it is important to mention that FeO alone was used as an anode material in LIBs. It exhibited a reversible capacity of 700 mAh/g which faded to 300 mAh/g at the end of 50^{th} cycle at a current density of 150 mA/g [12].

2.2.2 Graphene/MnO Composites

Information on manganese oxides as anode materials in LIBs is given in *Annexure 2*. In order to overcome the drawbacks (*Annexure 2*) associated with MnO and improve the cyclic performance of MnO based anodes in LIBs, effective approaches like reduction in particle size, coating carbon onto MnO and anchoring MnO onto graphene are studied. There are reports on the synthesis of MnO/graphene composites involve complex and time consuming multi-steps. These works are tabulated in Table 2.1. In addition, some of the chemicals used during the synthesis are highly toxic (For example: hydrazine) and explosive (For example: $Mn(NO_3)_2$). It can also be noted that the processes are mainly solution based and as a result

the final yield of the active electrode material is often low and limited to several mg. However, all of the materials developed in the works which are listed in Table 2.1 have been found to be useful as anode materials in LIBs. For convenience, the detailed lithiation characteristics of these materials are compared with those of EG/MnO composites developed in this work in Chapter 6.

Table 2.1. Reported synthesis methods of graphene/MnO composites.

Reference	Synthesis Details
Nano Energy 2014, 10, 172-180	The precursor MnO_2/GO was prepared by modified Hummers method and annealed at 400 °C in N_2 for 2 h.
J Mater Sci 2014, 49, 1861-1867	MnO_2 nanorods were prepared hydrothermally and mixed with GO solution to obtain a solid product that was calcinated at 600 °C for 2 h in Ar.
ACS Appl Mater Interfaces 2012, 4, 658-664	The solid precursor Mn_3O_4/rGO was prepared hydrothermally at 200 °C for 24 h and then heat treated at 800 °C for 5 h under NH_3 atmosphere.
Electrochim Acta 2011, 56, 8861-8867	Solid Mn–GO cakes prepared from GO + $Mn(NO_3)_2$ suspensions and heated at 400 °C for 2 h in 5 vol.% H_2 atmosphere.
Electrochim Acta 2014, 118, 112-117	GO (to prepare rGO) and rGO/$Mn(Ac)_2$ heated separately at 800 °C for 2h under 5 wt.% H_2/N_2 atmosphere.
Mater Lett 2012, 84, 9-12	rGO prepared at 900 °C for 3 h in Ar whilst rGO/ $Mn(NO3)_2$ were heat treated at 700 °C for 5 h in Ar atmosphere.
J Nanomater 2012, 2012, 10	rGO/$Mn(Ac)_2$ was reduced in $NH_4OH+N_2H_4$ solution to obtain rGO/MnO_x that was heated at 400 °C for 12 h in 5% H_2/Ar flow.
Electrochim Acta 2012, 66, 271-278	Mn_3O_4/rGO prepared hydrothermally at 200 °C for 24 h heated at 400 °C for 2 h in N_2/H_2 flow.
J Power Sources 2012, 216, 201-207	GO + $MnSO_4$ + NH_4HCO_3 precursor solution was prepared and heat treated at 600 °C for 1 h in N_2 atmosphere.
Electrochim Acta 2014, 132, 441-447	Precursor solution was prepared by mixing GO and $Mn(NO_3)_2 \cdot 6H_2O$ in distilled water and spray pyrolysis was carried out at 900 °C with nitrogen as the carrier gas.
Adv Funct Mater 2013, 23, 2436-2444	A solid precursor was prepared from aqueous solution of GO and $Mn(CH_3COO)_2 \cdot 4H_2O$ that was reduced with hydrazine; further reduction was carried out in 5% H_2 /Ar atmosphere for 5 h at 500 °C.

2.2.3 Graphene/MoO_2 Composites

Information on molybdenum oxides as anode materials in LIBs is given in *Annexure 3*. In order to overcome the drawbacks (*Annexure 3*) associated with MoO_2 and improve the cyclic performance of MoO_2 based anodes in LIBs, several synthetic approaches (Table 2.2, next page) have been reported for preparing MoO_2 based nanostructures like carbon coated MoO_2, nitride coated MoO_2 and Mo_2N nanolayer coated MoO_2, GO-MoO_2 and graphene-MoO_2 composites. However, easy and sustainable synthesis methods are unavailable to produce graphene-MoO_2 composites in bulk amounts. Moreover, the composites of MoO_2 with graphene reported so far are synthesized by various solvent medium assisted methods which involve multi-steps and use of toxic chemicals. In addition, solid precursors prepared were annealed in H_2 and/or C_2H_2 environments which increases the production cost. Few of these methods utilized separately prepared rGO or EG. In some cases reaction time is as long as 24 h. For convenience, the electrochemical characteristics of these MoO_2 based anode materials are compared with those of EG/MoO_2 composites developed in this work in Chapter 7.

2.2.4 Graphene/$A_2Mo_3O_8$ (A= Co, Mo and Zn) Composites

Information on mixed bimetallic oxides (ternary metal oxides) as anode materials in LIBs is given in *Annexure 4*. There are also few reports on graphene-complex metal oxide composites as discussed below. However, the synthesis of these materials is typically carried out using wet-chemical routes which typically involve the use of hazardous chemicals (commonly hydrazine hydrate) and time consuming multi-steps. Moreover, most of the times these materials can be used as anode materials in LIBs only after their post-synthesis purification. Additionally, yield of the wet-chemical methods is very less. Apart from the reports in *Annexure 4*, reports on the synthesis of graphene/$Co_2Mo_3O_8$ and graphene/$Zn_2Mo_3O_8$ composites including bare $Zn_2Mo_3O_8$ are unavailable exclusively for Li ion storage application.

Table 2.2. Reported synthesis methods of graphene/MoO_2 composites.

Reference	Synthesis Details
ACS Nano 2011, 9, 7100-7107	An aqueous solution of GO+$H_3PMo_{12}O_{40}\cdot xH_2O$ (PMA) reduced with Hydrazine hydrate under sonication for 3 h and thus obtained solid product was heated at 500 °C in 5% H_2/Ar atmosphere for 5 h.
J Phys Chem Lett 2012, 3, 309-314	GO+$(NH_4)_6Mo_7O_{24}\cdot 4H_2O$ (AHM) dispersed in ethanol + HNO_3 was solvothermally treated at 160 °C for 16 h.
J Phys Chem C 2014, 118, 24890-24897	Reaction mixture GO + Ethylene Glycol + Mo Powder + H_2O_2 hydrothermally heated at 200 °C for 24 h. (MoO_2-GO composite)
Electrochim Acta 2012, 79, 148-153	Precursor was prepared by hydrothermal (pH~1) reduction of GO + AHM + ascorbic acid at 180 °C for 10 h and calcined at 400 °C for 3 h in argon.
J Mater Chem 2012, 22, 16072-16077	The solid precursor of GO + PMA was heated under 10% H_2/Ar flow at 500 °C for 2 h.
J Mater Chem A, 2013, 1, 5949-5954	The aqueous solution of GO, dodecanethiol and $H_2MoO_4\cdot nH_2O$ was solvothermally heated at 200 °C for 16 h.
	The mixture of rGO (thermally reduced) and AHM was heated at 550 C for 2 h under gas mixtures of 5% C_2H_2 and 95% N_2.
J Mater Chem A, 2015, 3, 4706-4715	The mixture of rGO (thermally reduced) and PMA was heated at 550 C for 2 h under N_2 flow.
	The mixture of rGO (thermally reduced) and PMA was heated at 550 C for 2 h under 5% H_2/N_2 flow.
J Power Sources 2012, 216, 169-178	mixture of GO + AHM + citric acid + poly ethylene glycol heated hydrothermally at 180 °C for 26 h under vacuum.
J Power Sources 2015, 274, 142-148	The precursor was obtained hydrothermally at 180 °C for 24 h by using solution of GO + AHM + HNO_3. Next it calcined at 600 °C under N_2 flow for 3 h.
J Power Sources 2015, 275, 351-361	Microwave-assisted hydrothermal method at 200 °C and 500 Torr for 30 min was followed to prepare solid precursor by using aqueous solution of GO+AHM + ascorbic acid. Later it annealed at 500 °C for 5 h under N_2 flow.

There is only one work available on graphene/$Mn_2Mo_3O_8$ [13]. In this work aqueous solution of GO, $Mn(OOCCH_3)_2\cdot 4H_2O$ and $H_3PMo_{12}O_{40}\cdot xH_2O$ was reduced with hydrazine hydrate for 24 h at room temperature [13]. Stoichiometric mixture of $CoMoO_4$, MoO_3 and C (amorphous carbon, BET surface area ~230 m^2g^{-1}) was heated at 750 °C for 8 h in Ar environment to obtain $Co_2Mo_3O_8$ [14]. Similarly MnO_2 precursor was used to synthesize $Mn_2Mo_3O_8$ [1]. In

these works, first time heating did not give the purest form of the materials. The samples were grinded and reheated at the same temperatures for reduced time to obtain pure samples. Similarly to $Co_2Mo_3O_8$ and $Mn_2Mo_3O_8$, $Zn_2Mo_3O_8$ was prepared by taking ZnO precursor [15]. Recently, Li storage properties of graphene-$A_2Mo_3O_8$ (A = Mn, Fe) composites are also reported [16,17]. For convenience, the detailed electrochemical characteristics of the mixed bimetallic oxides and graphene-$A_2Mo_3O_8$ composites are compared with those of EG/complex metal oxide composites developed in this work in Chapter 8.

2.2.5 MgO decorated FLG Composites

The knowledge about burning of magnesium ribbons in dry ice (solid CO_2) has been demonstrated nearly six decades ago [18]. Burning of magnesium releases sufficient energy to breakdown the bonds in CO_2 to form MgO and elementary C. In 1978 Jerry A. Driscoll predicted that the reaction $2Mg(s) + CO_2(g) \rightarrow MgO(s) + C(s)$ is thermodynamically feasible as the reaction's formation energy was $\Delta H = -193.5$ kcal mol^{-1} *w.r.t* carbon [19]. The importance of this reaction was restricted to class room demonstration due to lack of physiochemical and structural characterization of resultant carbon. Very recently, it was unraveled that the elementary carbon is the most fascinating FLG [20,21]. A close observation this material revealed that the material is not pure FLG but MgO decorated FLG [21]. Trace amounts of MgO may not be a serious issue for the functioning of LIBs because MgO is electrochemically inactive [22-24]. Moreover its adsorbing and liquid electrolyte retaining capability [25], function as protective coating and role in enhancing ionic conductivity encourages the use of MgO decorated FLG composite as an anode for LIBs [23, 26-30]. In addition, presence of MgO nanoparticles with surface defects may become alternative doping components in FLG which may be a promising solution to stop clustering or electroplating and subsequent dendritic growth of Li atoms at the anode of LIBs [31].

References

[1] Das B, Reddy MV, Krishnamoorthi C, Tripathy S, Mahendiran R, Rao GVS, et al. Carbothermal synthesis, spectral and magnetic characterization and Li-cyclability of the Mo-cluster compounds, $LiYMo_3O_8$ and $Mn_2Mo_3O_8$. Electrochimica Acta. 2009;54:3360.

[2] Das B, Reddy MV, Chowdari BVR. Li-storage of Fe_3O_4/C composite prepared by one-step carbothermal reduction method. Journal of Alloys and Compounds. 2013;565:90-6.

[3] Gao M, Zhou P, Wang P, Wang J, Liang C, Zhang J, et al. FeO/C anode materials of high capacity and cycle stability for lithium-ion batteries synthesized by carbothermal reduction. Journal of Alloys and Compounds. 2013;565:97-103.

[4] Qiu D, Ma L, Zheng M, Lin Z, Zhao B, Wen Z, et al. MnO nanoparticles anchored on graphene nanosheets via in situ carbothermal reduction as high-performance anode materials for lithium-ion batteries. Materials Letters. 2012;84:9-12.

[5] Zeng L, Zheng C, Deng C, Ding X, Wei M. MoO_2-ordered mesoporous carbon nanocomposite as an anode material for lithium-ion batteries. ACS Applied Materials & Interfaces. 2013;5(6):2182-7.

[6] Xu Y, Yi R, Yuan B, Wu X, Dunwell M, Lin Q, et al. High capacity MoO_2/graphite oxide composite anode for lithium-ion batteries. The Journal of Physical Chemistry Letters. 2012;3:309-14.

[7] Yang S, Gong Y, Liu Z, Zhan L, Hashim DP, Ma L, et al. Bottom-up approach toward single-crystalline VO_2-graphene ribbons as cathodes for ultrafast lithium storage. Nano Letters. 2013;13(4):1596-601.

[8] Wu T, Tu F, Liu S, Zhuang S, Jin G, Pan C. MnO nanorods on graphene as an anode material for high capacity lithium ion batteries. Journal of Materials Science. 2014;49:1861-7.

[9] Zhao G, Huang X, Wang X, Connor P, Li J, Zhang S, et al. Synthesis and lithium-storage properties of MnO/reduced graphene oxide composites derived from graphene oxide plus the transformation of Mn(VI) to Mn(II) by the reducing power of graphene oxide. Journal of Materials Chemistry A. 2015;3(1):297-303.

[10] Greenwood NN, Earnshaw A. Chemistry of the Elements 2nd Edition; 1997.

[11] Gao MX, Zhou P, Wang P, Wang JH, Liang C, Zhang JL, et al. FeO/C anode materials of high capacity and cycle stability for lithium-ion batteries synthesized by carbothermal reduction. Journal of Alloys and Compounds. 2013;565:97-103.

[12] Poizot P, Laruelle S, Grugeon S, Dupont L, Tarascon JM. Nano-sized transition-metal oxides as negative-electrode materials for lithium-ion batteries. Nature. 2000;407(6803):496-9.

[13] Sun Y, Hu X, Luo W, Huang Y. Hierarchical self-assembly of $Mn_2Mo_3O_8$-graphene nanostructures and their enhanced lithium-storage properties. Journal of Materials Chemistry. 2011;21:17229.

[14] Das B, Reddy MV, Tripathy S, Chowdari BVR. A disc-like Mo-metal cluster compound, $Co_2Mo_3O_8$, as a high capacity anode for lithium ion batteries. RSC Advances. 2014;4:33883-33889.

[15] Das BK. Studies on metal oxides and cobalt nitride as prospective anodes for lithium ion batteries. PhD Thesis, National University of Singapore, 2010.

[16] Sun Y, Hu X, Luo W, Huang Y. Hierarchical self-assembly of $Mn_2Mo_3O_8$-graphene nanostructures and their enhanced lithium-storage properties. Journal of Materials Chemistry. 2011;21(43):17229-35.

[17] Sun Y, Hu X, Luo W, Shu J, Huang Y. Self-assembly of hybrid $Fe_2Mo_3O_8$-reduced graphene oxide nanosheets with enhanced lithium storage properties. Journal of Materials Chemistry A. 2013;1(14):4468-74.

[18] Rawlins GM. Demonstrations with solid carbon dioxide. School Science and Mathematics. 1944;44(8):724-9.

[19] Driscoll JA. A Demonstration of burning magnesium and dry ice. Journal of Chemical Education. 1978;55(7):450.

[20] Chakrabarti A, Lu J, Skrabutenas JC, Xu T, Xiao Z, Maguire JA, et al. Conversion of carbon oioxide to few-layer graphene. Journal of Materials Chemistry. 2011;21(26):9491-3.

[21] Rotte NK, Yerramala S, Boniface J, Srikanth VVSS. Equilibrium and kinetics of Safranin O dye adsorption on MgO decked multi-layered graphene. Chemical Engineering Journal. 2014;258(0):412-9.

[22] Zhou W, Upreti S, Whittingham MS. High performance Si/MgO/graphite composite as the anode for lithium-ion batteries. Electrochemistry Communications. 2011;13:1102-4.

[23] Wang Z, Wu C, Liu L, Wu F, Chen L, Huang X. Electrochemical evaluation and structural characterization of commercial $LiCoO_2$ surfaces modified with MgO for lithium-ion batteries. Journal of the Electrochemical Society. 2002;149:A466-A71.

[24] Chen J, Zhao H, He J, Wang J. Si/MgO composite anodes for Li-ion batteries. Rare Metals. 2011;30:166-9.

[25] Song M-S, Han S-C, Kim H-S, Kim J-H, Kim K-T, Kang Y-M, et al. Effects of nanosized adsorbing material on electrochemical properties of sulfur cathodes for Li/S secondary batteries. Journal of the Electrochemical Society. 2004;151:A791-A5.

[26] Mladenov M, Stoyanova R, Zhecheva E, Vassilev S. Effect of Mg doping and MgO-surface modification on the cycling stability of $LiCoO_2$ electrodes. Electrochemistry Communications. 2001;3:410-6.

[27] Gnanaraj JS, Pol VG, Gedanken A, Aurbach D. Improving the high-temperature performance of $LiMn_2O_4$ spinel electrodes by coating the active mass with MgO via a sonochemical method. Electrochemistry Communications. 2003;5:940-5.

[28] Zhao H, Gao L, Qiu W, Zhang X. improvement of electrochemical stability of $LiCoO_2$ cathode by a nano-crystalline coating. Journal of Power Sources. 2004;132:195-200.

[29] Zhecheva E, Mladenov M, Stoyanova R, Vassilev S. coating technique for improvement of the cycling stability of $LiCo/NiO_2$ electrode materials. Journal of Power Sources. 2006;162:823-8.

[30] Leo CJ, Subba Rao GV, Chowdari BVR. Effect of MgO addition on the ionic conductivity of $LiGe_2(PO_4)_3$ ceramics. Solid State Ionics. 2003;159:357-67.

[31] Liu Y, Artyukhov VI, Liu M, Harutyunyan AR, Yakobson BI. Feasibility of lithium storage on graphene and its derivatives. The Journal of Physical Chemistry Letters. 2013;4:1737-42.

Chapter 3 Experimental Work

3.1 Synthesis of Materials

3.1.1 Synthesis of Graphene Oxide

Graphene Oxide (GO) was synthesized from natural graphite (flake size ≤ 47 μm, Nacional de Grafite Ltda) using a slightly modified Hummers method [1]. In brief, 1 g of graphite was dispersed in 25 mL of concentrated H_2SO_4 (95-97%, Fluka) in a beaker and stirred about 5-10 minutes to ensure that the mixture is uniform. Then the beaker with the contents is transferred in to an ice bath in order to remove the excess heat generated during the exothermic reactions that take place due to the addition of oxidizers. 0.5 g of $NaNO_3$ (Sigma Aldrich, #7664-93-3) followed by 3 g of $KMnO_4$ (Sigma Aldrich, #7722-64-7) were then added gradually and after thorough mixing, the reaction mixture was stirred at room temperature (RT~25-35 °C) for 30 min. Subsequently, 50 mL of distilled H_2O was added into the solution and then immediately the temperature of reaction mixture was raised to 98-100 °C and maintained for 1 h. Next, the beaker was filled with large amount of distilled water and then 1 mL of 30% H_2O_2 (35%, Riedel-de Haen) was added and stirred for 5 min. The suspended GO in the solution (yellowish solution) was then left to settle down for a few hours before discarding the supernatant solution. The beaker was then filled with large amount of distilled H_2O and GO was then once again allowed to settle down. This step was to allow the soluble salts which are the side products like sulphate ions from H_2SO_4 to get washed out of the mixture so that high purity GO could be obtained. The process of sedimentation, discarding the supernatant solution, filling up with H_2O was repeated several times until the pH of the solution became 7 to ensure that most unwanted by-products have been completely washed out of the GO solution. At this stage, the suspended GO solution is then poured onto a filter paper in funnel and the excess water was removed. The residue (GO) on the filter funnel is then left in an oven for drying overnight at 80 °C. This step ensures removal of all water content. The

schematic representation of GO preparation is shown in Fig. 3.1. Thus prepared GO was then grinded into fine powders, ready to be added into the final reaction mixture in appropriate amounts. In another independent experiment GO1 was prepared by following aforesaid modified Hummers method but in this case concentration of H_2SO_4 used was 95-98% (Sigma Aldrich). Thus prepared GO1 possessed high extent of oxidation than GO and was especially used for the synthesis of EG/Fe_3O_4 composite.

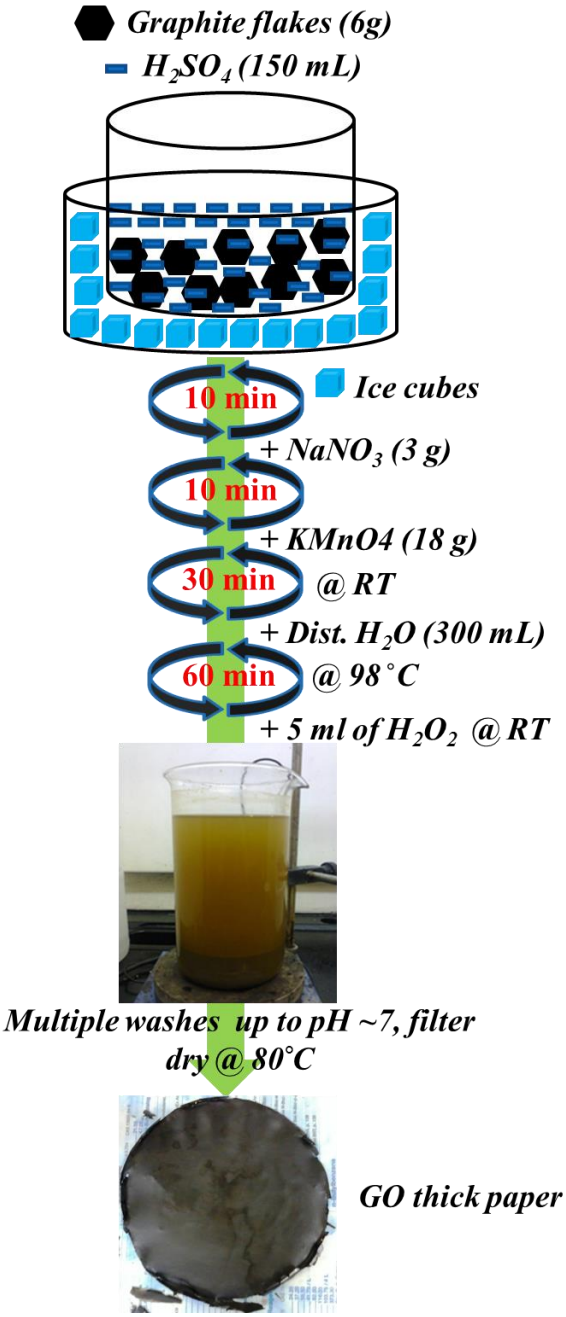

Figure 3.1. Schematic representation of GO preparation.

3.1.2 Synthesis of EG/MO Composite Materials

The GO discussed in Section 3.1.1 was used in the synthesis of EG/MO composites. GO and metal oxide precursors were taken in the required molar ratio as mentioned Table 3.1 and were mixed using mechanical milling for 30 min. Molecular formula of GO was adapted as $C_{2.2}H_{0.8}O_1$ for molar calculations [2]. The reaction mixture (6 g) was then place in a ceramic boat and transferred to tube furnace (Carbolite, UK). Heating was started after flushing out the atmospheric air in tube furnace with Ar gas and this flow maintained throughout the experiment. Thermal annealing of reaction mixtures was carried out at different temperatures as shown in Table 3.1. The heating and cooling rates are 5 ºC min^{-1}. The final product was a very smooth and black colored fine powder (~3 g) of EG/MOs which were directly (without any further treatment) used for further characterization and electrochemical analysis/battery testing. The above mentioned synthesis process was followed to obtain EG/Fe_3O_4 by using GO* (prepared with excess oxidizers, GO1 section 3.1.1) for 2 h heating time. The name of the process was names are Graphenothermal Reduction (GTR) process because GO was acting like a solid reducing agent in its reaction with the metal oxide precursors.

Table 3.1. GTR synthesis parameters of various EG/MOs composite materials.

Composite	Reaction Mixture	Temperature	Heating Time
EG/FeO	$2GO+Fe_2O_3$	650 ºC	5 h
EG/Fe_3O_4	$2GO^*+Fe_2O_3$	650 ºC	2 h
EG/MnO	$2GO+MnO_2$	650 ºC	8 h
EG/MoO_2	$4GO+MoO_2$	750 ºC	8 h
FLG/$Co_2Mo_3O_8$	$3.5GO+2Co(Ace)_2.4H_2O+3MoO_3$	750 ºC	8 h
FLG/$Mn_2Mo_3O_8$	$3.5GO+2Mn(Ace)_2.4H_2O+3MoO_3$	750 ºC	8 h
FLG/$Zn_2Mo_3O_8$	$3.5GO+2ZnO+3MoO_3$	750 ºC	8 h

*excess oxidized

3.1.3 Synthesis of MgO decorated FLG

MgO decorated FLG composite was obtained from Mr. Naresh Kumar Rotte [3] and used as-received. MgO decorated FLG composite was prepared from dry ice as follows: In brief, combustion of magnesium in dry ice and a subsequent simple acid treatment step resulted in MgO decorated FLG. Magnesium metal turnings (3 g) were transferred in to circular groove made in a dry ice block. This groove was covered tightly from top with another dry ice slab immediately when combustion process started upon ignition of magnesium turnings. Combustion results in ash-like material which was collected and then dissolved in 1 M HCl and kept for stirring for 24 h. Then the resultant material was filtered and subjected to multiple washes with distilled water. The washing was stopped when the pH of the solution was ~7. The washed material was filtered and dried in oven at 100 ºC for 12 h.

3.2 Characterization of Materials

3.2.1 Scanning Electron Microscopy

The morphology of materials prepared in this work are studied using field emission scanning electron microscope (FESEM) (Model Zeiss Ultra 55) operated at an accelerating voltage of 5 kV. The samples being conductive in nature they were not coated with any conductive materials such as gold or carbon. Energy-dispersive X-ray analysis (EDXA) was used to know the elemental composition of the samples.

3.2.2 Transmission Electron Microscopy

Morphological studies were also carried out by using transmission electron microscope (TEM) (Model FEI Technai G2 S-Twin, Type: 5021/20) operated at an accelerating voltage 200 kV. The electron micrographs were obtained at various magnifications. High resolution TEM (HRTEM) mode and selected area electron diffraction (SAED) were used to explore the local structural aspects of samples. In addition, EDXA was also carried out in TEM. All powder samples mentioned in the present study were dispersed in acetone/ethyl alcohol and

bath sonicated for half an hour. Thus prepared specimen solutions were carefully dropped on to holy carbon coated copper grids. After proper drying the copper grid with sample was used for the examination.

3.2.3 X-ray Diffraction

The bulk ensemble of microstructural features of powder samples was probed with X-ray diffraction (XRD) technique. XRD patterns were recorded at room temperature and in the range of 5 to 80° by using Cu Kα as the X-ray source (λ=1.54 Å); Bruker's AXS Model D8 Advance System or Philips X'PERT MPD unit, PANalytical system was used to carry out the XRD experiments. XRD patterns were used primarily for phase identification and quantification of crystallinity. In addition, they are used for determination of lattice parameters, space group, crystallite size, degree of crystallinity, *etc.* In some cases XRD patterns were further analysed by using Rietveld refinement via TOPAS (v2.1 and v3.0).

3.2.4 Raman Spectroscopy

The Raman spectra were recorded using an Nd-YAG 532 nm laser in the back scattering geometry in a CRM spectrometer equipped with a confocal microscope and 100× objective (1 μm diameter focal spot size) with a CCD detector (Model Alpha 300 of WI Tec, Germany). In some cases, Raman spectra (Renishaw Raman system 2000, at National University of Singapore) were recorded with auto excitation wavelength and auto confocality focussed by 100X objective lens (spot diameter ~1 μm). The Raman spectra obtained by using above both instruments were reordered under room conditions. The phase content with in the samples was investigated in a spectral region 200–4500 cm^{-1}.

3.2.5 Fourier Transform Infrared Spectroscopy

The Fourier transform infrared spectroscopy (FTIR) spectra of GO and GO[1] were obtained with Bruker Equinox 55 FTIR instrument. GOs were pressed into pellets with KBr matrix by applying 10 ton of force by using hydraulic press. IR spectra were interpreted in the

functional region (4000-1500 cm^{-1}) and the fingerprint region (1500-400 cm^{-1}). Peaks in the functional region are characteristic of specific types of bonds, and therefore can be used to identify whether a specific functional group is present. Peaks in the fingerprint region arise from complex deformations of the molecule. The obtained FTIR spectra of GO and GO[1] were analyzed for their extent of oxidation in terms of number and kind of functional groups present in them.

3.2.6 BET Surface Area Measurement

Specific surface area and porosity distribution were measured by performing N_2 physisorption at 77 K with Micromeritics (Tristar 3000, USA) using Brunauer–Emmett–Teller (BET) and Barrett-Joyner-Halenda (BJH) multipoint methods. Samples were preheated under N_2 flow for 1 h at 180 °C. To record isotherms of N_2 adsorption and desorption, NTP conditions were maintained around sample holder while a mixture of He and N_2 gases was flown-in according to the dynamic (flowing gas) technique. The adsorption and desorption isotherms data, specific surface area, pore size and volume, were imported to an excel sheet by automated computer programme attached to Micromeritics instrument.

3.2.7 X-Ray Photoelectron Spectroscopy

X-ray photoelectron spectroscopy (XPS) was carried out to understand different oxidation states of individual elements and their possible bonding with other species present in the composites. Binding energy values are evaluated using XPS using an AXIS ultra DLD spectrometer (Kratos Analytica) with monochromatic AlKα radiation. Casa XPS software was used to analyze XPS data. Survey spectra are obtained in the energy range 0–1200 eV. Charge referencing was carried out against adventitious carbon C (C1s binding energy = 284.6 eV). Further, the bonding possibilities were understood from deconvolution of individual high resolution spectra of M3d or 2p (M=metal), O1s and C1s *etc*. by using PeakFit (version 4.05) software.

3.2.8 Thermogravimetric Analysis

TA Instruments (SDT-2960 Simultaneous DTA-TGA) was used for the Thermogravimetric Analysis (TGA) of samples weighing ~10 mg in air or N_2 atmosphere. TGA of GO, GO^1 and corresponding reaction mixtures GO+MO and GO^1+MO (where MO stands for metal oxides) was performed in the range of 25 to 1000 °C at a heating rate of 5 °C min^{-1} in N_2 environment in order to understand the reduction process as well as to identified minimum temperatures required for obtaining desired composition of composites. In addition, TGA of GO, GO^1 and final products too were performed in the same temperature range as mentioned above in air at a heating rate of 10 °C min^{-1} in order to calculate the individual weight contents in the composites.

3.3 Li Ion Battery Testing

3.3.1 Coin cell fabrication

Electrochemical properties of the different electrode materials used in this study were investigated by preparing coin cells (type 2016; 20 mm diameter and 1.6 mm height). The coin cell fabrication involves mainly the following steps: a) preparation of electrodes of material in the form of coating onto a conducting thin foil like etched Cu and b) assembling the electrode into a coin cell. The details of these processes are described in the following paragraphs:

Using the synthesized graphene based compounds as the active material, polyvinylidene fluoride (PVDF) as a polymer binder (Kynar 2801), and Super-P carbon (ENSACO, MMM Super P, 230 m^2g^{-1}) as a conductive additive in the weight ratio of 70:15:15, and N-Methyl-2-pyrrolidone (NMP) as an organic solvent (Alfa Aesar), the anodes were fabricated by grounding the Super-P carbon and the anode material until they became fine powders. Super P-carbon was used for its high purity and surface area, and it improves the electrical conductivity of the compound. Next, PVDF was added in the mass ratio stated above,

together with the compounds into separate clean vials. PVDF not only brings in its piezoelectric effect to accumulate electrical charge, but its inert chemical nature over the potential range used will not react with Li or electrolyte used later, unlike other types of copolymers. Next, NMP was added till the slurry was of an appropriate consistency (approx. 3/4 of dropper). The NMP solvates the mixture, and will disperse the EG/RMO powders, super P carbon and binder thoroughly. It is a good choice to create a homogenous mixture, due to its low toxicity, volatility, and flammability. A clean magnetic stirrer was placed in the vial and left on a magnetic stirring plate overnight, which further ensures a uniform slurry being made, hence allowing the synthesized electrodes to be uniform too. After that, the slurry was used to coat onto an etched copper foil (Shenzhen Vanlead Tech. Co. Ltd, China) whose thickness is 10 μm, which will serve as a current collector. Copper was chosen over other materials as it does not affect or take part in reactions taking place at the anode. Doctor blade technique was used to coat the electrode uniformly with a slurry thickness of 25μm. The foil was then placed in an oven at 80 °C overnight. A twin roller machine (Soei Singapore Scientific Quartz Co.), applying 1500 kPa of pressure, was used to press the coated copper foil to increase contact between composite material and copper foil. The foil was then punched into discs with a 16 mm diameter (2.0 cm^2 geometric area) using an electrode cutter. Discs with the most uniform coating of the anode material were selected and weighed. The mass of the copper foil (0.0195 g) was subtracted from the reading and the value was then multiplied by 70% (as per the mass ratio above). The active material content in the electrodes was around 2-6 mg. The electrodes were then placed in a vacuum oven overnight to completely dry. After drying in vacuum oven electrodes were used as anodes to fabricate coin cells as discussed in the next paragraph.

Coin cells were assembled in an Argon filled glove box (MBraun, Germany) with O_2 and H_2O level maintained below 1 ppm. Li metal (Honjo Metal Co., Japan) foil (0.5 mm

thickness) that cut into 16 mm diameter disk as counter electrode. Glass microfiber filter (GF/F, Cat No. 1825 055, Whatman Int. Ltd., Maidstone, England) or Celgard (2502) polypropylene microporous membrane was used as the separator. The 1M $LiPF_6$ in ethylene carbonate (EC) and dimethyl carbonate (DMC) (1:1 by volume, Merck Selectipur LP40) was used as electrolyte.

The composite electrode was placed in the bottom cup of coin cell (stainless steel) with the active material facing upwards and the separator was placed above the electrode. Then ~10-20 µL of the liquid electrolyte was added to wet the separator, followed by placing lithium metal and the top cap welded with a wave spring (stainless steel). Finally, the coin cells were assembled by crimp sealing in a mechanical hand press. A plastic O-ring was used to prevent the direct contact of cathode and anode which can result in self short-circuiting of the cell. It also provides air tight sealing of the cell. A schematic diagram for the coin cell assembly is shown in Fig. 3.2. The fabricated coin cells were aged for 12 h for good percolation of electrolyte into the electrode materials before subjecting to electrochemical studies.

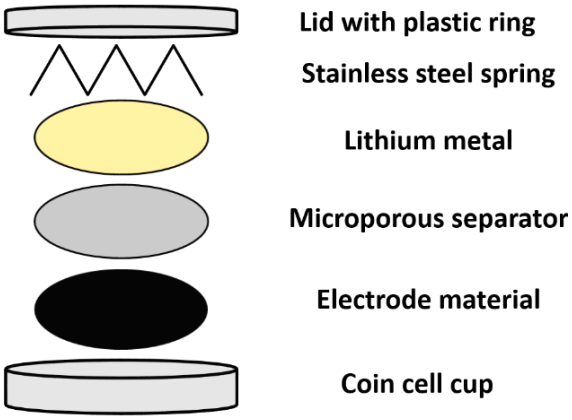

Figure 3.2. Schematic of coin cell assembly.

3.3.2 Galvanostatic Cycling

Galvanostatic cycling or constant current cycling of the fabricated batteries was carried out by using a computer controlled Bitrode multiple battery tester (model SCN, Bitrode, USA). All batteries were tested at room temperature after eight hours of relaxation after their

punching. The coin cells were tested in the voltage range of 0.005–3.0 V and current densities ranging from 50 mA g^{-1} to 2000 mA g^{-1}. Capacity values, cyclic performance, stability *etc.* of the materials were investigated by carrying out the lithium cycling for a fairly large number of charge-discharge cycles (say 50 cycles minimum).

In typical galvanostatic cycling test, the lithiation or de-lithiation capacity of an electrode material of the cell can be calculated as a function of time taken for either to charge or discharging the battery to a particular voltage and constant current applied to the cell as expressed by Equ. 3.1. The product of the applied current (in ampere) and the time taken (in hours) for the complete lithium insertion /removal is the total charge (in mAh) stored or released by the material and is termed as the capacity of the electrode material. The capacity obtained per unit mass of the active material is termed as specific capacity (C_s):

$$C_s = \frac{I \times t}{m} \qquad (3.1)$$

where C_s is in mAh g^{-1}, I is the current applied in mA, t is the time taken for complete discharge/charge in hours and m is the mass of active material in grams. The specific capacity of an electrode material can be theoretically calculated by the Equ. 1.7 (Chapter 1). Appropraite current rates for testing the batteries have been chosen (please see Section 1.1). Capacity retention for each case has been calculated.

3.3.3 Cyclic Voltammetry

The electrochemical readiness of the materials for lithiation was carried out with Cyclic Voltammetry technique by employing a computer controlled Mac-pile system (MacPile II, Biologic, France). Cyclic voltammograms of the electrode materials recorded by testing respective coin cells at a scan rate of 58 μV s^{-1}. The cells were tested in the voltage range of 0.005–3.0 V at room temperature and after relaxing the coin cells for eight hours. The current (I) at the working electrode is plotted against the applied voltage (V) to obtain the cyclic voltammogram of the analyte. The potential applied (between the reference electrode and the

working electrode) to the coin cell was ramped at a constant rate 58 μV s^{-1} starting from open circuit voltage (OCV) of coin cell to 0.005 V. The voltage was ramped in both forward (to 3.0 V) and backward (to 0.005V) directions for certain number of cycles and hence the name cyclic voltammetry. By IUPAC convention, the anodic current is positive and the cathodic current is negative. As the potential was swept back and forth, a current flown through the electrode that either oxidizes (anodic scan)/reduces (cathodic scan) the analyte and the corresponding current (I) between the working electrode and the counter electrode was measured and plotted against the potential. Thus obtained current peaks at particular voltages were used to understand and confirm the type of lithiation mechanism such as intercalation, conversion *etc.* For example, strong current redox peaks in the range 0.15–0.25 V in CV curves of graphite arise from Li's intercalation and de-intercalation into Van der Waal gaps of graphite through prismatic surfaces [4].

3.3.4 Electrochemical Impedance Spectroscopy

Electrochemical Impedance Spectroscopic (EIS) measurements of the coin cells were done with a Solartron impedance/gain-phase analyzer (model SI 1255) coupled with a potentiostat (SI 1268) at room temperature in the frequency range 0.18MHz to 0.003 Hz with an AC signal amplitude of 10 mV. The impedance data were analysed using Z-view software (version 2.2, Scribner Assoc., Inc., U. S. A.). The frequency dependent impedance of various electrode materials in the present study was obtained at various states of batteries i.e. at OCV, discharged to 0.005 V and charged to 3.0 V. Thus obtained data was plotted as Nyquist plots in which impedance data fits to a semicircle in the higher frequency range and a 45° inclined straight line in the lower frequency region in general [5]. Further, the impedance data was modeled for its equivalent circuit (combination of resistances, capacitances *etc.*) and values of various circuit elements were known by using Z-view software. Thus obtained equivalent circuits and their component values were used to analyze in details the kinetic and

mechanistic information about lithiation and de-lithiation process and the corresponding consequences.

3.3.5 Galvanostatic Intermittent Titration Technique

To calculate Li-diffusion coefficients of electrode materials Galvanostatic Intermittent Titration Technique (GITT) was used. GITT of coin cells was carried out by using a computer controlled Bitrode multiple battery tester (model SCN, Bitrode, USA). A discharge pulse of 50 mA g^{-1} is applied to the battery to discharge it to selected voltage and was subsequently allowed to rest for 5 h. Similar test was done during charging process as shown in Fig. 3.3. Next, diffusion coefficient (D_{Li}) for each discharge and charge pulse was calculated by using the Equ. 3.2 [6,7].

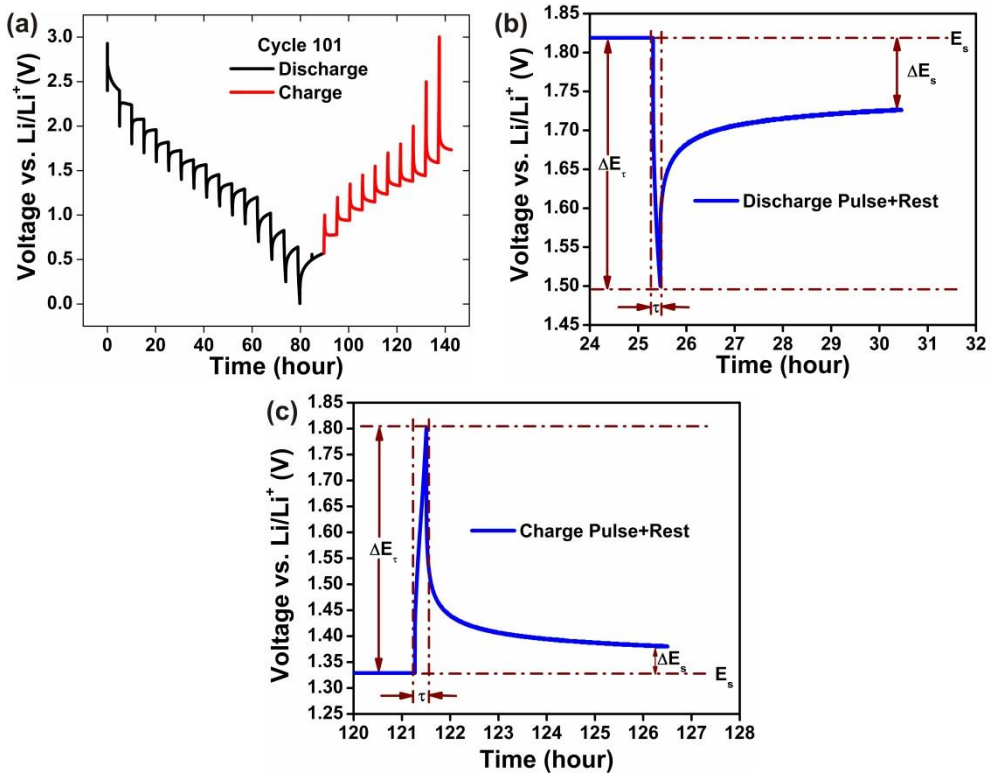

Figure 3.3. (a) GITT curve vs. time during discharge and charge at 50 mA g^{-1}, (b) and (c) are typical discharge and charge pulses respectively.

$$D_{Li} = \frac{4}{\pi\tau}\left(\frac{m_B V_m}{M_B A}\right)^2 \left(\frac{\Delta E_s}{\Delta E_\tau}\right)^2, (\tau << L^2 / D_{Li}) \quad (3.2)$$

In Equ. 3.2 τ is the duration of the current pulse (in sec); m_B is the number of moles (in mol) of the active material, M_B is molecular weight of the active material (in g) and V_m is the molar volume of the electrode (in cm^3/mol), A is the electrode/electrolyte contact area (in cm^2), ΔE_s is the steady-state voltage change due to the current pulse and ΔE_τ is the voltage change during the constant current pulse.

References

[1] Hummers WS, Offeman RE. Preparation of graphitic oxide. Journal of the American Chemical Society. 1958;80(6):1339-1339.

[2] Dreyer DR, Park S, Bielawski CW, Ruoff RS. The chemistry of graphene oxide. Chemical Society Reviews 2010;39(1):228-240.

[3] Rotte NK, Yerramala S, Boniface J, Srikanth VVSS. Equilibrium and kinetics of Safranin O dye adsorption on MgO decked multi-layered graphene. Chemical Engineering Journal. 2014;258(0):412-9.

[4] Gosser DK. Cyclic Voltammetry: Simulation and Analysis of Reaction Mechanisms. VCH: New York, USA, 1993.

[5] Orazem ME, Tribollet B. Electrochemical Impedance Spectroscopy. John Wiley & Sons, Inc.: Hoboken, NJ, USA, 2011.

[6] Wu Y, Reddy MV, Chowdari BVR, Ramakrishna S. Long-term cycling studies on electrospun carbon nanofibers as anode material for lithium ion batteries. ACS Applied Materials & Interfaces. 2013;5:12175-84.

[7] Su-Il Pyun H-CS, Jong-Won L, Joo-Young G, Chapter 2, Electrochemistry of Insertion Materials for Hydrogen and Lithium. Springer-Verlag Berlin Heidelberg: Heidelberg, Germany, 2012.

Chapter 4 GTR Mechanism: Reduction of Fe_2O_3 by GO as a Case Study

The degree of oxidation (DO) of GO was found to play a key role (in addition to temperature and heating time) in controlling the reduction of Fe_2O_3 by GO. GO with low DO follows conventional three stage reaction path '2GO+Fe_2O_3 →^{I}EG/Fe_3O_4 →^{II}EG/FeO →^{III}EG/Fe' at temperatures 650 and 750℃ depending on heating time. Whereas the GO with higher DO ceased reduction at stage I i.e. formation of EG/Fe_3O_4 only at 650℃ for 2 to 8 h of heating time and similar result is expected even at high temperatures like 750℃ by careful observation of TGA analysis. The rate of burning of GOs is found responsible for different reduction processes. The highly oxidized GO burnt rapidly than less oxidized GO and restricted its reducing nature to stage I because in-situ reaction environment created poor contacts between EG and Fe_3O_4. On the other hand slow burning of GO made it capable of continuing reduction to stage II and further to stage III depending on time of heating and temperature owing to good contacts between EG and reduced iron oxides.

Fe_2O_3 is very complex and sensitive in nature and therefore to control its reduction either by solid state (carbon) or gaseous (H_2, CO *etc.*) reducing species is difficult. Reduction of Fe_2O_3 by GO is totally different than the typically reduction process because GO offers its carbons while gaseous species are produced during the thermal treatment i.e., both solid and gaseous state reduction is possible in one go. In such circumstances it is difficult to control the reduction process and end product may be Fe_3O_4 or FeO or a mixture of both. It is therefore intriguing to understand the controlling parameters for reduction of Fe_2O_3 by GO such that desired iron oxides or their EG composites are produced in scalable amounts. In this regard, DO of GO, heating time and temperature are the controlling parameters for the reduction of Fe_2O_3 by GO. The end product can be EG/Fe_3O_4, EG/FeO and EG/Fe composites.

XRD patterns of graphite, GO1 and GO2 (please see Annexure 5 for the preparation of GO1 and GO2) are shown in Fig. 4.1(a). Graphite has shown a sharp and intense peak at 26.5° that corresponds to reflection from highly ordered (002) basal planes. This peak in GO1 and GO2

appeared to be shifted to 13.4° and 10.4°, respectively as a consequence of various functional groups anchored to basal planes. The observed peak shifting is equivalent to an increase in the inter-planar distance to 0.66 nm in GO1 and 0.85 nm in GO2 when compared to 0.34 nm in graphite. The observed increment in inter-planar distance signifies that the basal planes of GO2 are populated with more number of functional groups than GO1. Based on the XRD and XPS (Fig. 4.2) inferences [1,2] DOs of GO1 and GO2 are calculated as 48 and 63, respectively which are in well agreement with reported values [2].

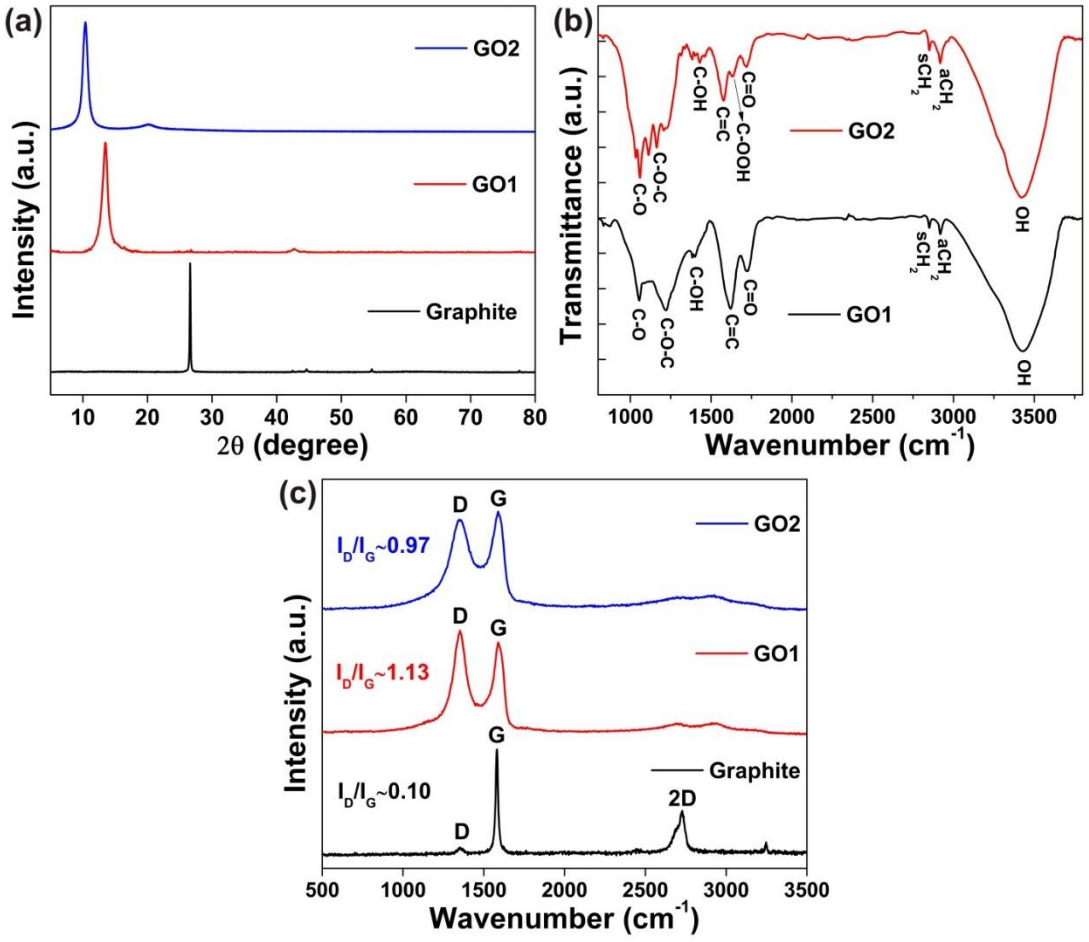

Figure 4.1. (a) X-ray diffractograms of Graphite, GO^1 and GO^2, (b) FITR transmittance spetra of GO1 and GO2, and (c) Raman scattering spectra of Graphite, GO1 and GO2.

The type of functional groups contributed to oxidation of GO1 and GO2 are elucidated by FITR spectra as shown in Fig. 4.1(b). GO1 contained strong absorption bands corresponding to functional groups C=O at 1723.7, C=C at 1621.7, C–OH at 1400.8, C–O–C at 1220.9 and

C–O at 1055.1 cm^{-1} whilst respective bands in GO2 are found at 1719.4, 1577.8, 1430.5, 1162.8 and 1059.4 cm^{-1} in addition an extra O=C–OH band was found at 1637.3 cm^{-1} [1-8]. In the case of GO2 the absorbance of C=C band has been observed to decrease whereas absorbance of C–O band has been observed to increase in comparison to the same in the case of GO1. Further, in GO2 the regions of C–OH and C–O–C bands have been split into two or three sub-bands owing to increase in their number as well as addition of new functional groups [3,5,8]. These FTIR inferences are an indication for increased oxidation in GO2 in good agreement with XRD results.

Raman spectroscopy results showed that DO has no influence on the positions of D and G bands (which are found at typically at ~1350 and ~1588 cm^{-1}) in both GO1 and GO2 cases as shown in Fig. 4.1(c). No change in G-band's position signifies that even though OD was increased by 15% there are no considerable new in-plane sp^3 carbon atoms in basal planes of graphene sheets [1,3]. This inference implies that basal planes in both GO1 and GO2 are anchored with similar and same amount of functional groups despite of increased DO and further indicates that DO increased due to attachment of more functional groups at edges and defect sites rather than in-plane. But increased DO influenced the D-band's intensity which decreased in good agreement with the reported work [3]. The significant decrease in intensity of D-band in GO2 relative to GO1 also indicates that high extent of oxidation took place [3]. Another important inference provided by Raman scattering analysis is the low discernablility of 2D-band (in both GO1 and GO2 cases) which is an indication for complete stacking disorder along the crystallographic c-axis [3,9]. Discernability is pretty low in the case of GO2 when compared to GO1 case, which is an evidence for high OD in GO2 [3,9].

Figures 4.2(a) and (b) show the high resolution C1s spectra of both GOs. The spectra in both the cases appear similar but peaks pertainint to GO2 are more intense than those pertraining to GO1 which is an indication for increased oxidation. C1s spectrum of GO1 could be

deconvoluted into five peaks which correspond to C=C (sp^2 C) centered at 284 eV, C–C/H (sp^3 C) centered at 284.8 eV, C–OH centered at 285.7 eV, C–O–C centered at 287 eV and C=O centered at 288.7 eV whereas C1s spectrum of GO2 could be deconvoluted too into five peaks which correspond to C–C/H centered at 284.8 eV, C–OH centered at 285.7 eV, C–O–C centered at 287 eV, C=O centered at 288 eV and C–OOH centered at 289 eV [1,3,4,10,11]. The absence of C=C signal, appearance of –COOH signal, increased intensity count of C–OH and C–O–C peaks clearly indicate that GO2 oxidized more than GO1. These observations are in tune with the inferences from FTIR spectroscopy studies.

The nature of remnants (EGs) of GO1 and GO2 after burning in the presence of Fe_2O_3 (in reaction mixtures) is studied by probing C1s spectra of EG/FeO and EG/Fe_3O_4 which are prepared under controlled conditions (at 650℃ and 5 h of heating time). The obtained C1s spectra (Figs. 4.2(c) and (d)) revealed that both EGs possessed residual functional groups in proportion to their predecessors GO1 and GO2. It is common to have residual functional groups such as hydroxyl (–OH), epoxide (C–O–C) and keto (C=O) which are proven to be sustained up to minimum lower temperature of 700℃ [4-6,8-13]. In brief, the C1s spectrum of EG/FeO was deconvoluted into four peaks centered at 284.8, 285.3, 286.2 and 287.5 eV which correspond to graphitic carbons in sp^2 and sp^3 bonding modes, carbons bonded to hydroxyl and epoxide groups, respectively in comparison to the C1s spectrum of GO1 (Fig. 4.2(a)). In addition to the peaks at 284.1, 285.1, 286.1 and 287.4 eV, there is an additional peak at 288.6 eV that corresponds to carbon bonded to oxygen (keto groups) in the case of C1s spectrum of EG/Fe_3O_4 (Fig. 4.2(d)) that too is in proportion and comparison to GO2 (Fig. 4.2(b)). Thus overall XPS study is in good agreemenr with XRD, FTIR and Raman analysis.

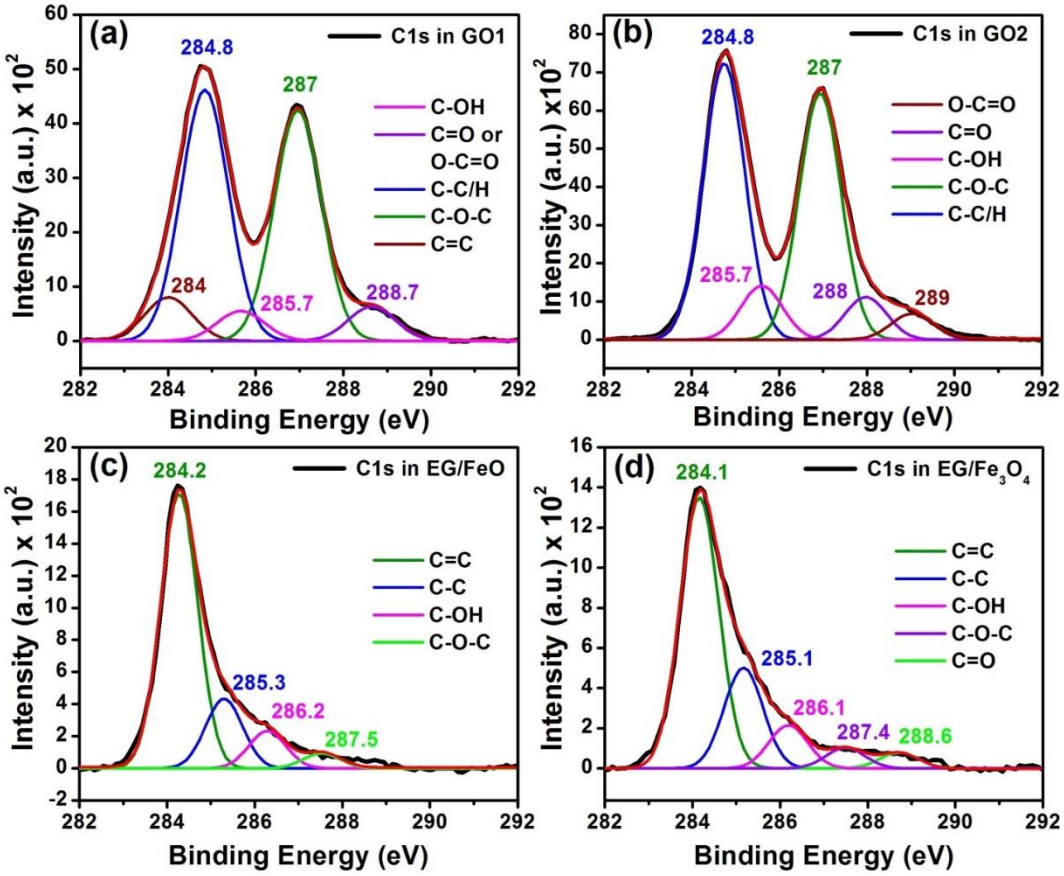

Figure 4.2. XPS spectra of C1s in GO1 (a), GO2 (b), EG/FeO (c) and EG/Fe_3O_4 (d).

TEM observations of GO1 and GO2 are found to be in well accordance with XRD, FTIR, Raman and XPS inferences. As shown in Fig. 4.3, GO2 is found to be more (semi) transparent than GO1which is an indication for higher oxidation. The SAED disordered ring pattern depicted for GO1 sheet signifies it as well oxidized compared to typical regular hexagon pattern of graphite. The ring pattern comprised of doublet and triplet atomic projections in the case of GO1. This is an indication for the presence of more number of graphene layers (basal planes) those are folded, crumpled etc. On the other hand GO2's ring pattern formed with blurred singlet atomic projections that signify that it is built-in with less number of graphene layers in comparison to GO1. Another inference it gives is that the basal plane is not much disordered [13] i.e., it possess less functional groups in strong agreement with Raman inferences. The elemental mapping showed that GO1 and GO2 possess O/C atomic ratio 0.408 and 0.625 which is again an indication for increased oxidation in GO2.

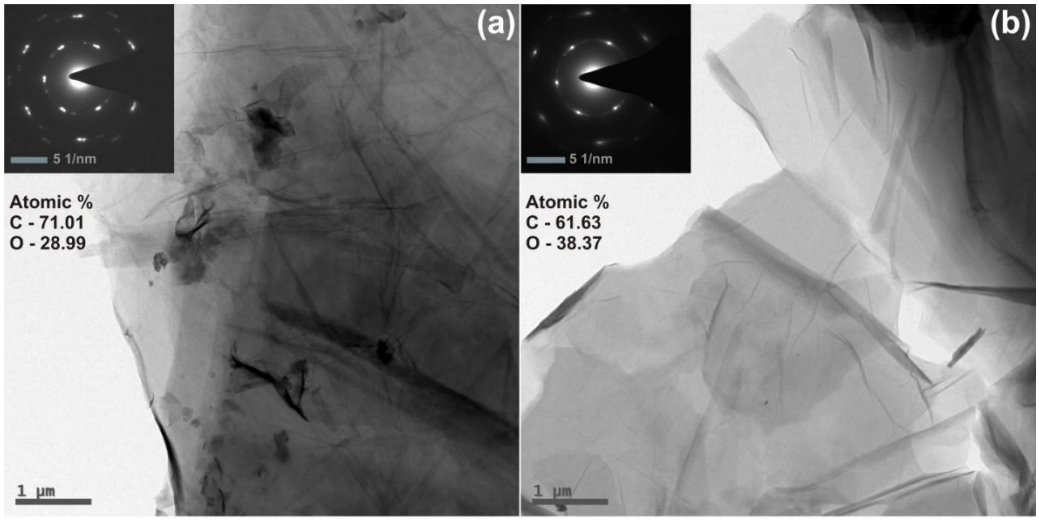

Figure 4.3. TEM images of (a) GO1and (b) GO2 with insets showing their SAED patterns.

The temperature dependent weight loss characteristics of both GOs and their corresponding reaction mixtures are studied in order to correlate with the reduction process. To bring more clarity about thermal decomposition, first order derivative of weight losses is plotted as shown in Figs. 4.4(a), (b), (d) and (e). GO1 showed two clear peaks centered at 179℃ (peak 1) and 592℃ (peak 2) that are representative of the breakup of functional groups and loss of carbon atoms, respectively from basal planes [5-8,10,12]. These two peaks are found to be centered at 197 and 549℃, respectively in the case of GO2 (Fig. 4.4(b)). It is noteworthy that area under peak1 of GO2 is greater than that of GO1 due to loss of more functional groups. This is in good agreement with XRD, FTIR, Raman and XPS inferences. The area under peak 2 of GO1 is greater than that of GO2 which is an indication for sublimation of more backbone carbons from GO1 than from GO2. The weight loss features of reaction mixtures (RM1 = GO1+Fe_2O_3, Fig. 4(d) and RM2 = GO2+Fe_2O_3, Fig. 4.4(e)) appeared as a replica of individual GOs' characteristics with slight broadening of peaks 1 and 2. In case of RM1, peaks 1 and 2 are centered at 189 and 499℃ respectively, whilst in the case of RM2 they are centered at 194 and 492 ℃, respectively. In addition, RM1 differs from RM2 by an extra small plateau type peak 3 centered around 680℃. The combine plotting of TGA curves of GOs clearly showed that GO2 burnt rapidly at slightly lower temperatures (20–50℃ less)

than GO1 as shown in Fig. 4.4(c). Corresponding reaction mixtures too have shown similar weight losses but difference between maximum weight losses widened by 100–200℃ as shown in Fig. 4.4(f). In all four cases initial incomplete weight loss derivative peaks can be accredited to the evaporation of water molecules preferably from GOs [5-8,10,12]. Now it is obvious that the weight loss (peak 1 related) in both RMs is contributed by GOs alone by giving up functional groups. But RM1 lost its maximum weight in between 500 and 750℃ (peak 2 and 3) that corresponds to the reduction of both GO1 (exfoliation to EG) and Fe_2O_3 as well as subsequent formation of iron oxides like Fe_3O_4 and FeO. A considerable weight loss around 570℃ (peak 2) is a good enough evidence for the formation and stabilization of FeO. Further weight loss might be plausibly reduction of FeO to form Fe (peak 3). Thus overall weight loss may represent the conventional three stage reduction path according to equation $2GO+Fe_2O_3 \rightarrow {}^{I}EG/Fe_3O_4 \rightarrow {}^{II}EG/FeO \rightarrow {}^{III}EG/Fe$. On the other hand RM2 possesses its maximum weight loss below 500℃ (peak 2) which corresponds to formation of only Fe_3O_4 as temperature is not enough to form FeO and Fe (which is consistent with XRD findings). In this case, reduction process may have been plausibly ceased at stage I *i.e.* $Fe_2O_3 \rightarrow {}^{I}Fe_3O_4$ for the reason that a feeble weight loss is observed between 500℃ and 1000℃. To know more about the type of iron oxides formed in the vicinity of peak 2 (as functional groups are released at peak 1 could be less effective in reducing Fe_2O_3 for the reason that the reaction temperature is less than 200℃) XRD studies were carried out. X-ray diffractograms of heat-treated RM1 and RM2 at different times and temperatures are considered for pin-pointing the reduction process by knowing the types of iron compounds retained as shown in Figs. 4.5(a) and (b). In order to correlate to the inferences of TGA and good exfoliation of GO (above 600℃ [4-6,8-13]), the structure of end products of RMs at 650 and 750℃ are probed as shown in Fig. 4.5. At these temperatures, the type of reducing species (CO and C mainly) and their participation in reduction of Fe_2O_3 is well-known.

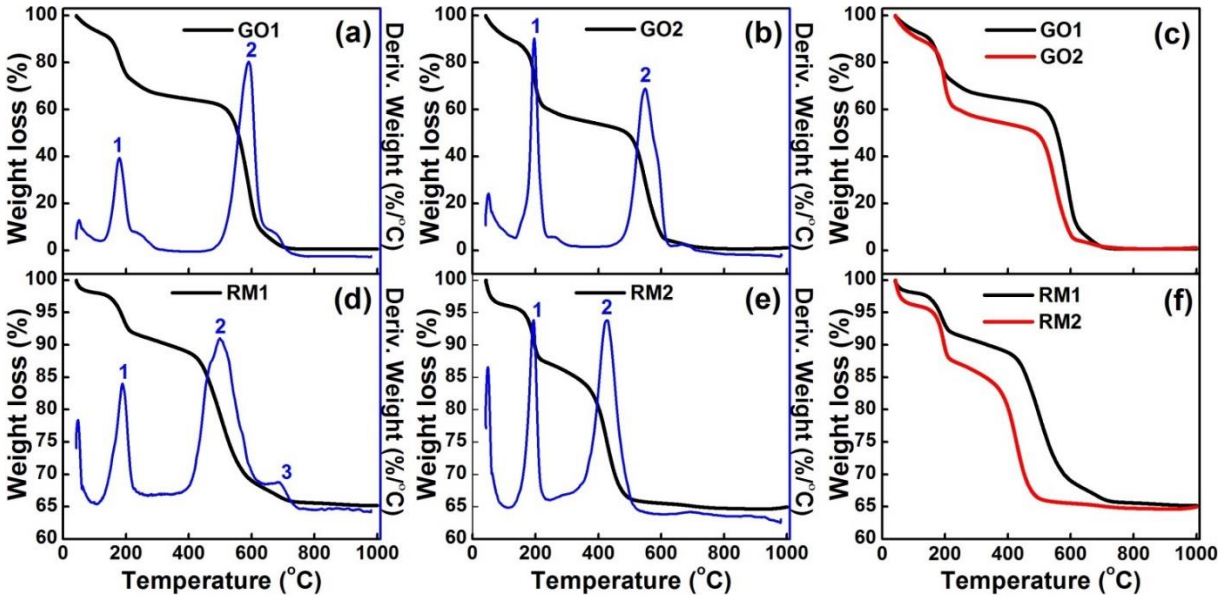

Figure 4.4. TGA of GOs and corresponding reaction mixtures at 5℃ min^{-1} heating rate in N_2.

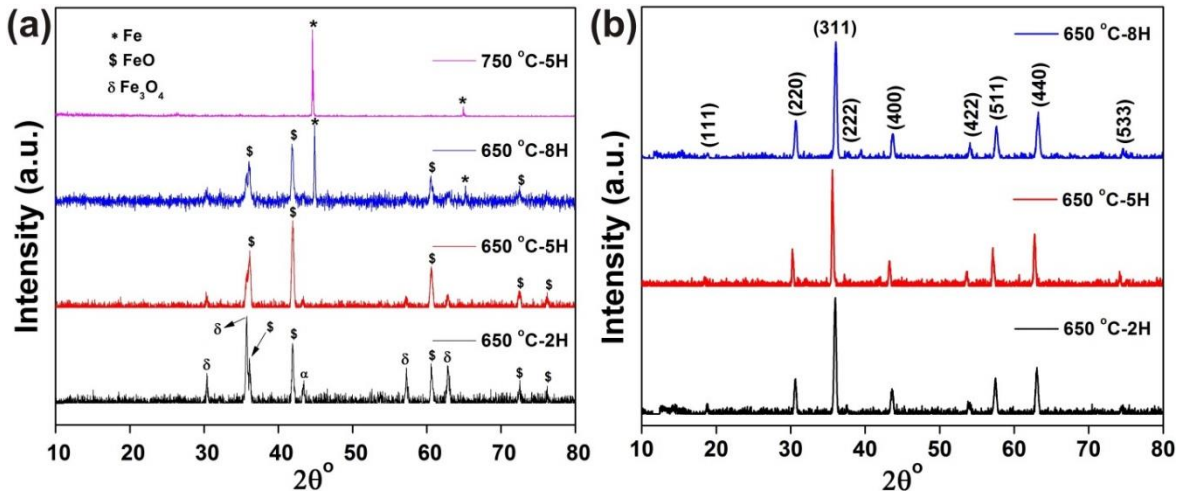

Figure 4.5. Effect of temperature and heating time on the structure of RM1 (a) and RM2 (b).

As shown in Fig. 4.5(a), at 650℃ RM1 showed the co-existence of Fe_3O_4 and FeO for 2 to 4 h of heating whilst 5 h of heating looks like the optimal heating time to retain pure FeO phase. Further prolonged heating say 6 h or more lead to the formation of Fe out of FeO. Similarly increase in the reaction temperature to say 750 ℃ lead to the direct formation of Fe which is an indication for rapid reduction. On the other hand at 650℃, RM2 contained pure Fe_3O_4 even for 2 h of heating. Thus formed Fe_3O_4 phase has been found intact upon prolonged heating say up to 8 h as shown in Fig. 4.5(b). Further, it can be expected that Fe_3O_4

phase could be retained even for higher temperatures beyond 650℃ as there is no significant weight loss as observed in TGA curve of RM2. Thus, the overall XRD findings are consistent with TGA analysis.

Morphology investigation of EG/Fe_3O_4 and EG/FeO composites that are prepared at 650℃ by heating for 2 and 5 h, respectively revealed the plausible causes for the already discussed XRD and TGA observations. Figures 4.6(a-c) show FESEM micrographs of EG/Fe_3O_4 composite with poor contacts between EG and Fe_3O_4 nanoparticles. This situation might have arisen due to rapid burning of GO i.e., its rapid exfoliation to form EG and the fast gust of various gaseous species those degasing from EG due to decomposition of various functional groups could be collectively pushed freshly and formed Fe_3O_4 particles away from contacting EG. Otherwise the topographic nature of EG does not readily allow freshly formed Fe_3O_4 particles to accommodate on it. Thus formed lose contacts between EG and Fe_3O_4 clarifies that why the reduction process stopped at stage I even for 2 to 8 h of heating time and negligible weight loss of RM2 beyond 500℃ as observed in TGA analysis. Plausibly highly oxidized GO loses its functional groups rapidly around 500℃ (within 20 min from 400 to 500℃) to form various gaseous species including H*/CO which might have simultaneously reduced Fe_2O_3 to Fe_3O_4 along with carbon atoms that are in contact with EG prior to exfoliation. As observed in TGA after 500℃ no more weight loss of reaction mixture means neither gaseous species nor carbon atoms are available for reduction as the temperature and time of heating increased in agreement with XRD results. Thus, further reduction either by gaseous or solid state reducing agents ceases and EG/Fe_3O_4 may retain for prolonged annealing times and even at high temperatures. On the other hand Fig. 4.6(d) shows existence of EG flakes and FeO particles together in a manner that they are tightly adhered with each other in EG/FeO composite. A close observation of FeO nanoparticles where they appear more aggregated visualizes their rough surface finishing along with presence the of small EG

flakes as shown in Fig. 4.6(d). This situation might be possible as a consequence of relatively slow burning of GO1 in comparison to GO2, which exfoliates slowly and releases less gaseous species compared to GO1 and provides good contacts between reduced iron compounds and EG throughout the heating time and temperatures as observed in XRD and TGA studies. In contrast to FeO, Fe_3O_4 particles possessed very smooth surface finish and there is no sign of EG's presence in between them as shown in Figs. 4.6(a-c).

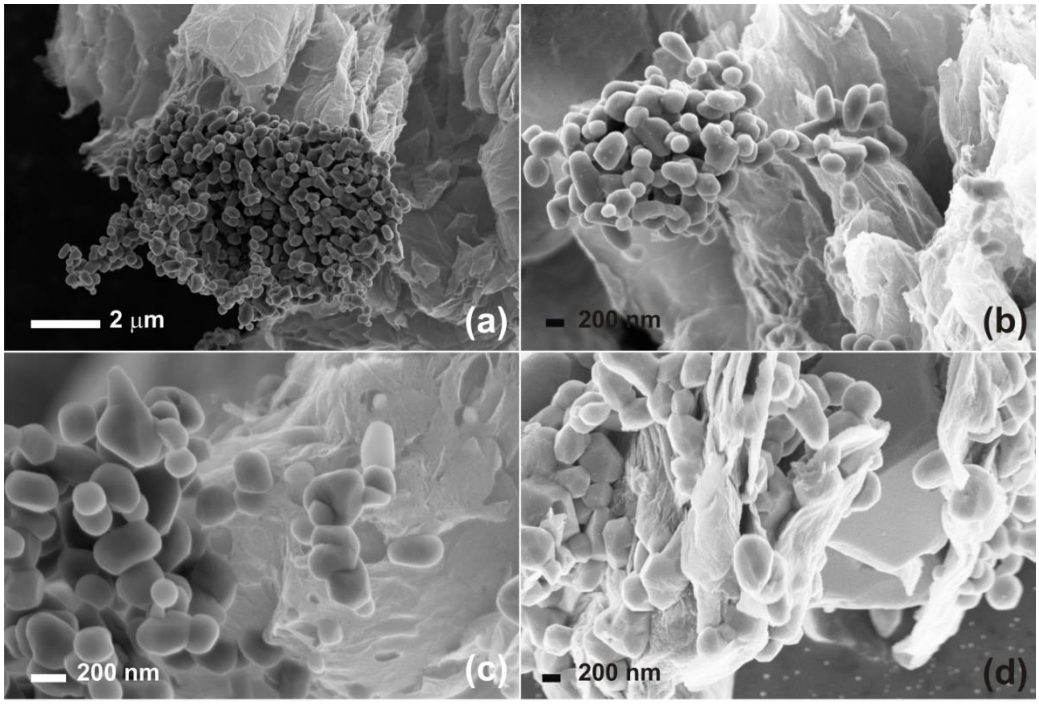

Figure 4.6. (a-c) show EG and smooth surface finished Fe_3O_4 nanoparticles well isolated and poor contacts between them in EG/Fe_3O_4-650℃-2h; (d) shows the existence of EG flakes and rough surface finished FeO nanoparticles together in EG/FeO-650℃-5h.

Close examination of individual iron oxides particles using TEM and HRTEM as shown in Fig. 4.7 revealed that FeO particles are either wrapped or covered by FLG (Figs. 4.7(a-b)) whilst Fe_3O_4 particles are in their purest form (Figa. 4.7(c-d)). Here, in-situ stabilization of FeO particles will be achieved when they are either wrapped or covered by FLG during either heating or cooling. Nonetheless, it is known that FeO phase readily converts back either to Fe_3O_4 or Fe_2O_3. Thus EG or FLG acts like a protecting layer to FeO similar to carbon coating

or organic surfactants. Combined morphology observations of FESEM and TEM suggest that reduction process in RM1 continued through all stages i.e., $2GO1+Fe_2O_3 \rightarrow {}^{I}EG/Fe_3O_4 \rightarrow {}^{II}EG/FeO \rightarrow {}^{III}EG/Fe$ depending on time of heating and temperature owing to good contacts between iron oxides and EG whilst in RM2 reduction stopped at stage II i.e. $2GO1+Fe_2O_3 \rightarrow {}^{I}EG/Fe_3O_4$ for all the considered heating times and even for all temperatures above 500℃ as illustrated by XRD and TGA analysis.

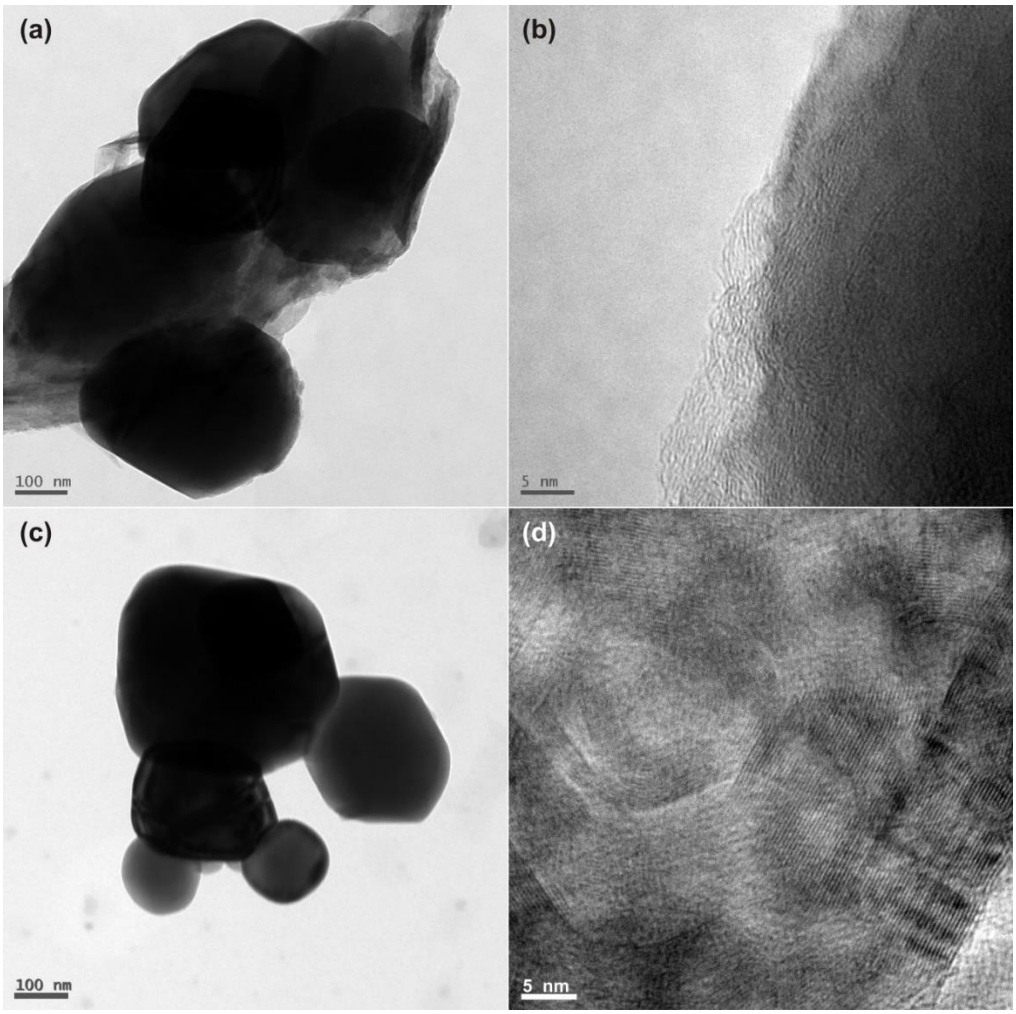

Figure 4.7. HRTEM images of (a–b) EG/FeO-650C-5h and (c–d) EG/Fe_3O_4-650C-2h.

Further, post synthesis XPS studies of EG/FeO and EG/Fe_3O_4 those prepared at 650℃ and 5h heating corroborated with the XRD studies. Fe 2p spectrum pertaining to EG/FeO looks similar to that of EG/Fe_3O_4 (pure Fe_3O_4) owing to the presence of trace amounts of Fe_3O_4

phase in it. But they mainly differ in their peak positions as shown in Figs. 4.8(a) and (c). The binding energies of characteristic doublet of Fe 2p in EG/FeO are found 1 eV lesser than EG/Fe_3O_4 in agreement with the available reports [14-18]. The positions of $2p_{3/2}$ and $2p_{1/2}$ peaks are centered at 710 and 723.8 eV, respectively in the case of EG/FeO those are matching well with reported values of Fe^{2+} in FeO [14-19]. The respective peaks in EG/Fe_3O_4 are found centered at 711 and 724.7 eV, consistent with $Fe^{2.5+}$ in Fe_3O_4 [19,20]. Moreover the absence of satellite peak(s) in-between $2p_{3/2}$ and $2p_{1/2}$ doublet is an indication for complete conversion of starting Fe_2O_3 to either FeO or Fe_3O_4 [15-18,20]. Further, O1s spectra (Figs. 4.8(b) and (d)) show peaks at 530.1 and 530.4 eV pertaining to EG/FeO and EG/Fe_3O_4, respectively that are linked to oxygen directly bonded to Fe in lattices of FeO and Fe_3O_4, respectively [20,21]. The other two peaks at 531.8 and 533.3 eV correspond to oxygen present in the residual functional groups of EG and adsorbed moisture, respectively [21].

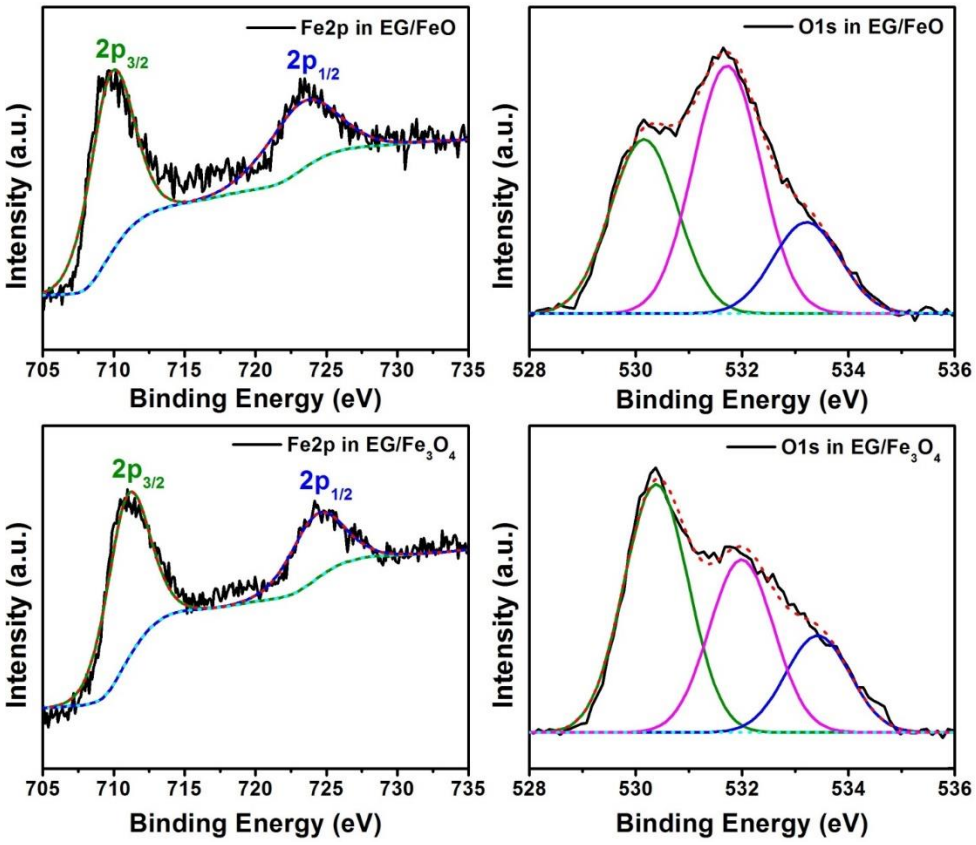

Figure 4.8. High resolution XPS spectra of Fe 2p (top left) and O1s (top right) in EG/FeO and Fe 2p (bottom left) and O1s (bottom right) in EG/Fe_3O_4.

References

[1] Kadam MM, Lokare OR, Kireeti KVMK, Gaikar VG, Jha N. Impact of the degree of functionalization of graphene oxide on the electrochemical charge storage property and metal ion adsorption. RSC Advances. 2014;4:62737-45.

[2] Yan H, Tao X, Yang Z, Li K, Yang H, Li A, et al. Effects of the oxidation degree of graphene oxide on the adsorption of methylene blue. Journal of Hazardous Materials. 2014;268:191-8.

[3] Krishnamoorthy K, Veerapandian M, Yun K, Kim SJ. The chemical and structural analysis of graphene oxide with different degrees of oxidation. Carbon. 2013;53:38-49.

[4] Bagri A, Mattevi C, Acik M, Chabal YJ, Chhowalla M, Shenoy VB. Structural evolution during the reduction of chemically derived graphene oxide. Nature Chemistry. 2010;2(7):581-7.

[5] Acik M, Mattevi C, Gong C, Lee G, Cho K, Chhowalla M, et al. The role of intercalated water in multilayered graphene oxide. ACS Nano. 2010;4(10):5861-8.

[6] Jeong H-K, Lee YP, Jin MH, Kim ES, Bae JJ, Lee YH. Thermal stability of graphite oxide. Chemical Physics Letters. 2009;470(4–6):255-8.

[7] Su C, Acik M, Takai K, Lu J, Hao S-j, Zheng Y, et al. Probing the catalytic activity of porous graphene oxide and the origin of this behaviour. Nature Communications. 2012;3:1298.

[8] Acik M, Lee G, Mattevi C, Pirkle A, Wallace RM, Chhowalla M, et al. The role of oxygen during thermal reduction of graphene oxide studied by infrared absorption spectroscopy. The Journal of Physical Chemistry C. 2011;115(40):19761-81.

[9] González Z, Botas C, Álvarez P, Roldán S, Blanco C, Santamaría R, et al. Thermally reduced graphite oxide as positive electrode in vanadium redox flow batteries. Carbon. 2012;50(3):828-34.

[10] Ganguly A, Sharma S, Papakonstantinou P, Hamilton J. Probing the Thermal deoxygenation of graphene oxide using high-resolution in situ X-ray-based spectroscopies. The Journal of Physical Chemistry C. 2011;115(34):17009-19.

[11] Pei S, Cheng H-M. The reduction of graphene oxide. Carbon. 2012;50(9):3210-28.

[12] Botas C, Álvarez P, Blanco C, Santamaría R, Granda M, Gutiérrez MD, et al. Critical temperatures in the synthesis of graphene-like materials by thermal exfoliation–reduction of graphite oxide. Carbon. 2013;52:476-85.

[13] Gao W, Alemany LB, Ci L, Ajayan PM. New insights into the structure and reduction of graphite oxide. Nature Chemistry. 2009;1(5):403-8.

[14] Swiatkowska-Warkocka Z, Kawaguchi K, Wang H, Katou Y, Koshizaki N. Controlling exchange bias in Fe_3O4/FeO composite particles prepared by pulsed laser irradiation. Nanoscale Research Letters. 2011;6(1):226.

[15] Jean-Baptiste M. From epitaxial growth of ferrite thin films to spin-polarized tunnelling. Journal of Physics D: Applied Physics. 2013;46(14):143001.

[16] Joseph Y, Ketteler G, Kuhrs C, Ranke W, Weiss W, Schlogl R. On the preparation and composition of potassium promoted iron oxide model catalyst films. Physical Chemistry Chemical Physics. 2001;3(18):4141-53.

[17] Yamashita T, Hayes P. Analysis of XPS spectra of Fe^{2+} and Fe^{3+} ions in oxide materials. Applied Surface Science. 2008;254(8):2441-9.

[18] Abreu GJP, Paniago R, Pfannes HD. Growth of ultra-thin FeO(100) films on Ag(100): A combined XPS, LEED and CEMS study. Journal of Magnetism and Magnetic Materials. 2014;349:235-9.

[19] Merte LR, Shipilin M, Ataran S, Blomberg S, Zhang C, Mikkelsen A, et al. Growth of ultrathin iron oxide films on Ag(100). The Journal of Physical Chemistry C. 2015;119(5):2572-82.

[20] Fujii T, De Groot F, Sawatzky G, Voogt F, Hibma T, Okada K. In situ XPS analysis of various iron oxide films grown by NO_2-assisted molecular-beam epitaxy. Physical Review B. 2001;59(4):3195-202.

[21] Eltouny N, Ariya PA. Competing reactions of selected atmospheric gases on Fe_3O_4 nanoparticles surfaces. Physical Chemistry Chemical Physics. 2014;16(42):23056-66.

Chapter 5 EG/FeO Composite

Graphenothermal Reduction process is used to obtain exfoliated graphene oxide (EG)/iron (II) oxide (FeO) composite. Structural and compositional analyses of the sample confirm the formation of EG/FeO composite. This composite shows a reversible capacity of 857 mAh g^{-1} at a current rate of 50 mA g^{-1} in the voltage range 0.005-3.0 V versus Li. An excellent capacity retention up to 60 cycles and high coulombic efficiency of 98% are also observed. Characteristic $Fe^{2+/0}$ redox peaks observed in Cyclic Voltammetry measurement are explained in correlation with lithium storage mechanism. Thermal, electrical and impedance spectroscopy studies of EG/FeO composite are discussed in detail. Comparative electrochemical cycling studies of EG/FeO composite with Fe_2O_3 and Fe_3O_4 materials prepared under controlled conditions are also discussed.

Secondary electron micrographs of EG/FeO composite recorded at different magnifications are shown in Fig. 5.1. It can be clearly observed from the micrographs that the obtained composite consists of sub–micron sized iron oxide particles with different morphologies. Some of these particles appeared to be wrapped by graphene layers, some appeared to be anchored on graphene layers and the rest appeared to be free standing. Graphene layers in EG appeared to have expanded along c-axis as shown in Fig. 5.1(a) and (b). Bright field transmission electron micrograph of EG/FeO composite is shown in Fig. 5.2(a). This micrograph clearly reveals that the obtained composite consists of agglomerated iron oxide particles which are wrapped by few layered graphene (FLG) sheets. The corresponding selected area electron diffraction (SAED) pattern shown in Fig. 5.2(a) depicts intense diffraction spots indexed to FeO and diffused ring pattern related to the presence of FLG. The SAED pattern (Fig. 5.2(d)) obtained from the edge of single iron oxide particle as shown in the Fig. 5.2(c) indicates that the obtained diffraction spots (perpendicular to the FCC [211] zone axis) are related to single crystal FeO with face centred cubic structure. The corresponding high resolution transmission electron micrograph (Fig. 5.2(b)) clearly reveals

that the synthesized composite contains thick FeO particles wrapped by FLG sheets. The FLG wrapped on top of FeO particles acts like a protective layer/coating and avoids easy conversion of FeO to other compounds. Thus FLG provides stability to FeO similar to carbon and surfactants coated FeO [1,2].

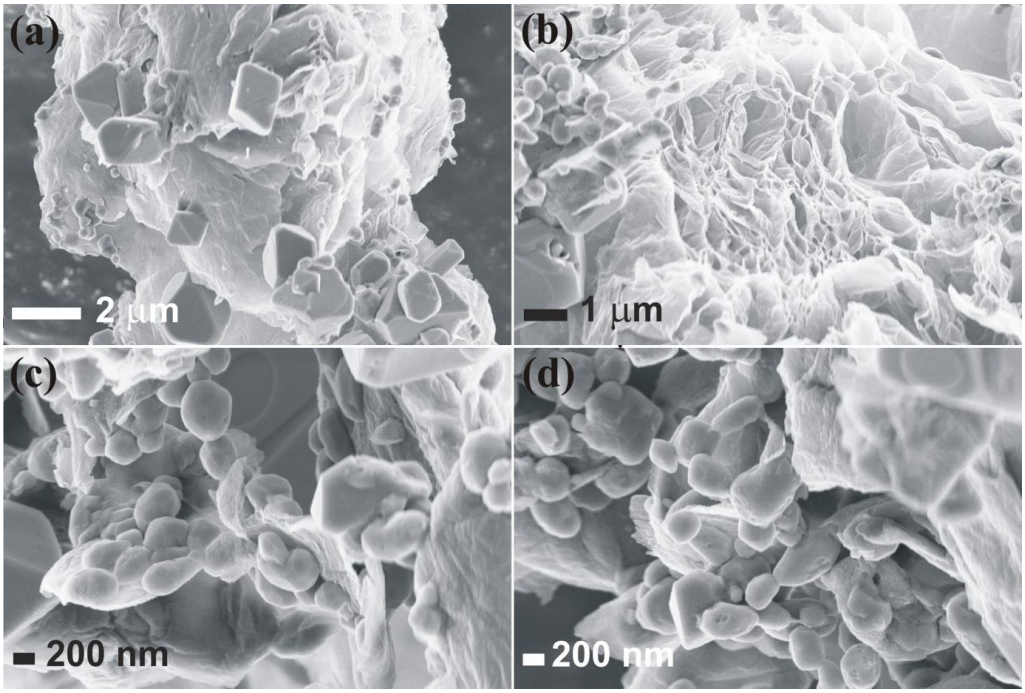

Figure 5.1. Secondary electron micrographs of EG/FeO composite.

X-ray diffraction (XRD) pattern being a result of bulk ensemble of microstructural features of the sample, it surprisingly revealed that all of the iron oxide particles irrespective of their different shapes and sizes have crystallized in to same lattice system. XRD pattern of the as-prepared EG/FeO composite powder (Fig. 5.3) suggests that iron oxide is present in the form of FeO with good crystallinity. The noise observed in XRD pattern might be either from disordered nature of EG or presence of other crystalline iron oxides. In tune with SAED results the refined XRD data showed that the composite consists of FeO with cubic crystal structure (Wuestite, JCPDS # 89-2468) as the major component with Wt.%-Rietveld around 99.6% and cubic Fe_3O_4 (Magnetite, JCPDS # 89-691) as the minor component with Wt.%-Rietveld around 0.4% (Table 5.1 and Annexure 6). This trace amount of Fe_3O_4 might be resulted either due to reduction path terminated at first stage ($Fe_2O_3 \rightarrow {}^{I}Fe_3O_4$) or converted

from FeO which is not covered by FLG. Thus overall minute amounts of Fe_3O_4 suggest that majority of FeO particles are well stabilized by FLG as observed in electron micrographs. After Rietveld refinement, the lattice parameter of FeO was found to be a = 4.3375 Å whilst the average crystallite size is ~42.5 nm. Apart from iron oxide diffraction peaks, a very low intensity graphitic (002) peak corresponding to EG is observed around 26.5º.

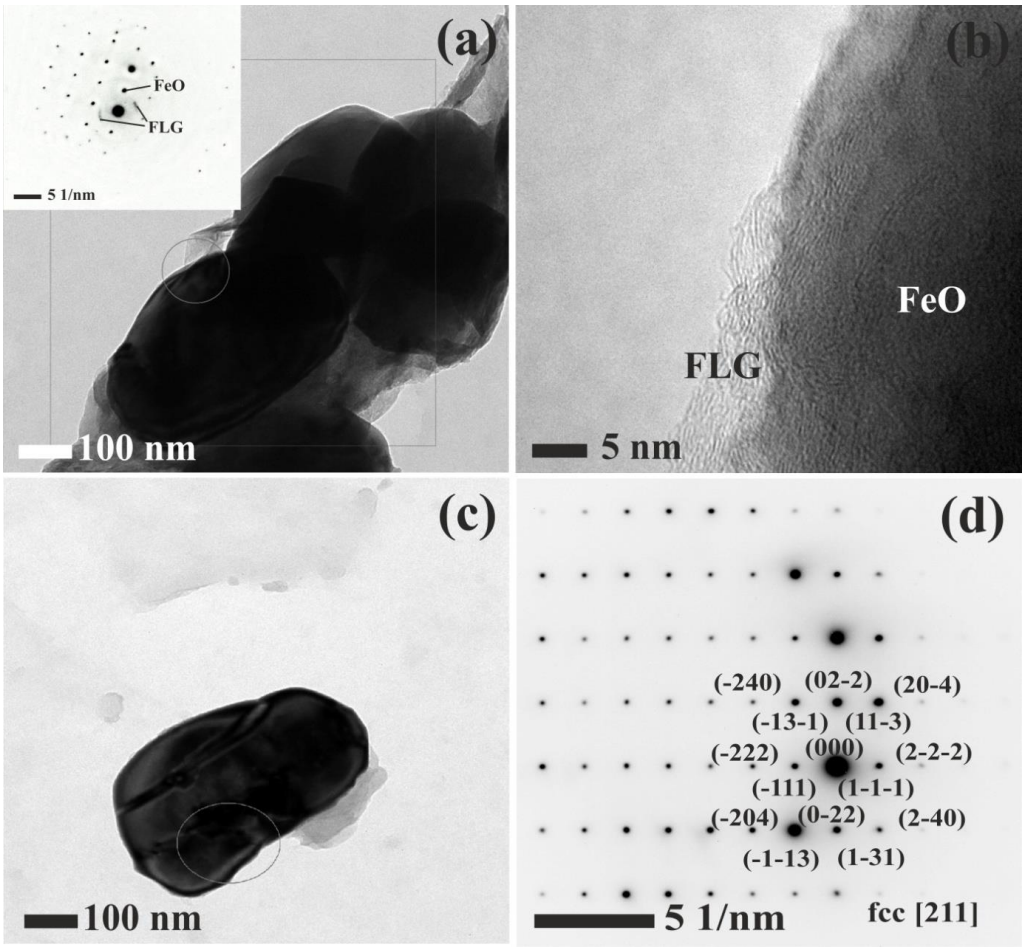

Figure 5.2. Transmission electron micrographs and SAED patterns of FeO particles wrapped by FLG (a), HRTEM image of FeO surface covered by FLG (b), single crystalline FeO nanoparticle (b) and its SAED pattern (d).

BET and Langmuir specific surface areas are 10.97 and 15.46 (±0.2) $m^2\ g^{-1}$, respectively. This very low specific surface area in comparison with thermally annealed graphene [3] indicates that the most of the active surface of EG is covered by FeO particles which may not readily allow nitrogen molecules to get adsorbed onto them unlike pristine graphene.

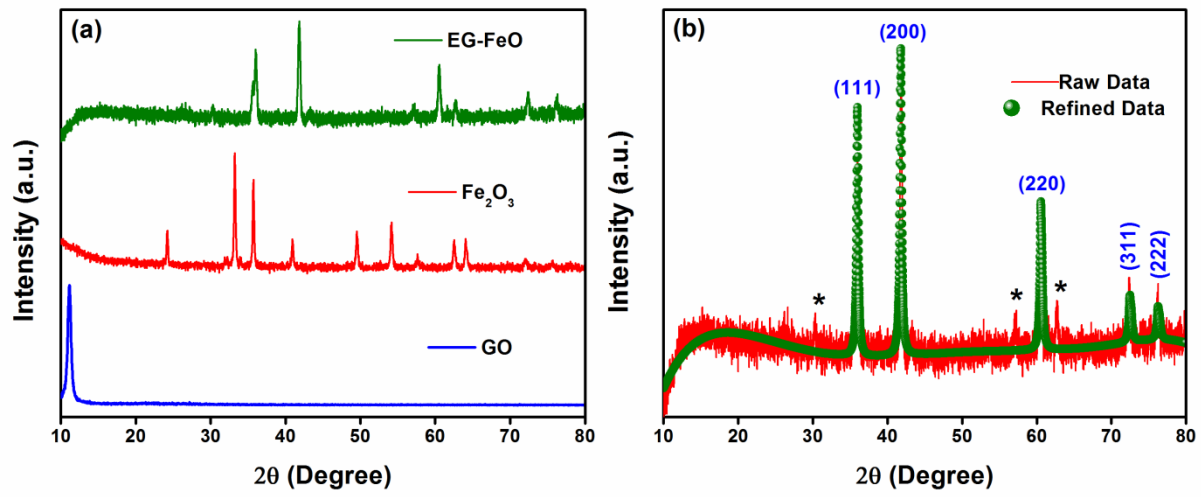

Figure 5.3. X-ray diffraction pattern of (a) GO, Fe_2O_3, EG/FeO and (b) Rietveld refinement results of EG/FeO (* peaks corresponding to Fe_3O_4).

Table 5.1. Rietveld refinement parameters of FeO and Fe_3O_4.

Structure	FeO	Fe_3O_4
Evaluated Lattice parameters	a = 4.3375 Å	8.4022 Å
Crystallite size (Lorentzian)	42.5 nm	27.1 nm
Space group	Fm-3m	Fd-3m
Lattice parameters	a = 4.3402 Å	a = 8.4022 Å
JCPDS file Number	JCPDS # 89-2468	JCPDS # 89-691
R-Bragg	0.062	0.257
Wt.%-Rietveld	99.596	0.404
R-Values	Rexp : 1.89 Rwp : 2.15 Rp : 1.70 GOF : 1.14 Rexp`: 38.55 Rwp`: 43.82 Rp` : 65.92 DW : 1.61	

The observed large hysteresis between N_2 adsorption and desorption isotherms (Fig. 5.4(a)) suggests mesoporous nature of EG/FeO composite. The average pore volume with a pore diameter of ~10.6 nm is found to be ~0.064 $cm^3 g^{-1}$. The quality of exfoliation of EG in terms of high disorder introduced into GO to form EG can be clearly understood from the increased intensity of D-band in the case of EG as shown in Fig. 5.4(b). The typical C_6 hexagon

breathing modes (G-band from E_{2g} mode and D-band from defect activated six-atom ring vibrations) [4] of EG and GO as measured by Raman spectroscopy are found at D_{EG} = ~1339.5 cm^{-1}, G_{EG} = ~1576.8 cm^{-1}, D_{GO} = ~1354.6 cm^{-1} and G_{GO} = ~1597.2 cm^{-1}. The shifting of positions of G, D and 2D (~2676 cm^{-1}) bands in EG towards lower wave numbers side (in comparison to GO) corresponds to decrease in number of graphene layers in EG than GO [4]. The evolution of stronger characteristic D-band than G-band in EG/FeO indicates the presence of more disordered carbon or graphene nanosheets in EG [4,5].

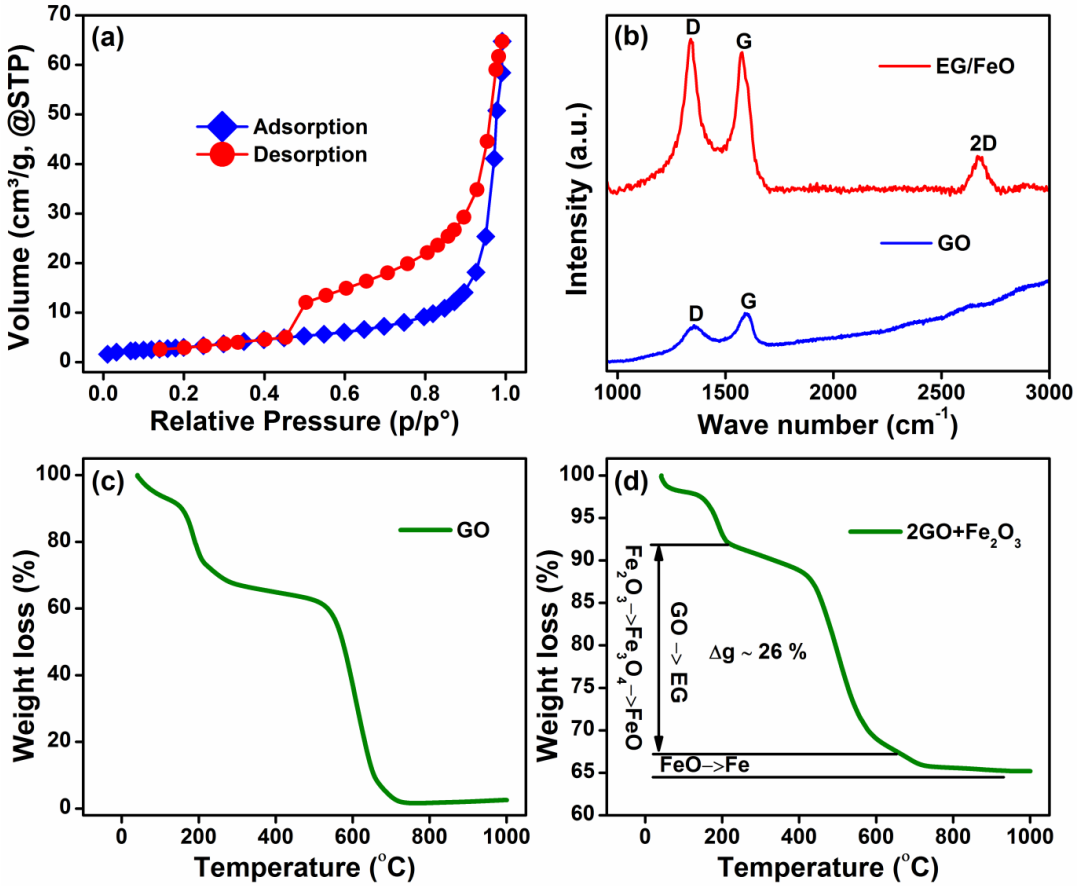

Figure 5.4. (a) N_2 adsorption and desorption isotherms, (b) Raman spectrum of EG/FeO in comparison to GO, (c,d) TGA weight loss curve of GO and reaction mixture of 2GO and Fe_2O_3, respectively.

It is well accepted that FeO forms and remains stable above 570 ºC [6,7] and hence it is worthy to discuss FeO formation possibilities in the present case around the operation temperature i.e. 650 ºC which is good enough to release reducing species like H_2/H^+ and CO

from GO [8,9]. By observing FeO morphology in electron micrographs it can be considered that both solid and gaseous state reduction is taking place. The reduction of Fe_2O_3 has plausibly taken place by free carbons of EG and by gaseous species like CO, H_2 *etc*. released from GO according to Equs. 5.1-5.6 as the free energy of these reactions at 650 ºC is negative ($\Delta G < 0$) [10]. This two-way reduction mechanism can be evidenced by the presence of FeO particles on surface and edges of EG, covered by FLG (reduced by carbon atoms) and free standing FeO (reduced by gases). The direct conversion of Fe_2O_3 to FeO may not possible because above 570 ºC reduction of hematite occurs in three stage i.e., through $Fe_2O_3 \rightarrow {}^{I}Fe_3O_4 \rightarrow {}^{II}FeO \rightarrow {}^{III}Fe$ path in the presence of C, CO, H_2 or their mixtures [7,10] and also trace amount of Fe_3O_4 phase found as per XRD analysis confirms that three stage reduction pathway preferably happens. In the present study, we have identified that annealing time is best parameter to control this reduction path at 650 ºC. Pure FeO with trace amounts of Fe_3O_4 impurity phase is observed for five hours of heating. Further prolonged heating (say 6 hours) or higher reduction temperature (750 ºC) leads to third stage i.e. conversion of FeO to Fe takes place (Annexure 6). Similar observation found in TGA analysis as shown in Fig. 5.4(d) in which continuous loss of weight of reaction mixture ($2GO+Fe_2O_3$) is observed up to 900 ºC. The weight loss of reaction mixture up to 200 ºC could be ascribed to removal of water (preferably from GO) as this portion of curve appears similar to GO (Fig. 5.4(c)). The maximum weight loss (~25%) of reaction mixture is observed in between 200-650 ºC which corresponds to the reduction of GO, Fe_2O_3 and Fe_3O_4 to form EG/FeO [6,7]. In-situ formation of FeO anchored on to or wrapped by FLG [6,7] helps in stabilization of FeO. The next weight loss step (650-900 ºC) can be associated to conversion of FeO to Fe [6,7]. Finally as-synthesised EG/FeO that obtained at 5h of heating is further analysed with TGA in air in order to understand the weight percentage of EG and FeO phases. Result indicated that the composite contains approximately 87 wt.% of FeO and 13 wt.% EG phase (Annexure 6).

With these weight percentages one can expect theoretical capacity of EG/FeO around 696 mAh g^{-1} (Annexure 6). Further, electrical conductivity of EG/FeO is measured from I-V characteristic curve that recorded at room temperature (Annexure 6). I-V characteristic curve resembled the resistive element with linear relation between current and voltage, and constant slope (resistance). Based on the slope of I-V curve we calculated conducitvity of EG/FeO around 0.23 $\Omega^{-1}cm^{-1}$ which is well above the value reported for wusite [11]. These findings facilitate the use of EG/FeO as an anode of LIBs.

$$C + 3Fe_2O_3 \xrightarrow{I} 2Fe_3O_4 + CO \quad (5.1)$$

$$CO + 3Fe_2O_3 \xrightarrow{I} 2Fe_3O_4 + CO_2 \quad (5.2)$$

$$H_2 + 3Fe_2O_3 \xrightarrow{I} 2Fe_3O_4 + H_2O \quad (5.3)$$

$$C + Fe_3O_4 \xrightarrow{II} 3FeO + CO \quad (5.4)$$

$$CO + Fe_3O_4 \xrightarrow{II} 3FeO + CO_2 \quad (5.5)$$

$$H_2 + Fe_3O_4 \xrightarrow{II} 3FeO + H_2O \quad (5.6)$$

The electrochemical response of EG/FeO composite is studied with CV technique and interestingly its CV characteristics are very consistent in all cycles despite of the different shape and sizes of FeO particles. The cyclic voltammograms of Fe-oxides and EG sample are shown in Fig. 5.5. During the first cathodic (reduction) scan EG/FeO (Fig. 5.5(a)) shows two successive peaks found at ~0.68 V vs. Li are ascribed to the electrochemical reaction of Li with FeO and ~0.5 V vs. Li corresponds solid electrolyte interphase (SEI) [12,13]. EG might have shown its individual identity as peak at ~0.5 V is observed for TEGO (Fig. 5.5(d)). The absence of 0.5 V peak and large difference between first and second reduction scans could be mainly attributed to loss of Li as a covalent constituent of SEI. The peak at ~0.68 V is plausibly due to crystal structure destruction by reduction of Fe(II) to Fe(0) to form amorphous Fe^0 nano particles surrounded by Li_2O phase. The significant increases in the reduction peak potential from 0.68 to 0.9V should be caused by the increase in the electro

activity of the reactants or change the reaction mechanism, similar trend was noted with galvanostatic cycles profiles of MO (M=Co, Ni, Fe) [12,13]. These finding are consistent with EG/Fe_3O_4 (Fig. 5.5(b)) and EG/Fe_2O_3 (Fig. 5.5(c)) along with earlier reports [1,3,14]. The other reduction peak close to ~0.005 V might be due to either intercalation or electrochemical absorption of Li through individual graphene sheets of EG as like observed for TEGO. In first anodic scan there is small amount of constant oxidation current resulted from electrochemical desorption of Li from EG was observed up to 1.25 V and similar is observed in the case of TEGO. One broad peak is observed around 1.6 V that correspond to oxidation of Fe to form FeO by releasing two Li ions. But this peak appears less broadened when compared with broad humped oxidation steps of EG/Fe_3O_4 and EG/Fe_2O_3 (Fig. 5.5 (e) and (f)) which is indication for single step oxidation is preferably happening. From second anodic scan onwards current due to EG is constant even though it lowered than first cycle while the observed decrease for conversion reaction peaks is compensated by peak broadening with slight shift towards higher voltage. Thus overall lithium ion insertion and extraction mechanism into EG/FeO is a combination of electrochemical absorption-desorption due to EG and reversible redox reactions of FeO [1,14] as per the Equs. 5.7-5.8.

$$FeO + 2Li^{+} + 2e^{-} \rightarrow Fe + Li_2O \text{ (Discharging)} \quad (5.7)$$

$$Fe + Li_2O \rightarrow FeO + 2e^{-} + 2Li \text{ (Charging)} \quad (5.8)$$

With the encouraging CV observations at the background, Li ion storage and release capacities of EG/FeO are elucidated with GC tests in the voltage window of 0.005-3.0 V and at current rates of 50 and 400 mA g^{-1}. For the considered current densities similar kind of voltage versus discharge-charge capacity profiles are observed (Figs. 5.6(a) and (b)). During 1st cycle, slope of discharging curves are consistent in starting from OCV to 1.5 V whereby slope changes constantly up to 0.75 V where the curves become quasi-perpendicular to the precedent portion and extend until voltage becomes 0.5 V (say up to 1000 mAh g^{-1}). As

inferred from CV curves, first cathodic scan in this portion matches to the large reduction current observed between 0.5 and 1.0 V that corresponds to reduction of FeO by Li to form metallic Fe and Li_2O as well as lithiation and SEI formation [12].

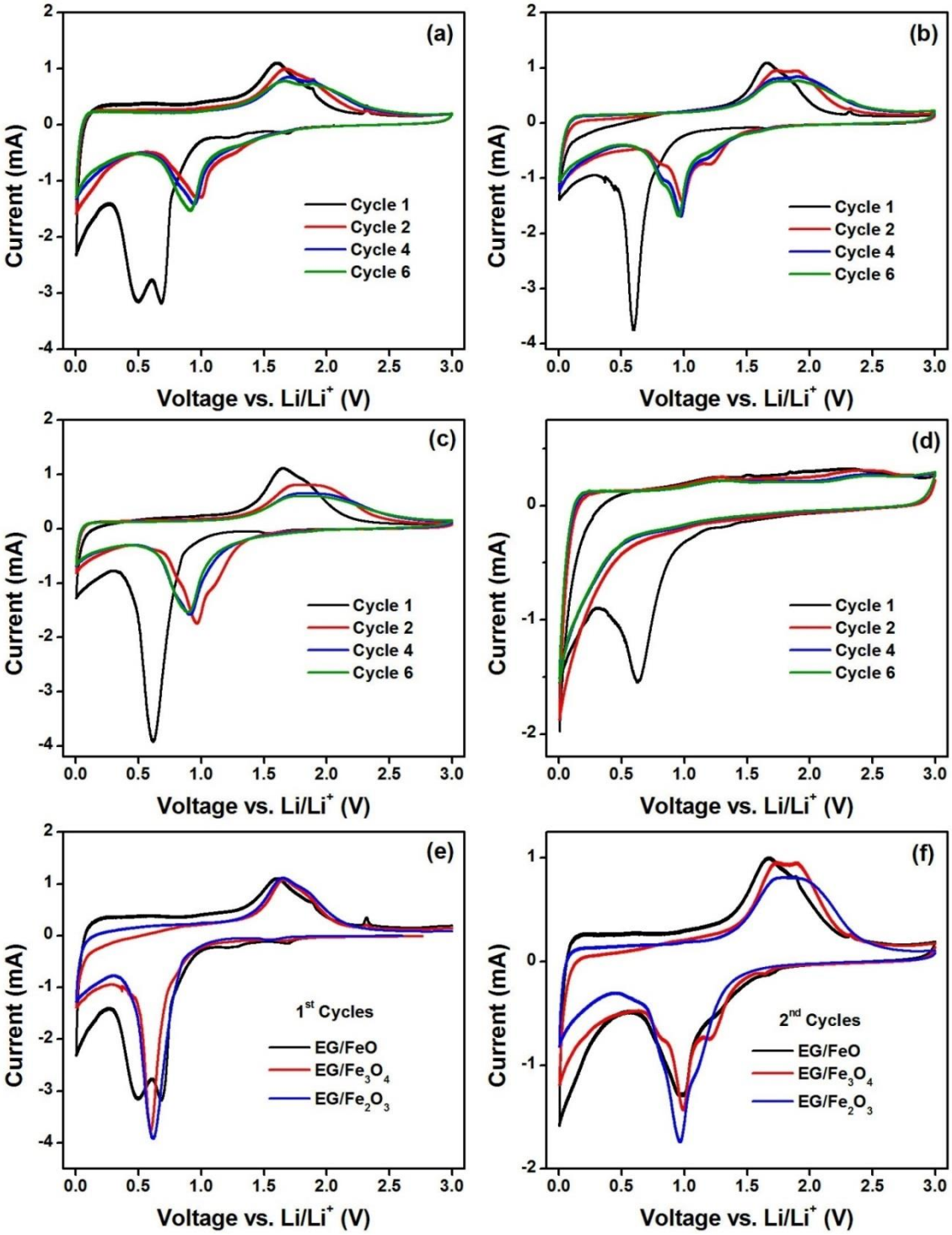

Figure 5.5. Cyclic voltammogram of (a) EG/FeO, (b) EG/Fe_3O_4, (c) EG/Fe_2O_3, (d) TEGO, (e) first cycles and (f) second cycles of three EG/Iron Oxide composites.

After the portion under discussion (pages 60-61), another sloping plateau is observed up to final voltage set point of 0.005 V that accounts to 600 mAh g^{-1} capacity which might be due to co-intercalation of solvated Li ions onto or in between individual graphene sheets of EG simultaneously which actively reduces (decomposes) electrolyte molecules. But the extent of capacity of this region visualizes the role of enhanced catalytic reduction nature of freshly formed Fe nano phases towards electrolyte decomposition not to be ruled out [12]. The excess capacity during first cycles is due reduction of solvent in the electrolyte and SEI formation [12], and partially due to formation of polymeric layer on metal nano particles [12,14,15]. Detailed SEI formation mechanism is well-documented [16]. The discharge cycling profiles of EG/Fe_3O_4 (Fig. 5.6(c)) and EG/Fe_2O_3 (Fig. 5.6(d)) are comparable to EG/FeO with minor differences in the peak voltages. During the first charging from 0.005 V to 3.0 V, the slope of the curves is a steady straight line until a voltage of 1.5 V, whereby it becomes moderate and stays at this gradient until a voltage of 1.8 V from which it becomes steeper once again up to 3.0 V. Upon first charging to 3.0 V the capacity reversed from first discharge capacity is only 52-57% depending on current rate as summarized in Table 5.2. The total discharging and charging capacities of first cycle at 50 mA g^{-1} current rate are 1489 and 857 mAh g^{-1}, respectively and results of remaining current densities are shown in Table 5.2. The second discharge curves are similar to first discharge curves but major difference is their discharge capacities are 43-48 % lesser than first discharge to 0.005 V. The long plateau due to SEI has disappeared as it was irreversible (ICL ~600-640 mAh g^{-1}) and the remaining small plateau feature corresponds to Li storage according to conversion reaction (Equ. 5.1) in agreement with reduction current peak around 1 V in CV profile. The second charging curves are also similar to first charging curves but they exhibited steeper initial and final slopes than the first charging. The remaining cycles displayed the same pattern as the second discharging and charging curves, although there is some capacity fading as the cycles wear on. At the end

of test the capacity is relatively constant with negligible fading and a small increase in capacity trend is observed in each current case. Thus overall, EG/FeO showed discharge and charge profiles are similar to EG/Fe_3O_4 (Fig. 5.6(c)) and EG/Fe_2O_3 (Fig. 5.6(d)) with slight difference in capacity values.

Table 5.2. Anodic performance of EG/FeO at various current densities.

Current Rate (mA g^{-1})	1st DC[1]	1st CC[2]	1st QE[3]	2nd DC	2nd CC	2nd QE	60th DC	60th CC	60th QE	60th CR[4]
50	1489	857	58	850	797	94	736	725	99	85
100	1476	829	56	819	770	94	710	700	99	85
200	1411	770	55	745	711	95	631	624	99	81
400	1280	674	53	675	639	95	533	526	99	78

[1]Discharge Capacity (mAh g^{-1}, ±5); [2]Charge Capacity (mAh g^{-1}, ±5); [3]Coulombic Efficiency (%); [4]Capacity Retention (%)

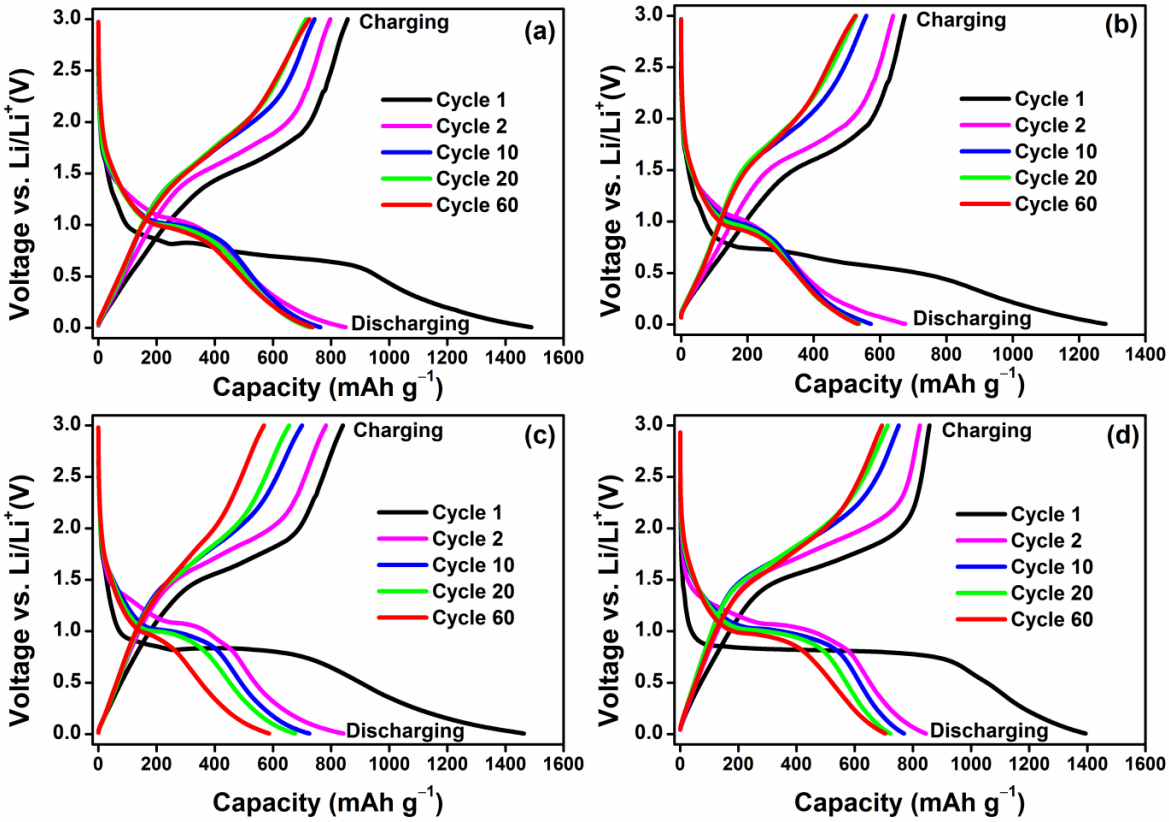

Figure 5.6. Galvanostatic discharge-charge profiles of (a, b) EG/FeO at 50 and 400 mA g^{-1} respectively; (c) EG/Fe_3O_4 at 50 mA g^{-1} and (d) EG/Fe_2O_3 at 50 mA g^{-1}.

To understand the cyclic performance of EG/FeO, GC results at different current rates i.e., 50, 100, 200 and 400 mA g^{-1} are interpreted in terms of capacity versus cycle number along with respective Coulombic efficiencies (%, QEs) as shown in Fig. 5.7. The observed QE values for first cycle are only 57-53 % (Table 5.2) which are increased to 93-94% in second cycle then soon they fluctuated between 98-99% and this scenario is continued up to end of the test. These poor first cycle QE values are resulted at expense of lithium loss in the form of SEI which is consequences as high ICL. During first discharge both EG and FeO actively intakes solvated lithium but during subsequent charging the same amount of lithium will not comes out. Thus in the case of EG/FeO extent of lithium loss is more which appeared as high ICL value which limited efficiency of anode to low values as tabulated in Table 5.2. This loss of lithium observed in further few cycles also and corresponding capacity fading continues till the 20th cycle, after which the capacity remains relatively constant with negligible fading and slight increase in capacity has observed. The initial cycle to cycle capacity fading is around 6% and for an average of 60 cycles it is less than 2%. Capacity retention of 84% at 50 mA g^{-1} and 78 % at 400 mA g^{-1} is observed even at the 60th charge and onwards.

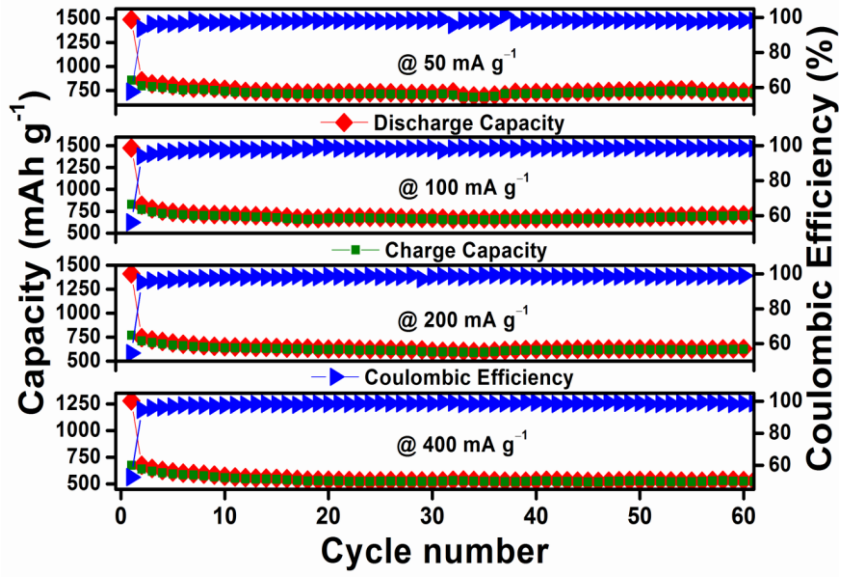

Figure 5.7. Cyclic performance of EG/FeO at various current rates.

Here, the continuous capacity decay and inferior reversible capacity associated with bare FeO particles [1] has been overcome by incorporating FeO particles into continuous conducting type matrix of EG. EG/FeO shown superior reversible capacities and constant cyclic performance than the similar class of materials like EG/Fe_3O_4 and EG/Fe_2O_3 (Annexure 6), bare FeO [30], carbon coated FeO (FeO/C) [13] and nanorods of FeOOH [17]. The observed superiority of EG/FeO than FeO/C could be attributed to enhanced lithiation capability of EG than carbon in addition to improved reversible conversion reactions of FeO nanoparticles.

Frequency dependent AC impedance of EG/FeO is shown in Fig. 5.8 as Nyquist plot which contained a typical semicircle (higher frequency range) and Warburg line (with 45° slope in lower frequency range) for various discharging (to 0.005V) and charging (to 3.0 V) cycles including fresh cell (at OCV). The respective equivalent electrical circuits used to fit impedance spectra are also included in the Fig. 5.8 and value of each circuit element is furnished in Table 5.3. The impedance data obtained at OCV and at each discharge is fitted to simple circuit but while charging fitting is more complex as shown in circuit diagrams. The electrolyte resistance R_e [18] is found in the range of 4.1-5.8 Ω for various states of anode as shown in Table 5.3. The resistance to charge transfer R_{ct} [18] is about 90-97 Ω up to first discharge but it has decreased to 38 and 29 Ω after 30^{th} and 60^{th} discharges, respectively. The corresponding capacitance of double layer formation CPE_{dl} is decreased to 35 µF during first discharge while for remaining cases it varied in between 88 and 97 µF. The impedance after charging is different from both OCV and discharges by an extra small irregular curved portion in high frequency region (inset of Fig. 5.8(b)) that might be preferably due to collective resistance of surface film formation R_{sf} [18] and R_{ct} as this portion fitted well when these two elements are considered as one. The compound resistance R_{sf+ct} is found relatively lower than R_e with increasing mode while CPE_{sf+dl} is higher than CPE_{dl} with decreasing tendency as number of cycles increased. The bulk resistance R_b due to electronic conductivity

of various components of electrode material [18] is in the range of R_e and respective CPE_b is also nearly equal to CPE_{sf+dl}. The condition $R_b > R_{sf+ct}$ signifies that faradaic reactions takes place very fastly, electrode is ideally conducting or ideally non-polarisable type and CPE_b equals to geometrical capacitance per area. The Warburg impedance Ws (resistance experienced by Li atoms during diffusion) [18] is found relatively very high in all cases. The other circuit elements C_i corresponds to Li ion intercalation capacitance was varied between 0.04 F and 1.8 F during discharge and it was kept constant at 0 F while charging so as impedance spectra fitted best. These values of C_i indicate that the kinetics of Li transport is mainly due to electrochemical absorption-desorption onto EG as CPE_b is found high while C_i is very less and fast conversion reactions of FeO consistent with CV results. Moreover the value of R_{sf+dl} (resistance to Li^+ extraction) lesser than R_{ct} (resistance to Li^+ insertion) indicates the ease of the composite with which it readily allows lithium ion to leave from it which accounts for good reversible capacities observed in GC profiles. Thus overall impedance of EG/FeO is found relatively very lower than graphene [19,20] or its iron oxide composites [21] which is a desirable aspect.

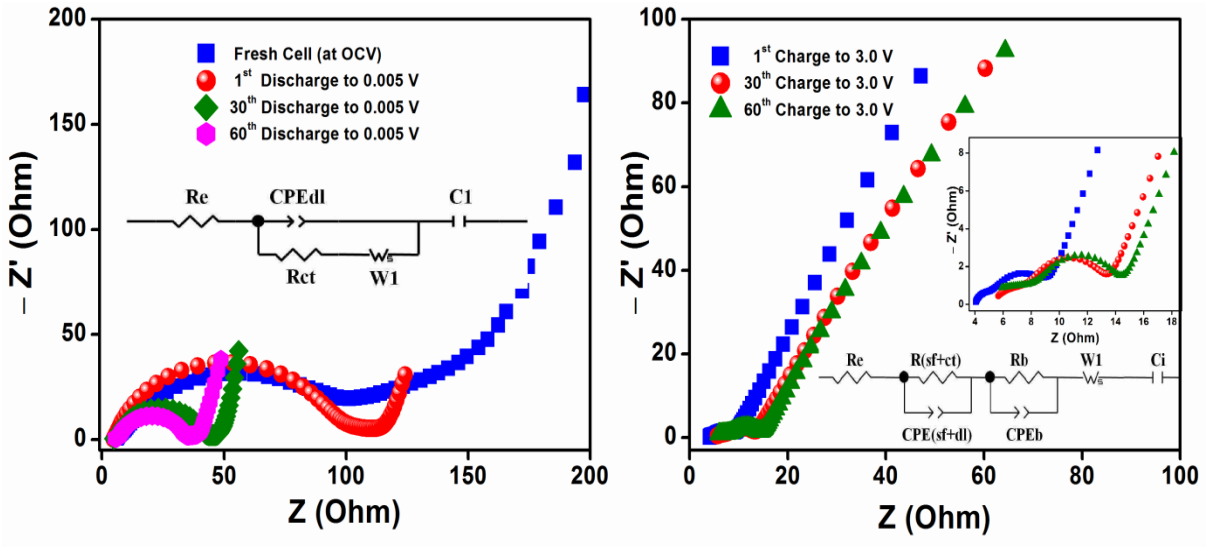

Figure 5.8. AC impedance of EG/FeO at OCV, different discharged (a) and charged states.

Table 5.3. EIS data of EG/FeO at OCV, various charge and discharge states.

Cycle Number	Discharging			Charging				
	R_e (Ω,±0.1)	R_{ct} (Ω,±1)	CPE_{dl} µF	R_e (Ω,±0.7)	$R_{(sf+ct)}$ (Ω, ±1.5)	$CPE_{(sf+ct)}$ µF	R_b (Ω,±1.2)	CPE_b µF
OCV	5.7	97	88	--	--	--	--	--
1st	4.7	90	35	4.1	1.6	610	3.7	605
30th	5.2	38	70	5.6	2.8	194	4.2	134
60th	5.8	29	97	5.8	3.3	148	4.5	112

References

[1] M.X. Gao, P. Zhou, P. Wang, J.H. Wang, C. Liang, J.L. Zhang, et al. FeO/C anode materials of high capacity and cycle stability for lithium-ion batteries synthesized by carbothermal reduction. Journal of Alloys and Compounds. 2013;565:97-103.

[2] Hou Y, Xu Z, Sun S. Controlled synthesis and chemical conversions of FeO nanoparticles. Angewandte Chemie International Edition. 2007;46(33):6329-32.

[3] Gonzalez Z, Botas C, Alvarez P, Roldan S, Blanco C, Santamaria R, et al. Thermally reduced graphite oxide as positive electrode in vanadium redox flow batteries. Carbon. 2012;50(3):828-34.

[4] Ferrari AC, Basko DM. Raman spectroscopy as a versatile tool for studying the properties of graphene. Nat Nano. 2013;8(4):235-46.

[5] Wang G, Shen X, Yao J, Park J. Graphene nanosheets for enhanced lithium storage in lithium ion batteries. Carbon. 2009;47(8):2049-53.

[6] Jette ER, Foote F. An X-Ray Study of the wustite (FeO) solid solutions. The Journal of Chemical Physics. 1933;1(1):29-36.

[7] Jozwiak WK, Kaczmarek E, Maniecki TP, Ignaczak W, Maniukiewicz W. Reduction behavior of iron oxides in hydrogen and carbon monoxide atmospheres. Applied Catalysis A. 2007;326(1):17-27.

[8] Acik M, Lee G, Mattevi C, Pirkle A, Wallace RM, Chhowalla M, et al. The role of oxygen during thermal reduction of graphene oxide studied by infrared absorption spectroscopy. The Journal of Physical Chemistry C. 2011;115(40):19761-81.

[9] Muge Acik, Chabal. YJ. A review on thermal exfoliation of graphene oxide. Journal of Materials Science Research. 2013;2(1):12.

[10] Wang H, Hu P, Pan Da, Tian J, Zhang S, Volinsky AA. Carbothermal reduction method for Fe_3O_4 powder synthesis. Journal of Alloys and Compounds. 2010;502(2):338-40.

[11] Thackeray MM, David WIF, Goodenough JB. Structural characterization of the lithiated iron oxides $Li_xFe_3O_4$ and $LixFe_2O_3$ ($0<x<2$). Materials Research Bulletin. 1982;17(6):785-93.

[12] Laruelle S, Grugeon S, Poizot P, Dollé M, Dupont L, Tarascon J-M. On the origin of the extra electrochemical capacity displayed by MO/Li cells at low potential. Journal of the Electrochemical Society. 2002;149(5):A627-A34.

[13] Poizot P, Laruelle S, Grugeon S, Dupont L, Tarascon JM. Nano-sized transition-metal oxides as negative-electrode materials for lithium-ion batteries. Nature. 2000;407(6803):496-9.

[14] Reddy MV, Yu T, Sow CH, Shen ZX, Lim CT, Subba Rao GV, et al. α-Fe_2O_3 nanoflakes as an anode material for Li-ion batteries. Advanced Functional Materials. 2007;17(15):2792-9.

[15] Aurbach D. Review of selected electrode-solution interactions which determine the performance of Li and Li ion batteries. Journal of Power Sources. 2000;89(2):206-18.

[16] Reddy MV, Subba Rao GV, Chowdari BVR. Metal oxides and oxysalts as anode materials for Li ion batteries. Chemical Reviews. 2013;113(7):5364-457.

[17] Xiao Z, Xia Y, Ren Z, Liu Z, Xu G, Chao C, et al. Facile synthesis of single-crystalline mesoporous α-Fe_2O_3 and Fe_3O_4 nanorods as anode materials for lithium-ion batteries. Journal of Materials Chemistry. 2012;22(38):20566-73.

[18] Reddy MV, Wei Wen BL, Loh KP, Chowdari BVR. Energy storage studies on $InVO_4$ as high performance anode material for Li-ion batteries. ACS Applied Materials & Interfaces. 2013;5(16):7777-85.

[19] Guo P, Song H, Chen X. Electrochemical performance of graphene nanosheets as anode material for lithium-ion batteries. Electrochemistry Communications. 2009;11(6):1320-4.

[20] Casero E, Parra-Alfambra AM, Petit-DomÃnguez MD, Pariente F, Lorenzo E, Alonso C. Differentiation between graphene oxide and reduced graphene by electrochemical impedance spectroscopy (EIS). Electrochemistry Communications. 2012;20(0):63-6.

[21] Wang G, Liu T, Luo Y, Zhao Y, Ren Z, Bai J, et al. Preparation of Fe_2O_3/graphene composite and its electrochemical performance as an anode material for lithium ion batteries. Journal of Alloys and Compounds. 2011;509(24):L216-L20.

Chapter 6 EG/MnO Composites

Exfoliated graphene oxide (EG)/Manganese (II) Oxide (MnO) composite powder is synthesized by simple solid state graphenothermal reduction process. Structural, chemical and morphological studies confirm the formation of EG/MnO composite in which cubic MnO crystallites are found to anchor onto EG surfaces. As-synthesized EG/MnO composite is constituted with 65 and 35 wt.% of MnO and EG, respectively. The EG/MnO composite exhibits a specific surface area of ~82 m^2 g^{-1} and an average pore size of ~12 nm. As an anode in lithium-ion batteries, EG/MnO composite shows a high reversible capacity of 936 mAh g^{-1} at a current rate of 75 mA g^{-1}. Capacity retention of ~84% (784 mAh g^{-1}) is observed even at the 100^{th} cycle which corresponds to a Coulomb efficiency of ~99%. Cyclic voltammetry studies on the composite show that Li storage is owing to reversible conversion reactions of MnO and electrochemical absorption/desorption by EG. Electrochemical impedance spectroscopy studies clearly show easy lithiation kinetics. Owing to the electrochemical performance of EG/MnO composite and owing to its easy, reproducible and scalable synthesis procedure, it is an excellent addition to the similar class of materials.

Different morphological features present in the as-synthesized EG/MnO composite are shown in Fig. 6.1. In Fig. 6.1(a) puffy EG (i.e. exfoliated GO here viewed along its thickness (c-axis)) is seen along with a lump of MnO particles on its edges. Figs. 6.1(b) and (c) show submicron sized lumps of MnO particles attached to the graphene sheets of EG. At several locations in Figs. 6.1(b) and (c) it can be seen that individual MnO particles are anchored onto cavities and troughs of EG. High magnification FESEM image (Fig. 6.1(d)) of a representative MnO lump clearly shows that it constitutes of a continuous network of MnO particles. The morphology and crystallinity (Fig. 6.2) of EG/MnO composite was further examined using TEM. Fig. 6.2(a-d) clearly shows that each MnO nanoparticle or lump is supported and partially covered by semitransparent few-layered graphene. Further investigation of MnO network is shown in Figs. 6.2(d) and (e). In these images it is clearly visible that individual MnO nanoparticles are connected with each other across edges (and

along their lengths). Selected area electron diffraction (SAED) pattern obtained at a shared edge of a MnO nanoparticle as depicted in Fig. 6.2(d) corresponds to FCC (100) facet and an underlying pattern belongs to FCC (310) facet. This observation indicates that each MnO nanoparticle could be a single crystal. The diffused diffraction rings correspond to EG.

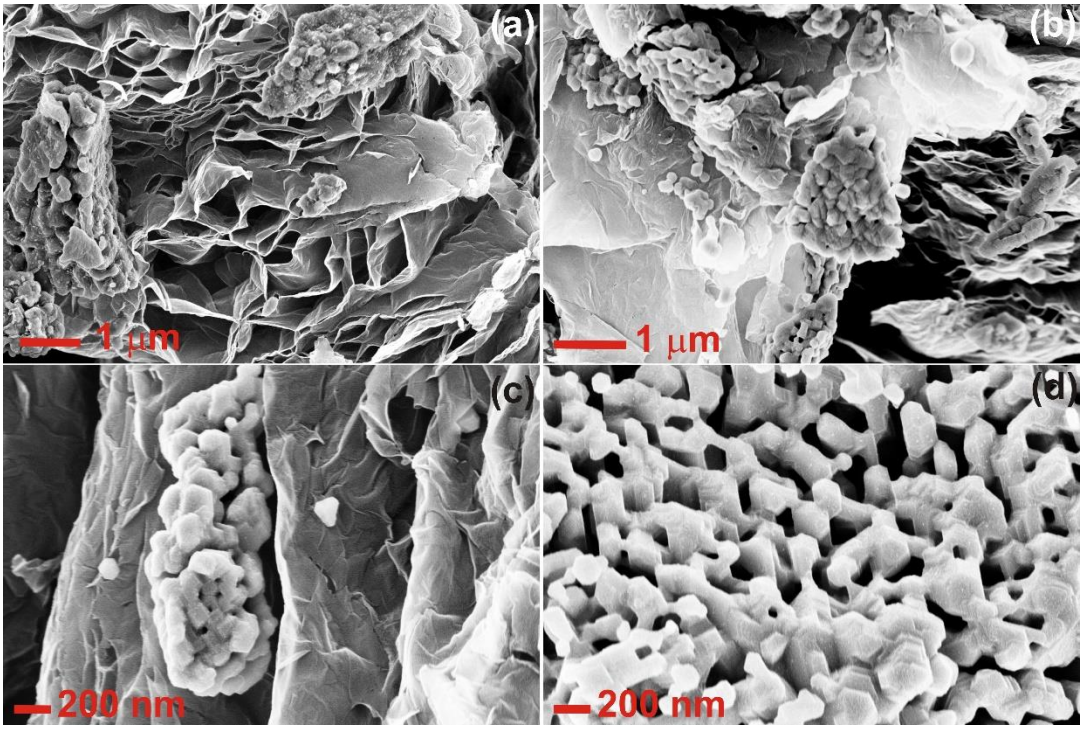

Figure 6.1. FESEM images of (a,b,c) EG/MnO composite at different locations and (d) MnO nano-network.

XRD pattern of EG/MnO composite powder in comparison to MnO_2 and GO powders is shown in Fig. 6.3(a). The diffraction peaks are indexed to cubic MnO (space group Fm-3m, JCPDS #75-257). The results are in close agreement with SAED analysis. This observation clearly indicates the transformation of tetragonal MnO_2 (space group P42/mnm, JCPDS #24-735) with lattice parameter values of a = 4.398 (6) Å; c =2.872 (5) (Å) to cubic MnO. Rietveld refinement of the XRD pattern of EG/MnO composite yields a lattice parameter of a = 4.444 (2) Å. The broadening of diffraction peaks is due to the smaller average crystallite size (average ~31 nm) of MnO in the sample. Here it is worth noting that the average crystallite size of MnO_2 is ~128 nm. Further randomly shaped MnO_2 particles ranging from

several hundred nanometers to few microns in size (Fig. 6.4) are transformed to networks of MnO. This observation indicates that GTR reaction not only results in phase (from MnO_2 to MnO) and morphology change but also in formation of small MnO crystallites. The low intensity broad hump at 15° (Fig. 6.3(a)) is attributed to the presence of EG.

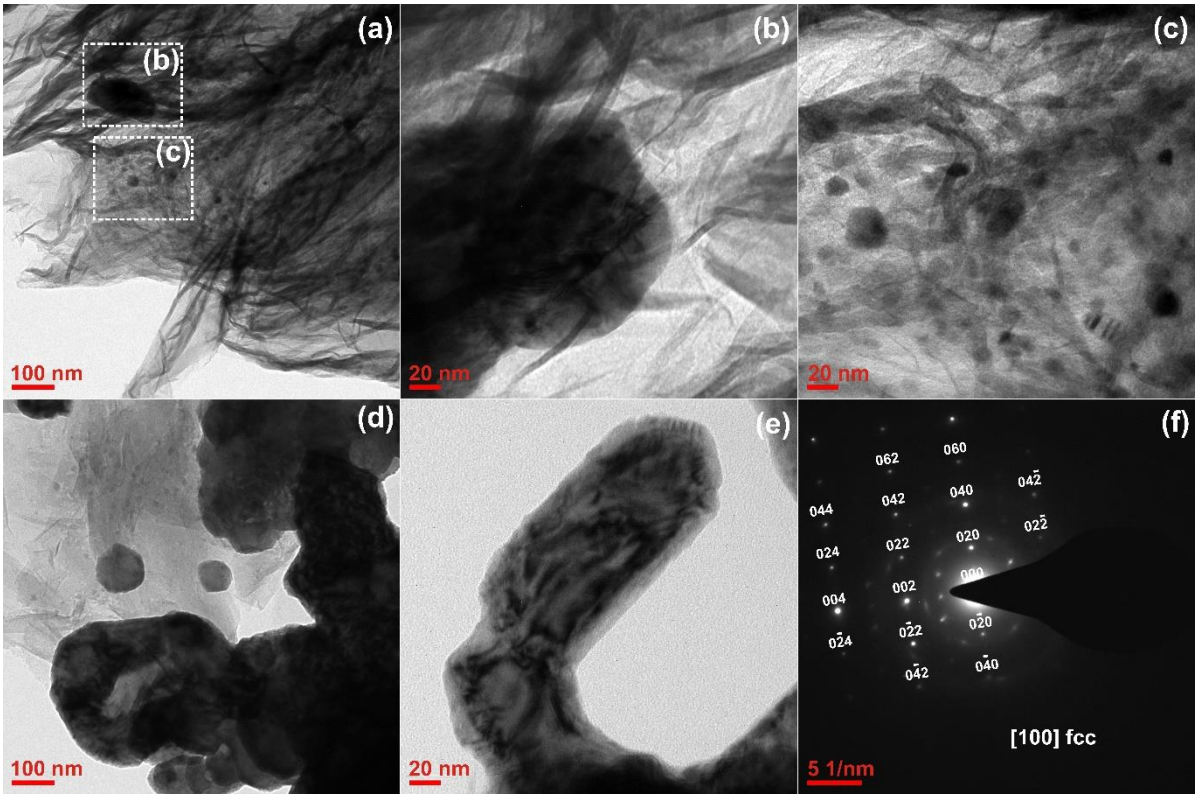

Figure 6.2. TEM images of EG/MnO composite: (a−c) MnO nanoparticles adhered to graphene sheets of EG, (d and e) edge shared MnO nanoparticles, and (f) SAED pattern obtained from the edge shared MnO nanoparticle.

XRD results indicate that the as-synthesized composite contains only crystalline MnO phase even though the morphology of individual MnO particles observed in electron micrographs is not the same. Raman spectra obtained from graphite, GO and EG/MnO composite samples are shown in Fig. 6.3(b). The spectrum of GO depicts only D and G bands centered at 1361 and 1600 cm^{-1}, respectively. After thermal exfoliation (GO→EG), D and G bands emerged very strongly (nearly sevenfold increase in intensity). The positions of D and G bands in EG are slightly shifted towards lower wave numbers i.e., to 1339 and 1597 cm^{-1}, respectively.

The small peak centered at 649 cm^{-1} corresponds to Mn-O vibration mode [1-3]. The intensity ratio I_D/I_G in the cases of GO, EG/MnO and graphite are found to be ~0.74, ~0.88 and ~0.1, respectively. The high I_D/I_G values in the cases of GO and EG indicate high extent of exfoliation or disorder imposed into graphite as a consequence of chemical oxidation followed by thermal annealing.

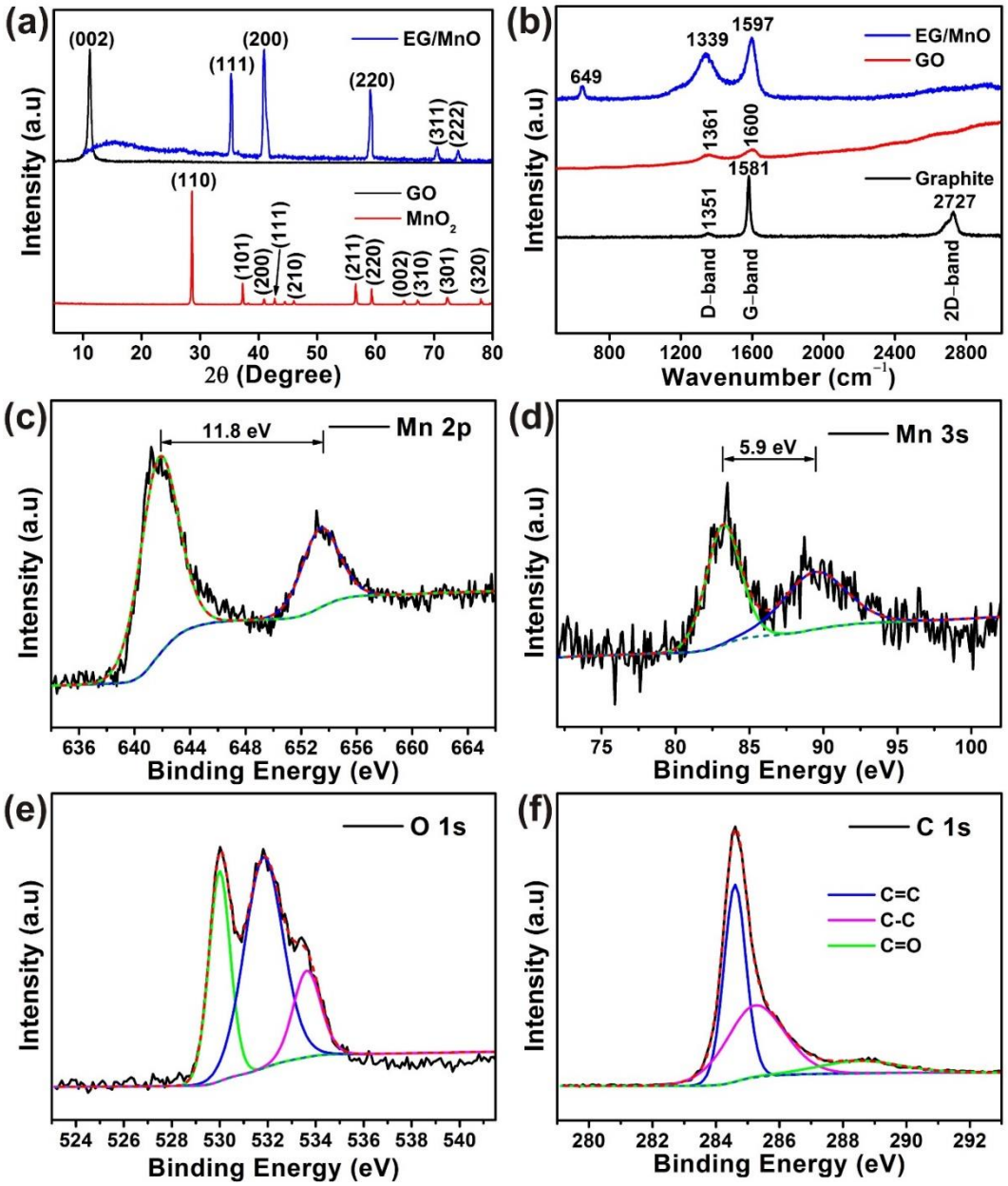

Figure 6.3. (a) XRD patterns of MnO_2, GO, and EG/MnO; (b) Raman spectra of graphite, GO and EG/MnO composites; XPS spectra of (c) Mn2p, (d) Mn3s, (e) O1s and (f) C1s.

The oxidation state of Mn was further confirmed by using XPS. The core level spectra for Mn 2p, 3s and O 1s are shown in Figs. 6.3(c), (d) and (e), respectively. The Mn $2p_{3/2}$ shows a binding energy (BE) close to 641.71 (±0.2) eV which is well-matched with BE of MnO/C [1, 4,5]. The satellite peak at 653.51 eV (Fig. 6.3(c)) is due to multiple splitting of the energy levels of Mn-ion. The calculated split width of Mn 2p orbital is ~11.8 eV which is in good agreement with the reported values [6]. In addition, Mn 3s (Fig. 6.3(d)) peak is deconvoluted into two distinct peaks centred at ~83.41 and ~89.31 eV corresponding to the splitting width of 5.9 eV which is consistent with previous reports [6,7]. XPS studies clearly show that Mn is in the +2 oxidation state. The O 1s spectrum showed peaks at 530.20, 531.6 and 533.8 eV (Fig. 6.3(e)). The main peak with a BE of 531.6 eV is related to the oxygen that is predominantly bonded to Mn-ions in the lattice while 530.19 and 533.83 eV are related the surface oxygen [5,8]. Further C 1s spectrum shown in Fig. 6.3(f) depicts peaks at 284.61, 285.31 and 288.61 eV that represent C=C, C-C and C=O bonds, respectively in EG [5,8,9]. This suggests that most of the functional groups in GO were removed during its thermal reduction (exfoliation) to form EG. But EG is not completely free from functional groups such as C=O and this observation justifies its nomenclature of exfoliated graphene oxide.

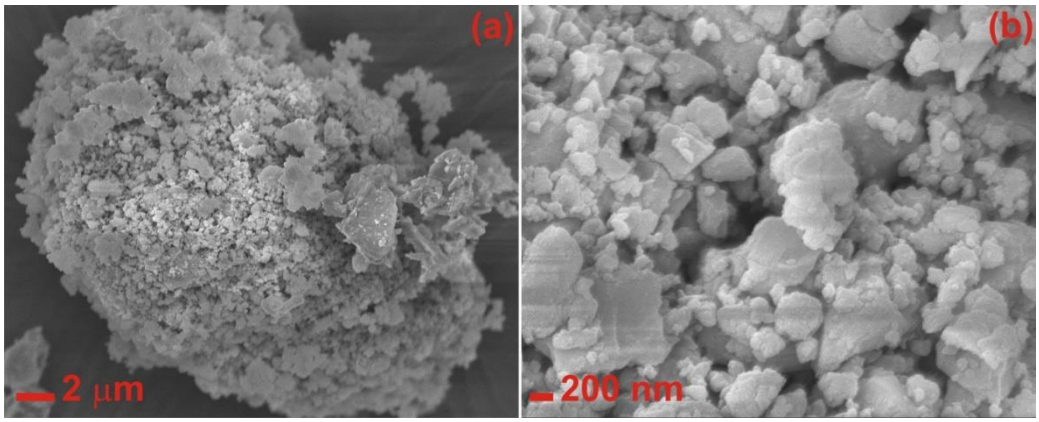

Figure 6.4. Electron micrographs (SEM) of MnO_2 bulk powder.

Specific surface area of EG/MnO composite was measured as ~81.7 (±0.5) m^2 g^{-1}. N_2 adsorption and desorption isotherms are shown in Fig. 6.5(a). The adsorption isotherm indicates characteristics of BET type III isotherm but the desorption isotherm resembles an intermediate between type III and type IV isotherm. This kind of mixed behavior and the observed hysteresis indicate a high degree of porosity in the composite. The measured average pore volume of ~0.24 cm^3 g^{-1} and average pore size of ~12 nm confirm that the composite powder is highly porous in tune with the morphological analysis.

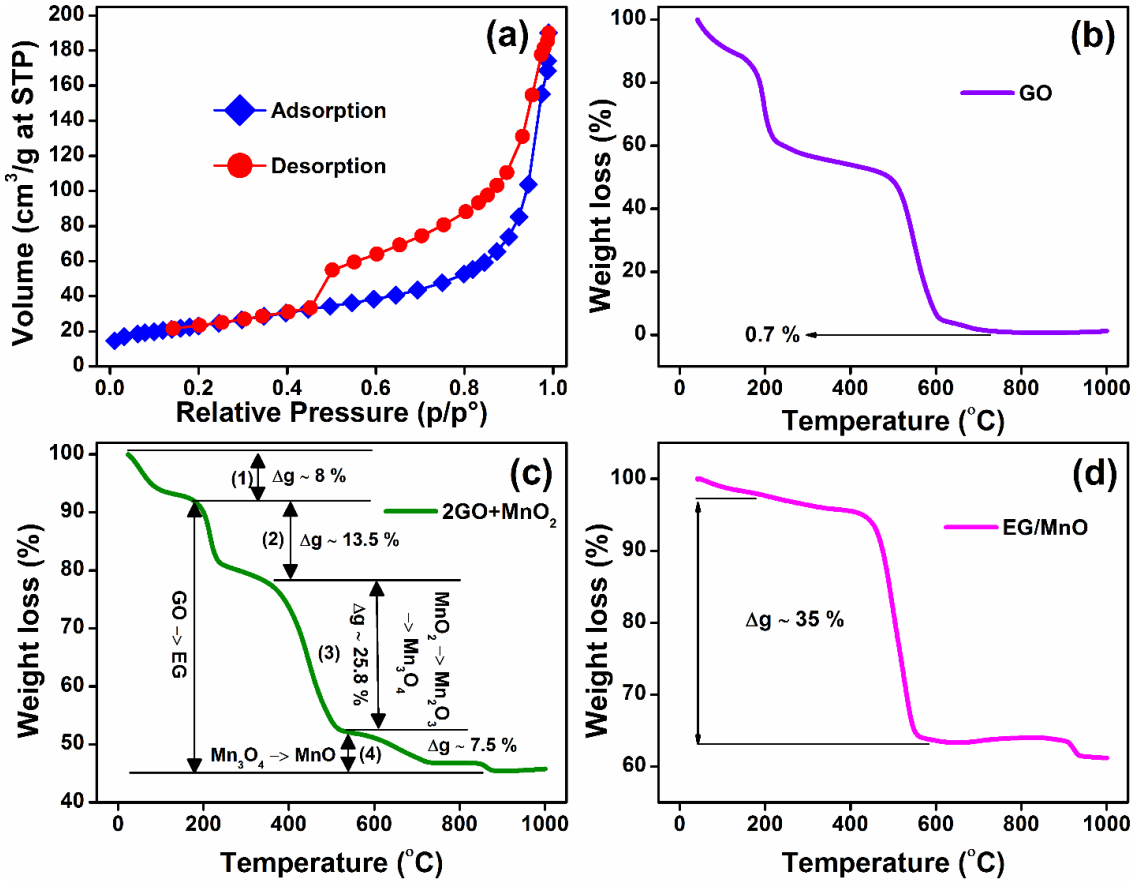

Figure 6.5. (a) N_2 adsorption and desorption isotherms of EG/MnO, (b) TGA of GO in N_2, and TGA of reaction mixture 2GO + MnO_2 in N_2 (c) and (d) TGA of EG/MnO in air.

TGA of GO and the reaction mixture (GO+MnO_2) was performed in order to understand the reduction process. The results are shown in Figs. 6.5(a-c). As shown in Fig. 6.5(c), the initial weight loss of ~8 % (up to 200 °C) is attributed to the removal of water molecules from GO whilst the subsequent weight loss of ~13.5% (up to 400 °C) corresponds to the pyrolysis of

GO's functional groups which contain oxygen to form steam, CO or CO_2 *etc.* [10]. The initial two weight losses are definitely linked to GO for the reason that MnO_2 is a proven stable phase up to 400 °C [11-14]. The weight loss characteristics (Fig. 6.5(c)) of the reaction mixture up to 400 °C is quite similar to that of GO shown in Fig. 6.5(b). The major weight loss of ~33% of the reaction mixture is observed in the range 400–900 °C which mainly corresponds to conversion of MnO_2 to MnO as well as simultaneous exfoliation of GO to EG according to reaction path '$2GO+MnO_2 \rightarrow {}^{I}EG/Mn_2O_3 \rightarrow {}^{II}EG/Mn_3O_4 \rightarrow {}^{III}EG/MnO$'. In detail, first MnO_2 undergoes structural changes starting from ~400 °C and subsequently it changes to Mn_2O_3 very rapidly at ~450 °C and therefore the corresponding rapid weight loss of ~33% in the range 400–500 °C as shown in Fig. 6.5(c) is observed [11-14]. Mn_2O_3 further changes to Mn_3O_4 starting from 570 °C till 920 °C [11-14]. The weight loss up to 880 °C seems to be not only corresponding to formation of Mn_3O_4 but also its in-situ reduction to MnO either by carbons of EG or CO released from it. This is owing to the fact that either self-decomposition of Mn_3O_4 to MnO or the reduction of MnO to Mn is highly impossible as it happens in the range 1300–1700 °C [12,15]. Even in the presence of reducing species like C, CO_2, CH_4 and H_2 further reduction of Mn_3O_4 to MnO will takes place well above 900 °C [13,14,16]. However, here the absence of any weight loss after 880 °C indicates that the reduction of Mn_3O_4 to MnO was completed before reaching 900 °C. Further reduction of MnO to Mn is highly impossible as it happens around 1500 °C [17] in the presence of either C or CO. Moreover, negligible weight loss observed in the temperature range 880–1000 °C confirms that the reduction of MnO to Mn is not possible. From the TGA it is clear that the exfoliating GO or EG will bring down the reduction temperature of $MnO_2/Mn_2O_3/Mn_3O_4$ to obtain MnO at temperatures lower than those required in conventional methods. Here it should be noted that TGA of the samples correlates well with the other observed structural characteristics of the same samples. However, more robust theoretical and experimental studies are required to

explore the exact reduction mechanism. The inferences from TGA prompted the choice of 650 °C as the reaction temperature and 8 h heating time to synthesize EG/MnO composites. It is also possible to obtain MnO at 750 °C. In this case it requires only 5 h of heating (Fig. 6.6). It was found through experimentation that a minimum of two moles of GO is required to reduce one mole of MnO_2 completely to MnO. The reduction of a mole of MnO_2 by heating with one mole of GO for 5 h resulted in a composite constituted by MnO_x (Mn_3O_4 and MnO, Fig. 6.7). Weight percentages of individual components of EG/MnO are obtained by carrying out TGA in air at a heating rate of 10 °C min^{-1} as shown in Fig. 6.5(d). In this analysis, MnO and EG are found to be 65 and 35 wt.%, respectively. With these weight percentages one can expect a theoretical capacity of ~614 mAh g^{-1} by considering the formation of LiC_6 and Mn plus Li_2O (from MnO conversion). The synthesis experiment at 750 ℃ for 5h could yield pure MnO phase in the composite. However, the composite's morphology (Fig. 6.8) showed that MnO particles aggregated more whilst its capacity (Fig. 6.9) was less than the one synthesized at 650 °C for 8h. The composite synthesized at 650 ℃ for 8h was found to be the optimal composite.

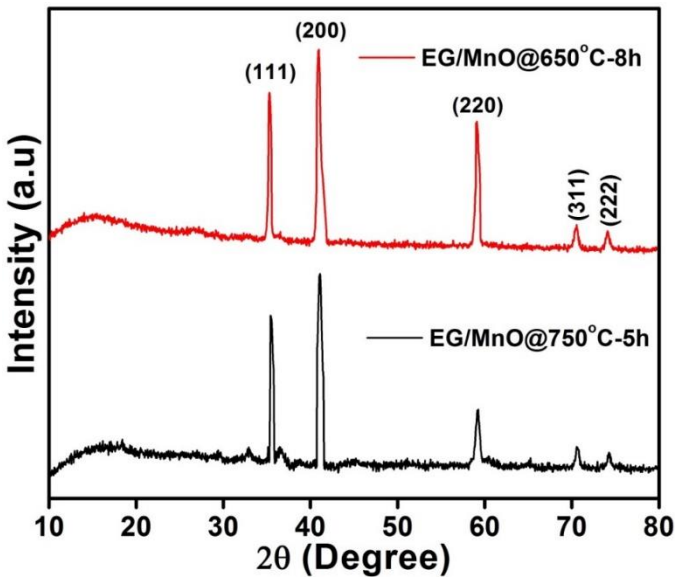

Figure 6.6. XRD patterns of EG/MnO@650 °C-8h and EG/MnO@750 °C-5h.

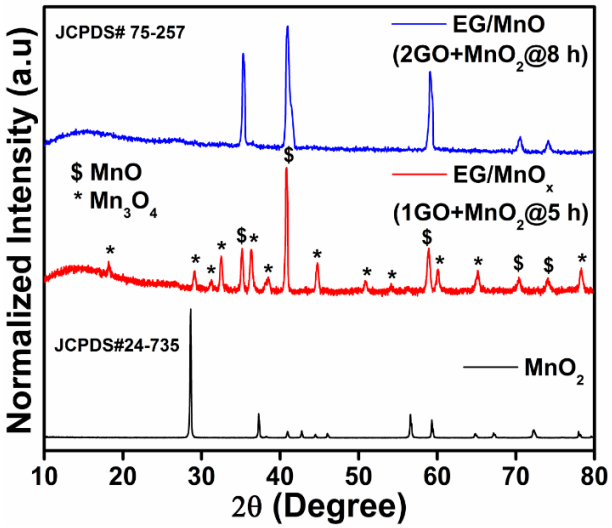

Figure 6.7. XRD patterns of 1GO+MnO_2 and 2GO+MnO_2 reaction mixtures heated for 5 and 8 h, respectively, in comparison to the XRD pattern of MnO_2.

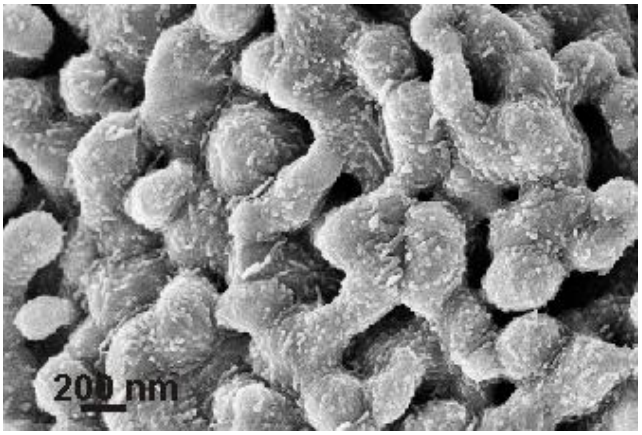

Figure 6.8. FESEM image of MnO aggregates in EG/MnO@750 °C-5h.

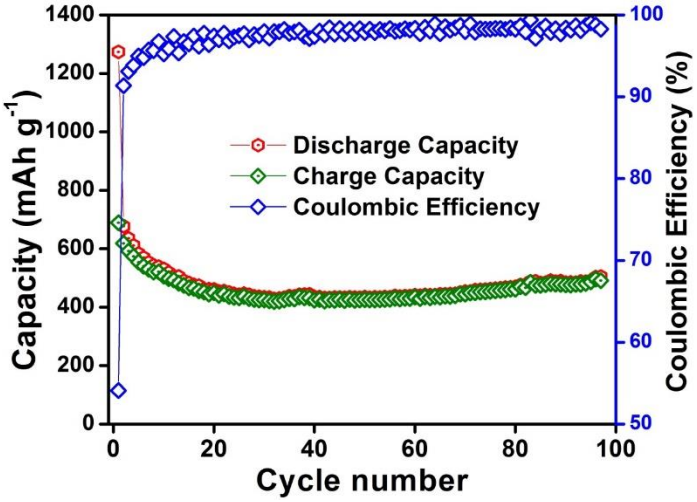

Figure 6.9. Cycling performance of EG/MnO @750 °C-5h at 75 mA g^{-1}.

Electrochemical affluence of EG/MnO composite for lithiation was scrutinized using CV and the corresponding curves are shown in Fig. 6.10(a). An increase in reduction current is observed in the voltage ranges 0.7-1.0 V and 0.005-0.25 V during the first cathodic scan. The first small increase corresponds to typical decomposition of electrolyte species, which is also observed in galvanostatic discharge. The stable current between 0.7 to 0.25 V might be due to crystal destruction of MnO as a consequence of electrochemical reaction between MnO and Li i.e., the formation of Li_2O and metallic Mn along with electrolyte decomposition [1,4,18,19]. The second large increase in current is the resultant of co-intercalation of solvated Li into EG. The evolution of the single large peak around 0.4 V that corresponds to the conversion reaction $2Li + MnO \rightarrow Li_2O + Mn$ [1,4,18-20] is observed from second reduction scan onwards as shown in Fig. 6.10(c). The large difference between first and second reduction curves is a consequence of irreversible chemical side-reactions that generate irreversible chemical compounds of Li and leads to the formation of solid electrolyte interface (SEI) [1,4,18,19]. There is only one oxidation peak centered on 1.25 V during all anodic scans. This peak represents the current due to de-lithiation reaction $Li_2O + Mn \rightarrow 2Li + MnO$ [1,4,18,19]. The redox current was observed throughout the voltage range 0.005-3.0 V, except in the case of conversion peaks during all redox scans plausibly resulted from electrochemical absorption and desorption of Li onto EG. It is important to note that the extent of hysteresis between redox curves observed especially in the voltage range 1.5–3.0 V is a clear evidence of EG's participation in lithiation and de-lithiation processes. Moreover this kind of hysteresis is negligible for bare MnO and even for various composites containing less graphene as referred in this paper. Thus over all CV characteristics of EG/MnO are consistent with galvanostatic cycling features and demonstrating the (de) lithiation by both MnO and EG phases.

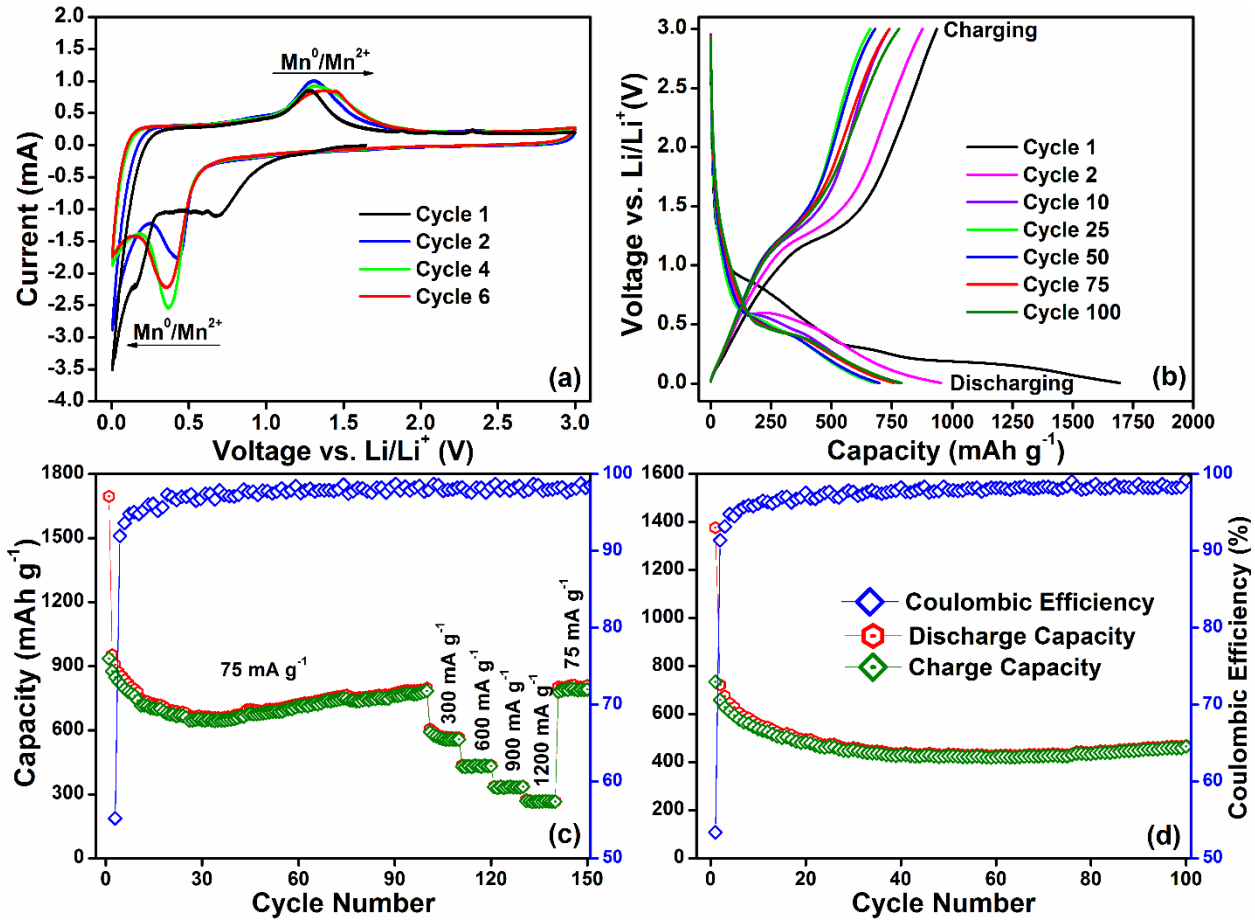

Figure 6.10. (a) CV curves at scan rate ~58 μV s^{-1} and (b, c) galvanostatic cycling results at 75 mA g^{-1} followed by rate capability and (d) cyclic performance at 600 mA g^{-1} of EG/MnO.

The performance of EG/MnO for lithiation is tested with galvanostatic cycling after confirming its readiness/ease for Li from CV study. The potential versus discharge and charge capacity characteristics at current density 75 mA g^{-1} are shown in Fig. 6.10(b). During the first discharge, major changes in slope of capacity curve are observed at 0.9 and 0.4 V which correspond to the starting of decomposition of electrolyte molecules and conversion reaction between Li and MnO [2,5,6,21,22]. Further, a minor change in curve was observed at 0.25 V which is related to intercalation of solvated Li in to EG and these features are consistent with first cathodic curve of CV test. The subsequent discharge capacity curves appeared similar with variation in capacity value and small sloping plateau around 0.5 V which represents lithiation by MnO/Mn (discharge potential) [2,5,6,21,22]. The first and

subsequent charging capacity curves are also found to be similar except for the capacity values and charging potential of Mn/MnO formation due to de-lithiation which is observed at 1.25 V in tune with CV anodic scans. The inclined nature of the charge capacity curves above 1.5 V (if graphene doesn't participate in the lithiation process, these curves should be almost vertical) and the discharge curves below 0.3 V resembled that of pristine graphene [23]. Thus galvanostatic cycling confirms both that EG and MnO are actively contributing in lithiation and de-lithiation processes. A capacity of 1696 mAh g^{-1} is observed for complete discharging to 0.005 V during first discharge. Out of this discharge capacity only ~55% that equals to 936 mAh g^{-1} is reversed during first charge to 3.0 V. The net capacity loss of ~45% at the end of first cycle is known as irreversible capacity loss that can be ascribed to loss of Li as covalent constituent of SEI [2,5,6,21,22]. Further decay in both charge and discharge capacity continued up to 25th cycle from where the recovery started and continued till the end of the test as shown in Fig. 6.10(b). This kind of behavior (which is known as electrode formation effect in which electrode material undergoes spatial changes and adjusts itself to achieve good contacts with current collector, proper percolation of electrolyte etc.,) is commonly observed in various graphene and carbon composites with MnO [2,4,5,21]. Such increase in capacity is attributed to reconstruction of the MnO/GNS through in-situ formation of ultrafine nanoparticles of manganese oxide [5]. The observed extra capacity might also be a consequence of electrolyte polymerization which is often accompanied by increase in capacity [21]. Another reason for increase in capacity could be due to the in-situ electro-chemical exfoliation of EG, which then accepts more Li [3,24]. An increase in Coulombic efficiency to 92% at 2nd cycle and >97% at 12th cycle which soon fluctuated in between 98 and 99% and the rate capability shown in Fig. 6.10(c) signifies EG/MnO as a commercial grade anode material. Finally capacity retention of ~84% (784 mAh g^{-1}) is observed even at 100th charge which corresponds to a Coulomb efficiency of ~99%.

Table 6.1. Comparison of performance of EG/MnO with other graphene/MnO composites.

Ref.	Synthesis method	Graphene Content (wt.%)	Reversible capacity (mAh g^{-1})		Current Rate (mA/g)
			1st cycle	After aging	
EG/MnO [This work]	GTR @650°C	35	936	784 (100th cycle)	75
Ref[25]	MnO_2/GO prepared by modified Hummers method and annealed at 400 °C in N_2 flow for 2h	35.6	730*	860 (50th cycle)	50
Ref[26]	MnO_2 nanorods (hydrothermally prepared)/GO calcined at 600 °C for 2h in Ar flow	7.58	747	705 (100th cycle)	50
Ref[21]	Mn_3O_4/rGO prepared hydrothermal method at 200 °C for 24 h and heated at 800 °C for 5 h under NH_3 atmosphere	8.9	829	772 (90th cycle)	50
Ref[6]	Mn–GO cakes prepared by GO + $Mn(NO_3)_2$ suspension and heated at 400 °C for 2 h in 5 vol.% H_2 atmosphere	--	635	--	75
Ref[2]	GO and rGO/$Mn(Ac)_2$ heated separately at 800 °C for 2h under 5wt% H_2/N_2 atmosphere	6	952	950* (5th cycle)	100
Ref[22]	rGO prepared at 900 °C for 3h in Ar whilst rGO/ $Mn(NO_3)_2$ heat treated at 700 °C for 5h in Ar flow	75	700	782 (60th cycle)	100
Ref[27]	rGO/$Mn(Ac)_2$ reduced in NH_4OH+ N_2H_4 solution to prepare rGO/MnO_x which heated at 400 °C for 12h in 5% H_2/Ar flow	42	838	719* (10th cycle)	50
Ref[9]	Mn_3O_4/rGO prepared hydrothermal method at 200 °C for 24 h heated at 400 °C for 2 h in N_2/H_2 flow	12	867	825* (30th cycle)	50
Ref[28]	Precursor obtained from solution of GO+$MnSO_4$+ NH_4HCO_3 heat treated at 600 °C for 1h in N_2 flow	72.5	648	665 (50th cycle)	100

**values are approximated from images unless specifically claimed by authors, -- not available.*

As shown in Fig. 6.10(d), EG/MnO shows good cyclability even at current density of 600 mA g^{-1} that is equivalent to theoretical capacity (with the respective amounts in the composite as anticipated from TGA weight percentages). Thus the reversible capacities exhibited by EG/MnO are superior in comparison to that of MnO, MnO/C and Graphene/MnO (Table 6.1) composites. The overall electrochemical performance of EG/MnO is similar to the different MnO/C and Graphene/MnO composites cited in this study. However, the composites in the present study are synthesized using an easy and scalable synthesis process. Therefore EG/MnO composite is an excellent addition to the similar class of materials.

Nyquist plots pertaining to fresh cell, cells after first discharge and first charge, and their equivalent electrical circuits are shown in Fig. 6.11. The impedance spectra contained only one semicircle whose diameter corresponds to the resistance to charge transfer (R_{ct}) and the quasi straight line with ~45° inclination represents resistance to Li-ion diffusion (Warburg component, W_s). The relatively small contact resistance element R_e around 5.5, 6.8 and 6.3 (±0.1) **Ω** is noticed for fresh cell (open circuit potential, OCP), cell discharged to 0.005 V and cell charged to 3.0 V, respectively. The respective R_{ct} values have shown a decreasing trend (88, 56 and 45 (±0.5) **Ω**, respectively) which signifies that the insertion and extraction of Li becomes easier upon ageing of the cathode material. The values of capacitance element CPE_{dl} that are equivalent to the formation of double layer charge are found to be 54, 80 and 68 (±3) μF for the three cases, respectively. The simulated R_e, R_{ct} and CPE_{dl} values are tabulated in Table 6.2. The values of W_s are found to be relatively very high when compared to R_e and R_{ct} values in all states of coin cells. The capacity element C_i (capacitance due to Li intercalation) (Table 1) was found to be < 1 F at OCV and 3.0 V which is the evidence for absence of solid state diffusion of Li into the anode matrix in tune with CV observations. The observed increase in C_i value to 2.283 F at 0.005V is an indication for intercalation of Li into MnO matrix. The higher values of R_{ct} for OCP and discharge than charging indicates easy removal

of Li rather than insertion which is also visualized as high reversible capacities observed in galvanostatic cycling.

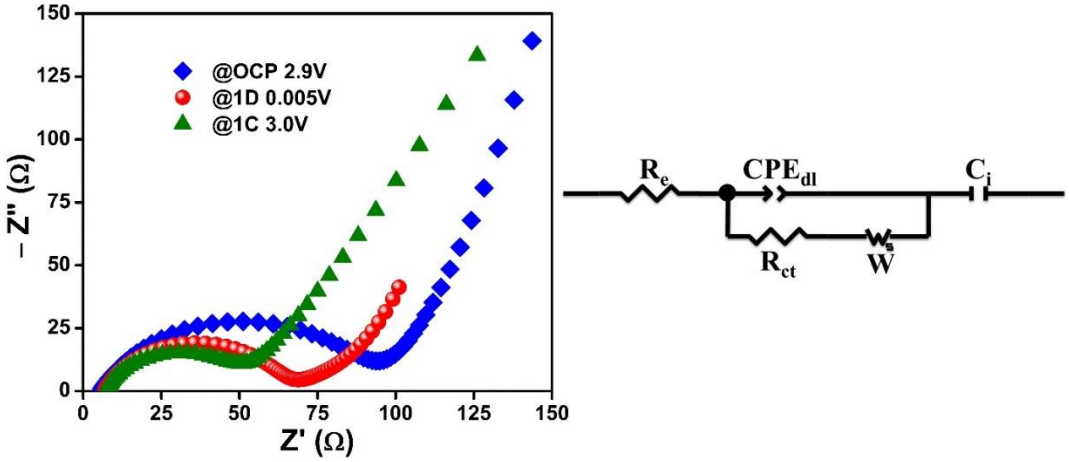

Figure 6.11. Nyquist plots of EG/MnO at OCP, first discharge, first charge after fitting, and corresponding equivalent circuit.

Table 6.2. EIS simulated values of various equivalent electrical circuit components pertaining to EG/MnO composite.

Battery Status	R_e (±0.1, Ω)	R_{ct} (±0.5, Ω)	CPE_{dl} (±3, μF)	C_i (±0.05, F)
OCP	5.5	88	54	0.021
Discharged to 0.005 V	6.8	56	80	2.283
Charged to 3.0 V	6.3	45	68	0.020

References

[1] Gao M, Zhou P, Wang P, Wang J, Liang C, Zhang J, et al. FeO/C anode materials of high capacity and cycle stability for lithium-ion batteries synthesized by carbothermal reduction. Journal of Alloys and Compounds. 2013;565:97-103.

[2] Zang J, Qian H, Wei Z, Cao Y, Zheng M, Dong Q. Reduced graphene oxide supported MnO nanoparticles with excellent lithium storage performance. Electrochimica Acta. 2014;118:112-7.

[3] Liao Q, Li N, Cui H, Wang C. Vertically-aligned graphene@MnO nanosheets as binder-free high-performance electrochemical pseudocapacitor electrodes. Journal of Materials Chemistry A. 2013;1:13715-20.

[4] Luo W, Hu X, Sun Y, Huang Y. Controlled synthesis of mesoporous MnO/C networks by microwave irradiation and their enhanced lithium-storage properties. ACS Applied Materials & Interfaces. 2013;5:1997-2003.

[5] Sun Y, Hu X, Luo W, Xia F, Huang Y. Reconstruction of conformal nanoscale MnO on graphene as a high-capacity and long-life anode material for lithium ion batteries. Advanced Functional Materials. 2013;23:2436-44.

[6] Hsieh C-T, Lin C-Y, Lin J-Y. High reversibility of Li intercalation and de-intercalation in MnO-attached graphene anodes for Li-ion batteries. Electrochimica Acta. 2011;56:8861-7.

[7] Dreyer DR, Park S, Bielawski CW, Ruoff RS. The chemistry of graphene oxide. Chemical Society Reviews. 2010;39:228-40.

[8] Hsu Y-K, Chen Y-C, Lin Y-G, Chen L-C, Chen K-H. Birnessite-type manganese oxides nanosheets with hole acceptor assisted photoelectrochemical activity in response to visible Light. Journal of Materials Chemistry. 2012;22:2733-9.

[9] Liu S-Y, Xie J, Zheng Y-X, Cao G-S, Zhu T-J, Zhao X-B. Nanocrystal manganese oxide (Mn_3O_4, MnO) anchored on graphite nanosheet with improved electrochemical Li-storage properties. Electrochimica Acta. 2012;66:271-8.

[10] Mu B, Zhang W, Shao S, Wang A. Glycol assisted synthesis of graphene-MnO_2-polyaniline ternary composites for high performance supercapacitor electrodes. Physical Chemistry Chemical Physics. 2014;16:7872-80.

[11] Agopsowicz A, Hitchcock JL, Tye FL. Thermal behaviour of partially reduced γ-MnO_2 in argon atmosphere. Thermochimica Acta. 1979;32:63-71.

[12] Dose WM, Donne SW. Manganese dioxide structural effects on its thermal decomposition. Materials Science and Engineering: B. 2011;176:1169-77.

[13] Stobbe ER, de Boer BA, Geus JW. The reduction and oxidation behaviour of manganese oxides. Catalysis Today. 1999;47:161-7.

[14] Kor GJW. The thermal decomposition of Mn_2O_3 and the reduction of Mn_3O_4 by C and CO. Metallurgical Transactions B. 1978;9:307-11.

[15] Alonso E, Hutter C, Romero M, Steinfeld A, Gonzalez-Aguilar J. Kinetics of Mn_2O_3–Mn_3O_4 and Mn_3O_4–MnO redox reactions performed under concentrated thermal radiative flux. Energy & Fuels. 2013;27:4884-90.

[16] Sorensen B, Gaal S, Tangstad M, Ringdalen E, Kononov R, Ostrovski O. Properties of manganese ores and their change in the process of calcination. Proceedings 12th Int Ferroalloy Congress, Helsinki, Finland; p. 5-7.

[17] Blagus A, Dankwah JR, Sahajwalla V. Interfacial reactions between Coke/HDPE blends and high carbon ferromanganese slag. ISIJ international. 2013;53:41-7.

[18] Reddy MV, Subba Rao GV, Chowdari BVR. Metal oxides and oxysalts as anode materials for Li ion catteries. Chemical Reviews. 2013;113:5364-457.

[19] Wang S, Xing Y, Xu H, Zhang S. MnO nanoparticles interdispersed in 3D porous carbon framework for high performance lithium-ion batteries. ACS Applied Materials & Interfaces. 2014;6:12713-8.

[20] Lee SM, Choi SH, Lee J-K, Kang YC. Electrochemical properties of graphene-MnO composite and hollow-structured MnO powders prepared by a simple one-pot spray pyrolysis process. Electrochimica Acta. 2014;132:441-7.

[21] Zhang K, Han P, Gu L, Zhang L, Liu Z, Kong Q, et al. Synthesis of nitrogen-doped MnO/graphene nanosheets hybrid material for lithium ion batteries. ACS Applied Materials & Interfaces. 2012;4:658-64.

[22] Qiu D, Ma L, Zheng M, Lin Z, Zhao B, Wen Z, et al. MnO nanoparticles anchored on graphene nanosheets via in-situ carbothermal reduction as high-performance anode materials for lithium-ion batteries. Materials Letters. 2012;84:9-12.

[23] Li N, Song H, Cui H, Wang C. Sn@graphene grown on vertically aligned graphene for high-capacity, high-rate, and long-life lithium storage. Nano Energy. 2014;3:102-12.

[24] Geim AK. Graphene: Status and prospects. Science. 2009;324:1530-4.

[25] Zhang S, Zhu L, Song H, Chen X, Zhou J. Enhanced electrochemical performance of MnO nanowire/graphene composite during cycling as the anode material for lithium-ion batteries. Nano Energy. 2014;10:172-80.

[26] Wu T, Tu F, Liu S, Zhuang S, Jin G, Pan C. MnO nanorods on graphene as an anode material for high capacity lithium ion batteries. J Mater Sci. 2014;49:1861-7.

[27] Cheekati SL, Yao Z, Huang H. The impacts of graphene nanosheets and manganese valency on lithium storage characteristics in graphene/manganese oxide hybrid anode. Journal of Nanomaterials. 2012;2012:10.

[28] Mai YJ, Zhang D, Qiao YQ, Gu CD, Wang XL, Tu JP. MnO/reduced graphene oxide sheet hybrid as an anode for Li-ion batteries with enhanced lithium storage performance. Journal of Power Sources. 2012;216:201-7.

Chapter 7 EG/MoO_2 Composites

'Exfoliated Graphene Oxide (EG)/MoO_2' composites are synthesized by GTR method. Graphene Oxide (GO) is used as a reducing agent to reduce MoO_3 and as a source for EG. The formation of different submicron sized morphologies such as spheres, rods, flowers, etc., of monoclinic MoO_2 on EG surfaces is confirmed by complementary characterization techniques. As-synthesized EG/MoO_2 composite with higher weight percentage of EG performed excellently as an anode material in LIBs. The galvanostatic cycling studies aided with post-cycling cyclic voltammetry and galvanostatic intermittent titrations followed by ex-situ structural studies clearly indicate that Li intercalation into MoO_2 is transformed into conversion upon aging at low current densities whilst intercalation mechanism is preferably taking place at higher current rates. The intercalation mechanism is found to be promising for steady state capacity throughout the cycling owing to excess graphene and higher current density even in the operating voltage window of 0.005–3.0 V in which MoO_2 undergoes conversion below 0.8 V.

FE-SEM micrographs depicting the morphology of as-prepared 4EG/MoO_2 composite powder are shown in Fig.7.1. From the micrographs it is obvious that the EG surfaces are decorated with MoO_2 nanoparticles which vary both in shape and size. Figs. 7.1 (a) and (b) show less populated sub-micron sized MoO_2 quasi-spherical particles which are randomly dispersed across the edges of the EG surfaces where exfoliation appears to be more pronounced when compared with other regions. This indicates that during the exfoliation of GO, freshly forming individual MoO_2 nanoparticles (along the edges of EG) are pushed away along with the exfoliating graphene layers and therefore eventually the chance of their agglomeration is reduced. But when there are a higher number of MoO_2 particles, they still tend to agglomerate forming rods and sheets which further form flower-like morphologies as shown in Figs. 7.1 (c) and (d). However, 2EG/MoO_2 composite powders (*Annexure 7*) depict a distinct microstructure. In this case too MoO_2 particles acquired similar shapes as in the case of 4EG/MoO_2 composite except for the flower-like morphology which is now replaced

by needle-like morphology. It is clearly observe that MoO_2 are densely populated, and evenly distributed. Micron sized rods might evolve as a result of prolonged agglomeration. This situation might have arisen due to the presence of high amount of MoO_3 and less amount of GO platelets during exfoliation and reduction process. This indicates that there is a shortage of EG content (in other words of GO during the reaction) in the case of 2EG/MoO_2. In view of this, two moles of excess GO was used while synthesizing 4EG/MoO_2 composite in order to ensure a smaller number of fine MoO_2 particles and also to keep them isolated from each other. The synthesized 4EG/MoO_2 contained more layers of EG as shown in Figs. 7.1 (a) and (b) in comparison to the layers in 2EG/MoO_2 as shown in *Annexure 7*. The increased amount of EG has produced more robust and interconnected features. In addition, flower-like features which comprised of sheets of MoO_2 as observed in Figs. 7.1 (c) and (d) suggest that the extent of agglomeration is scaled down in comparison to that in 2EG/MoO_2 composite. Nonetheless, at the first glance, the morphology of both 4EG/MoO_2 and 2EG/MoO_2 composites seems to be similar.

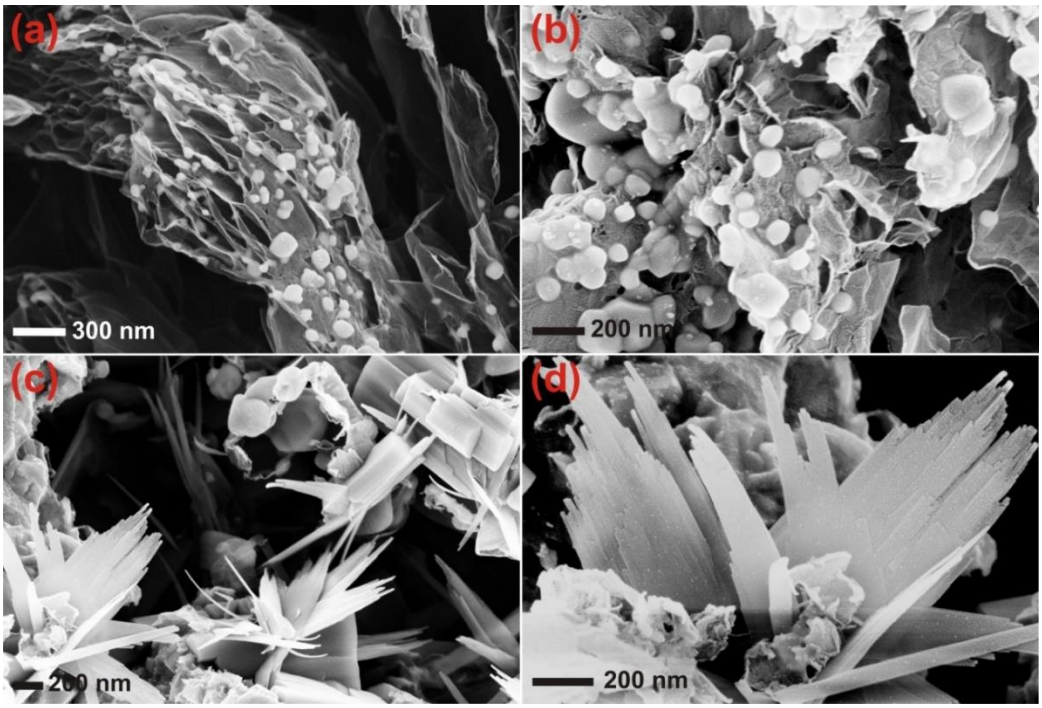

Figure 7.1. SEM images of 4EG/MoO_2 composite. (a) and (b) MoO_2 nanoparticles at edges of EG and (c) and (d) flower-like morphology of MoO_2 particles.

Figs. 7.2 (a) and (b) show randomly shaped MoO_2 nanoparticles adhered on either side of the transparent graphene sheets complementing Figs. 7.1 (a) and (b). Three types of morphologies of MoO_2 i.e. quasi-spherical, rods and sheets which contributed to flower-like morphology are probed for their structure using selected area electron diffraction (SAED) pattern as shown in insets of Figs. 7.2(a), (c) and (d). The SAED patterns depicted in the insets of Figs. 7.2 (a), (c) and (d) are ascribed to the planes perpendicular to the zone axes [-1-10], [01-1] and [001] of monoclinic crystal system, respectively.

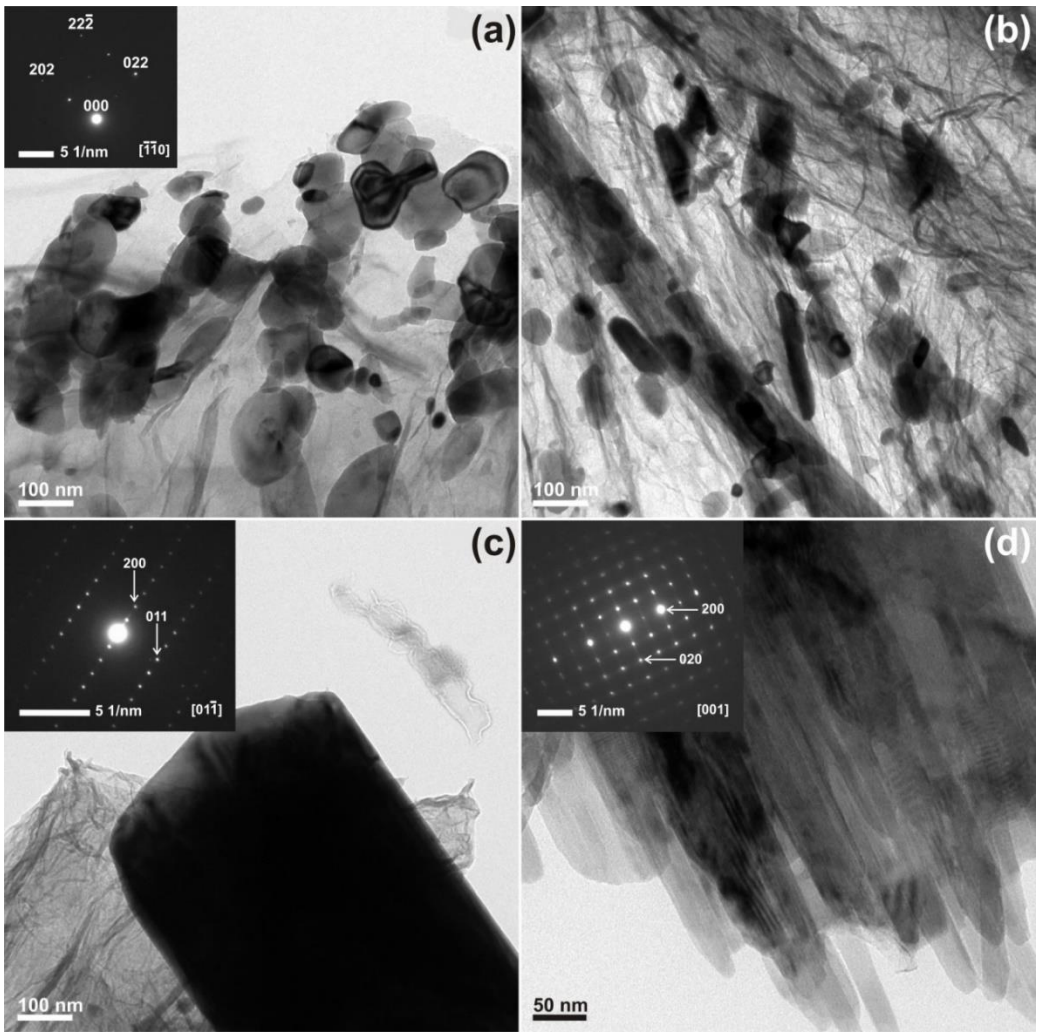

Figure 7.2. TEM images of 4EG/MoO_2: MoO_2 nanoparticles (a) adhering to edges and (b) sheets of EG, (c) MoO_2 nanorods partially wrapped by EG, and (d) magnified view of the flower-like morphology of MoO_2 particles. The SAED patterns depicted in insets of (a), (b) and (c) correspond to single MoO_2 nanoparticle, MoO_2 nanorod and flower-like MoO_2, respectively.

It is very interesting to have such different sized and shaped MoO_2 nanoparticles in single crystalline system. It is intriguing to evaluate electrochemical properties of such mixed morphology material systems similar to EG/FeO and EG/MnO composites. SAED patterns show that obtained individual MoO_2 particles are single crystalline and monoclinic in nature.

XRD pattern pertaining to the as-prepared 4EG/MoO_2 composite in comparison with MoO_3 (PDF#65-2421) is shown in Fig. 7.3(a). The pattern matches with monoclinic crystal structure (Space Group P21/c; PDF#78-1069) that mainly corresponds to MoO_2 phase in the composite while diffraction signals from EG phase are absent. The lattice parameters are found to be a (Å) = 5.6207, b (Å) = 4.8676, c (Å) = 5.6355 and β (°) = 120.88 from Rietveld refinement. There is negligible difference in lattice parameter values between the diffractograms of 2EG/MoO_2 and 4EG/MoO_2 (*Annexure 7*) but their average crystallite sizes are found to ~42 and ~33 nm, respectively (*Annexure 7*). The observed decrease in crystallite sizes clearly indicates that agglomeration of MoO_2 has been controlled with the increased amount of EG. This complies with the inferences from the electron micrographs. XRD results comply with SAED analysis. This indicates that MoO_2 particles are well crystallized. Further, XRD patterns of GO and GO' (graphene oxide with a greater degree of oxidation; the interplanar spacing is ~0.782 nm in comparison to ~0.655 nm in GO) in comparison to that of graphite flakes as shown in Fig. 7.3(b) revealed that both GO and GO' are well oxidized. The increase in interplanar distance is a direct consequence of more number of functional groups bonded to basal planes (more oxidation and hence higher degree of oxidation) [1,2]. GO' was considered to find out if degree of oxidation has any influence on the reduction MoO_3.

The extent of exfoliation of GO in forming EG and the type of molybdenum oxide present in the composite after reduction is studied using Raman spectroscopy. Raman spectrum of 4EG/MoO_2 composite depicted strong bands pertaining to EG and MoO_2 contents as shown in Fig. 7.3(c) in which Raman spectrum of GO is also included for comparison. Raman bands

observed at 993 and 818, 664, 332, and 281 cm^{-1} correspond to M=O stretching, O-M-O stretching, O-M-O bending and O-M-O wagging modes of vibrations in MoO_2 [3], respectively (*Annexure 7*). The other two Raman bands observed at 1344 and 1586 cm^{-1} are well known as D and G bands [3], respectively pertaining to EG in the composite. The intensity ratio I_D/I_G is found to be ~1.07 in the case of EG which is higher than that in the case of GO (I_D/I_G ~0.85) indicating that there is increased disorder in EG which further indicates that good exfoliation has taken place [3]. Similar Raman scattering response was observed from 2EG/MoO_2 and the only noted difference is the higher intensity of MoO_2 peaks along with less exfoliation of EG when compared with 4EG/MoO_2 (*Annexure 7*). EG/MoO_2 composites' Raman scattering results are consistent with other MoO_2-graphene nanocomposites [3-6].

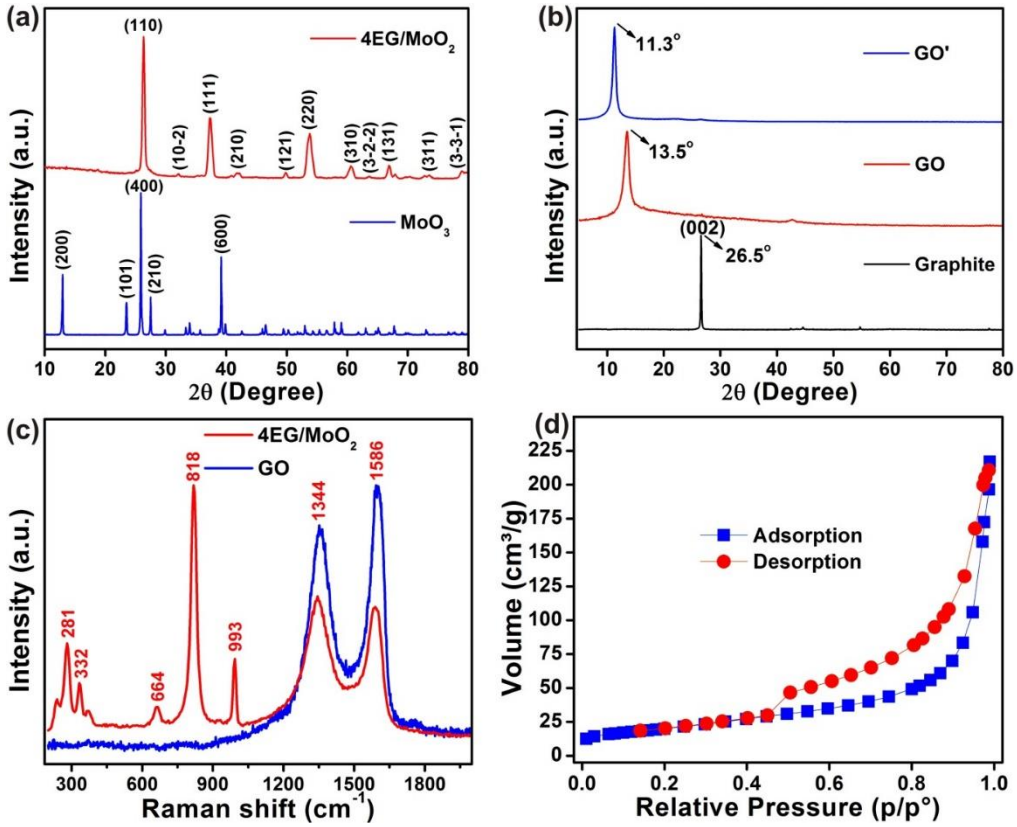

Figure 7.3. (a) XRD patterns of 4EG/MoO_2 and MoO_3, (b) XRD patterns of GO, GO' and graphite, (c) Raman spectra of 4EG/MoO_2 and GO, and (d) BET (N_2) adsorption-desorption isotherms of 4EG/MoO_2.

Raman analysis of EG/MoO_2 composites clearly shows that the reaction temperature chosen in this work yields good exfoliation to GO as well as complete reduction of MoO_3 to MoO_2. Raman analysis is in good agreement with XRD results.

The result of a N_2 physisorption experiment for the 4EG/MoO_2 composite is shown in Fig. 7.3(d). The observed N_2 adsorption and desorption isotherms are found to be matching with type IV BET classification. BET and Langmuir surface areas of 4EG/MoO_2 are found to be 71.4±0.2 and 177±11 m^2/g, respectively. The corresponding average pore volume is found to be ~0.244 cm^3/g with an average pore diameter of ~13.69 nm. The specific surface area and pore volume pertaining to 4EG/MoO_2 are noticed to be much larger (20 times larger) in comparison to those pertaining to 2EG/MoO_2 (*Annexure 7*).

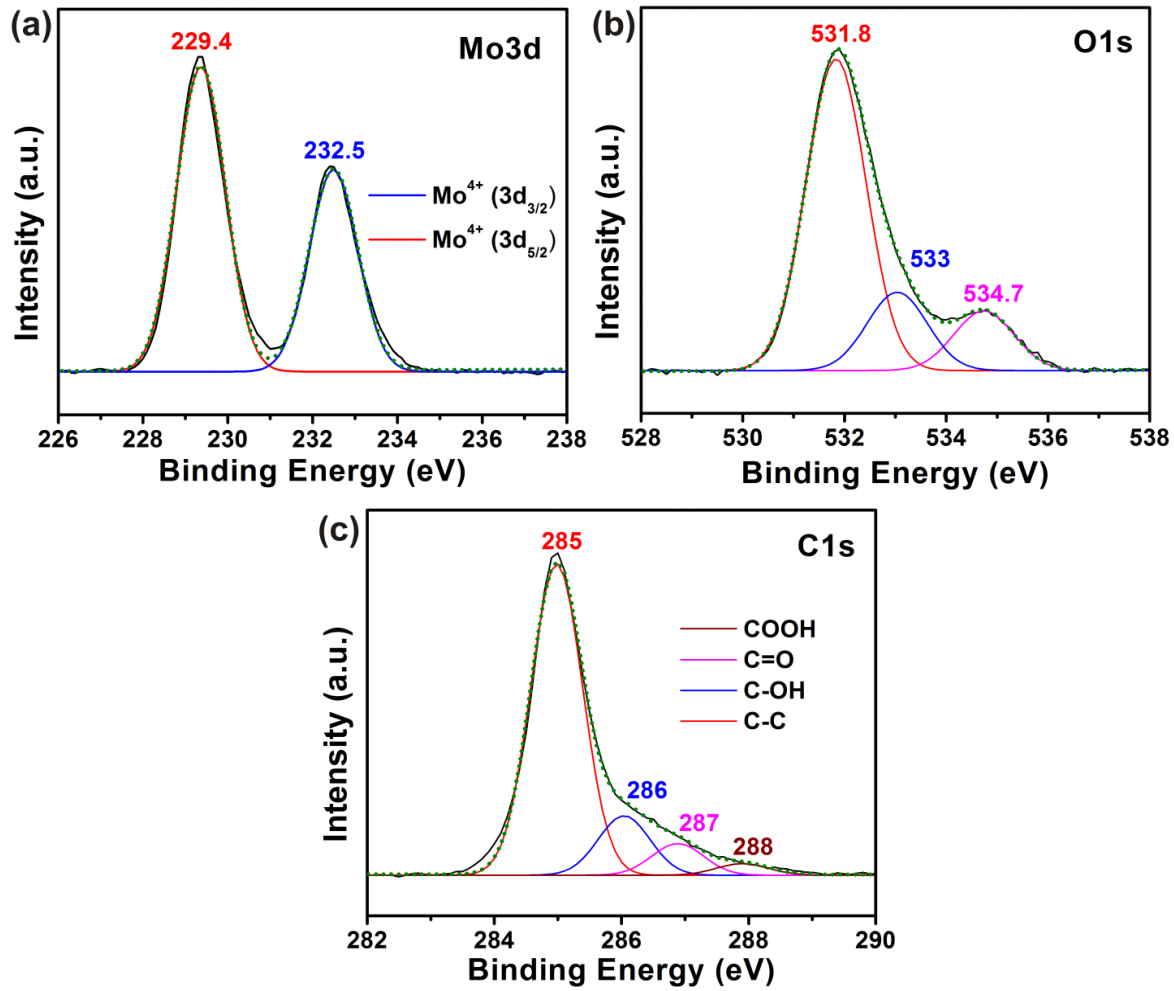

Figure 7.4. High resolution XPS spectra of (a) Mo3d, (b) O1s and (c) C1s of 4EG/MoO_2.

The larger surface area has plausibly resulted from the additional EG content, resulting in more disordered porous layered morphologies observed in electron micrographs. The additional exfoliation could also prevent MoO_2 particles from agglomerating, thus further increasing the specific surface area. The larger hysteresis as shown in Fig. 7.3(d) between N_2 adsorption and desorption isotherms of 4EG/MoO_2 indicates that it possess a greater extent of mesoporosity. Further, the chemical nature of MoO_2 in terms of oxidation states of individual elements was obtained though XPS analysis. The high resolution spectra of Mo3d, O1s and C1s are shown in Figs. 7.4(a), (b) and (c), respectively. The spectrum of Mo3d shows two distinct peaks at 229.4 and 232.5 eV, which represent the core-levels Mo^{4+} $3d_{5/2}$ and Mo^{4+} $3d_{3/2}$, respectively [7-9]. This characteristic doublet corresponds to oxidation state IV of Mo in MoO_2 [7-9]. The spectrum of O1s is deconvoluted into three peaks centred at 531.8, 532.0 and 534.7 eV. Amongst these three peaks, the first one at 531.8 eV is associated with oxygen that is bonded to molybdenum in the crystal structure of MoO_2 [7-9]. The second peak at 532.0 eV is either due to metallic nature of MoO_2 or it might correspond to surface oxygen [7,9]. The third peak plausibly arises from either surface oxygen or adsorbed moisture [7-9]. The C1s spectrum shows non-oxygenated carbon (C=C/C–C) peak at 285 eV whilst oxygenated carbon peaks are observed at 286 (C–OH), 287 (C=O) and 288 eV (COOH) [6,7]. The presence of oxygenated carbon peaks justifies abbreviating exfoliated graphene oxide as EG. These inferences from XPS study clearly indicate EG/MoO_2 composite formation which is consistent with the XRD and Raman scattering analysis.

TGA of GO and the reaction mixture 2GO+MoO_3 in N_2 environment was done in order to understand the reduction process from the thermal decomposition behaviour of the constituents. TGA of as-synthesized 4EG/MoO_2 in air was also carried out to determine the contents of EG and MoO_2 in the composite. As shown in Fig. 7.5(b), the initial weight loss of the reaction mixture that took place in comparison to GO up to 200 °C (Fig. 7.5(a)) could be

attributed to evaporation of water molecules preferably from GO [10]. The next weight loss up to 500 °C is due to the decomposition of various functional groups from GO [10, 11].

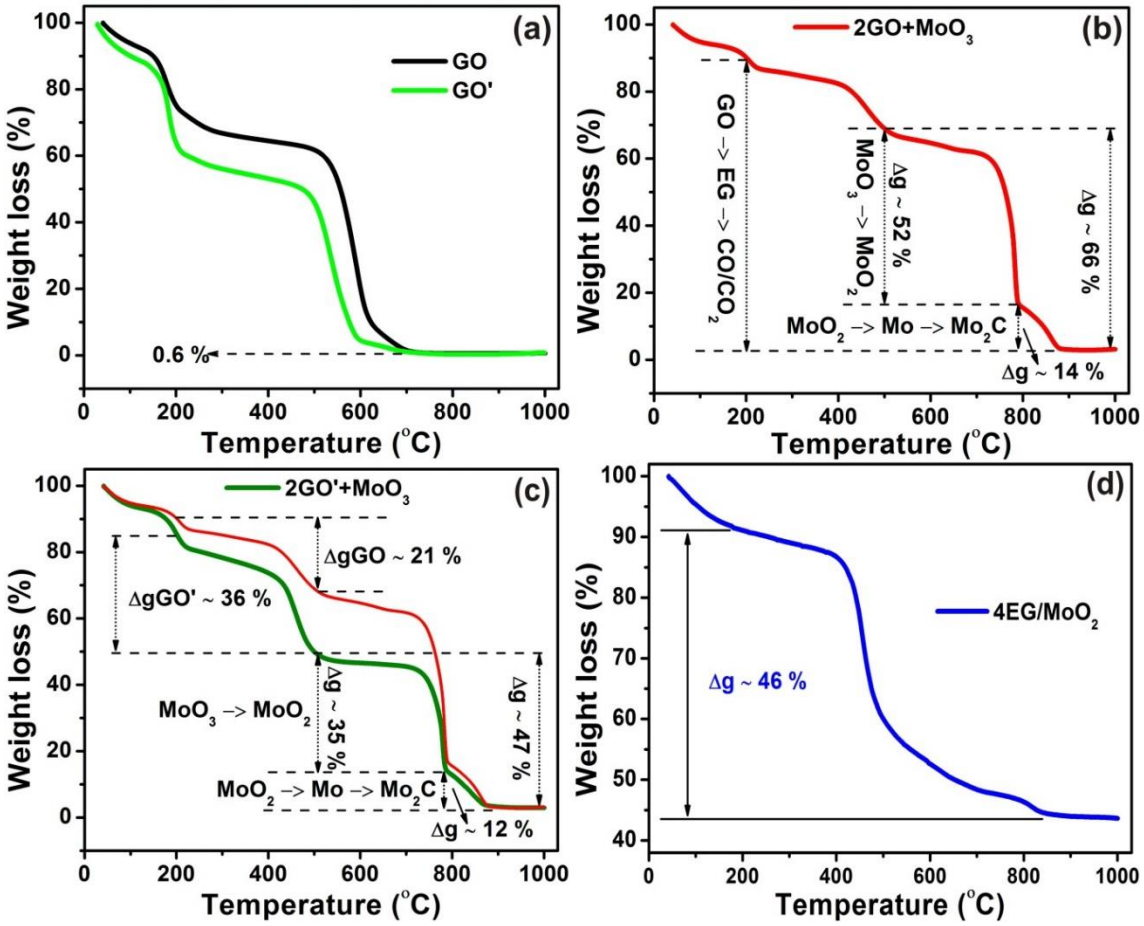

Figure 7.5. TGA of (a) GO and GO', (b) reaction mixtures 2GO+MoO_3 and (c) 2GO'+MoO_3 in N_2 environment, and (d) as-prepared 4EG/MoO_2 in air.

Further, the exfoliating GO (EG) also losses its weight either by releasing CO/CO_2 gaseous species or by giving up C from its skeleton which will reduce $MoO_3/MoO_2/Mo/Mo_2C$ as the temperature rises to 1000 °C [10-15]. A minimum of 500 °C is required to start the reduction of MoO_3 and thus beyond 500 °C the major share of the total weight loss corresponds to reduction of MoO_3 as well as subsequently formed molybdenum compounds up to 1000 °C [12-15]. The weight loss from 500 to 800 °C might be mainly corresponding to the reduction of MoO_3 to MoO_2 either by C (>500 °C) or CO (>650 °C) [12-15]. Next phase reduction of MoO_2 to Mo or Mo_2C might also be possible above 800 °C [12-15]. As shown in Fig. 7.5(b)

a rapid weight loss of ~66% was observed in the range 700-900 °C and only ~3% residual mass was found at the end of the test. This suggests that entire GO/EG was sublimated together with complete reduction of MoO_3 to Mo/Mo_2C [12-15]. Hence to retain EG as much as possible and to stop the reduction process at MoO_2 phase, the reaction temperature of 750 °C was chosen so as to synthesize an optimal EG/MoO_2 composite.

In an another experiment, TGA of GO' and the reaction mixture 2GO'+MoO_3 in N_2 environment was also carried out in order to understand the influence of degree of oxidation of GO on reduction process. As shown in Fig. 7.5(a), both GO and GO' are observed to show similar weight loss characteristics but GO' was burnt rapidly and at slightly lower temperatures than GO as a result of higher oxidation. Similar weight loss behaviour is observed when GO and GO' are burnt in the presence of MoO_3 (Fig. 7.5(c)). It was noted that GO' burnt 15% more than GO in their respective reaction mixtures up to 500 °C. It is worth to note that in both cases weight loss characteristics are found almost same especially beyond 500 °C (except a 19% difference in weight losses) strongly suggesting that degree of oxidation of GO has negligible role in reducing MoO_3 and its substantial by-products. Further, TGA of 4EG/MoO_2 in air (Fig. 7.5(d)) suggested that approximately 46 wt.% of EG is present in the composite. This observation facilitates the estimation of EG content to be ~23 wt.% in 2EG/MoO_2. Thus obtained weight percentages of individual components can correspond to theoretical capacities of 624 and 730 mAh g^{-1} for 4EG/MoO_2 and 2EG/MoO_2, respectively by considering complete reduction of MoO_2 (possible to form Mo and $2Li_2O$) and formation of LiC_6.

Galvanostatic charge-discharging features of both 2EG/MoO_2 and 4EG/MoO_2 in the voltage window 0.005–3.0V are shown in Fig. 7.6. The first discharge curve of 2EG/MoO_2 appeared very steep starting from open circuit voltage (OCV) to 1.6 V where first change in slope is observed; further, the curve declined up to 1.25 V where second change in slope observed

and beyond this, a continuous decline is observed up to 0.005 V as discharge progressed. The second and few subsequent discharge curves are found to be similar to the first discharge curve but distinct capacity ramps are observed in-between 1.55 and 1.25 V which correspond to Li-intercalation into MoO_2 but they did not appear as cycling continued and final discharging curve was found similar to that of pristine graphene [7,16,17].

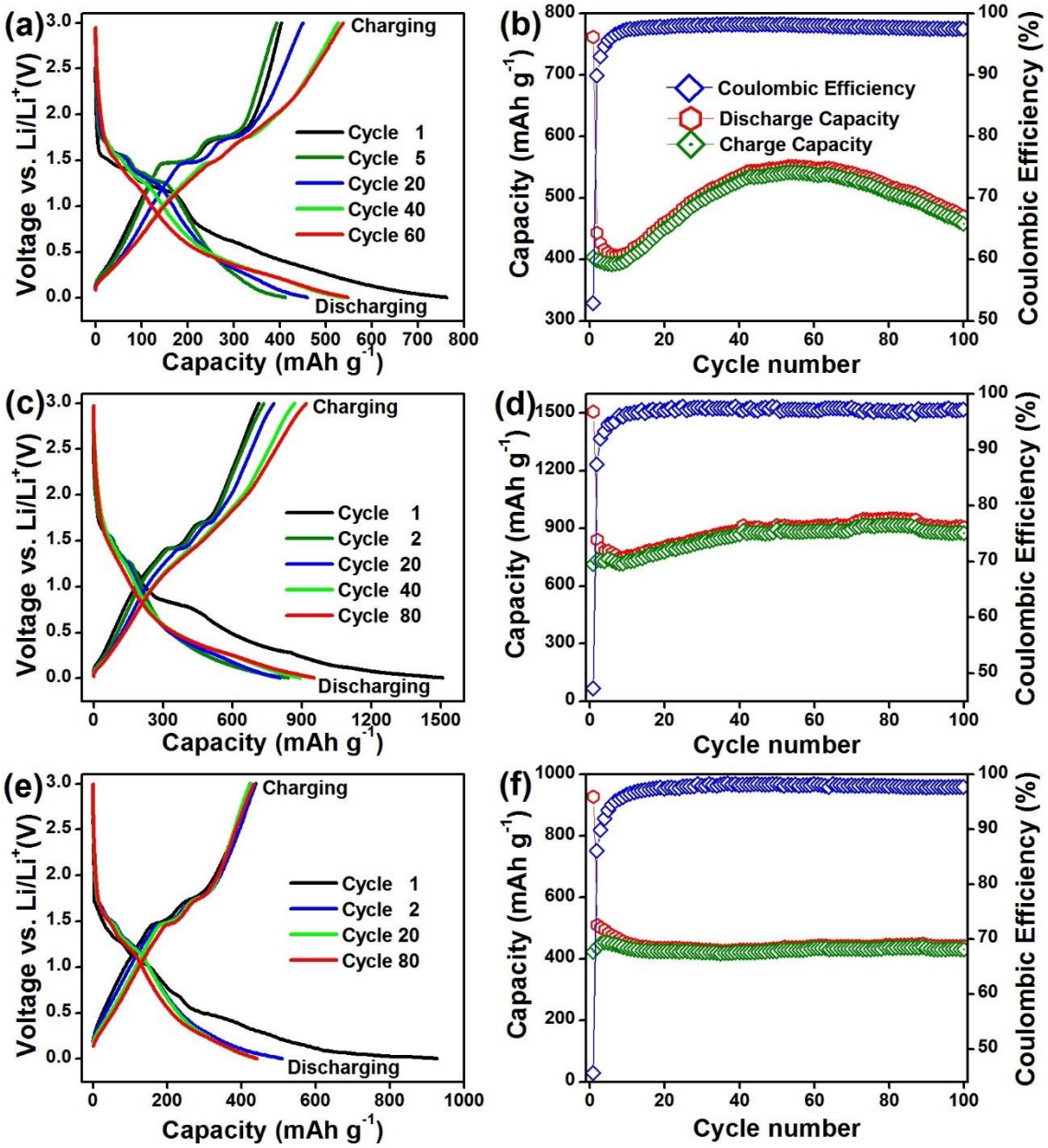

Figure 7.6. Galvanostatic cycling results of (a,b) 2EG/MoO_2 at 500 mA g^{-1}, (b,c) 4EG/MoO_2 at 100 mA g^{-1} and (e,f) 4EG/MoO_2 at 1000 mA g^{-1}.

During each discharge, capacity values dramatically decreased over the first few (about 5) cycles and then increased up to 60 cycles before once again decreasing for the remaining cycles as shown in Fig. 7.6(b). The net loss of capacity between first and second discharges is due to Li loss owing to solid electrolyte interface (SEI) formation [16]. The first charging curve is observed to incline continuously up to 1.4 V at which a first change in slope is noted followed by a second change at 1.72 V. At each of these features that correspond to Li de-intercalation from MoO_2 [7,16,17], the curve turns into a nearly flat ramp for about 100 mAh g^{-1}; beyond these changes the curve finally became inclined (but steeper) as charging progressed to 3.0 V. For the charging capacity as a function of cycle number, the same trend as discussed above for the discharging curves is observed (Fig. 7.6(b)). The ramps around 1.4 and 1.72 V are shifted to higher capacity values as cycling progressed but they do not appear almost immediately plausibly due to increased conversion of MoO_2 to metallic Mo (Li to Li_2O) and final charging curves also resembled those of pristine graphene [7,16,17]. The initial capacity decrease could be ascribed to continuous formation of SEI [16], the subsequent increase understood from the progressive conversion reactions between MoO_2 and Li which is known as electrode activation/formation effect [16] and the final decay might be due to the aggregation of metallic Mo to form metal clusters which no longer participate in the conversion reactions. This aggregation of metallic Mo could be avoided and Mo can be kept active for lithiation either by intercalation or conversion mechanism by simply increasing amount of EG in the composite like in the case of 4EG/MoO_2. As shown in Fig. 7.6(c) and (e), the voltage versus charge-discharge capacity profiles of 4EG/MoO_2 at 100 and 1000 mA g^{-1} current rates respectively are found similar to those of 2EG/MoO_2. The slight decrease in capacity values of ramps as a consequence of decrease in wt.% of MoO_2 is observed in both the cycles. But these are not observed at all for cycling at 100 mA g^{-1} which is an indication for absence of intercalation of Li into MoO_2. In contrast to 100 mA g^{-1} case,

the cycling at 1000 mA g^{-1} retained ramps suggesting that Li storage by MoO_2 prefers intercalation mechanism at higher current densities. Thus the extent of fading shown in Fig. 7.6(b) could be controlled with excess amount of EG (in tune with TGA) which offers good electrical contacts to MoO_2/Mo in a manner isolating them from aggregation and keeping them active in reversible traversing of Li-ions either by conversion reactions or intercalation as shown in Fig. 7.6(d) and (f), respectively depending on current density applied. From this it is clear that cyclability has improved far better than in the case of 2EG/MoO_2 either by continuous cycle to cycle increase or steady state capacity values as shown in Figs. 7.6 (d) and (f), respectively. Cyclic performance characteristics of the aforementioned EG/MoO_2 composites are tabulated in Table 7.1. The overall voltage versus capacity profile features are in tune with various redox peaks found in CV curves (Figs. 7.7 (a) and (b)). The cyclic performance of 4EG/MoO_2 is noted to be not only superior to that of 2EG/MoO_2 in the present study but also to that of various MoO_2 materials [16,18] and GO or Graphene-MoO_2 composites. The brief comparison between 4EG/MoO_2 and its class of some Graphene-MoO_2 composites prepared so far by complex multi-step methodologies are enumerated in Table 7.2. As listed in Table 7.2, 4EG/MoO_2 outperformed some of its kind of materials and can be able to outperform other similar composites after suitable modifications like carbon or nitrogen coating or doping or involving solvent phase mixing of initial reagents *etc*.

Table 7.1. Cyclic performance of EG/MoO_2 composites.

Composite/ Rate	DC1	CC1	QE1	DC50	CC50	QE50	DC100	CC100	QE100
2EG/MoO_2@500 mA g^{-1}	762	403	53	548	539	98	470	459	98
4EG/MoO_2@100 mA g^{-1}	1508	713	47	918	895	98	907	878	98
4EG/MoO_2@1000 mA g^{-1}	928	424	46	434	426	98	441	431	98

DC-Discharge Capacity and CC-Charge Capacity (±5 mAh g^{-1}*); QE-Coulombic Efficiency (%)*

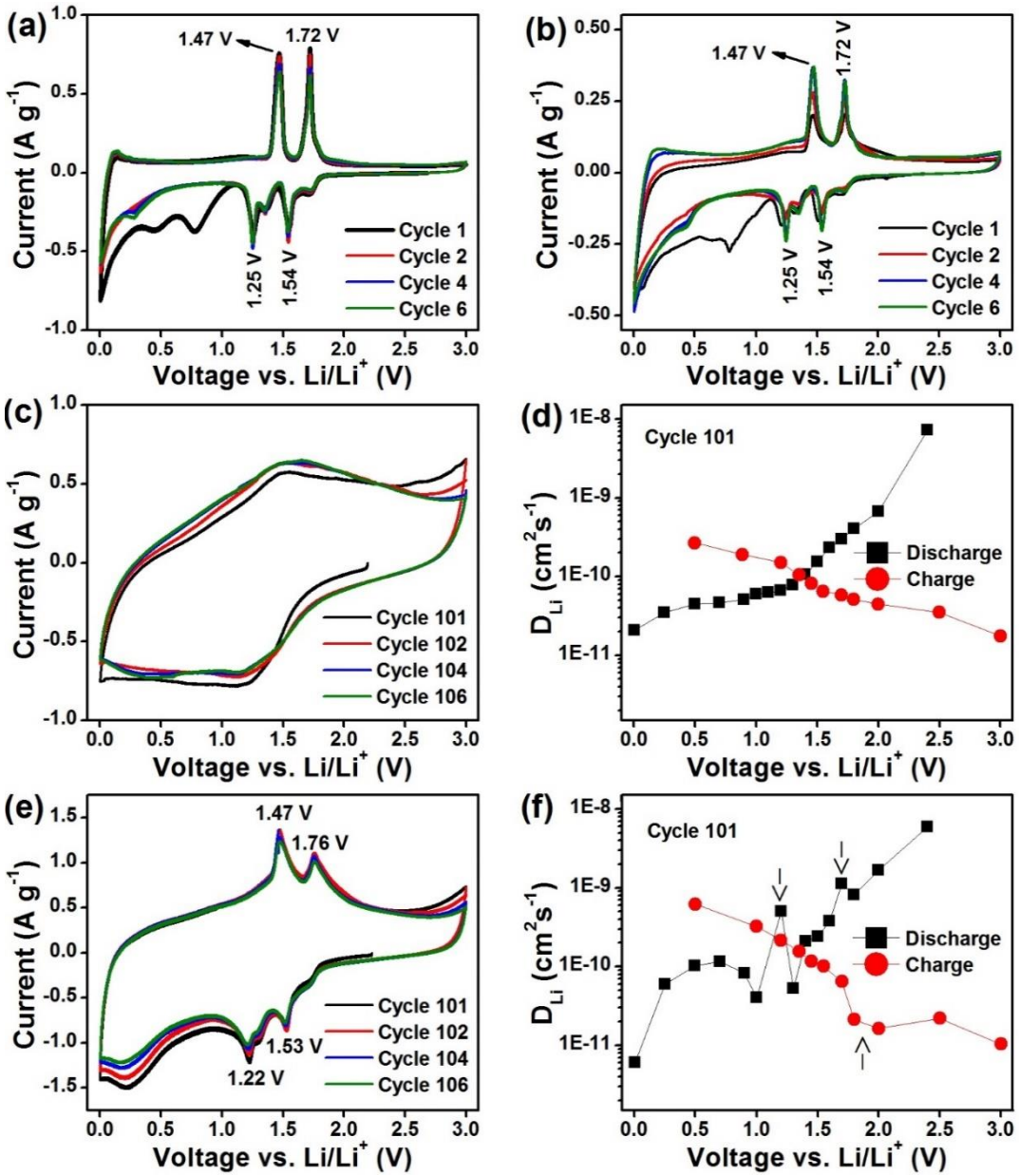

Figure 7.7. Cyclic Voltammetry results of (a) 2EG/MoO_2, (b) fresh 4EG/MoO_2, and (c) 4EG/MoO_2 after cycled at 100 mA g^{-1} and (e) 1000 mA g^{-1} and (d) and (f) corresponding diffusion coefficients, respectively.

The type of electrochemical reactions involved in securing capacities observed in GC are probed by CV measurements at a scan rate of 58 μV s^{-1} and in the voltage range of 0.005–3.0 V. CV curves of both 2EG/MoO_2 and 4EG/MoO_2 contained strong redox couples at 1.25/1.47 and 1.54/1.72 V as shown in Figs. 7.7(a) and (b), which corresponds to Li intercalation and de-intercalation into MoO_2, respectively [16,19]. The large difference between first and second reduction scans are attributed in general to the formation of SEI [16].

Table 7.2. Cyclic performance of 4EG/MoO_2 versus graphene/MoO_2 composites reported.

Ref.	Synthesis method	Wt.% of graphene	Reversible capacity (mAh g^{-1})		Current rate (mA g^{-1})
			1st cycle	After aging	
	Present study 4EG/MoO_2	46	713 424	878 (100th cycle) 431 (100th cycle)	100 1000
[7]	Aqueous solution of GO and PMA reduced with Hydrazine hydrate under sonication for 3 h and thus obtained solid product was heated at 500 °C in a 5% H_2/Ar flow for 5 h.	11.2	342	597 (70th cycle)	1000
[20]	GO+AHM dispersed in ethanol + HNO_3 was solvothermally treated at 160 °C for 16 h.	10	862	712 (30th cycle)	100
[21]	Solution of GO + Ethylene Glycol + Mo powder + H_2O_2 was heated hydrothermally at 200 °C for 24 h.	--	779 373	503 (30th cycle) 298 (30th cycle)	100 500
[3]	Hydrothermal reduction of GO, AHM and ascorbic acid at 180 °C for 10 h followed by calcination at 400 °C for 3 h under argon flow.	10.4	429 400*	1009 (60th cycle) 519 (60th cycle)	100 500
[5]	The solid precursor of GO + PMA was heated under 10% H_2/Ar at 500 °C for 2 h.	22	480* 620	640 (50 cycles) 480 (100 cycles)	200 1000
	Thermally reduced GO and AHM was heated at 550 C for 2 h under gases 5% C_2H_2 and 95% N_2.	51.7	758 730	752 (100 cycles) 600*(100 cycles)	100 1000
[22]	Thermally reduced GO and PMA was heated at 550 °C for 2 h under N_2 flow.	45.8	626 616	472 (100 cycles) 440*(100 cycles)	100 1000
	Thermally reduced GO and PMA was heated at 550 C for 2 h under 5% H_2/N_2 flow.	46.8	602 613	433 (100 cycles) 500*(100 cycles)	100 1000
[6]	Solution of GO, AHM, citric acid and poly ethylene glycol was heated hydrothermally at 180 °C for 26 h in vacuum.	33.2	703 703 550	769 (83 cycles) 530(1000 cycles) 497 (50 cycles)	540 540 1040
[23]	The precursor obtained from solution of GO, AHM, and HNO_3 by hydrothermally at 180 °C for 24 h was calcined at 600 °C under N_2 for 3 h.	--	-- 440*	769 (60 cycles) 400* (5 cycles)	100 1000

**values are approximated from images unless specifically claimed by authors, -- not available, PMA- phosphomolybdic acid ($H_3PMo_{12}O_{40}·xH_2O$) and AHM- ammonium heptamolybdate ($(NH_4)_6Mo_7O_{24}·4H_2O$).*

The large reduction current observed nearby 0.005 V is due to co-interaction of solvated lithium into EG during first cycle and from second cycle onwards only corresponds to Li-insertion alone. The two CV curves mainly differed in the current (corresponding to the redox couple of 2EG/MoO_2) which decreased cycle to cycle whilst it increased in the case of 4EG/MoO_2 while the area under the curves of 2EG/MoO_2 is noticed to be constant whereas the same increased in the case of 4EG/MoO_2. In addition, the observed area under the curves of the former seems to be smaller in comparison to 4EG/MoO_2. The CV curves of 2EG/MoO_2 is an indication for lesser capacity with fading in tune with galvanostatic cycling shown in Fig. 7.6(a) and (b). The increased amount of EG has been observed to decrease the current of MoO_2 redox peaks in 4EG/MoO_2 when compared with 2EG/MoO_2. The observed decrease was compensated with increased area under the curves which is plausibly ascribed to electrochemical absorption and desorption of Li onto EG surfaces. CV curves of 4EG/MoO_2 cycled at 100 and 1000 mA g^{-1} for 100 cycles are shown in Figs. 7.7(c) and (e), respectively. Their corresponding diffusion coefficients calculated during 101^{st} discharge and charge are shown in Fig. 7.7(d) and (f). As shown in Fig. 7.7(c), features indicating the redox couples cannot be observed at all giving rise to a broad hump whose current and area under the curve increased enormously after aging at 100 mA g^{-1}. This situation resembles the psuedocapacitive property observed for MoO_2-RGO hybrid [19]. The respective Li-diffusion coefficient values (SI6) showed a nonlinear relation with decreasing tendency during both discharging and charging as shown in Fig. 7.7(d). The aging at 1000 mA g^{-1} is totally different from 100 mA g^{-1} as shown in Fig. 7.7(e). In this case, a slightly broadened redox peaks with three fold increase in current are noticed and the area under the curves also increased in proportion to redox couple. The respective Li-diffusion coefficient values (SI6) are shown in Fig. 7.7(f) which are also found in nonlinear relation. But unlike in the 100 mA g^{-1} case, here a sudden increase and decrease in the diffusion coefficient values are observed

during discharge and charge processes, respectively as pointed by arrow marks. This change in diffusion coefficient value signifies the Li-intercalation and de-intercalation from MoO_2 in tune with the inference from CV studies. The overall observations found in CV studies are well in agreement with inferences of galvanostatic cycling results shown in Fig. 7.6.

Retaining of crystallinity by MoO_2 after 100^{th} cycle at 1000 mA g^{-1} as shown in Fig. 7.8(a) clarifies the Li intercalation/de-intercalation into MoO_2. On the other hand aging at 100 mA g^{-1} (100 cycles, Fig. 7.8(a)) caused total amorphisation of MoO_2 which is an indication for conversion reactions between MoO_2 and Li. As shown in Figs. 7.8(b) and (c), most of the rod and flower like MoO_2 particles are found almost intact as per the SAED patterns and contributed to retention of crystallinity even after 100 cycles of aging at 1000 mA g^{-1}. Thus, post cycling *ex-situ* XRD, electron micrographs and corresponding SAED patterns, CV studies and the corresponding Li- diffusion coefficients are consistent with each other and clearly indicate that Li- intercalation mechanism is retained at higher current rate cycling whilst conversion mechanism preferably takes place at low current rates. But conversion reactions involvement seems to be beneficial up to about 60 or 70 cycles from where decay is observed for various MoO_2, MoO_2/C, GO-MoO_2 and Graphene-MoO_2 composites reported similar to the present case as-observed for 2EG/MoO_2 (Figs. 7.6 (a) and (b)). However, both intercalation and conversion mechanisms could to be promising for enhanced capacity and good cyclic performance when an excess amount of graphene is present. Another advantage of excess graphene is that it can postpone/prevent the conversion reaction in higher current rate applications even for voltage window 0.005–3.0 V as shown in Figs. 7.6 (e) and (f), unlike in the case of limited voltage window to 1.0–2.2 V to avoid conversion reaction of MoO_2 below 0.6-0.8 V [17].

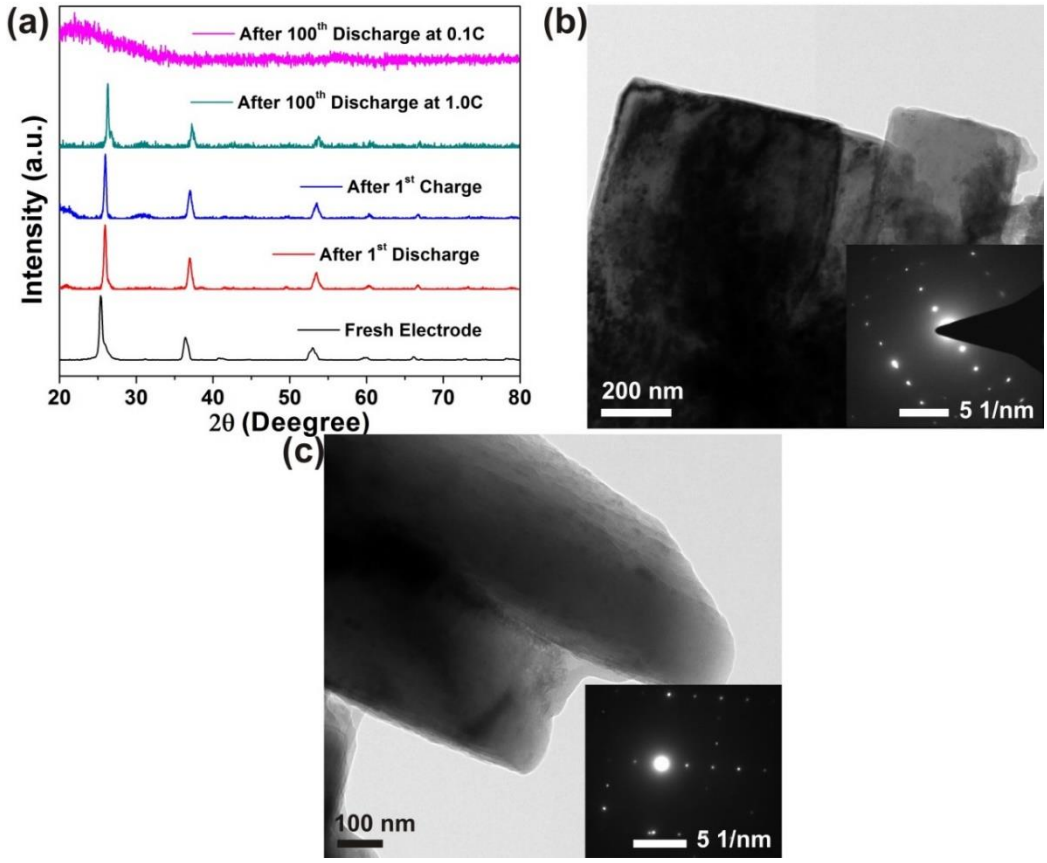

Figure 7.8. (a) Post cycling *ex-situ* XRD patterns of 4EG/MoO_2 (intensities normalized), (b) rods and (c) sheets, and corresponding SAED patterns of MoO_2 in 4EG/MoO_2 that are cycled at 1000 mA g^{-1} for 100 cycles.

In order to understand the Li kinetics and charge transfer mechanisms EIS has been carried out on a fresh cell followed by measurements in the discharged and charged states. The frequency dependent AC impedance of 4EG/MoO_2 at various states are shown in Fig. 7.9 as Nyquist plots (–Z'' vs. Z') along with the equivalent circuit into which impedance data fitted the best. The equivalent circuit comprised of R_e (contact/electrolyte resistance), R_{ct} (resistance to charge transfer), CPE_{dl} (double layer capacitance/ constant phase element), Warburg diffusion element W_s (lithium diffusional component) and C_i (lithium intercalation capacitance). The value of R_e fitted to 4.14 Ω at OCV. It later increased slightly to 5.47 Ω after first discharge to 0.005 V and once again slightly decreased to 4.14 Ω after first charging to 3.0 V. The resistance to charge transfer R_{ct} is found to be 79.32 Ω at OCV which is reduced to 59.49 and 14.77 Ω after the first discharge and charge, respectively. The nearly

fivefold decrease in impedance for both composites during first charging than discharging signifies that the material readily allows lithium to leave it (low resistance to Li extraction). The values of CPE_{dl} are found to increase from 38 μF (OCV) to 41 μF (at 0.005 V) and then to 320 μF (at 3.0 V) as a consequence of easy de-lithiation in tune with R_{ct} values. The overall impedance of 4EG/MoO_2 is found nearly one and half time less than 2EG/MoO_2 that plausibly resulted from excess EG (*Annexure 7*). The observed values of C_i >1F for 2EG/MoO_2 and <1F for 4EG/MoO_2 confirm that lithium intercalation mechanism predominates when EG is in lesser amounts in the composite. This is in good agreement with the CV results.

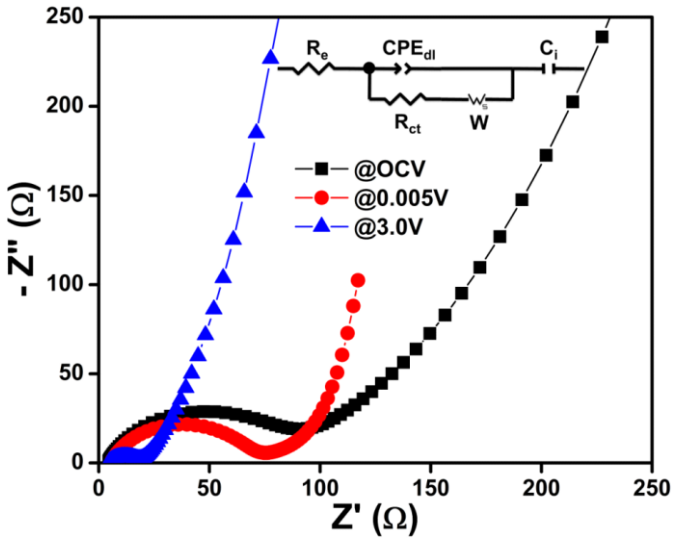

Figure 7.9. Nyquist plots of 4EG/MoO_2 at various states with the equivalent circuit.

References

[1] Kadam MM, Lokare OR, Kireeti KVMK, Gaikar VG, Jha N. Impact of the degree of functionalization of graphene oxide on the electrochemical charge storage property and metal ion adsorption. RSC Advances. 2014;4:62737-45.

[2] Yan H, Tao X, Yang Z, Li K, Yang H, Li A, et al. Effects of the oxidation degree of graphene oxide on the adsorption of methylene blue. Journal of Hazardous Materials. 2014;268:191-8.

[3] Tang Q, Shan Z, Wang L, Qin X. MoO_2-graphene nanocomposite as anode material for

lithium-ion batteries. Electrochimica Acta. 2012;79:148-53.

[4] Yang L, Liu L, Zhu Y, Wang X, Wu Y. Preparation of carbon coated MoO_2 nanobelts and their high performance as anode materials for lithium ion batteries. Journal of Materials Chemistry. 2012;22:13148-52.

[5] Seng KH, Du GD, Li L, Chen ZX, Liu HK, Guo ZP. Facile synthesis of graphene-molybdenum dioxide and its lithium storage properties. Journal of Materials Chemistry. 2012;22:16072-7.

[6] Bhaskar A, Deepa M, Rao TN, Varadaraju UV. Enhanced nanoscale conduction capability of a MoO_2/graphene composite for high performance anodes in lithium ion batteries. Journal of Power Sources. 2012;216:169-78.

[7] Sun Y, Hu X, Luo W, Huang Y. Self-Assembled hierarchical MoO_2/graphene nanoarchitectures and their application as a high-performance anode material for lithium-ion batteries. ACS Nano. 2011;5:7100-7.

[8] Liu J, Tang S, Lu Y, Cai G, Liang S, Wang W, et al. Synthesis of Mo_2N nanolayer coated MoO_2 hollow nanostructures as high-performance anode materials for lithium-ion batteries. Energy & Environmental Science. 2013;6:2691-7.

[9] Scanlon DO, Watson GW, Payne DJ, Atkinson GR, Egdell RG, Law DSL. Theoretical and experimental study of the electronic structures of MoO_3 and MoO_2. The Journal of Physical Chemistry C. 2010;114:4636-45.

[10] Acik M, Lee G, Mattevi C, Chhowalla M, Cho K, Chabal YJ. Unusual infrared-absorption mechanism in thermally reduced graphene oxide. Nat Mater. 2010;9(10):840-5.

[11] Jeong H-K, Lee YP, Jin MH, Kim ES, Bae JJ, Lee YH. Thermal stability of graphite oxide. Chemical Physics Letters. 2009;470:255-8.

[12] Ōya A, Kasahara M, Ohashi H, Ōtani S. Carbothermal reduction of the molybdenum oxide/phenanthroline complex. Journal of the American Ceramic Society. 1991;74:1439-41.

[13] Chaudhury S, Mukerjee SK, Vaidya VN, Venugopal V. Kinetics and mechanism of carbothermic reduction of MoO_3 to Mo_2C. Journal of Alloys and Compounds. 1997;261:105-13.

[14] Gruner W, Stolle S, Wetzig K. Formation of COx species during the carbothermal reduction of oxides of Zr, Si, Ti, Cr, W, and Mo. International Journal of Refractory Metals and Hard Materials. 2000;18:137-45.

[15] Zhu H-y, Li Z-b, Yang H-s, Luo L-g. Carbothermic reduction of MoO_3 for direct

alloying process. Journal of Iron and Steel Research, International. 2013;20:51-6.

[16] Reddy MV, Subba Rao GV, Chowdari BVR. Metal oxides and oxysalts as anode materials for Li ion batteries. Chemical Reviews. 2013;113:5364-457.

[17] Kumar Sen U, Shaligram A, Mitra S. Intercalation anode material for lithium ion battery based on molybdenum dioxide. ACS Applied Materials & Interfaces. 2014;6(16):14311-9.

[18] Qiu S, Lu G, Liu J, Lyu H, Hu C, Li B, et al. Enhanced electrochemical performances of MoO_2 nanoparticles composited with carbon nanotubes for lithium-ion battery anodes. RSC Advances. 2015;5:87286-94.

[19] Kim H-S, Cook JB, Tolbert SH, Dunn B. The development of pseudocapacitive properties in nanosized-MoO_2. Journal of the Electrochemical Society. 2015;162:A5083-A90.

[20] Xu Y, Yi R, Yuan B, Wu X, Dunwell M, Lin Q, et al. High capacity MoO_2/graphite oxide composite anode for lithium-ion batteries. The Journal of Physical Chemistry Letters. 2012;3:309-14.

[21] Hu S, Yin F, Uchaker E, Chen W, Zhang M, Zhou J, et al. Facile and green preparation for the formation of MoO_2-GO composites as anode material for lithium-ion batteries. The Journal of Physical Chemistry C. 2014;118:24890-7.

[22] Guo L, Wang Y. Standing carbon-coated molybdenum dioxide nanosheets on graphene: morphology evolution and lithium ion storage properties. Journal of Materials Chemistry A. 2015;3:4706-15.

[23] Wang X, Xiao Y, Wang J, Sun L, Cao M. Facile fabrication of molybdenum dioxide/nitrogen-doped graphene hybrid as high performance anode material for lithium ion batteries. Journal of Power Sources. 2015;274:142-8.

Chapter 8 FLG-Complex Metal Oxide ($A_2Mo_3O_8$, A= Co, Mn and Zn) Composites

GTR method is used to obtain few layered graphene (FLG)–complex metal oxide ($A_2Mo_3O_8$, A= Co, Mn and Zn) composites. Carbons of the exfoliating GO are used as an aid to reduce metal precursors to $A_2Mo_3O_8$. As-synthesized composites are used as anode materials in Li ion batteries. In 0.005-3 V potential window and at 60 mA/g current density, FLG–$Co_2Mo_3O_8$, FLG–$Mn_2Mo_3O_8$ and FLG–$Zn_2Mo_3O_8$ composites exhibit high reversible capacities of 785, 495 and 630 mAh/g respectively, even at the end of 50th cycle. The composites show far better cycling performance and rate capability than Mo-metal cluster compound. Amongst the three composites, FLG–$Co_2Mo_3O_8$ shows excellent capacity retention (~87%) and Coulombic efficiency (~98%). Cyclic voltammetry shows that: i) redox couples of $A_2Mo_3O_8$ and ii) electrochemical adsorption and desorption by FLG in the composites are responsible for Li storage and release.

Figure 8.1 shows that morphologies of all the samples. Secondary electron (SE) micrographs of FLG-$Co_2Mo_3O_8$ composite powder are shown in Figs. 8.1(a,b). The micrograph depicts ~65 nm thick hexagonal shaped sub-micron sized particles that are stacked on one another to form a group of particles. This arrangement left gaps between such neighboring groups. Fig. 8.2(a) shows the bright field transmission electron micrograph of FLG-$Co_2Mo_3O_8$ composite platelets. High resolution transmission electron micrograph (Fig. 8.2(b)) confirmed that the sample contains crystalline $Co_2Mo_3O_8$ particles wrapped by FLG. Similarly, SE micrographs of FLG-$Mn_2Mo_3O_8$ (Fig. 8.1(c, d)) show hexagonal particles with an approximate thickness of ~55 nm. These hexagonal shaped nanoplatelet particles are closely packed when compared with the FLG-$Co_2Mo_3O_8$ case. Unlike in FLG-$Co_2Mo_3O_8$ composite, some of these particles are covered by semi-transparent FLG sheets (encircled by a black colored line) as observed in Fig. 8.1(d). Fig. 8.2(c) shows the bright field transmission electron micrograph of FLG-$Mn_2Mo_3O_8$ composite particles wrapped by graphene layers.

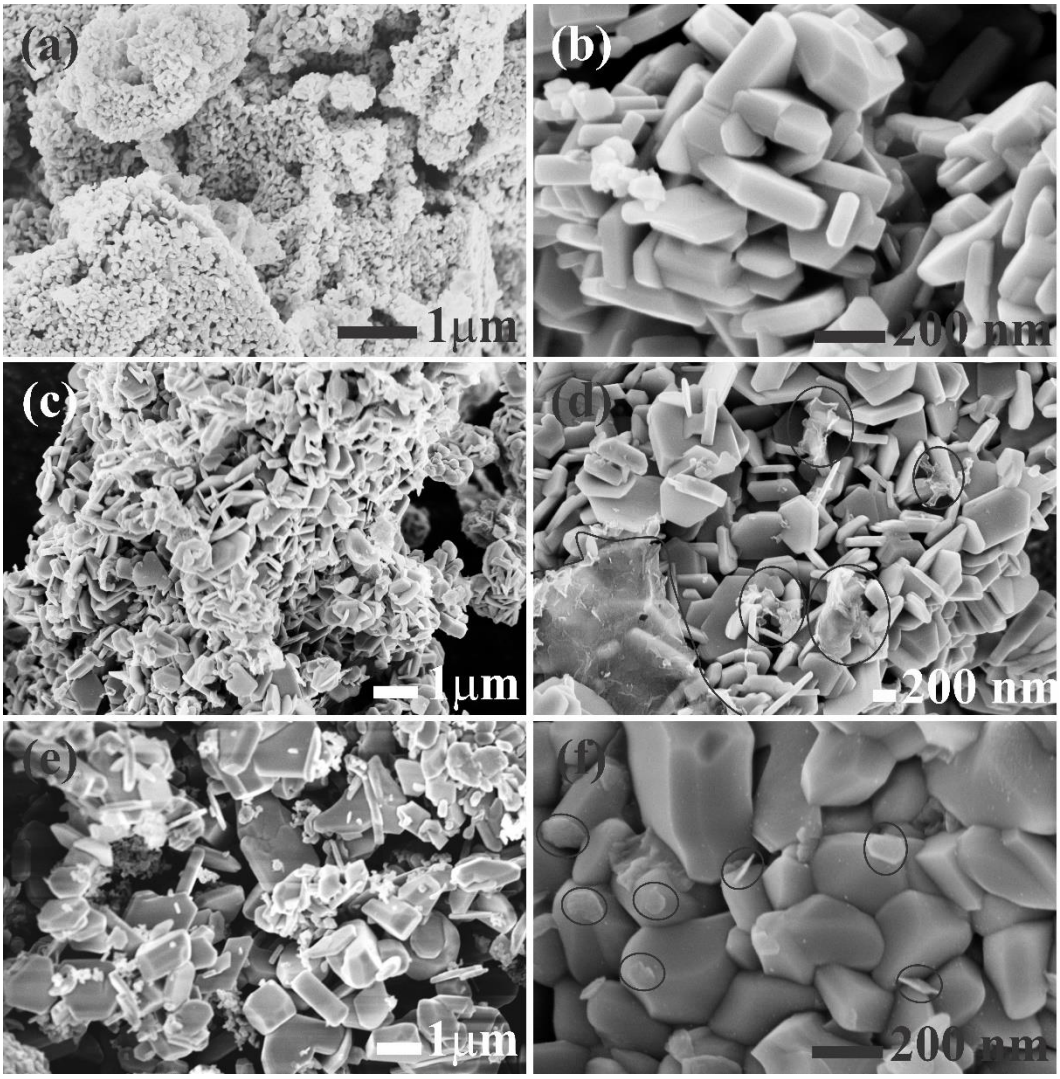

Figure 8.1. Secondary electron micrographs of (a,b) FLG-$Co_2Mo_3O_8$, (c,d) FLG-$Mn_2Mo_3O_8$ and (e,f) FLG-$Zn_2Mo_3O_8$ composites, respectively.

High resolution transmission electron micrograph (Fig. 8.2(d)) also confirms that the obtained material is the hexagonal $Mn_2Mo_3O_8$ mixed metal oxide (d-spacing 0.255 nm corresponds to (004) plane) and these particles are wrapped by semi-transparent FLG layers (~2-3 layers, marked with a line). SE micrographs of FLG-$Zn_2Mo_3O_8$ composite are shown in Figs. 8.1(e,f). In this case, even though the sample possesses a morphology similar to the morphologies shown by FLG-$Co_2Mo_3O_8$ and FLG-$Mn_2Mo_3O_8$, particles are observed to agglomerate comparatively more. FLG sheets are encircled in Fig. 8.1(f). Fig. 8.2(e) shows the bright field transmission electron micrograph of FLG-$Zn_2Mo_3O_8$ composite.

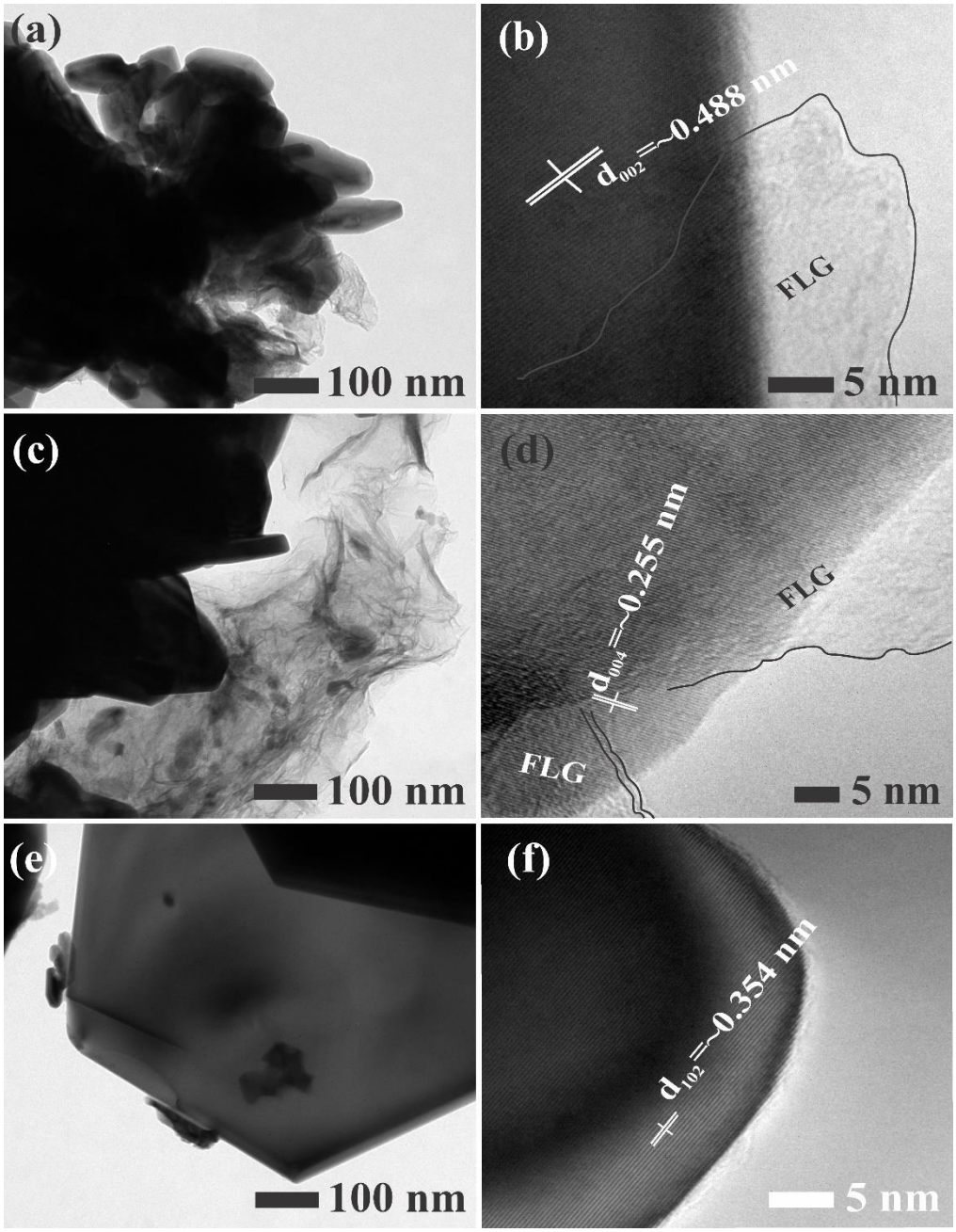

Figure 8.2. (a,c,e) Bright field transmission electron micrographs and (b,d,f) high resolution transmission electron micrographs of FLG-$Co_2Mo_3O_8$, FLG-$Mn_2Mo_3O_8$ and FLG-$Zn_2Mo_3O_8$ composites, respectively.

High resolution transmission electron micrograph (Fig. 8.2(f)) also confirms from the measured d-spacing that the obtained material is highly crystalline $Zn_2Mo_3O_8$. One unique feature observed on comparing all electron micrographs is that the size and agglomeration of the particles are more in the case of high atomic number element A constituting FLG-$A_2Mo_3O_8$ composite. The FLG sheets in FLG-$A_2Mo_3O_8$ composites are not discernable in

Figs. 8.1(b) and 1(f). However, they are clearly observed in the bright field and high resolution transmission electron micrographs. X-ray diffraction patterns of FLG-$Co_2Mo_3O_8$, FLG-$Mn_2Mo_3O_8$ and FLG-$Zn_2Mo_3O_8$ (shown in Fig. 8.3) are matched with JCPDS data file numbers #34-0511, #34-0510 and #20-0682, respectively.

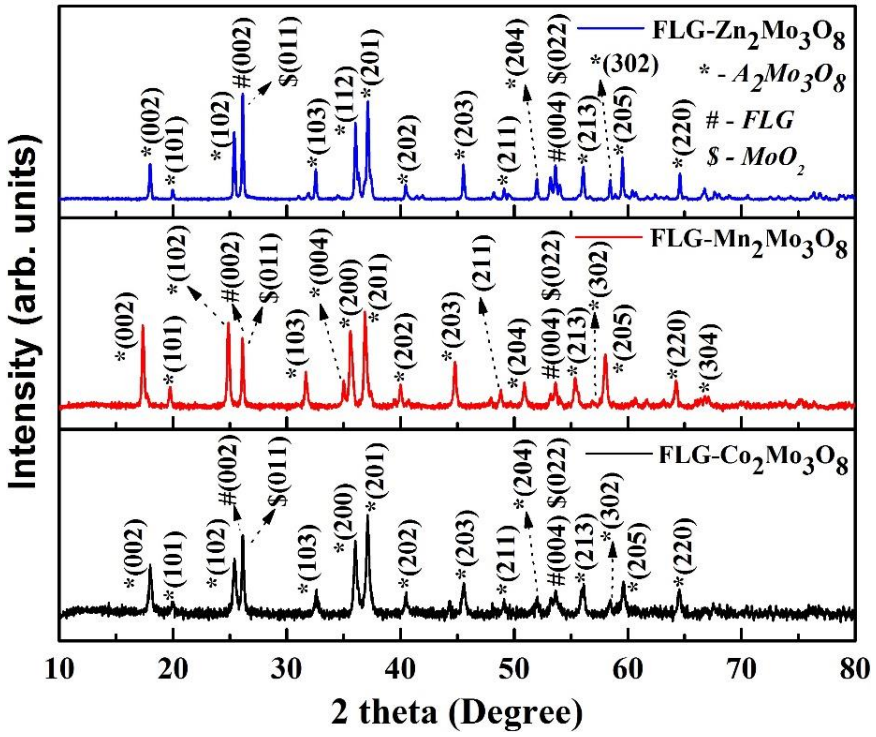

Figure 8.3. X-ray diffractograms of FLG-$Co_2Mo_3O_8$, FLG-$Mn_2Mo_3O_8$ and FLG-$Zn_2Mo_3O_8$ composites.

Thermal stability of FLG–$A_2Mo_3O_8$ (A= Co, Mn and Zn) composite is studied in air ambience, in the temperature range of 50-1000 ^{0}C and at a heating rate of 10 °C/min in order to evaluate the amount of FLG present in the respective composite. The calculated weight fraction of FLG in FLG−$Co_2Mo_3O_8$, FLG−$Mn_2Mo_3O_8$ and FLG−$Zn_2Mo_3O_8$ composites is found as 17.23, 7.70 and 6.74 wt.%, respectively. As shown in Fig. 8.4 all the three composites showed weight gain between 400 and 600 °C which corresponds to oxidation of $A_2Mo_3O_8$ [1]. The net weight loss found between 200 and 800 °C which corresponds to the decomposition of FLG [2].

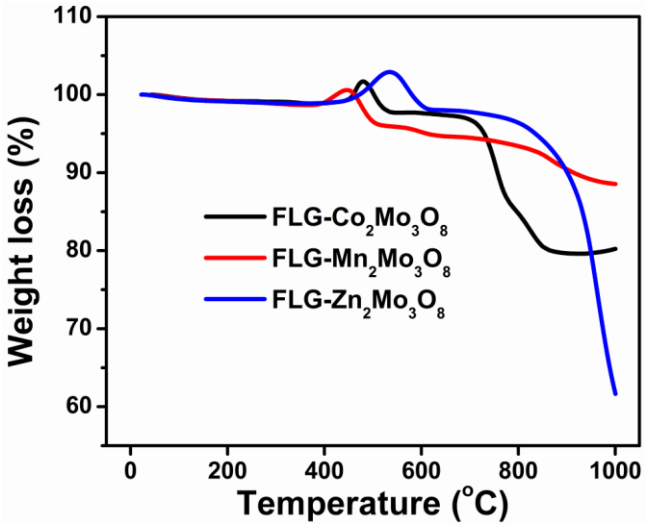

Figure 8.4. TGA curves of FLG–$Co_2Mo_3O_8$, FLG–$Mn_2Mo_3O_8$ and FLG–$Zn_2Mo_3O_8$ composites.

Raman spectra in Fig. 8.5 show D (~1360 cm^{-1}), G (~1599 cm^{-1}) and very weak and broadened 2D (~2700 cm^{-1}) bands which confirm the presence of FLG in all three composites. D-band's high intensity is due to the presence of many defects in the material resulted due to annealing and the presence of complex MO. High intensity of G-band than D-band indicates the presence of more number of regular carbon hexagons which in turn implies that FLG is of good quality. For crystalline $A_2Mo_3O_8$ (space group, $P6_3mc$), a maximum of 15 Raman active modes ($3A_1+6E_1+6E_2$) are allowed [3]. Raman spectrum of FLG-$A_2Mo_3O_8$ composite shows 13 peaks and among which 11 of the expected 15 Raman modes correspond to $A_2Mo_3O_8$. Based on the available literature [4], the bands at 360 and 435 cm^{-1} are assigned to (O-$(Mo\text{-}Mo)_{cluster}$-O) and (Mo-O-Mo) bending vibrations, respectively [3]. The peaks at and below 326 cm^{-1} are assigned to A-O bending vibrations of the AO_4-tetrahedra and AO_6-octahedra in the structure. Other higher order combinational modes are also observed at 726, 809 and 928 cm^{-1}. The measured BET surface area and porosity values pertaining to FLG-$Co_2Mo_3O_8$, FLG-$Mn_2Mo_3O_8$ and FLG-$Zn_2Mo_3O_8$ composites are listed in Table. 8.1 whilst N_2 adsorption and desorption isotherms pertaining to the composites are shown in Fig. 8.5. All isotherms (Fig. 8.6) resemble the type IV isotherm of IUPAC standard adsorption-

desorption isotherms. The measured pore size values categorize the composites into mesoporous materials. This is owing to the enhanced particle size and agglomeration of particles in the case of higher atomic number elements which in turn leads to the decrease in surface area of the corresponding composite. Low specific surface area is also owing to the high annealing temperature which leads to densely packed hexagonal crystal system of the major $A_2Mo_3O_8$ phase in the respective composites. Nonetheless, amongst the three composites, FLG-$Co_2Mo_3O_8$ composite exhibited superior BET surface area.

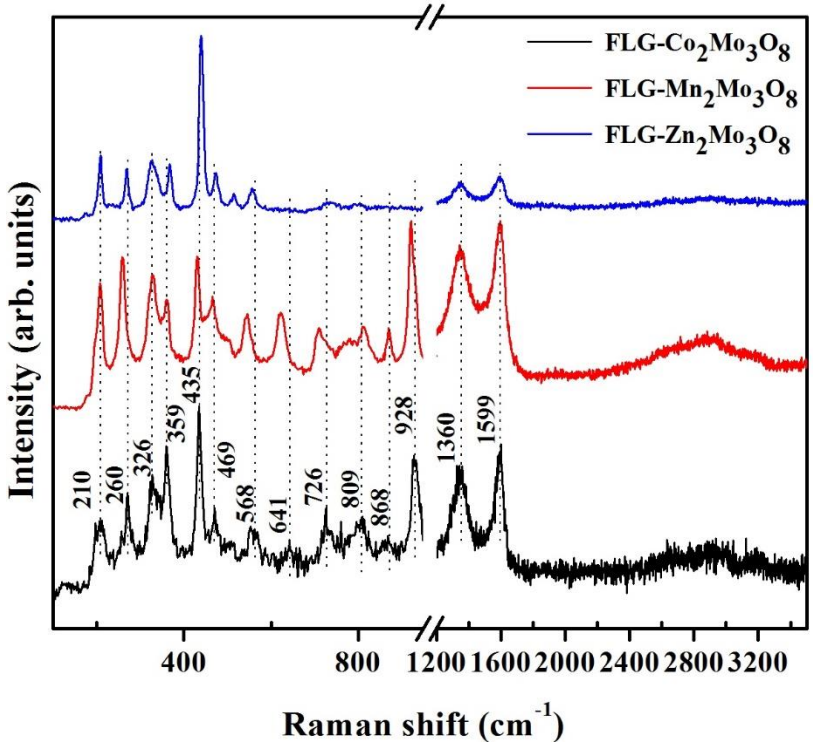

Figure 8.5. Raman spectra of FLG-$Co_2Mo_3O_8$, FLG-$Mn_2Mo_3O_8$ and FLG-$Zn_2Mo_3O_8$ composites.

Table 8.1. BET surface area, average pore size and average pore volume of FLG-$Co_2Mo_3O_8$, FLG-$Mn_2Mo_3O_8$ and FLG-$Zn_2Mo_3O_8$ composites.

Composite	BET Surface Area (m^2/g)	Average Pore Size (nm)	Average Pore Volume (cm^3/g)
FLG-$Co_2Mo_3O_8$	14.42	9	0.0319
FLG-$Mn_2Mo_3O_8$	3.49	14	0.0121
FLG-$Zn_2Mo_3O_8$	2.76	8	0.0057

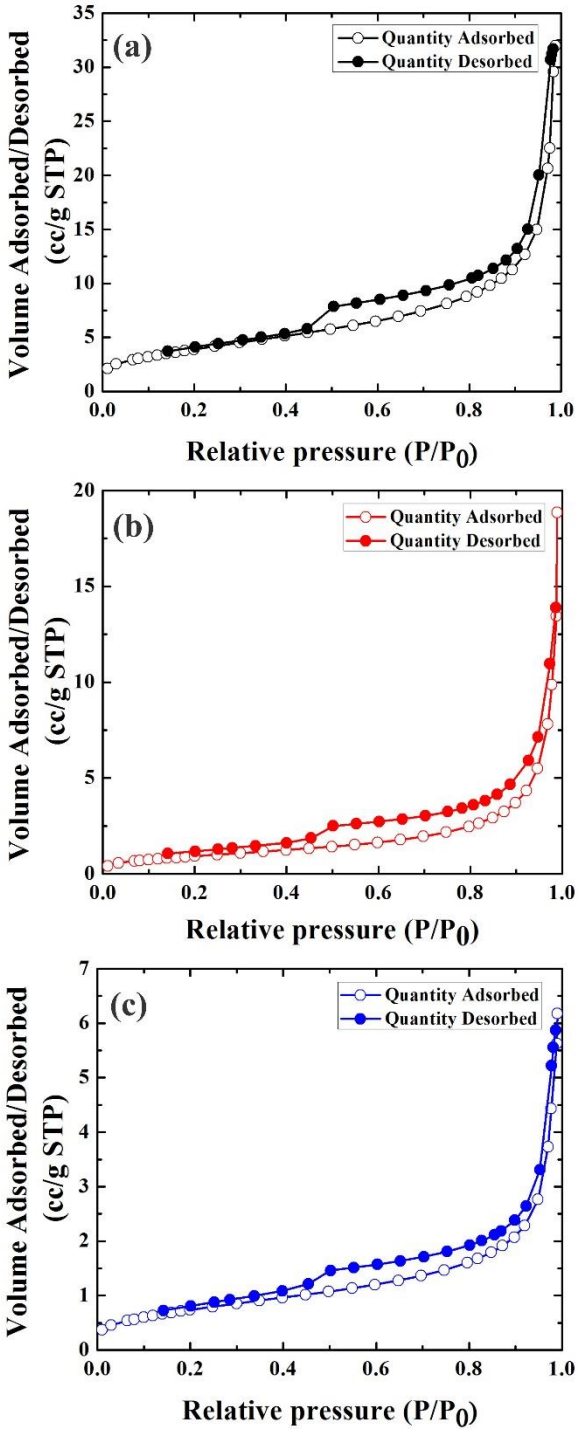

Figure 8.6. N_2 adsorption and desorption isotherms of (a) FLG-$Co_2Mo_3O_8$, (b) FLG-$Mn_2Mo_3O_8$ and (c) FLG-$Zn_2Mo_3O_8$ composites.

The voltage versus capacity profiles of FLG-$Co_2Mo_3O_8$ composite at 60 mA/g current density are shown in Fig. 8.7(a). It is observed that the first discharging curve is steeper starting from the open circuit voltage (OCV ~2.61 V) with a negligible change in slope up to 1.5 V. Thereafter slope changed continuously until 0.005 V. Change in slope is noticed at 1.25, 0.9

and 0.7 V and a continuous plateau is observed beyond 0.5 V which is in good agreement with CV results shown in Fig 8.7(b).The typical slope change between 0.9-0.7 V is attributed to irreversible reaction between Li^+ and FLG-$Co_2Mo_3O_8$ and initial electrolyte decomposition which leads to the formation of solid electrolyte interphase (SEI) [5,6]. The first charging curve is steeper up to 1.25 V and thereafter there is a change in slope while a second change is noticed around 1.75 V which continued until the voltage became 2.0 V from which point the charging curve once again became steeper up to a final voltage of 3.0 V with negligible changes in slope. This is again consistent with CV results. The subsequent cycles showed similar features as that of the first cycle except for a slight decrease in capacity value as the cycle number increased.

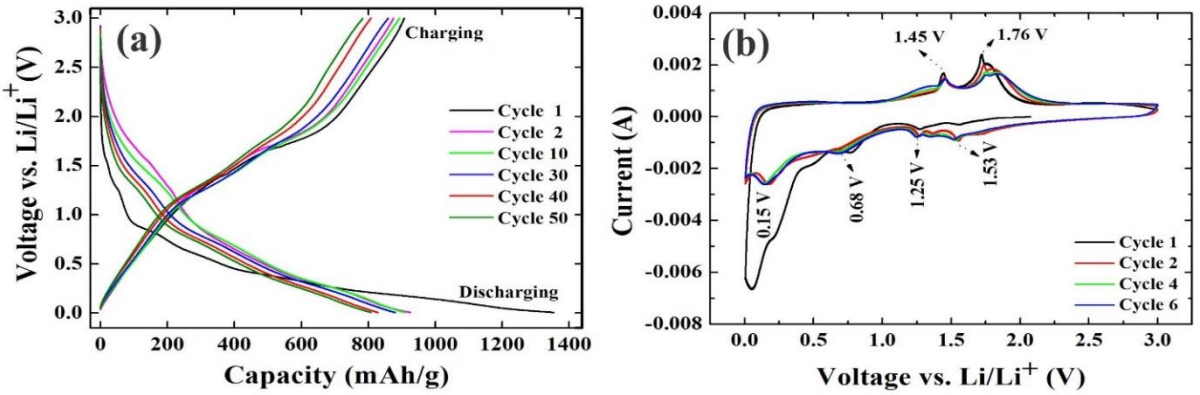

Figure 8.7. (a) GC at 60 mA/g and (b) CV results of FLG-$Co_2Mo_3O_8$.

The first cycle total discharging and charging capacities of FLG-$Co_2Mo_3O_8$ are 1355 and 907 mAh/g, respectively. These values are greater than the corresponding values pertaining to pure $Co_2Mo_3O_8$ as reported in our previous publication [5]. This is expected due to good interaction between two dimensional (2D)-$Co_2Mo_3O_8$ and FLG (as observed in Fig. 8.2 (d)) and presence of FLG which facilitates a conducting network for electrolyte to get adsorbed throughout the composite which in turn enhances Li-ion transportation in the composite. The capacity values at different current densities are given in Table 8.2. The net difference (~448 mAh/g) between first discharge and charge is considered as irreversible capacity loss (ICL)

that normally originates from SEI formation in which Li is irreversibly trapped at the anode owing to the formation of covalent compounds [5,6]. ICL values at current rates of 60, 90 and 180 mA/g are found to be 448, 402 and 330 mAh/g, respectively whilst Coulombic efficiencies (QEs) are more than 67% at all the considered current densities. FLG-$Co_2Mo_3O_8$ composite has shown excellent cycling behavior.

Table 8.2. Specific capacity (mAh/g) of FLG-$Co_2Mo_3O_8$, FLG-$Mn_2Mo_3O_8$and FLG–$Zn_2Mo_3O_8$ composites at different current densities and different discharging (D) and charging (C) cycles.

	Current Rate								
	60 (mA/g)			90 (mA/g)			180 (mA/g)		
Composite	1D	1C	QE%	1D	1C	QE%	1D	1C	QE%
FLG-$Co_2Mo_3O_8$	1355	907	67	1229	827	67	895	599	67
FLG-$Mn_2Mo_3O_8$	1361	937	69	1349	942	70	1368	905	66
FLG–$Zn_2Mo_3O_8$	845	448	53	787	403	51	738	351	48
	50D	50C	QE%	50D	50C	QE%	50D	50C	QE%
FLG–$Co_2Mo_3O_8$	808	785	97	762	733	97	622	607	98
FLG–$Mn_2Mo_3O_8$	505	495	98	523	512	98	530	518	98
FLG–$Zn_2Mo_3O_8$	639	630	98	554	545	98	590	579	98

D-Discharge cycle, C-Charge cycle, QE%-Coulombic efficiency

QEs fluctuated around 98% up to 50 cycles as shown in Fig. 8.8 while the capacity retentions at the end of the tests are found to be greater than 85%. CV characteristics of FLG-$Co_2Mo_3O_8$ during both cathodic and anodic scans are shown in Fig. 8.7(b) for the first six cycles. In the 1st cathodic scan two main reduction current peaks are observed, a small peak around 0.7 V and a broad peak between 0.5 to 0.005V with increasing current. From 2nd cycle onwards these peaks are centered at 0.68 and 0.15V with constant reduction currents which correspond to Li intercalation into both FLG and $Co_2Mo_3O_8$ which are active to take Li in this voltage

range [5]. The large current difference between 1st and 2nd scans and peak shift towards lower voltages are attributed to SEI formation as well as electrode formation effect [5-7]. Another two new reduction peaks at 1.25 and 1.53V (which were feebly visible during 1st cathodic scan) became prominent. Evolution of these peaks might be originated from MoO_2 formed during 1st cycle through crystal structure destruction of $Co_2Mo_3O_8$ during Li insertion (1st reduction) that eventually leads to formation of metal nanoparticles in amorphous Li_2O phase (during 1st discharge) and conversion of these metal nanoparticles to metal oxides (during 1st charging) according to Equ. 8.1 (after 1st discharge) [5].

$$Co_2Mo_3O_8 + 16\ Li^+ + 16\ e^- \rightarrow 2\ Co^\circ + 3\ Mo^\circ + 8\ Li_2O \qquad (8.1)$$

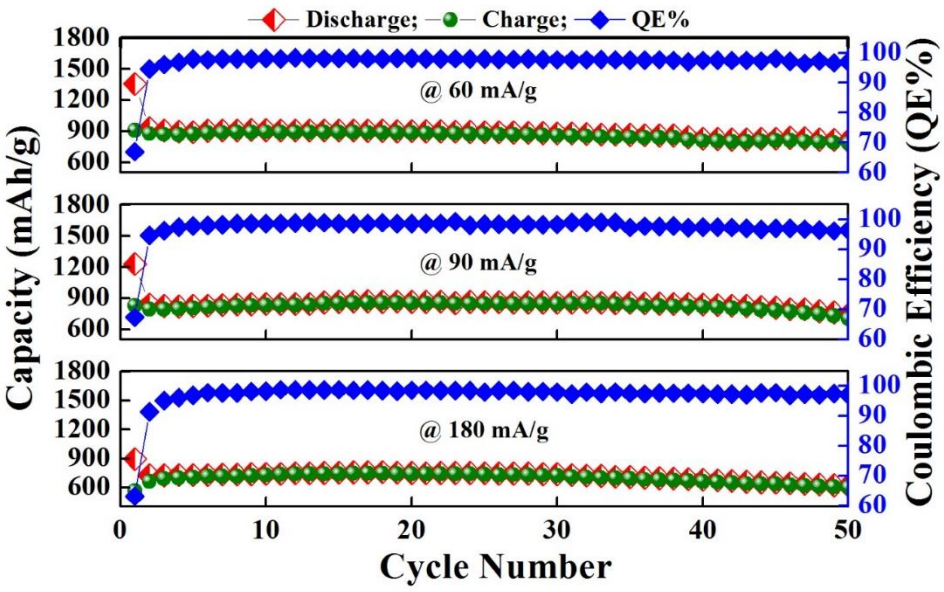

Figure 8.8. Cyclic performance of FLG-$Co_2Mo_3O_8$ at 60, 90 and 180 mA/g.

There are only two peaks observed at 1.45 and 1.76 V in the case of $Co_2Mo_3O_8$ during the first anodic scan wherein the current decreased up to 3rd scan and then became constant in later scans with a slight shift in the peak position towards higher potential. The redox couples at 1.53/1.76 and 1.25/1.45 V correspond to phase transition of MoO_2 due to partial lithiated Li_xMoO_2 phase from monoclinic phase to orthorhombic phase and from orthorhombic phase to monoclinic phase during Li insertion and extraction process, respectively [8,9]. The

constant area under these redox curves is in tune with stable cyclability whereas decrease in current of oxidation peaks indicates light capacity fading as observed in GC results while the overall CV features of FLG-$Co_2Mo_3O_8$ are consistent with GC results. GC profiles (at 60 mA/g) of FLG-$Mn_2Mo_3O_8$ are shown in Fig. 8.9(a). The 1st discharging curve is steep from OCV (~2.06V) to 1.0 V including a negligible slope change around 1.5V while the typical slope change corresponding to SEI formation is observed around 0.9V. The curve further declined with this gradient until a final change in slope is observed at 0.25V. Thereafter a long voltage plateau up to the cut-off voltage of 0.005V is observed. The 1st charging curve has major slope changes between 1.2 and 2.0V and beyond this voltage range the curve is steeper on either end sides of the charging. The slope changes observed during the 1st discharging and charging are in good agreement with CV current peaks (Fig. 8.9(b)). The 2nd and subsequent discharging and charging curves are found similar to the1st discharging and charging curves but a gradual decrease in capacity is observed. During the 1st cycle high reversible capacities in the range 905-942 mAh/g are observed with ICL values in the range 407-463 mAh/g which correspond to QEs in the range 66-70% which soon fluctuated between 97-98% resulting in capacity retentions of 53-57% as shown Table 8.2.

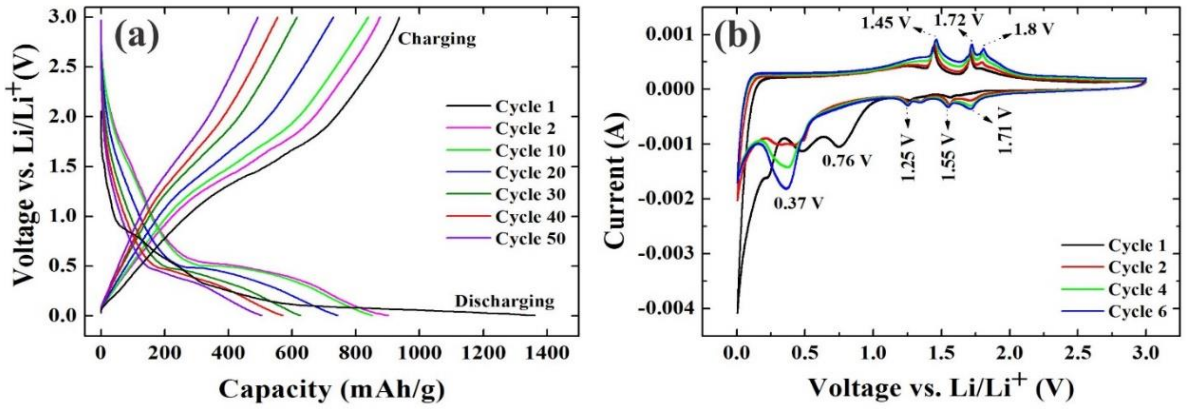

Figure 8.9. GC at (a) 60 mA/g and (b) CV results of FLG-$Mn_2Mo_3O_8$.

The gradual decay in capacity values are observed despite of high reversible capacities and QEs (Fig. 8.10). This is primarily linked to the formation of non-reducible Mn^{2+} ions which

act as an inert matrix. This is also found true from the corresponding CV results wherein there is no oxidation peak around 1.2 V which corresponds to Li release by forming MnO [3]. However the rapid capacity-fading associated with cycling of bare $Mn_2Mo_3O_8$ as reported in our previous publication [3] has now gradually decayed due to the presence of FLG. However FLG-$Mn_2Mo_3O_8$ demands further modification to achieve constant capacity throughout the cycling similar to the case of FLG-$Co_2Mo_3O_8$.

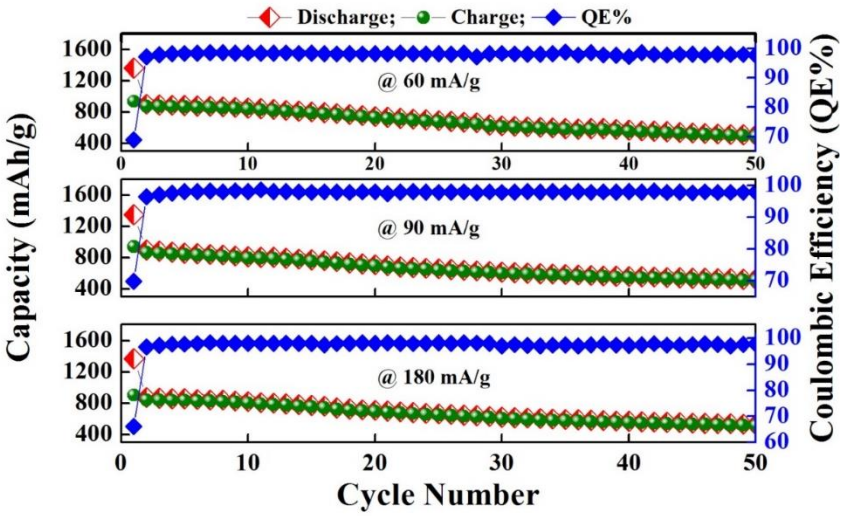

Figure 8.10. Cyclic performance of FLG-$Mn_2Mo_3O_8$ at 60, 90 and 180 mA/g.

The increased current features with cycling as-observed in CV results of FLG-$Mn_2Mo_3O_8$ are contradictory to the GC profiles in which continuous capacity decay is observed. This observation is a plausible outcome of very slow rate kinetics of lithiation due to a very low scanning rate of 58 μV/s (kinetic limitations) and this phenomenon might be very effective on FLG-$Mn_2Mo_3O_8$. However positions of various current peaks during both redox cycles do match well with galvanostatic profiles. During the 1st reduction scan there are two small peaks which correspond to Li insertion into $Mn_2Mo_3O_8$ and are found around 1.55 and 1.25 V. The intensity of these peaks increased from 2nd cycle onwards which might be due to increased interaction between Li and MoO_2 to form metallic Mo and Li_2O according to the Equs. 8.2 and 8.3 [3]. Further, major changes in 1st reduction curve are found at 0.76, 0.5 and

0.005 V. But these changes are not discernable from 2nd cycle onwards and could be ascribed to SEI formation. Among these, the peak nearby 0.005 V that might be related to Li intercalation into FLG appears to be very large which is consistent with large horizontal line-like feature of 1st discharging curve found in galvanostatic profile. From 2nd cathodic scan onwards there are two extra peaks with increasing intensity, one at 1.71 V which is small and the other at 0.37 V which is large and both these peaks correspond to $Mn_2Mo_3O_8$ [3]. In the 1st anodic scan there are three oxidation peaks of $Mn_2Mo_3O_8$ at 1.45, 1.72 and 1.8 V whose intensity also increased till the end of the CV test. The overall redox couples observed in between 1-2 V correspond to either Li intercalation into MoO_2 or conversion reactions between Li and MoO_2 [3]. These oxidation peaks are fitting well in the range 1.2-2.0V in which slope of the charging curves changed as observed in galvanostatic profile as reported earlier [3,10].

$$Mn_2Mo_3O_8 + 12\ Li^+ + 12e^- \rightarrow 2\ MnO + 3\ Mo^\circ + 6\ Li_2O \quad (8.2)$$

$$Mn_2Mo_3O_8 + 6x\ Li^+ + 6x\ e^- \rightarrow 2\ MnO + 3\ MoO_y + (3x)\ Li_2O\ (0<y<2.0;\ (x+y)=2.0) \quad (8.3)$$

The voltage versus capacity profiles of FLG-$Zn_2Mo_3O_8$ at the current rate of 60 mA/g are shown in Fig. 8.11(a). These profiles appeared similar to Co- and Mn-Mo clusters but with a trend of increasing capacity. During the 1st discharging (from OCV ~2.51V) the slope of the curves started to change below 1.5 V. However the change is clearly observed at 0.9 V corresponding to SEI formation. Further change in slope continued up to 0.25V beyond which the curve remained unchanged as voltage decreased to 0.005 V. The first charging curve is consistently steep up to 1.4 V then it is accompanied by three voltage plateaus at 1.5, 1.7 and 2.0 V and beyond which it is raised to 3.0V. The 2nd and subsequent discharging curves are slightly different from 1st discharging curves but their capacity values kept on increasing as cycling continued and changes in slope became more distinct as per the

reduction current peaks observed in CV results (Fig. 8.11(b)). The second and few subsequent charging curves are found similar to the first charging case but the capacity increased as number of cycles increased while the voltage plateaus are observed between 1.4-2.1 V in agreement with CV oxidation peaks which are absent and curves in this region are flat after 15th cycle. The observed reversible capacities are in the range 351-448 mAh/g have caused to bag initial QEs in the range 47-53%. The increase in capacity might be resulted from formation cycle effect [6] and a series of conversion and alloying reactions of $Zn_2Mo_3O_8$ according to Equs. 8.4-8.7 [8] those are not taking place during the first few cycles. As a consequence, an increase in capacity to more than 40% of the first charging capacity is observed at the end of the test as shown in Fig. 8.12 and Table 8.2.

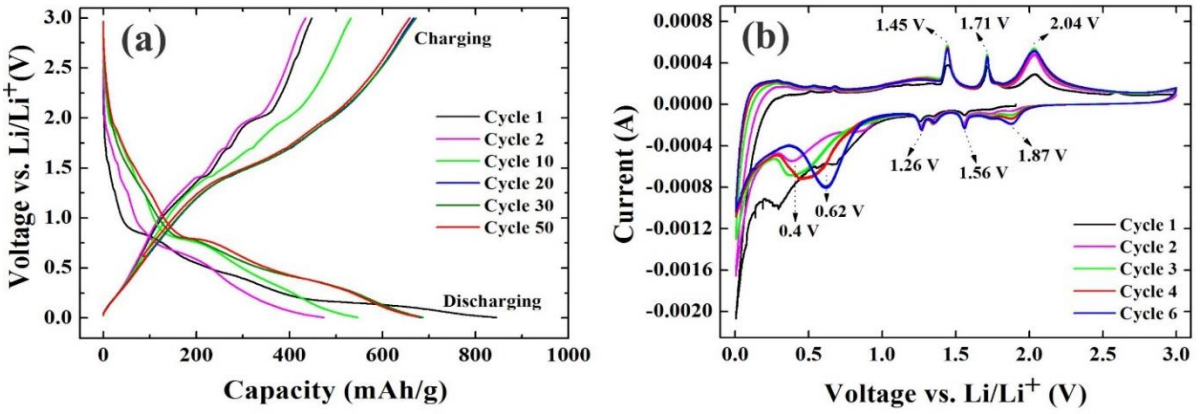

Figure 8.11. GC at (a) 60 mA/g and (b) CV results of FLG-$Zn_2Mo_3O_8$.

CV characteristics of FLG-$Zn_2Mo_3O_8$ up to 6thcycle are shown in Fig. 8.11(b). There are three small peaks observed at 1.55, 1.33 and 1.25 V during first cathodic scan followed by broad peaks with large current around 0.75, 0.25 and nearby 0.005 V. There is an extra small peak at 1.87 V from the second cycle onwards in addition to existing peaks between 1.55 and 1.25 V. But current of all these peaks increased consistently. Further, the peak at 0.25V seems to be shifted to 0.62 V through an intermediate peak at 0.4 V for which current also increased cycle to cycle whilst the peak current nearby 0.005V reduced. This might be related to Li intercalation into FLG. During first and subsequent cathodic scans three peaks with

increasing current are observed at 1.44, 1.71 and 2.04 V along with a small hump below 0.3 V which plausibly corresponds to Li deintercalation from FLG. Thus, consistent increase in current of various redox peaks of $Zn_2Mo_3O_8$ between 1.1 and 2.1 V including MoO_2 peaks indicated capacity increase as observed in galvanostatic profile.

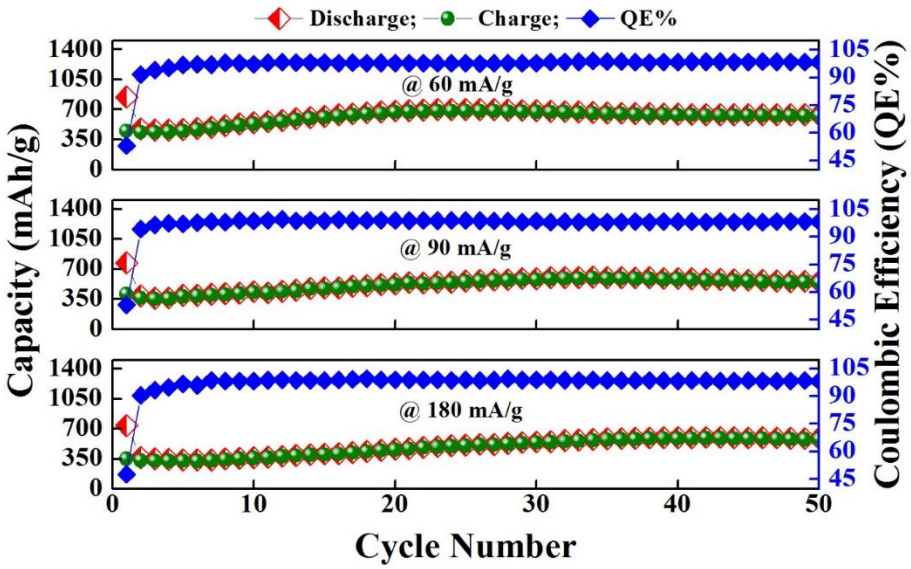

Figure 8.12. Cyclic performance of FLG-$Zn_2Mo_3O_8$ at 60, 90 and 180 mA/g.

$$Zn_2Mo_3O_8 + Li^+ + e^- \rightarrow Li(Zn_2Mo_3O_8) \quad (8.4)$$

$$Li(Zn_2Mo_3O_8) + 15\ Li^+ + 15\ e^- \rightarrow 2\ Zn + 3\ Mo^\circ + 8\ Li_2O \quad (8.5)$$

$$2\ Zn + 2\ Li^+ + 2\ e^- \leftrightarrow 2\ ZnLi \quad (8.6)$$

$$2\ Zn + 2\ Li_2O \leftrightarrow 2\ ZnO + 4\ Li^+ + 4\ e^- \quad (8.7)$$

EIS results of FLG-$Co_2Mo_3O_8$, FLG-$Mn_2Mo_3O_8$ and FLG-$Zn_2Mo_3O_8$ composites are plotted as Nyquist plots and their corresponding equivalent circuits are shown in Fig. 8.12. The impedance data of FLG-$Co_2Mo_3O_8$ and FLG-$Mn_2Mo_3O_8$ are best fitted to equivalent circuit I while the data of FLG-$Zn_2Mo_3O_8$ was fitted to the simple equivalent circuit II as shown in Fig. 8.12(d). The contact (solvent) resistance R_e [11] of all three compounds is found in between 2.3 and 6.8 Ω as shown in Table 8.3. The resistance to charge transfer R_{ct} [11] is found to be different for the three composites.

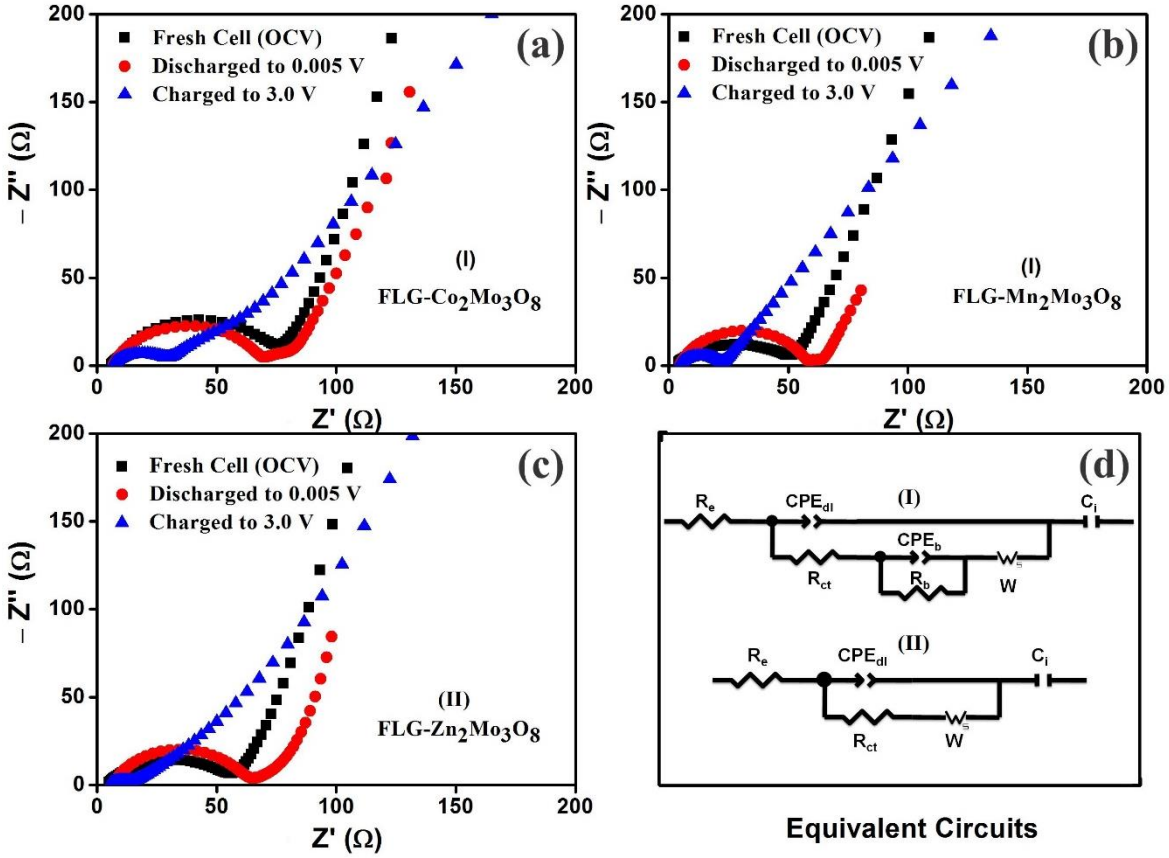

Figure 8.13. Nyquist plots of (a) FLG-$Co_2Mo_3O_8$, (b) FLG-$Mn_2Mo_3O_8$, (c) FLG-$Zn_2Mo_3O_8$ and (d) their equivalent circuits (for fitting).

The R_{ct} values of FLG-$Co_2Mo_3O_8$ are found to be lower than those of the other two composites. This is expected owing to presence of higher amount of FLG in FLG-$Co_2Mo_3O_8$ composite. Moreover, these values decreased under both charging and discharging in the case of FLG-$Co_2Mo_3O_8$ but in the case of the other two composites, a slight increase in R_{ct} value was followed by a substantial decrease in the value under discharging and charging states, respectively as shown in Table 8.3. The double layer capacitance CPE_{dl} [11] values of FLG-$Co_2Mo_3O_8$ and FLG-$Zn_2Mo_3O_8$ are found to first decrease when discharged and increase when charged whilst continuous decreasing trend is observed in the case of FLG-$Mn_2Mo_3O_8$. The circuit element R_b that represents bulk resistance [11] decreased in the case of FLG-$Co_2Mo_3O_8$ composite while it increased in the case of FLG-$Mn_2Mo_3O_8$ composite. Another circuit element CPE_b that represents double layer capacitance [11] increased in the case of

FLG-$Co_2Mo_3O_8$ composite while it first increased and then decreased in the case of FLG-$Mn_2Mo_3O_8$ composite. Intercalation capacity C_i [11] in all the three cases is found very small while Warburg element W_s (resistance to Li ion diffusion) is found relatively very high when compared to R_e and R_{ct}. The relatively very low R_{ct} value during charging signifies easy removal of Li ions that aided in bagging high reversible capacities. Very low value of C_i indicates that Li storage preferably takes place either by redox couples of Mo-clusters or electrochemical adsorption by FLG.

Table 8.3. EIS results of FLG-Mo-clusters at OCV, discharged and charged states.

Composite/Condition	R_e (Ω)	R_{ct} (Ω)	CPE_{dl} (μF)	R_b (Ω)	CPE_b(mF)	C_i (F)
FLG-$Co_2Mo_3O_8$ Fresh cell	5.9±0.09	9.9±0.2	18.9±0.4	58.5±0.03	0.19	0.009
FLG-$Co_2Mo_3O_8$ Discharged state	6.2±0.01	5.1±0.1	8.9±0.3	54.1±0.1	0.23	0.428
FLG-$Co_2Mo_3O_8$ Charged state	6.2±0.02	4.8±0.5	83±1.8	30.8±0.4	26	0.095
FLG-$Mn_2Mo_3O_8$ Fresh cell	2.3±0.14	51.3±0.8	174 ±1.5	4.2±2.1	0.7	0.037
FLG-$Mn_2Mo_3O_8$ Discharged state	4.7±0.01	53.3±0.2	45	6.2±0.5	53	0.512
FLG-$Mn_2Mo_3O_8$ Charged state	4.4±0.07	5.2±3.4	7.7	13.2±3.4	0.41	0.157
FLG-$Zn_2Mo_3O_8$ Fresh cell	4.2±0.02	54.8±0.5	111.7±6.3	--	--	0.024
FLG-$Zn_2Mo_3O_8$ Discharged state	6.8±0.03	53.6±0.7	44.7±1.5	--	--	0.788
FLG-$Zn_2Mo_3O_8$ Charged state	4.8±0.15	9.7±0.52	146±3.5	--	--	0.375

References

[1] Sun Y, Hu X, Luo W, Huang Y. Hierarchical self-assembly of $Mn_2Mo_3O_8$-graphene nanostructures and their enhanced lithium-storage properties. Journal of Materials Chemistry. 2011;21(43):17229-35.

[2] Petnikota S, Rotte NK, Reddy MV, Srikanth VVSS, Chowdari BVR. MgO-decorated few-layered graphene as an anode for Li-ion batteries. ACS Applied Materials & Interfaces. 2015;7(4):2301-9.

[3] Das B, Reddy MV, Krishnamoorthi C, Tripathy S, Mahendiran R, Rao GVS, et al. Carbothermal synthesis, spectral and magnetic characterization and Li-cyclability of the Mo-cluster compounds, $LiYMo_3O_8$ and $Mn_2Mo_3O_8$. Electrochimica Acta. 2009;54(12):3360-73.

[4] Das B, Reddy MV, Subba Rao GV, Chowdari BVR. Synthesis of Mo-cluster compound, $LiHoMo_3O_8$ by carbothermal reduction and its reactivity towards Li. Journal of Solid State Electrochemistry. 2008;12(7-8):953-9.

[5] Das B, Reddy MV, Tripathy S, Chowdari BVR. A disc-like Mo-metal cluster compound, $Co_2Mo_3O_8$, as a high capacity anode for lithium ion batteries. RSC Advances. 2014;4:33883-33889.

[6] Petnikota S, Rotte N, Srikanth VSS, Kota BR, Reddy MV, Loh K, et al. Electrochemical studies of few-layered graphene as an anode material for Li ion batteries. Journal of Solid State Electrochemistry. 2014;18:941.

[7] Reddy MV, Subba Rao GV, Chowdari BVR. Long-term cycling studies on 4V-cathode, lithium vanadium fluorophosphate. Journal of Power Sources. 2010;195:5768.

[8] DAS BK. Studies on metal oxides and cobalt nitride as prospective anodes for lithium ion batteries. PhD Thesis, National University of Singapore, 2010.

[9] Han P, Ma W, Pang S, Kong Q, Yao J, Bi C, et al. Graphene decorated with molybdenum dioxide nanoparticles for use in high energy lithium ion capacitors with an organic electrolyte. Journal of Materials Chemistry A. 2013;1(19):5949-54.

[10] Sun Y, Hu X, Luo W, Huang Y. Hierarchical self-assembly of $Mn_2Mo_3O_8$-graphene nanostructures and their enhanced lithium-storage properties. Journal of Materials Chemistry. 2011;21(43):17229-35.

[11] Reddy MV, Wei Wen BL, Loh KP, Chowdari BVR. Energy storage studies on $InVO_4$ as high performance anode material for Li-ion batteries. ACS Applied Materials & Interfaces. 2013;5:7777.

Chapter 9 MgO Decorated FLG

Morphology and crystallinity of MgO decorated few-layred graphene (FLG) is a part of another study [1]. However, for convenience a brief discussion is presented here. Morphological studies showed that nanosized MgO fragments decorated FLG at several locations. Figures 9.1(a) and (b) show the images of MgO (bright spots) decorated graphene sheets. Further, semi-transparent FLG cube-like features with varying sizes are also observed as shown in Figs. 9.1(c) and (d). Diffraction and Raman scattering analyses showed the presence of MgO and FLG in MgO decorated FLG.

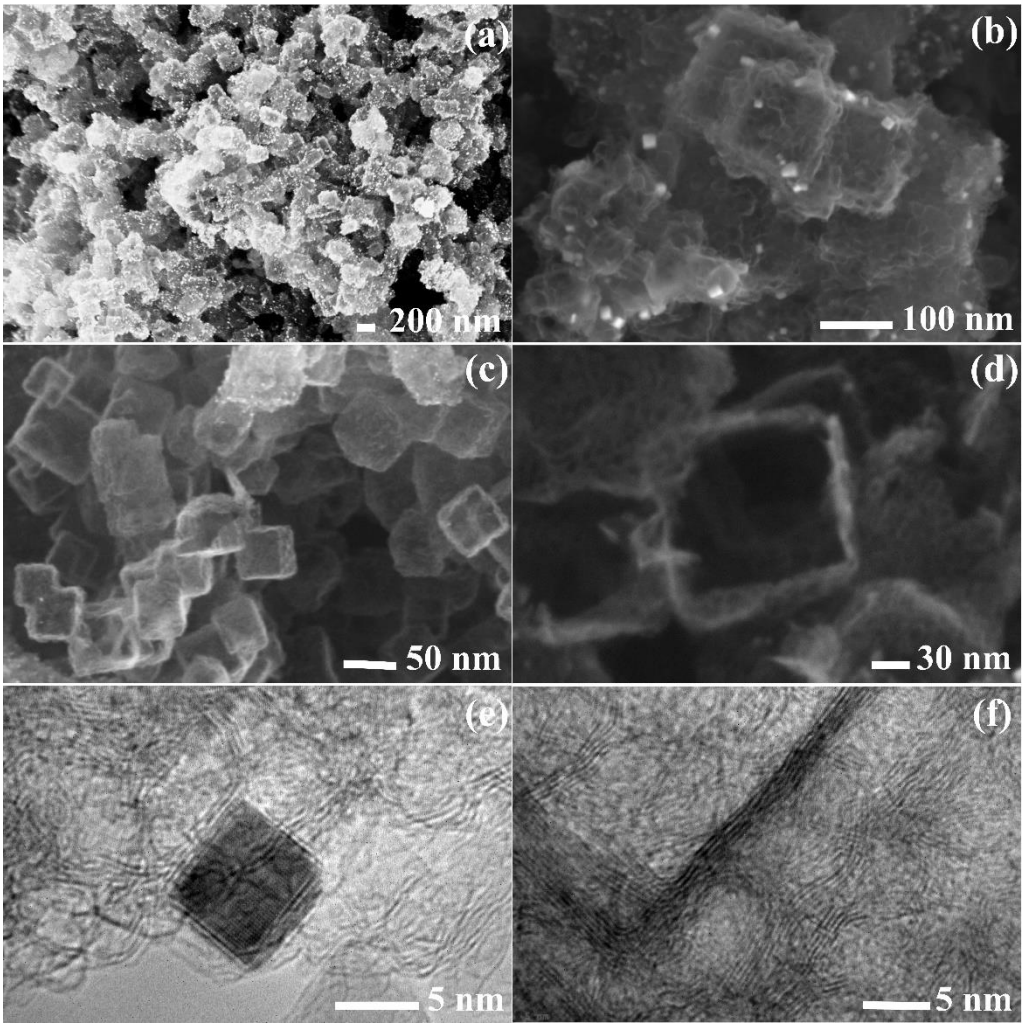

Figure 9.1. (a,b) FESEM images of the MgO decorated FLG, (c,d) transparent and semi-transparent FLG cube-like features. HRTEM images of MgO nanoparticle wrapped by (e) bi-layered graphene and (f) an edge of FLG cube.

Raman analysis showed that there are about 6 graphene layers in each FLG feature in agreement with TEM images of FLG shown in Figs. 9.1(e) and (f). In Fig. 9.1(e), TEM image shows that MgO nanocube is fully wrapped by bi-layer graphene sheets. This morphology explains the reason for the retention of MgO nanoparticles even after the acid treatment. Recent experimental and theoretical works showed that graphene is a perfect insulating membrane to various kinds of chemical species. It will not even allow H^+ ions to pass through its aromatic rings [3]. Thus graphene acts like protective coating to MgO and prevents its decomposition by acids like HCl. Before conducting the battery performance tests, elemental composition (Table 9.1) of the sample was obtained. It revealed that carbon and MgO are present in 70:30 wt.%. This composition is in close agreement with thermo gravimetric analysis (TGA) (Fig. 9.2) of the sample carried out in air in order to evaluate amount of MgO.

Table 9.1. Elemental composition of FLG/MgO obtained from energy dispersive x-ray analysis of K x-ray lines of the corresponding elements.

Element	Weight %	Atomic %
C	68.66	77.13
O	18.98	16.01
Mg	12.36	6.85

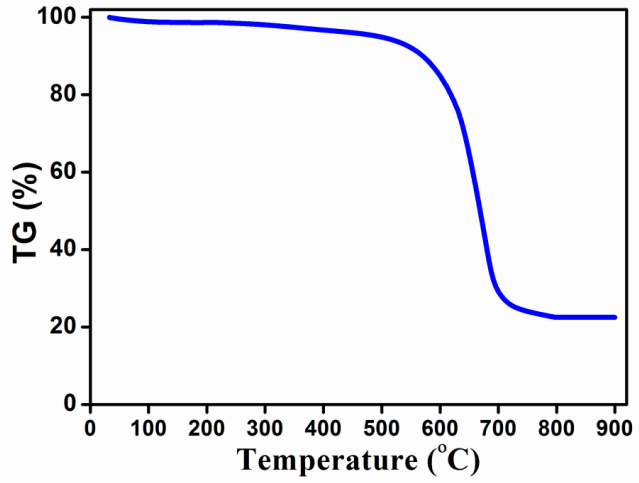

Figure 9.2. TGA curve of the MgO decorated FLG.

As shown in Fig. 9.2, the composite is found to be stable up to 550 °C whilst maximum decomposition is observed between 600 and 700 °C which corresponds to total weight loss of 77%. Beyond this temperature no more decomposition is observed and ~23 wt.% of residual MgO is measured. The high negative zeta potential value (-49.2 mV at pH = ~7, Fig. 9.3) measured for the sample indicates strong negative charge on the sample's surfaces. This value is slightly greater than the value of pure graphene materials and this might be resulted from presence of negatively charged MgO [4-6]. The high zeta potential value also implies that individual graphene sheets decorated with MgO will show good stability when dispersed in aqueous solutions [4-6]. This will facilitate easy fabrication of anodes. However for convenience these observations are again discussed in this work while comparing them with the observations after battery performance tests.

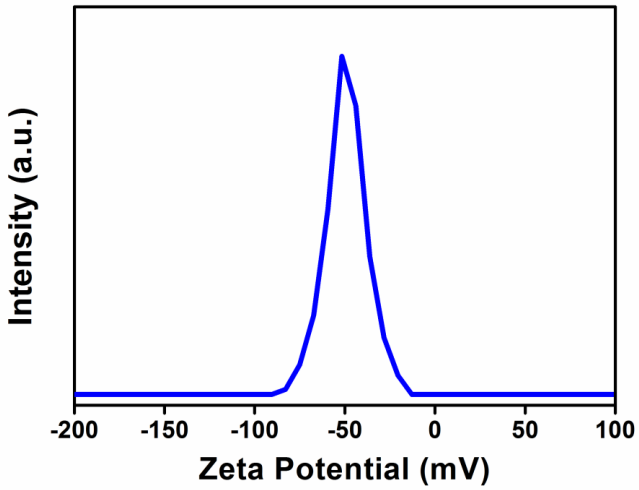

Figure 9.3. Zeta potential value of MgO decorated FLG.

MgO decorated FLG shows very stable and similar discharge-charge versus voltage profiles for current rates at 0.1, 0.5 and 1.0 C as shown in Figs. 9.4(a), (b) and (c), respectively. During first discharge, irrespective of current rate, the slope of the curve is consistent up to 1 V and from there it changed drastically to form a long plateau region around 0.9-0.7V that extended up to ~1350 mAh/g. Further, the discharge curves display continuous change in slope until voltage attained a final set value of 0.005 V. The first and next subsequent

charging curves are found to be similar except for a slight decrease in capacity followed by an increase with an increase in cycle number. All charge curves are observed to undergo a subtle variation in slope below 0.5 V and above 2.5 V whilst the remaining portion of the curves resembled a straight line. In contrast to the behavior during first discharge, long plateau region is not at all observed during second discharging whilst the slope of the curve (below 1.0 V region) continuously changed similar to the cases of various graphene materials [7-10] and carbon nanotubes [11-14] (Fig. 9.4(d)) and their composites [15]. The third and next successive discharging curves are similar to the second discharge curves and the change of capacity value is identical to that obtained using charging curves. The large plateau feature observed in the case of MgO decorated FLG is absent in the case of graphene obtained by various methods in which slope of first discharge curve changes continuously [7-10]. This type of characteristic long plateau feature is however observed in the case of various kinds of carbon nanotubes (CNTs) [11-14] and multi-walled carbon nanotubes (MWCNTs) that are also tested in this work at 0.25 C for comparison purpose and shown in Fig. 9.4(d). The initiation of the plateau region around 0.9 V could be ascribed to the formation of solid electrolyte interphase (SEI) which results from typical initial solvent decomposition where in Li irreversibly inserted as covalent compounds like Li_2O and Li_2CO_3 *etc.* [16]. This unusual large plateau around 0.9-0.7 V that extends up to very high capacity could be ascribed to high specific surface area and high porosity. Conversion of MgO to amorphous phase (by enhancing solvent decomposition on its active surfaces) could also contribute to the above mentioned large SEI as indicated by the XRD analysis (to be discussed). The mesopores with large pore volume (~0.9 cm^3/g) can intake more electrolyte solvent which eventually decomposes more electrolyte leading to large SEI similar to that observed in the case of carbon nanotubes [13].

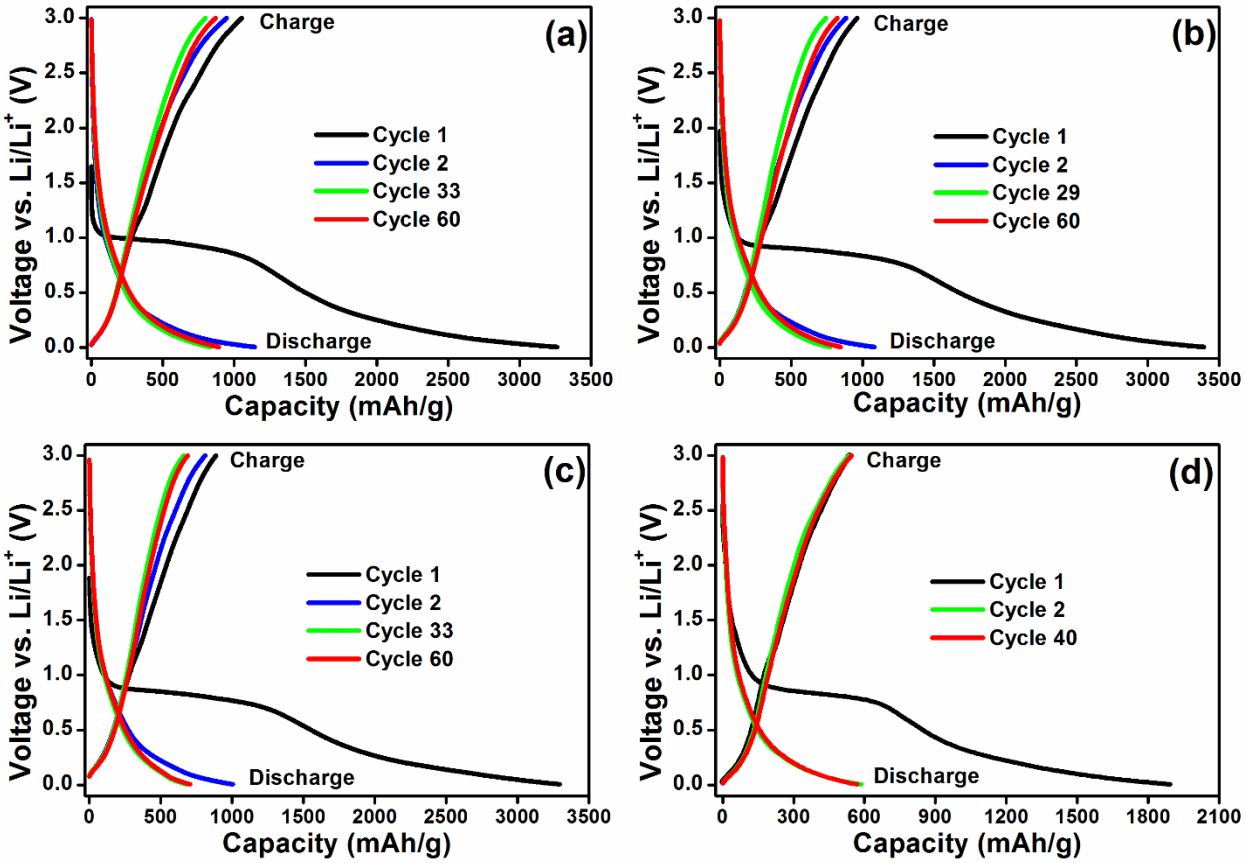

Figure 9.4. Charging-discharging characteristics of MgO decorated FLG at current densities (a) 0.1 C, (b) 0.5 C, and (c) 1.0 C. (d) Charging-discharging characteristics of MWCNTs at 0.25 C.

The specific surface area and porosity distribution which are connected to large SEI formation in the present study are probed with N_2 adsorption and desorption onto fresh MgO decorated FLG powder followed by BET formulation. A large hysteresis was observed between N_2 adsorption and desorption isotherm curves pertaining to the sample as shown in Fig. 9.5(a) and this type of behaviour illustrates material's high porosity. BET and Langmuir surface areas obtained for the sample are ~394±2.4 m^2/g and ~921±43 m^2/g, respectively. The average pore volume and pore diameter calculated are ~0.869 cm^3/g and ~8.82 nm, respectively. It may not be possible to distinguish the individual contributions of graphene and MgO to total surface area as both are capable of showing very high specific surface areas for example graphene can show very high experimental value to theoretical value of 2630

m^2/g [17] while MgO's experimental area reported in the range of 50-600 m^2/g [18-21]. But high negative zeta potential and battery testing results in this present study clearly indicate that MgO surfaces contain either highly catalytic nature or defects which might also lead to this high surface area in addition to the contribution from FLG. Interaction of Li (or electrolyte molecules) with MgO decorated FLG was also indicated by Raman scattering analysis (Fig. 9.5(b)). After cycling, the positions of typical Raman bands (D, G and 2D-bands) are found to be unaltered except for the intensity of G-band which decreased whilst 2D-band enormously broadened. These observations are indicative of the interaction of Li (or electrolyte molecules) with the active material. Starting material exhibited an intensity (I) ratio I_D/I_G of ~0.49 which increased to ~0.92 after 100 cycles of battery testing at 2 C. The increase in I_D/I_G ratio indicates the increase in defects or disorder [22] that might be owing to the continuous insertion and extraction of Li ions which eventually increases interplanar distance between individual graphene sheets. This complimented well with the inferences from diffraction studies on the material after battery testing.

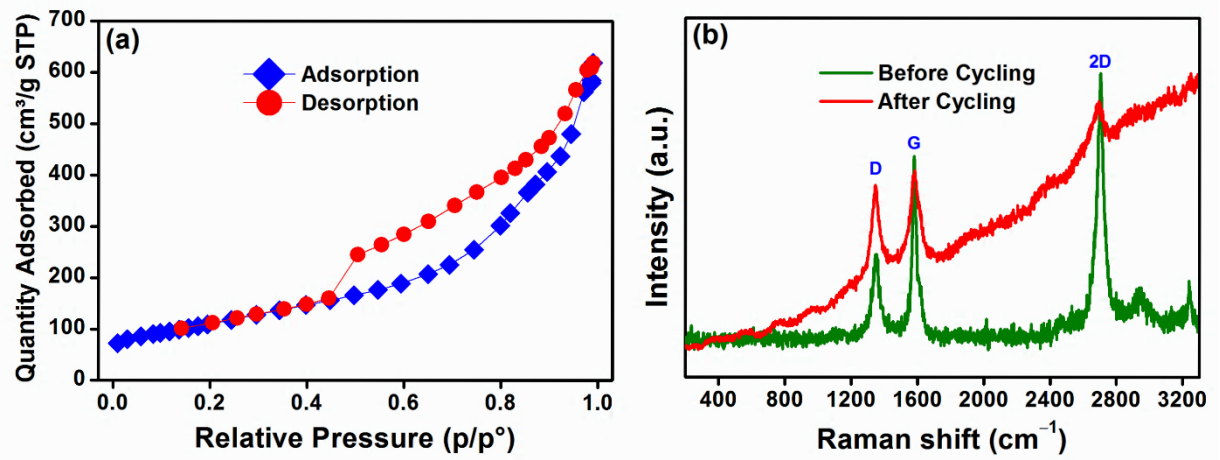

Figure 9.5. (a) N_2 adsorption and desorption isotherms of MgO decorated FLG; (b) Raman spectra of MgO decorated FLG before and after galvanostatic cycling.

The XRD pattern obtained from the sample after galvanostatic cycling test is totally different from the original pattern as shown in Fig. 9.6. The first discharged state pattern showed that most of the MgO crystalline phase converted to amorphous. This conversion might be

resulted from decomposition of electrolyte molecules which consumes oxygen of MgO to form covalent compounds like Li_2O and LiOH *etc.* which eventually builds up SEI [16]. The observed conversion might be aided by highly catalytic natured surface of MgO and its unique surface chemistry might also play key role in this conversion [19]. The observed crystal destruction of MgO might be due to loosely bounded edge sharing oxygen anions which could be diffused out from MgO by leaving Mg^{2+} ions dispersed in anode matrix. The observed large unusual SEI which is absent for various graphene materials referred in this study might not be possible without MgO's contribution. Now it is clarified that conversion of MgO to amorphous could also be ascribed to large SEI formation in addition to FLG's reducing nature. Moreover Mg^{2+} ions easily diffuses deep into anode matrix as their ionic radius equivalent to Li^+ ions and presence of well dispersed Mg^{2+} ions is proved to enhance electrochemical properties by improving electronic and ionic conductivity [23,24]. The graphitic (002) diffraction peak of fresh MgO decorated FLG is found at ~26° which became very broad and appeared like hump that centered around 23° after first discharge. Further shifting and broadening of graphitic peak towards 20° is observed with increase in cycle number as shown in Fig. 9.6. This broadening and shifting is an indication of increase in interplanar distance (d-spacing) of graphene sheets. The observed increase in d-spacing plausibly resulted from further exfoliation of graphene sheets due to continuous lithiation and de-lithiation (electrochemical exfoliation). This observation correlates well with the inferences from Raman scattering and TEM analyses. Inferences from the XRD and Raman data are further supported by inferences from electron microscopy results as shown in Fig. 9.7. After battery testing (Figs. 9.7(c) and (d)) MgO is not distinctly observed due to its conversion to a different phase during cycling. Increase in d-spacing in the case of graphene after cycling is also observed. Selected area electron diffraction (SAED) pattern of the sample after cycling clearly indicates the conversion of MgO into a different amorphous phase.

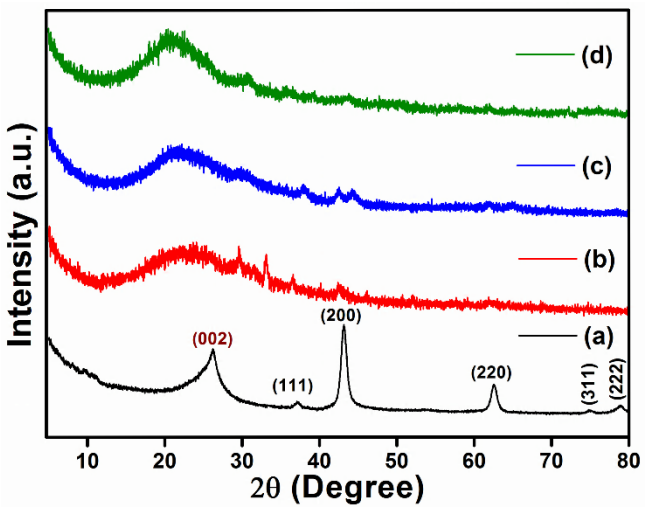

Figure 9.6. XRD pattern of MgO decorated FLG: (a) before galvanostatic cycling, (b) after 1st discharge to 0.005 V, (c) after 35th discharge to 0.005 V and (d) after rate performance.

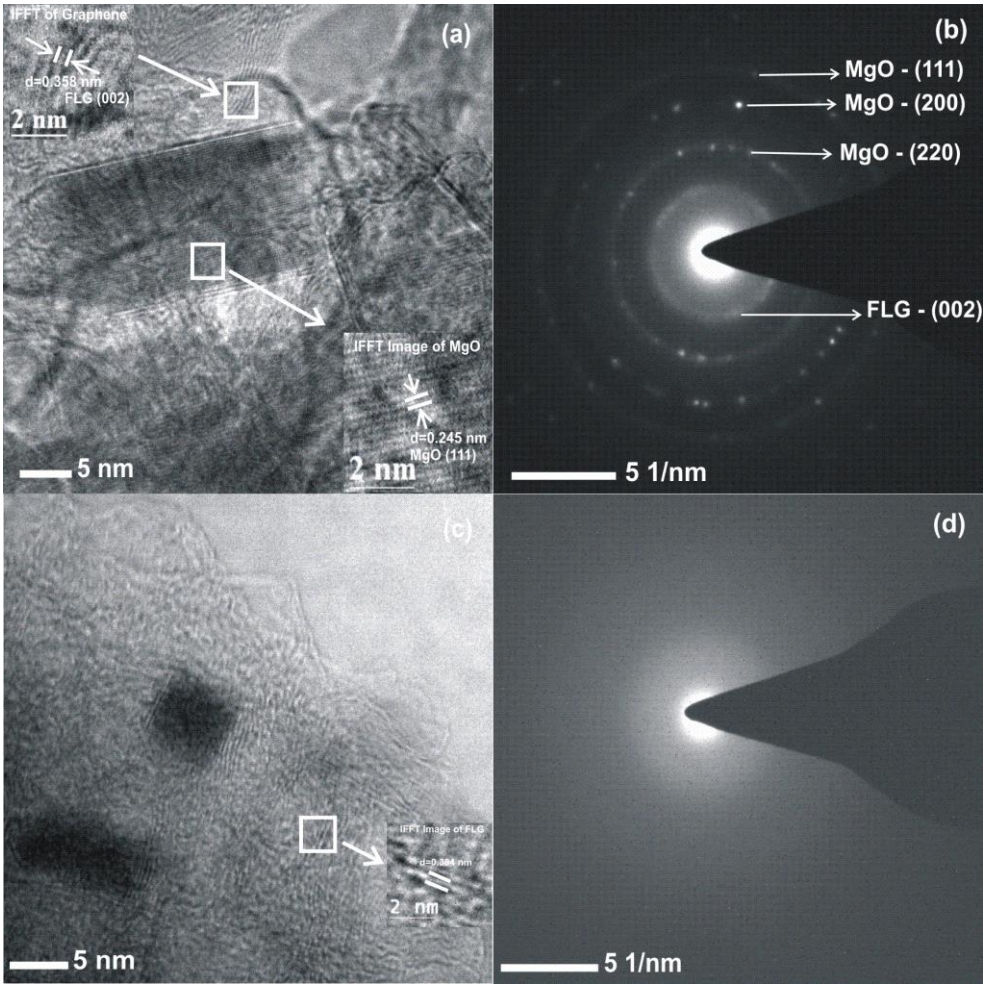

Figure 9.7. (a) HRTEM image of MgO decorated FLG with IFFT image in the inset and (b) SAED pattern of MgO decked Graphene before cycling; (c) HRTEM with IFFT image of FLG in the inset and (d) SAED pattern of FLG after cycling.

A very high first discharge capacity around 3295, 3391, 3261 mAh/g is observed for complete discharge to 0.005 V at 0.1, 0.5 and 1.0 C, respectively. The respective reversible capacities are found to be 1052, 962 and 887 mAh/g during first charge to 3.0 V. Even though Li reversibility is only 28-32% during first cycle, the corresponding capacity value is quite large compared to graphite's theoretical capacity (372 mAh/g). A net 70% capacity loss (about 2200-2300 mAh/g) between first discharge and charge is considered as irreversible capacity loss (ICL) that could plausibly resulted from large SEI like in carbon nanotubes [12] along with Li that covalently bonds with free dangling carbons at edges and defects of graphene layers [25,26]. Below 0.5 V, the continuous change in slope of second and subsequent discharging and charging curves indicates that there is feeble amount of Li (de)intercalation type mechanism contributing to total discharge and charge capacities while maximum Li storage is credited to electrochemical absorption and desorption complying with CV results (Fig. 9.8).

MgO decorated FLG as an anode material in LIBs has shown excellent cycling performance as shown in Figs. 9.8(a), (b), and (c). Respective details are furnished in Table 9.2. At low current rate of 0.1 C, reversible capacity around 1052 mAh/g that corresponds to first cycle is faded slowly to 797 mAh/g at 33rd charge cycle and finally increased to 869 mAh/g at the end of the test. The initial decrease in capacity can be attributed to long time solvent decomposition and an eventual desirable increase might be due to either proper percolation of electrolyte which enhances Li reversibility known as cycle formation effect [27] or increased interplanar distance between graphene sheets that can create extra active surface area available for additional Li storage [28]. Even Mg^{2+} ions dispersion in anode matrix which enhances electronic and ionic conductivity could also be contributed to capacity increase as inferred from XRD results. Coulombic efficiency (QE) is increased randomly in case of lower current rate but at higher current rates it increases constantly. Very low QE values in

between 26.92 and 32.26% during first cycle are increased to ≥ 82 % in second cycle and soon became > 95% after 16th cycle and finally reaching 97-98% from 35th cycle onwards in all the three cases as shown in Figs. 9.8(a), (b) and (c).

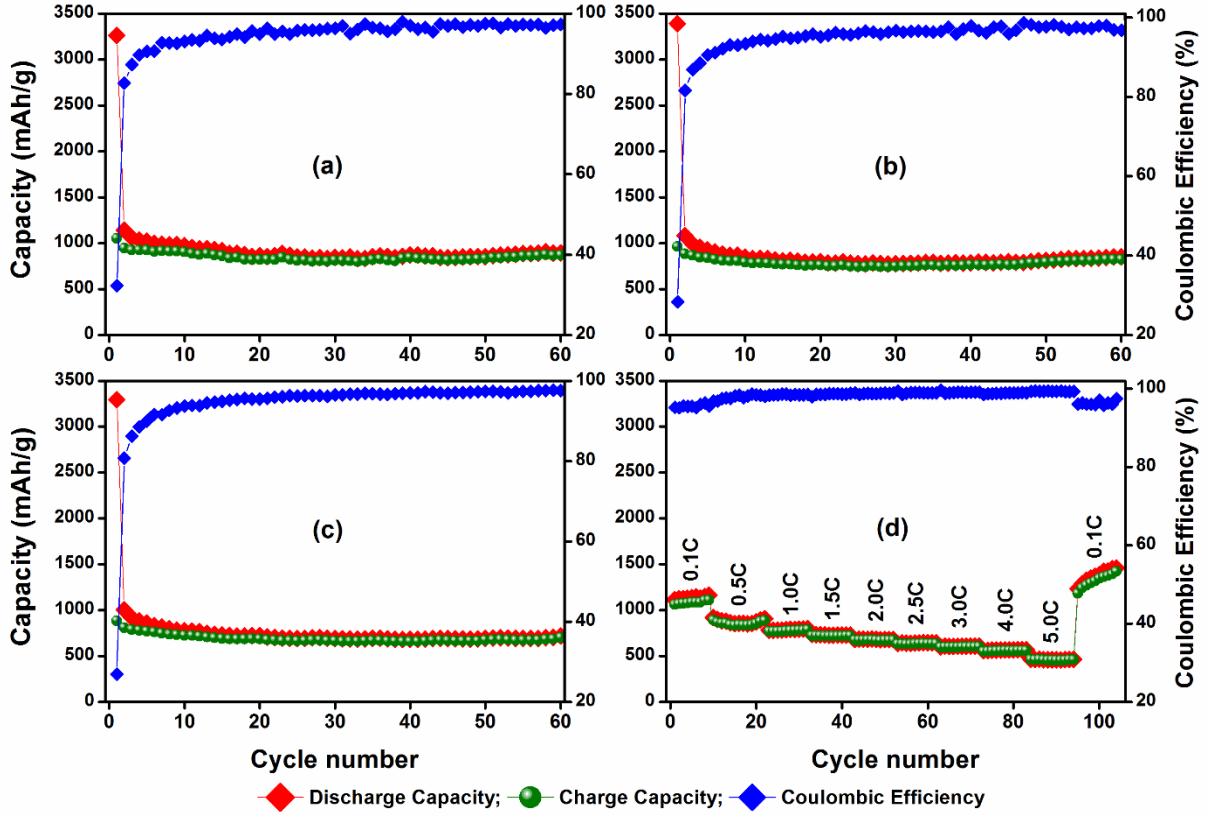

Figure 9.8. Cyclic performance at (a) 0.1 C, (b) 0.5 C, (c) 1.0 C and (d) rate capability of MgO decorated FLG.

Table 9.2. Cycling performance of MgO decorated FLG at various current densities.

Current Rate	1st DC^{I}	1st CC^{II}	1st QE%	60th DC	60th CC	60th QE%	60th CR^{III}
0.1 C	3295	1052	32.26	893	869	97.31	82.65
0.5 C	3391	962	28.36	850	823	96.85	85.60
1.0 C	3261	887	26.92	721	703	97.65	79.31

*^{I}Discharge Capacity (*mAh/g, ±5), *^{II}Charge Capacity (*mAh/g, ±5), *^{III}Capacity Retention %*

Rate performance test is carried out with battery cycled at 1.0 C current rate as shown in Fig. 9.8(d). In this rate capability test MgO decorated FLG proved to be an excellent anode material for high current applications as it has shown reversible capacity of more than 460 mAh/g even at very high current rate of 5.0 C (1860 mA/g) which is slightly greater than the theoretical capacity of graphite. A significant increase in capacity is observed after changing

current rate from high to low i.e., from 1.0 to 0.1 C and 5.0 to 0.1 C as shown in Fig. 9.8(d). To further confirm whether this capacity increase is sustained over long range cycling, the battery that was cycled at 0.5 C is tested at higher current rates starting from 5.0 to 1.0 C as shown in Fig. 9.9. In this case capacity increased by a significant amount to 1619 mAh/g even at 1.0 C at the end of the test. This increase might be a result of electrochemical exfoliation of graphene sheets (increased d-spacing as indicated by diffraction and Raman scattering analysis). This seems to be more at higher current rate and capable of bringing extra Li into active traverse between electrodes. Exfoliation of graphene sheets is proven to create additional room (increase in active specific surface area) for increased Li adsorption onto their surfaces [28]. This kind of increase in capacity due to volumetric changes caused by exfoliation of graphene sheets was observed in the case of carbon nanofibers [28] upon long term cycling but in the case of MgO decorated FLG it is observed at a much early stage of aging. Here the surfaces of MgO nanoparticles which are expected to possess highly catalytic nature are activated by defects like O^-, O_2^- *etc.* [18] are expected to avoid Li dendrite formation by decreasing the repulsive interactions between Li-Li ions like electron deficient dopants do in the case of modified graphene [29]. Thus MgO nanoparticles are also reasonably supporting sustainability of anode with enhanced capacity.

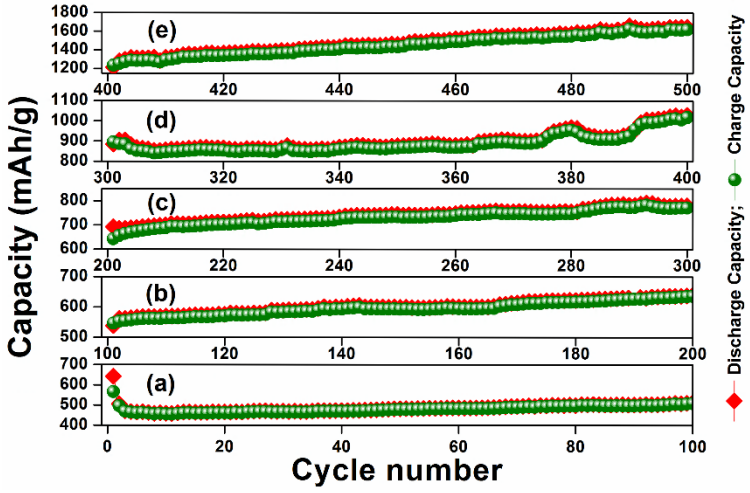

Figure 9.9. Long-term cycling of MgO decorated FLG at (a) 5.0 C, (b) 4.0 C, (c) 3.0 C, (d) 2.0 C and (e) 1.0 C.

Cyclic voltammetry results of MgO decorated FLG for first 6 cycles are shown in Fig. 9.10. During first cathodic scan there are two large reduction current peaks observed at 0.69 V which corresponds to SEI formation and at 0.005 V that related to co-intercalation of the solvated lithium ions into FLG [30]. Starting from the very first anodic scan no significant oxidation current peak is observed except a small hump around 0.1 V with feeble increase in current. From 2nd cathodic scan onwards there is only one reduction current peak is noticed nearby 0.005 V that related to Li insertion into FLG [31]. Absence of large reduction current peak around 0.69 V from 2nd cycle could be attributed to SEI formation on electrode surface which is in good agreement with large plateau region observed in galvanostatic cycling which in turn results in high ICL value. The constant redox current at all voltages between 0.5 and 3.0 V might be originated as a consequence of fast faradaic reactions taking place on the surface of graphene sheets i.e. redox currents of Li owing to electrochemical absorption and desorption onto graphene planes or defects in it (pseudocapacitance) [25,32]. From the 4th cycle onwards the decrease in redox current is negligible and curves are overlapped strongly with each other and this can explain stable capacity behaviour of MgO decorated FLG as seen in galvanostatic cycling results. Thus overall, absence of strong redox couple indicates that solid-state intercalation/diffusion of Li is not taking place [33].

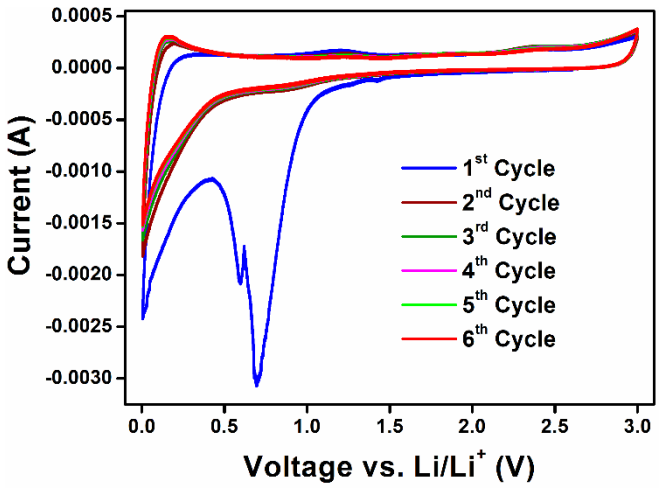

Figure 9.10. Cyclic voltammetry results of MgO decorated FLG.

Theoretical capacity of graphene varies based on the Li adsorption mechanisms which are adsorption on both sides [34] of graphene and double [35] layer formation between two successive graphene sheets which have a high reversible capacity of 744 mAh/g. In the case of MgO decorated FLG it is ~1100 mAh/g (at 0.1C) which is the case of triple [36] layer formation of Li ions in-between graphene sheets. Here Li storage at edges and defects will contribute the least to the capacity as the quality of FLG is very good. The reversible capacity increased to ~1600 mAh/g at 1C owing to electrochemical exfoliation of FLG. This capacity value suggests that there is a possibility of the formation of four Li ion layers, the feasibility of which is not yet reported. These unusual Li storage phenomena might take place due to the presence of Mg^{2+} ions which not only can enhance the electronic and ionic conductivity but also can influence the repulsion between Li−Li ions and thus most plausibly contribute to the stable aforesaid configurations. It is also worth noting that the Mg^{2+} ions are responsible for the prevention of Li electroplating or dendritic growth which typically leads to the capacity decay. However this is not the case in the present study. However, further robust theoretical studies are needed in order to pinpoint the exact Li storage configuration(s) and the corresponding voltage range.

Electrochemical Impedence Spectroscopy (EIS) was carried out to understand the kinetics of lithiation and de-lithiation, and resistance to charge transfer in MgO decorated FLG for first two cycles. The typical Nyquist plot in which semicircles and Warburg line are present is shown in Fig. 9.11 along with respective equivalent electrical circuits (values of circuit elements are shown in Table 9.3). The electrolyte (solution) resistance R_e is found to be ~1.5-3.5 Ω for various states of battery (SI4). The resistance to charge transfer R_{ct} is found to be ~48 Ω at OCV which increased to ~94 Ω after 1st discharge and once again decreased to ~59 Ω after 2nd discharge. But this value dramatically decreased to ~8 Ω and ~6 Ω after 1stand 2nd charges, respectively. This observed R_{ct} value is very low compared to the pristine and doped

graphene materials reported in the literature [37,38]. This change might be due to release of Mg^{2+} ions into anode matrix after first discharge which eventually improves ionic and electronic conductivity. The noticeable decrease in R_{ct} indicates that the faradaic reactions are occurring at a very fast rate and MgO decorated FLG is partially behaving like an ideal conducting type electrode (or the battery as non-polarizable cell). The value of R_{ct} during charge process is very low when compared with discharge and this observation indicates that Li is desorbing very easily than absorption into anode matrix. The low value of intercalation capacity C_i (<1 F) suggests that Li insertion-extraction by intercalation contributes less to the overall capacity which is matching with the observed CV characteristics. The Warburg resistance W_s (resistance to Li ion diffusion) is found relatively higher than R_e and R_{ct}. Thus overall low impedance values imply that MgO decorated FLG is a promising anode material.

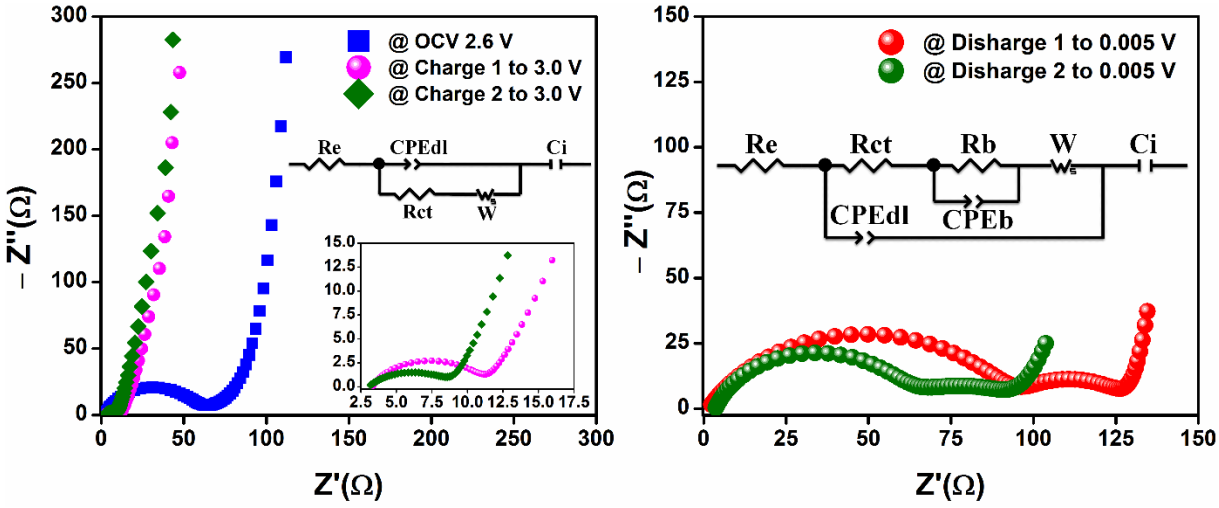

Figure 9.11. Nyquist plots of MgO decorated FLG (after fitting) and equivalent circuits of (a) fresh cell, (b) cell discharged to 0.005 V and (c) cell charged to 3.0 V.

Table 9.3. Values of equivalent circuit elements obtained by EIS.

Battery condition	R_e (Ω) (±0.1)	R_{ct} (Ω) (±0.5)	R_b (Ω) (±0.5)	CPE_{dl} (μF)	CPE_b (mF)
Fresh Cell (OCV)	3.0	48.7	--	25	--
1st Discharge to 0.005 V	1.5	94.1	31.8	36	11.5
1st Charge to 3.0 V	3.3	7.99	--	251	0.3
2nd Discharge to 0.005 V	3.5	59.6	30.38	47	13.2
2nd Charge to 3.0 V	3.0	6.04	--	524	--

MgO decorated FLG with a high specific surface area and high mesoporosity has been tested as an anode material in LIBs. MgO decorated FLG has shown a high reversible capacity and excellent constant cyclic performance despite of high ICL observed during the 1st discharge. The coulombic efficiency fluctuated around 98% with capacity retention of more than 80% even at 60th cycle. High ICL value was attributed to the electrolyte decomposition due to high specific surface area, porosity and phase conversion of MgO to amorphous. The electrochemical adsorption and desorption of Li onto graphene (pseudo capacitance) is understood from CV studies. The capacity increase over long-term cycling was mainly ascribed to electrochemical exfoliation of graphene layers that can create more room to accommodate extra Li. EIS studies confirmed easy lithiation kinetics in the fabricated LIBs and ideal conducting electrode nature of MgO decorated FLG. All in all, MgO decorated FLG was found to exhibit excellent anodic performance and could prevent initial losses upon modification (such as pre-lithiation) in order to make it commercially viable.

References

[1] Rotte NK, Yerramala S, Boniface J, Srikanth VVSS. Equilibrium and kinetics of Safranin O dye adsorption on MgO decked multi-layered graphene. Chemical Engineering Journal. 2014;258:412-9.

[2] Das A, Chakraborty B, Sood AK. Raman spectroscopy of graphene on different substrates and influence of defects. Bulletin of Materials Science. 2008;31:579-84.

[3] Berry V. Impermeability of graphene and its applications. Carbon. 2013;62:1-10.

[4] Li D, Muller MB, Gilje S, Kaner RB, Wallace GG. Processable aqueous dispersions of graphene nanosheets. Nature Nanotechnology. 2008;3:101-5.

[5] Lotya M, Hernandez Y, King PJ, Smith RJ, Nicolosi V, Karlsson LS, et al. Liquid phase production of graphene by exfoliation of graphite in surfactant/water solutions. Journal of the American Chemical Society. 2009;131:3611-20.

[6] Si Y, Samulski ET. Synthesis of water soluble graphene. Nano Letters. 2008;8:1679-82.

[7] Kumar A, Reddy ALM, Mukherjee A, Dubey M, Zhan X, Singh N, et al. Direct synthesis of lithium-intercalated graphene for electrochemical energy storage application. ACS Nano. 2011;5:4345-9.

[8] Yoo E, Kim J, Hosono E, Zhou H-s, Kudo T, Honma I. Large reversible li storage of graphene nanosheet families for use in rechargeable lithium ion batteries. Nano Letters. 2008;8:2277-82.

[9] Bhardwaj T, Antic A, Pavan B, Barone V, Fahlman BD. Enhanced electrochemical lithium storage by graphene nanoribbons. Journal of the American Chemical Society. 2010;132:12556-8.

[10] Lian P, Zhu X, Liang S, Li Z, Yang W, Wang H. Large reversible capacity of high quality graphene sheets as an anode material for lithium-ion batteries. Electrochimica Acta. 2010;55:3909-14.

[11] Landi BJ, Ganter MJ, Schauerman CM, Cress CD, Raffaelle RP. Lithium ion capacity of single wall carbon nanotube paper electrodes. The Journal of Physical Chemistry C. 2008;112:7509-15.

[12] Landi BJ, Ganter MJ, Cress CD, DiLeo RA, Raffaelle RP. Carbon nanotubes for lithium ion batteries. Energy & Environmental Science. 2009;2:638-54.

[13] Kawasaki S, Iwai Y, Hirose M. Electrochemical lithium ion storage properties of single-walled carbon nanotubes containing organic molecules. Carbon. 2009;47:1081-6.

[14] Landi BJ, Dileo RA, Schauerman CM, Cress CD, Ganter MJ, Raffaelle RP. Multi-walled carbon nanotube paper anodes for lithium ion batteries. Journal of Nanoscience and Nanotechnology. 2009;9:3406-10.

[15] Vinayan BP, Nagar R, Raman V, Rajalakshmi N, Dhathathreyan KS, Ramaprabhu S. Synthesis of graphene-multiwalled carbon nanotubes hybrid nanostructure by strengthened electrostatic interaction and its lithium ion battery application. Journal of Materials Chemistry. 2012;22:9949-56.

[16] Aurbach D. Review of selected electrode–solution interactions which determine the performance of Li and Li ion batteries. Journal of Power Sources. 2000;89:206-18.

[17] Zhu Y, Murali S, Cai W, Li X, Suk JW, Potts JR, et al. Graphene and graphene oxide: Synthesis, properties, and applications. Advanced Materials. 2010;22:3906-24.

[18] Sterrer M, Diwald O, Knözinger E. Vacancies and electron deficient surface anions on the surface of MgO nanoparticles. The Journal of Physical Chemistry B. 2000;104:3601-7.

[19] Stark JV, Park DG, Lagadic I, Klabunde KJ. Nanoscale metal oxide particles/clusters as chemical reagents. Unique surface chemistry on magnesium oxide as shown by enhanced adsorption of acid gases (sulfur dioxide and carbon dioxide) and pressure dependence. Chemistry of Materials. 1996;8:1904-12.

[20] Stoimenov PK, Klinger RL, Marchin GL, Klabunde KJ. Metal oxide nanoparticles as bactericidal agents. Langmuir. 2002;18:6679-86.

[21] Bakardjieva S, Šubrt J, Štengl V, Opluštil F, Olšanska M. Magnesium oxide nanoparticles as destructive sorbent for toxic agents. Microscopy and Microanalysis. 2004;10:476-7.

[22] Ferrari AC, Basko DM. Raman spectroscopy as a versatile tool for studying the properties of graphene. Nature Nanotechnology. 2013;8:235-46.

[23] Wang B, Xu B, Liu T, Liu P, Guo C, Wang S, et al. Mesoporous carbon-coated $LiFePO_4$ nanocrystals co-modified with graphene and Mg^{2+} doping as superior cathode materials for lithium ion batteries. Nanoscale. 2014;6:986-95.

[24] Yang Z, Xia J, Zhi L, Zhang W, Pei B. An improved solid-state reaction route to Mg^{2+}-Doped $LiFePO_4$/C cathode material for Li-ion battery. Ionics. 2014;20:169-74.

[25] Zhamu A, Chen G, Liu C, Neff D, Fang Q, Yu Z, et al. Reviving rechargeable lithium metal batteries: Enabling next-generation high-energy and high-power cells. Energy & Environmental Science. 2012;5:5701-7.

[26] Sato K, Noguchi M, Demachi A, Oki N, Endo M. A Mechanism of lithium storage in disordered carbons. Science. 1994;264:556-8.

[27] Petnikota S, Rotte N, Srikanth VSS, Kota BR, Reddy MV, Loh K, et al. Electrochemical studies of few-layered graphene as an anode material for Li Ion Batteries. Journal of Solid State Electrochemistry. 2014;18:941-9.

[28] Wu Y, Reddy MV, Chowdari BVR, Ramakrishna S. Long-term cycling studies on electrospun carbon nanofibers as anode material for lithium ion batteries. ACS Applied Materials & Interfaces. 2013;5:12175-84.

[29] Liu Y, Artyukhov VI, Liu M, Harutyunyan AR, Yakobson BI. Feasibility of lithium storage on graphene and its derivatives. The Journal of Physical Chemistry Letters. 2013;4:1737-42.

[30] Yin S, Zhang Y, Kong J, Zou C, Li CM, Lu X, et al. Assembly of graphene sheets into hierarchical structures for high-performance energy storage. ACS Nano. 2011;5:3831-8.

[31] Zhou W, Upreti S, Whittingham MS. High performance Si/MgO/Graphite composite as the anode for lithium-ion batteries. Electrochemistry Communications. 2011;13:1102-4.

[32] Simon P, Gogotsi Y. Materials for electrochemical capacitors. Nature Materials. 2008;7:845-54.

[33] Nazri GA, Pistoia G. Lithium Batteries: Science and Technology: Springer; 2009.

[34] Lee E, Persson KA. Li absorption and intercalation in single layer graphene and few layer graphene by first principles. Nano Letters. 2012;12:4624-8.

[35] Suzuki T, Hasegawa T, Mukai SR, Tamon H. A theoretical study on storage states of Li ions in carbon anodes of Li ion batteries using molecular orbital calculations. Carbon. 2003;41:1933-9.

[36] Chan Y, Hill J. Lithium ion storage between graphenes. Nanoscale Research Letters. 2011;6:203.

[37] Zhao X, Hayner CM, Kung MC, Kung HH. Flexible holey graphene paper electrodes with enhanced rate capability for energy storage applications. ACS Nano. 2011;5:8739-49.

[38] Wu Z-S, Ren W, Xu L, Li F, Cheng H-M. Doped graphene sheets as anode materials with superhigh rate and large capacity for lithium ion batteries. ACS Nano. 2011;5:5463-71.

Chapter 10 Conclusions and Future Scope

10.1 Conclusions

For the first time graphenothermal reduction (GTR) method was demonstrated to synthesize EG/FeO, EG/Fe_3O_4, EG/MnO, EG/MoO_2, FLG/$Co_2Mo_3O_8$, FLG/$Mn_2Mo_3O_8$ and FLG/$Zn_2Mo_3O_8$ composites. On the other hand, a rutile combustion synthesis method was used to obtain MgO decorated few-layered graphene. EG/MO composites and MgO decorated few-layered graphene were then characterized by variety of techniques to understand their structure, morphology, chemical nature, surface characteristics etc. EG/MO composites and MgO decorated few-layered graphene were characterized by cyclic voltammetry, galvanostatic cycling and electrochemical impedance spectroscopy to undertheir electrochemical behaviour. Finally, the as-synthesized composites where tested as anode materials in Li ion batteries by fabricating coin cells. All the materials considered in this thesis work exhibited excellent specific capacities and in general, were found to be suitable as anode materials in Li ion batteries. The rate capabilities of the composites and the current rates at which the testing was carried out are tabulated in Table 10.1.

Table 10.1 Rate capability of EG/MO and MgO decorated FLG composites.

Composite	Rate Capability (mAh/g)	Current Rate (mA/g)
EG/FeO	858-674	50-400
EG/MnO	936-735	75-600
EG/MoO_2	919-436	100-1000
FLG/$Co_2Mo_3O_8$	907-607	60-180
FLG/$Mn_2Mo_3O_8$	942-905	60-180
FLG/$Zn_2Mo_3O_8$	630-579	60-180
MgO decorated FLG	1058-1622	37-1860

10.2 Future Scope

The study on GTR method needs to be advanced in order to figure out the predominant reduction mechanism because it facilitates controlling the end products. Modification of GTR method for controlling size and crystallinity of metal/metal oxide phase in the final product is another aspect that needs to be taken up. Adopting GTR method to synthesize cathode materials for Li ion batteries is also an attractive future scope. As discussed in this thesis, MgO decorated FLG has shown excellent cyclic performance as an anode of Li-ion battery with reversible capacity twice that of graphite despite a huge irreversible capacity loss during the first cycle. Exploring suitable modifications such functionalization and/or pre-lithiation so as to make it an alternative to graphite can be pursued. It will also be interesting to introduce modifications by conducting robust theoretical calculations and in-situ cycling and ex-situ post cycling studies in order to identify the lithiation mechanism by MgO decorated FLG. Similar work can also be pursued on FLG-$A_2Mo_3O_8$ composites. The composites studied in this thesis work are also promising for electrochemical energy storage through Na-ion and Li-air batteries and supercapacitors. The possibilities of MgO decorated FLG for storing Na-ions [1-3] and for electrochemical or electric double layer capacitors or supercapacitors [4,5] will be especially interesting. MgO decorated FLG may also be a promising negative electrode material for Li-air batteries similar to the pristine graphene [6]. EG/FeO and EG/Fe_3O_4 composites for i) supercapacitors and Na-ion batteries, ii) magnetic, hyperthermia and EMI shielding applications and iii) for removal of heavy metals and other toxic species from polluted water are yet to be reported [7-16]. EG/MnO and EG/MoO_2 composites synthesized by GTR method can be used in supercapacitors similar to the reports available on graphene-MnO and graphene-MoO_2 composites synthesized by other methods [18]. The above mentioned scope is for the immediate future exploration. This accomplishes the completeness to this present thesis work.

References

[1] Raccichini R, Varzi A, Passerini S, Scrosati B. The role of graphene for electrochemical energy storage. Nature Materials. 2015;14(3):271-9.

[2] Wang Y-X, Chou S-L, Liu H-K, Dou S-X. Reduced graphene oxide with superior cycling stability and rate capability for sodium storage. Carbon. 2013;57:202-8.

[3] Yabuuchi N, Kubota K, Dahbi M, Komaba S. Research development on sodium-ion batteries. Chemical Reviews. 2014;114(23):11636-82.

[4] Zhu Y, Murali S, Stoller MD, Ganesh KJ, Cai W, Ferreira PJ, et al. Carbon-based supercapacitors produced by activation of graphene. Science. 2011;332(6037):1537-41.

[5] El-Kady MF, Strong V, Dubin S, Kaner RB. Laser scribing of high-performance and flexible graphene-based electrochemical capacitors. Science. 2012;335(6074):1326-30.

[6] Xiao J, Mei D, Li X, Xu W, Wang D, Graff GL, et al. Hierarchically Porous Graphene as a Lithium–Air Battery Electrode. Nano Letters. 2011;11(11):5071-8.

[7] Ai L, Zhang C, Chen Z. Removal of methylene blue from aqueous solution by a solvothermal-synthesized graphene/magnetite composite. Journal of Hazardous Materials. 2011;192(3):1515-24.

[8] Bai L-Z, Zhao D-L, Xu Y, Zhang J-M, Gao Y-L, Zhao L-Y, et al. Inductive heating property of graphene oxide-Fe_3O_4 nanoparticles hybrid in an AC magnetic field for localized hyperthermia. Materials Letters. 2012;68:399-401.

[9] Geng Z, Lin Y, Yu X, Shen Q, Ma L, Li Z, et al. Highly efficient dye adsorption and removal: a functional hybrid of reduced graphene oxide-Fe_3O_4 nanoparticles as an easily regenerative adsorbent. Journal of Materials Chemistry. 2012;22(8):3527-35.

[10] He H, Gao C. Supraparamagnetic, conductive, and processable multifunctional graphene nanosheets coated with high-density Fe_3O_4 nanoparticles. ACS Applied Materials & Interfaces. 2010;2(11):3201-10.

[11] Karthikeyan K, Kalpana D, Amaresh S, Lee YS. Microwave synthesis of graphene/magnetite composite electrode material for symmetric supercapacitor with superior rate performance. RSC Advances. 2012;2(32):12322-8.

[12] Kumar PR, Jung YH, Bharathi KK, Lim CH, Kim DK. High capacity and low cost spinel Fe_3O_4 for the Na-ion battery negative electrode materials. Electrochimica Acta. 2014;146(0):503-10.

[13] Mishra M, Singh AP, Singh BP, Singh VN, Dhawan SK. Conducting ferrofluid: a high-performance microwave shielding material. Journal of Materials Chemistry A. 2014;2(32):13159-68.

[14] Singh K, Ohlan A, Pham VH, R B, Varshney S, Jang J, et al. Nanostructured graphene/Fe_3O_4 incorporated polyaniline as a high performance shield against electromagnetic pollution. Nanoscale. 2013;5(6):2411-20.

[15] Sun H, Cao L, Lu L. Magnetite/reduced graphene oxide nanocomposites: One step solvothermal synthesis and use as a novel platform for removal of dye pollutants. Nano Research. 2011;4(6):550-62.

[16] Wang T, Liu Z, Lu M, Wen B, Ouyang Q, Chen Y, et al. Graphene–Fe_3O_4 nanohybrids: Synthesis and excellent electromagnetic absorption properties. Journal of Applied Physics. 2013;113:024314

[17] Kim H-S, Cook JB, Tolbert SH, Dunn B. The development of pseudocapacitive properties in nanosized-MoO_2. Journal of the Electrochemical Society. 2015;162(5):A5083-A90.

[18] Han P, Ma W, Pang S, Kong Q, Yao J, Bi C, et al. Graphene decorated with molybdenum dioxide nanoparticles for use in high energy lithium ion capacitors with an organic electrolyte. Journal of Materials Chemistry A. 2013;1(19):5949-54.

Annexures

Annexure 1

Iron oxides are considered promising candidates for lithium storage. Moreover these are more abundant, inexpensive and non-hazardous in nature. Among the iron oxides (FeO, Fe_2O_3 and Fe_3O_4) FeO as an anode material possess light weight, least volume changes upon lithiation and improved electronic conductivity which are crucial for achieving high capacity and cycling stability [1-5]. FeO has possess theoretical capacity of 744 mAh g^{-1} close to MO (M= Ni, Cu, Co, Mn) [6-9] which is slightly less than the theoretical capacities of Fe_3O_4 (928 mAh g^{-1}) and Fe_2O_3 (1007 mAh g^{-1}) [10]. For the reason FeO being a simple oxide it may not results in excessive amount of Li_2O formation and aggregation of metallic Fe which partly becomes irreversible and causes capacity decay compared with Fe_3O_4 and Fe_2O_3[10]. These favorable properties of FeO encourage using it as an anode of LIBs. Not many reports on FeO as anode material because of issues related to its synthesis and structural stabilization [10-12]. Early work on FeO as an anode in LIBs was reported by Poizot *et al.*[7], they have shown continuous decay in capacity upon cycling and obtained a capacity 200 mAh g^{-1} at the end of 50^{th} cycle [7]. In year, 2011 Reddy *et al*. [13] attempted to prepare pure FeO using carbothermal method using Fe_2O_3 and calculated amount of carbon, mixed and heated at 750 °C in Argon gas. They reported reversible capacity of 680 mAh g^{-1} and 78 % capacity retention from 2 to 118 cycles [13].

[1] M.M. Thackeray, W.I.F. David, J.B. Goodenough, Materials Research Bulletin, 17 (1982) 785-793.
[2] D.S. Tannhauser, Journal of Physics and Chemistry of Solids, 23 (1962) 25-34.
[3] A. Ponrouch, P.-L. Taberna, P. Simon, M.R. PalacÃn, Electrochimica Acta, 61 (2012) 13-18.
[4] B. Tian, J. Åšwiatowska, V. Maurice, S. Zanna, A. Seyeux, L.H. Klein, P. Marcus, The Journal of Physical Chemistry C, 117 (2013) 21651-21661.

[5] I.T. Kim, A. Magasinski, K. Jacob, G. Yushin, R. Tannenbaum, Carbon, 52 (2013) 56-64.

[6] S. Laruelle, S. Grugeon, P. Poizot, M. Dollé, L. Dupont, J.-M. Tarascon, Journal of the Electrochemical Society, 149 (2002) A627-A634.

[7] P. Poizot, S. Laruelle, S. Grugeon, L. Dupont, J.M. Tarascon, Nature, 407 (2000) 496-499.

[8] M.V. Reddy, C. Yu, F. Jiahuan, K.P. Loh, B.V.R. Chowdari, ACS Applied Materials & Interfaces, 5 (2013) 4361-4366.

[9] M.V. Reddy, G. Prithvi, K.P. Loh, B.V.R. Chowdari, ACS Applied Materials & Interfaces, 6 (2014) 680-690.

[10] M. Gao, P. Zhou, P. Wang, J. Wang, C. Liang, J. Zhang, Y. Liu, Journal of Alloys and Compounds, 565 (2013) 97-103.

[11] X. Zhao, D. Xia, K. Zheng, Journal of Alloys and Compounds, 513 (2012) 460-465.

[12] Y. Hou, Z. Xu, S. Sun, Angewandte Chemie International Edition, 46 (2007) 6329-6332.

[13] M.V. Reddy, G.V. Subba Rao, B.V.R. Chowdari, Chemical Reviews, 113 (2013) 5364-5457.

Annexure 2

MnO exhibits high theoretical capacity of 755 mAh g^{-1} (which is more than twice the capacity of carbonaceous materials) and a low discharge-charge potential (around 0.5 V vs. Li/Li^+). Moreover, it is a low-cost material, naturally abundant and eco-friendly [1]. However, drawbacks such as low electronic conductivity and rapid capacity fading are observed in MnO electrodes owing to pulverization which is a consequence of volume changes upon lithiation and delithiation processes [1-3].

[1] Y. Liu, X. Zhao, F. Li, D. Xia, Electrochimica Acta. 2011;56:6448-52.
[2] M.V. Reddy, G.V. Subba Rao, B.V.R. Chowdari, Chemical Reviews. 2013;113:5364-457.
[3] S.M. Lee, S.H. Choi, J.-K. Lee, Y.C. Kang, Electrochimica Acta. 2014;132:441-7.

Annexure 3

Molybdenum dioxide (MoO_2) has attracted a great attention as an anode material in LIBs owing to its ability (theoretical capacity is ~838 mAh g^{-1}) to host Li in higher amounts than graphite either by intercalation or conversion mechanisms [1-11]. MoO_2 can be easily obtained by reducing MoO_3 [1,7]. In comparison to MoO_3, MoO_2 has superior electronic conductivity, less charging potential and higher volumetric capacity, which are highly important for considering it as an anode material in LIBs [1,7,9,12,13]. On the other hand, MoO_2 suffers from pulverization as a consequence of Li insertion and extraction, which blocks the electrical contacts with current collectors and leads to a rapid capacity decay making it eventually unfit as an anode material in LIBs [1,5,6,8,11-13]. Efforts have been made to overcome the drawbacks of MoO_2 by scaling down its dimensions to nanoscale. This reduces both electrical and ionic resistivity by shortening the transport lengths for both electrons and Li^+ ions [5,9,13-15]. In addition, nano-structuring offers higher surface reactivity inducing higher effective electrical contact area. However, previous research work on MoO_2 in this context has led to the realization that nanostructuring alone cannot eliminate the inherent problems for efficient lithiation as elucidated in this study.

[1] M.V. Reddy, G.V. Subba Rao, B.V.R. Chowdari, Chemical Reviews. 2013;113:5364-457.
[2] J.H. Ku, Y.S. Jung, K.T. Lee, C.H. Kim, S.M. Oh, Journal of the Electrochemical Society. 2009;156:A688-A93.
[3] X. Zhang, X. Song, S. Gao, Y. Xu, X. Cheng, H. Zhao, et al. Journal of Materials Chemistry A. 2013;1:6858-64.
[4] U. Kumar Sen, A. Shaligram, S. Mitra. ACS Applied Materials & Interfaces. 2014;6(16):14311-9.
[5] X. Zhao, M. Cao, B. Liu, Y. Tian, C. Hu. Journal of Materials Chemistry. 2012;22:13334-40.
[6] Y. Liang, S. Yang, Z. Yi, X. Lei, J. Sun, Y. Zhou. Materials Science and Engineering: B. 2005;121:152-5.
[7] L.C. Yang, Q.S. Gao, Y. Tang, Y.P. Wu, R. Holze. Journal of Power Sources.

2008;179:357-60.

[8] L.C. Yang, Q.S. Gao, Y.H. Zhang, Y. Tang, Y.P. Wu. Electrochemistry Communications. 2008;10:118-22.

[9] Y. Sun, X. Hu, J.C. Yu, Q. Li, W. Luo, L. Yuan, et al. Energy & Environmental Science. 2011;4:2870-7.

[10] Z. Yufei, Z. Yuxia, Y. Zhiyu, Y. Yiming, S. Kening. Science and Technology of Advanced Materials. 2013;14:043501.

[11] Y. Lei, J. Hu, H. Liu, J. Li. Materials Letters. 2012;68:82-5.

[12] Q. Tang, Z. Shan, L. Wang, X. Qin. Electrochimica Acta. 2012;79:148-53.

[13] Y. Sun, X. Hu, W. Luo, Y. Huang. ACS Nano. 2011;5:7100-7.

[14] L. Yang, L. Liu, Y. Zhu, X. Wang, Y Wu. Journal of Materials Chemistry. 2012;22:13148-52.

[15] J. Liu, S. Tang, Y. Lu, G. Cai, S. Liang, W. Wang, et al. Energy & Environmental Science. 2013;6:2691-7.

Annexure 4

Among the transition metal oxides, mixed bimetallic oxides (ternary metal oxides) possess high theoretical capacity and long cycle life and are therefore considered as interesting host materials for Li insertion. Moreover, since these oxides can be easily formed into different crystal structures, a large variety of them can be modeled and explored for Li insertion. In this context, molybdenum (Mo)-based oxides in particular, have proven their potential as anode materials in LIBs. These oxides exhibit rich electrochemistry associated with multiple oxidation states of the metal ions and high mass density which are favorable for improving the volumetric energy density of the anode. Few reports on $AMoO_4$ (A = Cu, Zn, Ni, Fe, Mn and Co) and A_2MoO_4 (A = Li, Na and K) type of materials [1-3] are available. Works on hexagonal MO_3-cluster compounds namely $LiHoMo_3O_8$, $LiYMo_3O_8$, $Mn_2Mo_3O_8$ and $Co_2Mo_3O_8$ are also available [4-6].

[1] N.N. Leyzerovich, K.G. Bramnik, T. Buhrmester, H. Ehrenberg, H. Fuess, Journal of Power Sources. 2004;127(1–2):76-84.

[2] C.T. Cherian, M.V. Reddy, S.C. Haur, B.V.R. Chowdari, ACS Applied Materials & Interfaces. 2013;5:918.

[3] S. Komaba, N. Kumagai, R. Kumagai, N. Kumagai, H. Yashiro, Solid State Ionics. 2002;152-153:319-26.

[4] B. Das, M.V. Reddy, G.V.S. Rao, B.V.R. Chowdari, Journal of Solid State Electrochemistry. 2008;12(7-8):953-9.

[5] B. Das, M.V. Reddy, C. Krishnamoorthi, S. Tripathy, R. Mahendiran, G.V.S. Rao, et al., Electrochimica Acta. 2009;54(12):3360-73.

[6] B. Das, M.V. Reddy, S. Tripathy, B.V.R. Chowdari, RSC Advances. 2014;4:33883-33889.

Annexure 5

GOs were synthesized from natural graphite (flake size ≤ 47 μm, Nacional de Grafite Ltda) by modified Hummer's method. Fe_2O_3 used in the present study was obtained by slow (3 ºC/min) heating of $FeC_2O_4 \cdot 2H_2O$ (Alfa Aesar #6047-25-2) at 600℃ for 6 hours in air. To prepare GO with low DO (GO1), each 1g of graphite flakes were dispersed uniformly in 25 mL of H_2SO_4 (95-97%, Sigma Aldrich, #7664-93-9) at a temperature less than 5℃ with the aid of an ice bath. Next, $NaNO_3$ (Sigma Aldrich, #7664-93-3) 0.5g and $KMnO_4$ (Ajax Chemicals, Sydney) 3g were mixed very slowly one after another as they mentioned. After stirring for 30 min at room temperature 25 mL of distilled water was poured into the reaction mixture. Subsequently internal temperature of reaction mixture raised to ~98℃ and stirring was continued at this elevated temperature for 1 h by external heating. Finally, 1 mL of H_2O_2 (35%, Riedel-de Haen) was added to the reaction mixture after cooling back to room temperature and allowed to settled down. Thus formed GO1 sediment was subjected to multiple washes with distilled water until its pH became ~7. In another independent experiment above mentioned process was repeated as it is except by changing H_2SO_4 (95-98%, Sigma Aldrich, #7664-93-9) and 50 mL of distilled water added (instead of 25 mL) in order to prepare GO with higher DO (GO2). Finally both GOs were filtered and dried for 12 h in a hot air oven at 80 ºC. Then, reaction mixtures GO1+Fe_2O_3 (RM1) and GO2+Fe_2O_3 (RM2) were prepared by taking 2mol of GO for each 1mol of Fe_2O_3. Bothe reaction mixture powders were mixed using mechanical grinding for 30 min. Molecular formula $C_{2.2}H_{0.8}O$ was adapted for GOs for molar calculations from elsewhere. Then both reaction powders about 6 g each were taken into separate ceramic boats and heated separately in a tube furnace (Carbolite, UK) as follows. Heating of both reaction powders was carried out in argon environment at a heating and cooling rate of 5℃ min^{-1}. Thermal annealing of reaction powders was performed in the temperature range of 650–750℃ and for 2–8 h. As a result of each heating a very smooth and black colored fine powder about 3 g of exfoliated GO/iron oxide/iron composite powders were obtained which further directly used for various morphological and structural characterizations.

Annexure 6

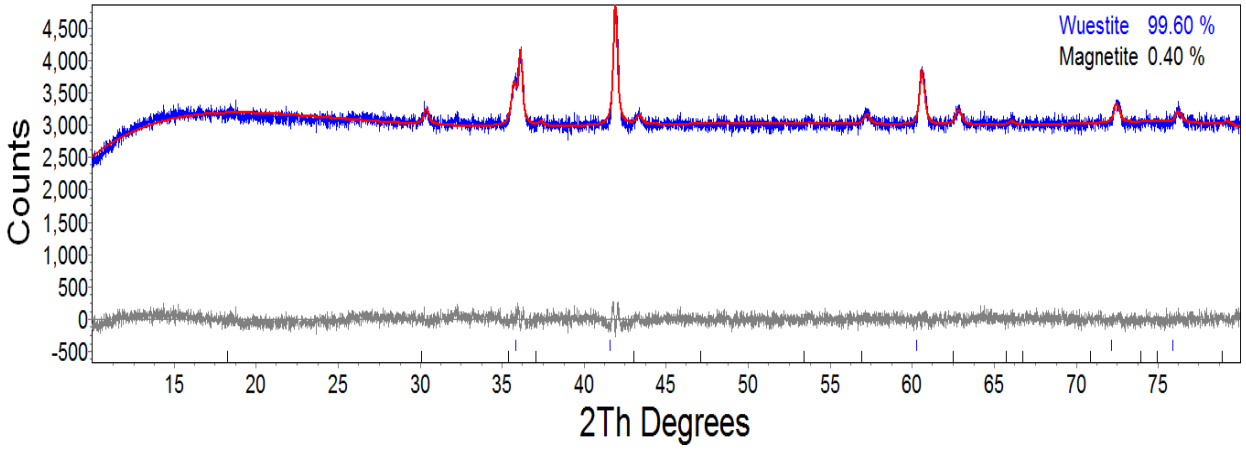

Rietveld refinement results of EG/FeO.

Annealing time and temperature effect on GO+Fe_2O_3 mixture:

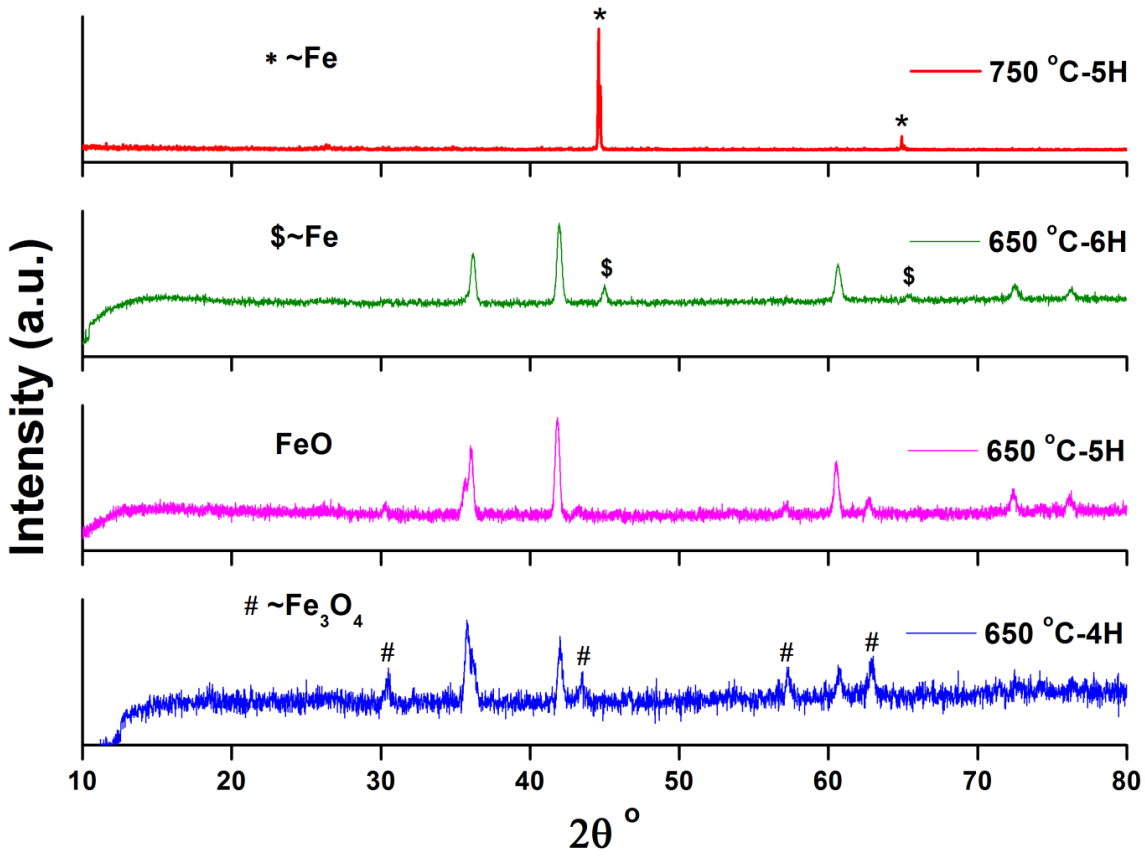

XRD patterns of GO+Fe_2O_3 mixture annealed at different times and temperatures.

Thermal gravimetric analysis (TGA): As shown in the below TGA curve, EG/FeO exhibited a initial weight loss upto 278.5 °C from where a small gain in weight is observed until 391 °C. This small increase in weight ~0.57% corresponds to oxidation of FeO. Then the curve steeply descended around 450 °C and loss in weight stopped at 596 °C and 87.93%. The remaining portion of TGA curve is unchanged up to 1000 °C with no significant loss in weight. Thus a net weight loss that corresponds to decomposition of carbon to CO/CO_2 is found to be 12.64 wt.% and remaining 87.36 wt.% belongs to FeO phase. Depending on these weight percentages the theoretical capacity of EG/FeO composite was calculated as follows:

Theoretical capacity of EG/FeO composite = (Wt.% of FeO X Theoretical capacity of FeO) + (wt.% of EG X Theoretical capacity of LiC_6)

= (0.87 X 744)+(0.13 X 372)mAh g^{-1} = 696 mAh g^{-1}

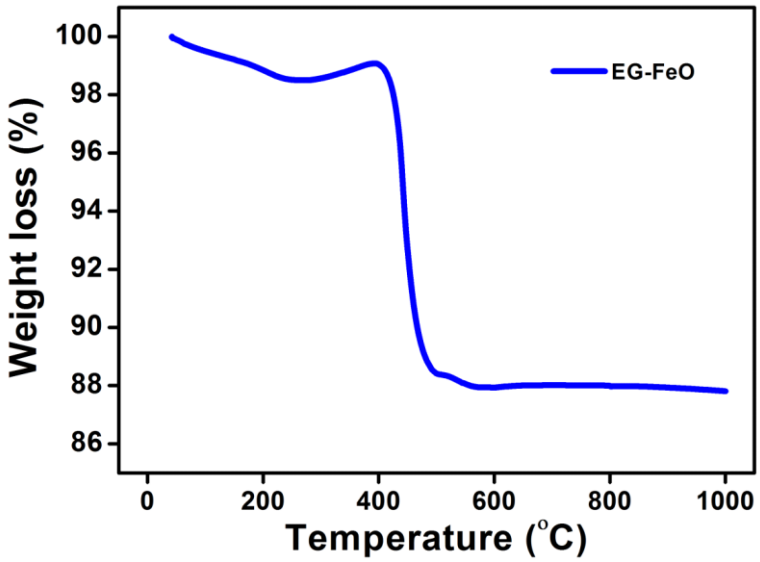

TGA curve of EG/FeO in Air with heating rate 10 °C/min.

I-V Characteristics of EG/FeO: I-V response of EG/FeO pellet is recorded in the range of -0.1 to +0.1 V (voltage step 0.01V) at room temperature (25 °C) with Keithley 2400 insturment. The slope (1/R) of (the curve shown in Fig. S4 is found to be ~2.69. Based on this slope value conducitvity of EG/FeO was calculated as ~0.23 $\Omega^{-1}cm^{-1}$.

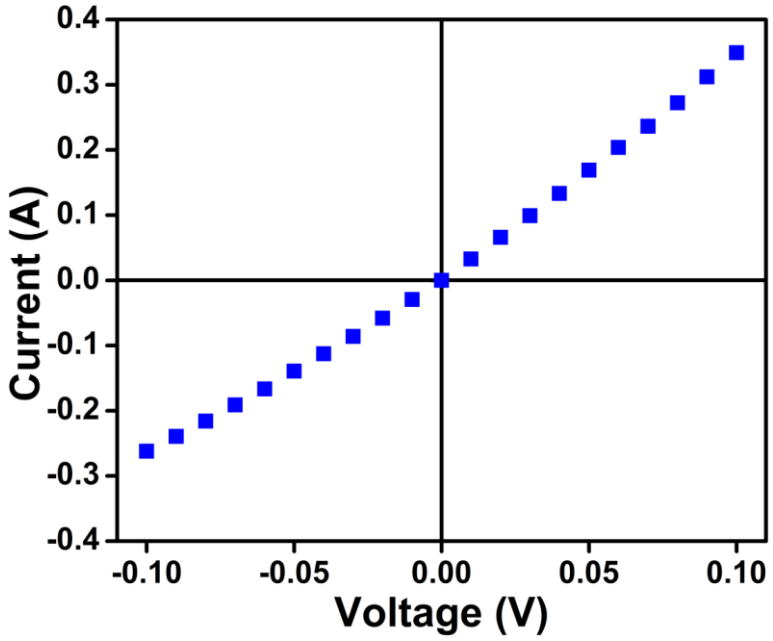

I-V characteristics of EG/FeO at room temperature.

Cyclability of EG/FeO in comparison with EG/Fe_3O_4 and EG/Fe_2O_3:

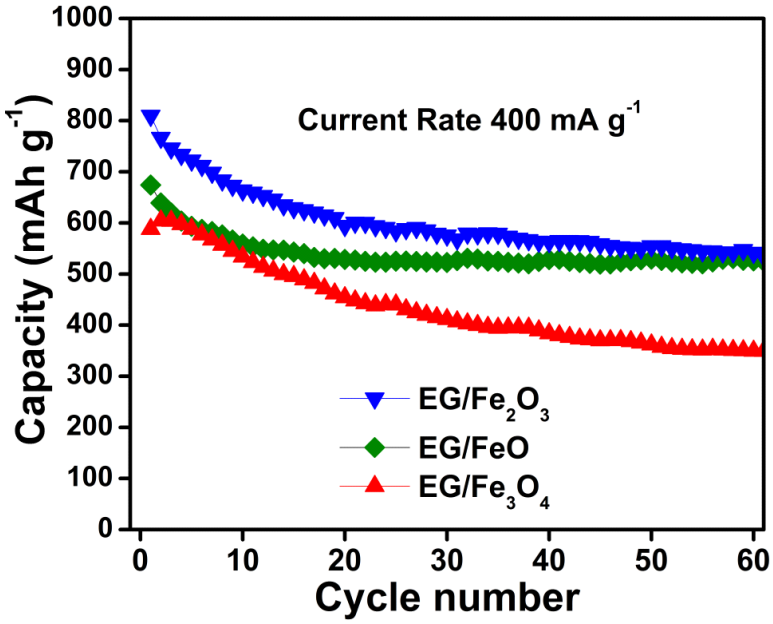

Charge capacities of EG/FeO, EG/Fe_3O_4 and EG/Fe_2O_3.

Annexure 7

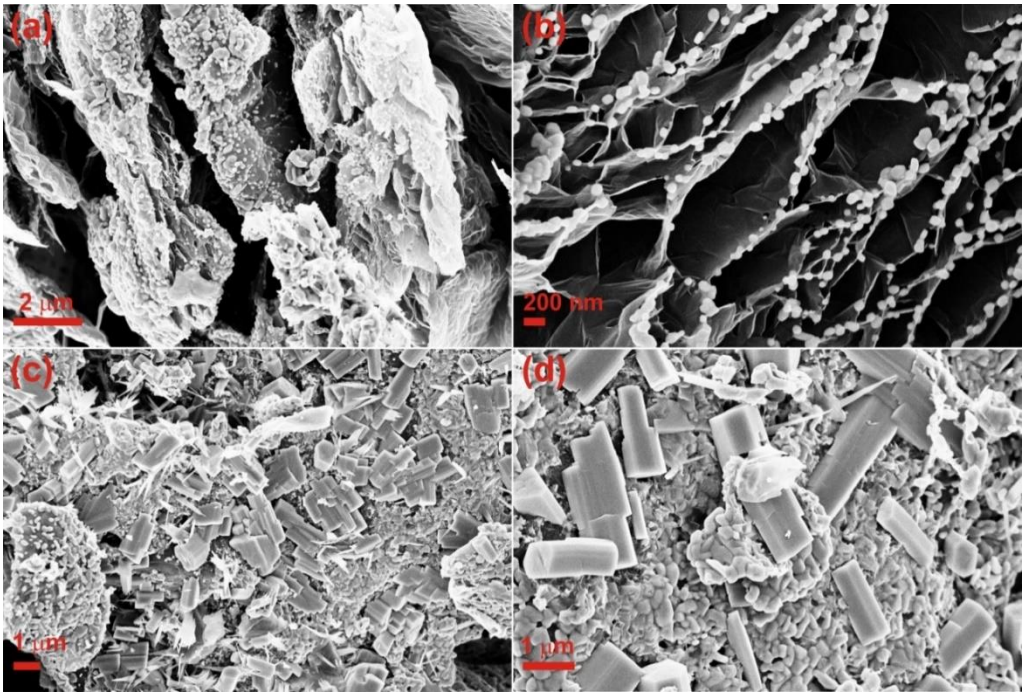

FESEM images of 2EG/MoO_2 at various magnifications.

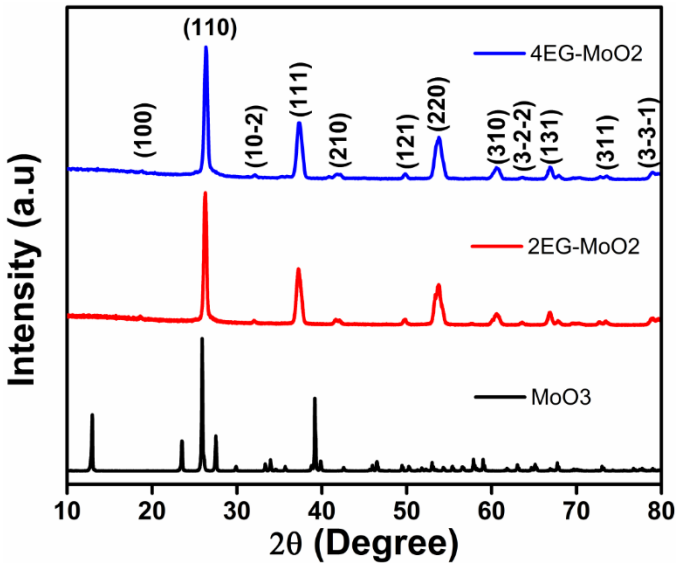

XRD pattern of 2EG/MoO_2 in comparison with those of 2EG/MoO_2 and MoO_3.

Rietveld refinement parameters.

Structure	2EG/MoO_2	4EG/MoO_2
Evaluated lattice parameters	a (Å) = 5.6133488 b (Å) = 4.8607358 c (Å) = 5.6275005 β (°) = 120.8861	a (Å) = 5.6207147 b (Å) = 4.8676393 c (Å) = 5.6355005 β (°) = 120.879
Crystallite size (Lorentzian)	~42 nm	~33 nm
Space Group	P21/c	P21/c
JCPDS file Number	JCPDS # 78-1069	JCPDS # 78-1069
R-Bragg	2.393	1.905

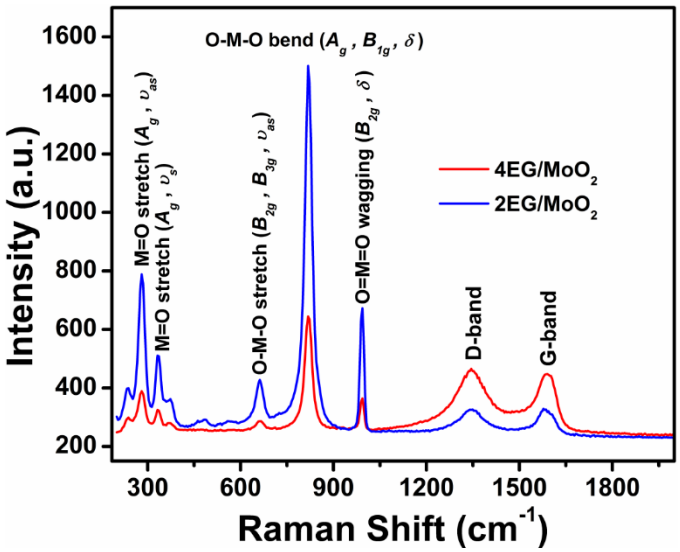

Raman spectra of 2EG/MoO_2 and 4EG/MoO_2 composites.

Specific surface area measurements: BET and Langmuir surface areas of 2EG/MoO_2 are found to be 3.15 and 4.43 m^2/g respectively. This small specific surface area might be due to the high synthesis temperature, inert nature of the agglomerated MoO_2 surfaces and also due to the covering of active surfaces of EG by MoO_2. The average pore volume is 0.0121 cm^3/g with average pore diameter of 15.63 nm. The moderate hysteresis between nitrogen

adsorption and desorption isotherms of EG/MoO_2 indicates that it possess mesoporosity which might be due to cavities and gaps formed between exfoliated individual graphene layers.

BET surface area and porosity details of EG/MoO_2 composites.

Composite	BET Surface Area	Avg. Pore Size	Avg. Pore Volume
2EG/MoO_2	3.15 m^2/g	~15.63 nm	0.0121 cm^3/g
4EG/MoO_2	71.4 m^2/g	~13.69 nm	0.244 cm^3/g

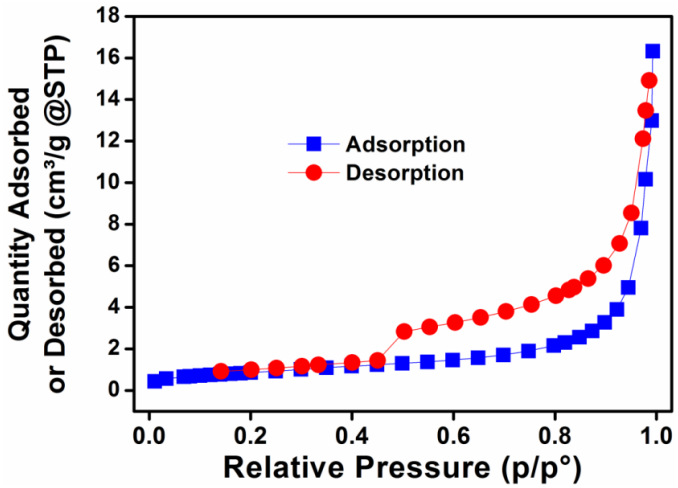

BET (N_2) adsorption-desorption isotherms of 2EG/MoO_2.

Galvanostatic Intermittent Titration Technique (GITT): To calculate the diffusion coefficients of cycled 4EG/MoO_2, GITT technique was used as follows. A discharge pulse of 50 mA g^{-1} was applied to the battery cycled at 1000 mA g^{-1} to discharge it to a selected voltage and subsequently battery was allowed to rest for 5 h and similar it was done during charging as shown in the Figure (next page). Next, the diffusion coefficient for each discharge and charge pulse was calculated by using formula given in Chapter 3 (section 3.3.5). The diffusion coefficients of battery cycled at 100 mA g^{-1} are also calculated using above process.

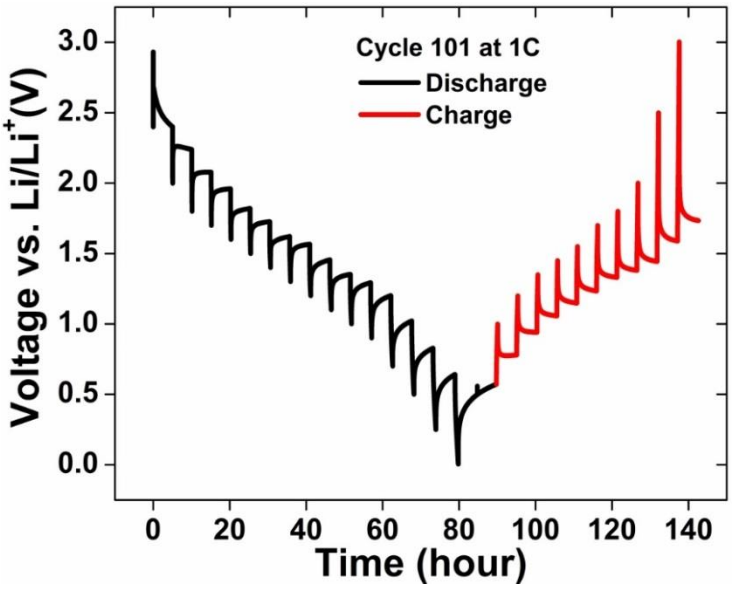

Discharge/charge GITT curves of 4EG/MoO_2 cycled at 1000 mA g^{-1}.

Electrochemical impedance spectroscopy results of EG/MoO_2 composites:

Simulated equivalent circuit component values of EG/MoO_2 composites.

	R_e (±0.1, Ω)	R_{ct} (±2, Ω)	CPE_{dl} (μF)	C_i (F)
2EG/MoO_2@OCV	5.1	98.4	38	0.027
2EG/MoO_2@1D	5.6	62.4	41	1.430
2EG/MoO_2@1C	5.4	20.6	170	0.029
4EG/MoO_2@OCV	4.1	79.32	26.6	0.014
4EG/MoO_2@1D	4.5	59.49	38.9	0.640
4EG/MoO_2@1C	4.1	14.77	320	0.070